Imperial College London

Flexible Robotic Device for Spinal Surgery

by

Samir Morad

A thesis submitted to Imperial College London in accordance with the requierement for award of the degree of Doctor of Philosophy and the Diploma of Imperial College London

Department of Mechanical Engineering

Medical Engineering

Imperial College London

June 2015

Declaration of originality

I declare that:

The content of this thesis is original and of my own work. All assistance received and sources of materials (data, theoretical analysis, figures, and text) have been acknowledged; and the work has not been submitted to any other institution for any degree or diploma.

Decleration of copyright

The copyright of this thesis rests with the author and is made available under a **Creative Commons Attribution Non-Commercial No Derivatives Licence**. Researchers are free to copy, distribute or transmit the thesis on the condition that they attribute it, that they do not use it for commercial purposes and that they do not alter, transform or build upon it. For any reuse or redistribution, researchers must make clear to others the licence terms of this work.

Abstract

Surgical robots have proliferated in recent years, with well-established benefits including: reduced patient trauma, shortened hospitalisation, and improved diagnostic accuracy and therapeutic outcome. Despite these benefits, many challenges in their development remain, including improved instrument control and ergonomics caused by rigid instrumentation and its associated fulcrum effect. Consequently, it is still extremely challenging to utilise such devices in cases that involve complex anatomical pathways such as the spinal column.

The focus of this thesis is the development of a flexible robotic surgical cutting device capable of manoeuvring around the spinal column. The target application of the flexible surgical tool is the removal of cancerous tumours surrounding the spinal column, which cannot be excised completely using the straight surgical tools in use today; anterior and posterior sections of the spine must be accessible for complete tissue removal. A parallel robot platform with six degrees of freedom (6 DoFs) has been designed and fabricated to direct a flexible cutting tool to produce the necessary range of movements to reach anterior and posterior sections of the spinal column. A flexible water jet cutting system and a flexible mechanical drill, which may be assembled interchangeably with the flexible probe, have been developed and successfully tested experimentally. A model predicting the depth of cut by the water jet was developed and experimentally validated. A flexion probe that is able to guide the surgical cutting device around the spinal column has been fabricated and tested with human lumber model. Modelling and simulations show the capacity for the flexible surgical system to enable entering the posterior side of the human lumber model and bend around the vertebral body to reach the anterior side of the spinal column. A computer simulation with a full Graphical User Interface (GUI) was created and used to validate the system of inverse kinematic equations for the robot platform. The constraint controller and the inverse kinematics relations are both incorporated into the overall positional control structure of the robot, and have successfully established a haptic feedback controller for the 6 DoFs surgical probe, and effectively tested in vitro on spinal mock surgery. The flexible surgical system approached the surgery from the posterior side of the human lumber model and bend around the vertebral body to reach the anterior side of the spinal column. The flexible surgical robot removed 82% of mock cancerous tissue compared to 16% of tissue removed by the rigid tool.

To my beloved parents

And

To my ... breath... heartbeat... and soul

Meina ... Mariam... & Jian

With love

Acknowledgements

This work would not have been possible without the support, guidance and drive of my supervisor Dr Ravi Vaidyanathan. He has always set the example by working very hard and being available to give support and advice whenever needed. His attention to details and constant quest for better results has truly helped me towards the completion of the work reported in this thesis. Thanks for believing in me and giving me the possibility to work in such a great and multidisciplinary environment.

I would like to thank Professor Kim Parker. His achievements are an inspiration and I consider myself fortunate to have had the opportunity to work alongside and learn from him. I would also like to thank Dr Christian Ulbricht for his great help, advice and patience as he introduced me to the field of spinal surgery and during all the work along the way.

Throughout this project, I have been very fortunate to work closely with exceptional persons. Thanks to Paul Harkin for his invaluable contribution in the construction of the robot platform. Thanks to Justin Chan for his incredible contribution in the control and haptic aspects of the system. Thanks to Philip Wilson for his excellent contribution in the manufacturing of the mechanical parts of the system, his enthusiasm to help and work hard until the last minute before the deadline was remarkable.

Many other people have contributed in different ways to the work presented here. I would like to thank Dr Ruth Brooker, Vimmendra Patel, Jianmo Li, and Asanka Munasinghe.

I would like to thank Professor Stuart Burgess and Professor Etienne Burdet for serving as my examiners, theire input has made the work stronger.

Table of Contents

List of Figures

15

23

List of Tables

List of Acronyms

AESOP	Automated Endoscope Optimal Positioning	MRI	Magnetic Resonance Imaging
AIM	Image-Guided Microstereotactic	MSS	Master-slave systems
AWJ	Abrasive Water jet	NBR	Nitrile Butadiene Rubber
CABG	Coronary Artery Bypass Grafting	NiTi	Nickel Titanium
CAD	Computer-Assisted Design	PCB	Printed Circuit Board
CAM	Computer-Assisted Machining	PD	Positive-Displacement
DC	Direct Current	PID	Proportional-Integral-Derivative
CFD	Computation Fluid Dynamic	PMU	Parallel Manipulation Unit
CIS	Computer-Integrated Surgery	PPSU	Polyphenylsulfone
CNC	Computer Numerical Control	PSU	Power Supply Unit
CT	Computerised Tomography	PTFE	Polytetrafluoroethylene
DDU	Distal Dexterity Units	PWJ	Pure/Plain Water Jet
DoF	Degrees of Freedom	QFD	Quality Function Deployment
FEM	Finite Element Modelling	RMA	Rutgers Mega-Ankle Robot
GUI	Graphical User Interface	RRR	revolute-revolute-revolute
HARP	Highly Articulated Robotic Probe	RPUR	revolute-prismatic- universal-revolute
HD	High Definition	SLU	Snake-Like Unit
IC	Integrated Circuit	SMA	Shape Memory Alloy
MARS	Miniature Robot for Surgery	SSR	Solid State Relay
MIS	Minimal Invasive Surgery	UPS	Universal- Prismatic- Spherical

1 Introduction

The integration of robotic technologies in surgical instrumentation has contributed to the further development of surgical procedures, aimed at reducing patient trauma and hospitalization costs. The main requirement for such procedures is the ability of surgical tools to reach the operative target through complex anatomical pathways. However, the use of long, rigid tools inserted into the patient via the small incisions typical in Minimal Invasive Surgery (MIS), can introduce a range of ergonomic challenges. The loss of wrist articulation together with the fulcrum effect, due to the inversion of motion direction at the trocar, strongly limits the manual dexterity of the surgeon.

Enhanced control and dexterity are the main benefits of using robotic technologies for MIS. Improved surgical instrumentation has been designed to compensate for the loss of wrist articulation caused by the traditional approach. Together with the introduction of master-slave control, this has contributed to the safety and consistency of MIS. However, even with the current robotic surgical systems, such as the da Vinci from *Intuitive Surgical Inc.*, the surgical tools used are still rigid and require careful port placement to ensure the required access and workspace for a given procedure.

The present generation of surgical tools is reliant on drills and cutting tools, which vary in their principles of operation. Several research projects explored the development of a tool capable of going around corners [1, 2]. However, most of these tools are non-surgical tools, and no one has done it for spine surgery.

The target application for the flexible surgical tool in this thesis is the removal of cancerous tumours surrounding the spinal column (Figure 1) [3].

This procedure targets the removal of cancerous tumours sitting on top of and around the lumber vertebrae. At present, the surgeon approaches the patient from the back of the body, and the tumour was removed only from the posterior side of the spinal column using the available rigid tools, which are typically hand-held. This approach, however, makes the removal of cancerous tissue on the anterior side of the spinal column extremely challenging. In extreme cases, the surgeon may attempt to remove additional tumour growth by entering

through the mouth or front part of the neck; however, this entails additional (typically unacceptable) risk for the patient and is extremely challenging for the surgeon.

Figure 1: Non-reachable cancerous tissue (red) on the anterior side of the spinal column (left) (Image source: Institute of spine physicians (3)), and photographs of the actual surgery taken as a part of this study.

This project proposes to develop specialised instrumentation to provide enhanced flexibility and stability in going around the spinal column for removal of tissue on both the anterior and posterior sides of the spinal column. The system is comprised of three components: the flexible surgical cutting device, the robot, and the control unit. The cutting device must be able to cut through and take the cancerous tissues off the bone/spinal vertebrae. The cutting devices integrated with the flexible device, which is able to bend to a J-shape configuration. A 6DoF parallel robot framework is developed to act as a mount for the flexible surgical cutting device, providing high stability, precision, and producing the desired range of movements. This has allowed the positioning and movement of the surgical device around the dorsal parts of the patient's body. The parallel platforms are of greater interst in this project over other types of platforms for its high stability, accuracy, and producing a movement within a desired workspace for surgical application of this project.The robot framework controlled through a computer-programmed interface using the haptic-enabled device as the physician input. A force feedback interface built within a computer simulation environment implemented to constrain the user/surgeon from moving the device beyond a pre-defined surgical control path. The depth of water jet cut studied experimentally and a method of controlling the depth was established.

The integrated units of the system would allow the removal of tumour growth on the anterior part of the spinal column without the need for additional invasive entry; thus, the risk to the patient would reduce considerably.

1.1   Key research challenges and objectives

The development of a flexible robotic device designed to address the clinical requirements presents a number of technical challenges. These summarised as:

1. Design and construct a miniaturised flexible device that has the ability to access through a small incision surrounded by critical tissues and then go around corners with minimum angulations of 90°.

2. Design and construct a surgical cutting device that must integrate with the flexible device and has the ability to dissect soft tissues.

3. Design and build a robot platform that used in operating theatre and has the ability to guide surgical tools in order to perform surgical procedures.

4. Develop a physician Tele-operative interface so that the operation controlled remotely. This will involve building an electrical/electronic system contain a number of components that controlled by a programmable position controller.

5. Develop and test a working positional control structure that incorporates haptic technology in a flexible surgical probe.

This thesis focused on addressing research issues related to the above engineering challenges. In the following chapters, a detailed description of the instrument design, and the system modelling, configuration, and validation will be presented.

Chapter 2 presents a detailed review of the relevant concepts, focusing on surgical robots and flexible instrumentation in surgery. In addition, an extensive review of key units that are involved in building the overall system were presented. These include water jet cutting technology, parallel manipulators, and haptic feedback technology.

Chapter 3 investigates preliminary solutions to Challenge 1 through designing a flexible probe prototype that matches all the clinical requirements. In this chapter, a complete engineering design process has been conduct to scope the features of the first prototype. The design process was carryout by applying a simple pairwise analysis and Quality Function Deployment (QFD) method. The design and fabrication of the prototype were extensively described. This was supported with the modelling and simulation necessary for analysing its design issues. Moreover, the prototype was experimentally tested and the outcomes discussed.

Chapter 4 focuses on designing a miniaturised flexible surgical cutting device (Challenges 1 and 2). This chapter considers a solution to limitations that appeared in the preliminary prototype. However, principles of the design of the preliminary prototype were applied in the designing and manufacturing of the new prototype during this chapter. Also, a flexible drill has been designed which is serving as a surgical tool that is integrated to the flexion device.

Chapter 5 describes the water jet cutting method as an alternative surgical tool that used for dissecting tissues (Challenge 1). This chapter includes a Computational Fluid Dynamic (CFD) study that performed to analyse the fluid parameters of the water jet system. In addition, this chapter will tackle some of the clinical challenges of using the water jet in surgery, such as controlling the depth of the water jet cut. This was done by conducting experiments followed by an analysis of the results.

Chapter 6 describes the design and fabrication of a parallel six degrees of freedom (DoFs) manipulator (Challenge 3). This robot was then integrated with surgical tools that were designed in Chapters 3 and 4. The environment of the operation theatre was taken into consideration when designing the surgical robot such that it fits in the operation theatre setup without blocking the vision and hands of the surgeon and his/her assistants.

Chapter 7 describes the implementation of all the hardware and software necessary to control the movement of the surgical robot (Challenges 4 and 5). This includes gathering all the electronics in a single printed circuit board (PCB) and using Arduino and MATLAB software to build the entire coding essential for the function of the system. Also, a haptic feedback method is applied to perform safe surgical procedures (Challenge 5). The haptic feedback method is based on regional constraints, in which the end effector of the surgical robot is controlled in the way that it is prohibited from entering forbidden regions of the surgical field. This work supported with all the calculations, analysis, and mock surgery required testing the feasibility of such a method. In addition, the active regional constraint method combined with the outcomes of the experimental analysis of measuring the depth of water jet cut, obtained in Chapter 5, to develop a robust method of controlling the depth of the water jet cut.

Finally, **Chapter 8** summarises the main technical achievements of the thesis and the potential pitfalls of the existing approaches. Future research directions for the flexible robotic devices for spinal surgery are also outlined.

1.2   Original Contributions of the Thesis

The original technical contribution of the thesis, which describes the first surgical robot used in the removal of cancerous tissue around the spinal column, includes:

I.   Flexible surgical tool:

- Development of a flexible probe that is able to navigate through complex anatomical structures and integrate with other surgical tools.

- Principles of the design of a flexible surgical drill that is able to navigate around small bones were established.

- Development of a novel flexible surgical water jet system that is able to go around corners and dissect tissues in the application of spinal surgery. This method may support surgeons in approaching challenging spinal surgeries in a safe and effective manner.

- The characteristics of the depth of the water jet cut were experimentally measured and a practical method of controlling the depth of the water jet cut was identified.

- The principles of haptic control of the depth of the water jet cut were established. This is done by combining the experimental results of measuring the depth of the water jet cut with the haptic feedback method of controlling the movement of the tool by applying the active regional constraints.

II.   Parallel robot manipulation:

- Development of a 6DoF parallel robot, designed with novel connector joints, using flexible, slightly elastic cord instead of universal or spherical joints, which gives high flexibility and smooth robot motion. This design may be particularly suitable for use in medical applications.

- The robot platform could integrate with various external surgical tools for the removal of cancerous tissue around the spinal column.

III.   Human-robot machine interface:

- A system that controls the 6 DoFs motion of the robot manipulator has been designed with the aid of a force feedback system.

- Development of a single user interface such that it controls all the functions of the surgical robot system, including: control the movement of the robot end effector,

control the flexible probe's articulation of the flexible probe, and control the water jet system's operation.

- The resultant robust control algorithm may directly apply to a variety of robot architectures.

The work presented in this thesis has resulted in a number of publications in conference proceedings. The main publication papers related to this thesis include:

- S. Morad, C. Ulbricht, P. Harkin, J. Chan, K. Parker, and R. Vaidyanathan (2014). Flexible Robotic Device for Spinal Surgery. Proceedings of the IEEE International Conference on Robotics and Biomimetics, 253-240.
- Institute of Mechanical Engineers. 2015. Kinetic Frame Needs New Backers. (ONLINE) Available at: http://www.imeche.org/news/engineering/kinetic-frame-needs-new-backers.
- S. Morad, C. Ulbricht, P. Harkin, J. Chan, K. Parker, and R. Vaidyanathan (2015). Modelling and control of a water jet cutting probe for flexible surgical robot. IEEE International Conference on Automation Science and Engineering. (to be presented)

2   Literature Review

2.1   Surgical Robotics

The present improvement of surgical robotics is the result of extensive research in the field of robotics and Tele-robotics over the past five decades. The involvement of robotics in surgery begins with the PUMA 560 robot by *Kwoh et al.* [4] in the mid-1980's to perform a CT-guided brain biopsy. Soon thereafter, *Davies et al* [5] performed a transurethral resection of the prostate using the PUMA 560. This system eventually led to the development of PROBOT which was developed at Imperial College London specifically to aid the resection of prostate tissue [6]. In 1991, the first system to provide image guidance in real-time, Minerva, was designed at University of Lausanne, Switzerland, to direct tools into the brain under real-time CT guidance [7, 8]. In 1992, *Integrated Surgical Supplies Ltd.* introduced ROBODOC which is used in Orthopaedics to aid in total hip replacement [9-11]. Further development of robotic systems was carried out by *Intuitive Surgical Inc.* with the introduction of the da Vinci Surgical System [12] and *Computer Motion Inc.* with the AESOP [13] and the ZEUS [14] robotic surgical systems.
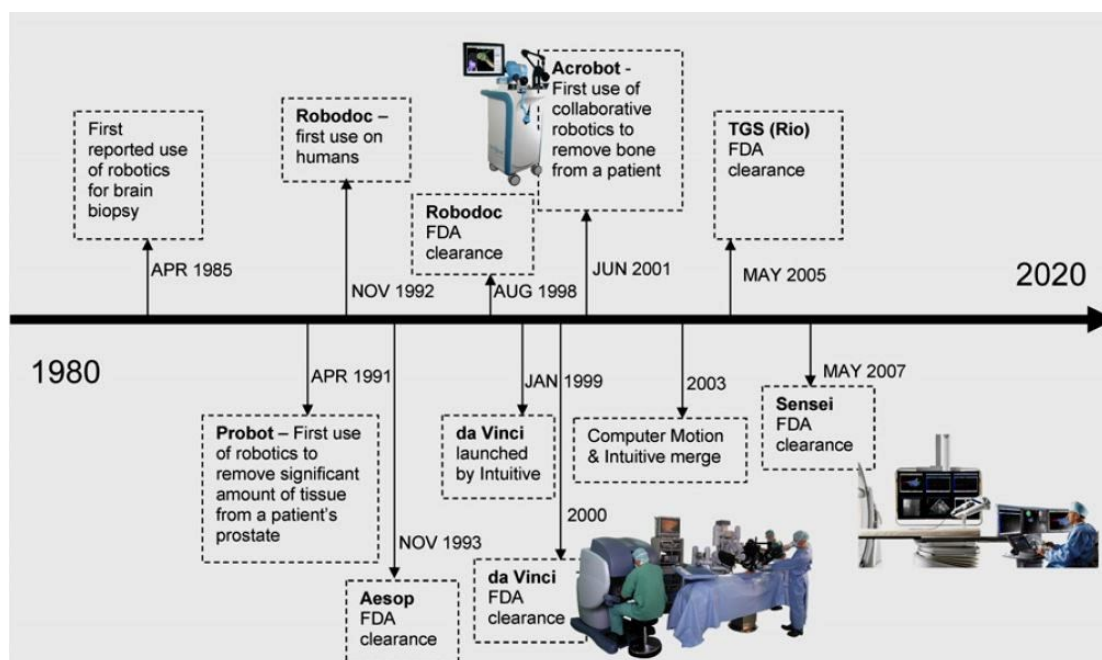
Figure 2: Timeline of the development of the surgical robots from using the robot for brain biopsy in 1985 to the development of robotic catheter system in 2007. (Image source: Gomes (13))

Figure 2 [15] shows the time line of the development of the surgical robots. An extensive research report into the history, development timeline, and applications of the surgical robot can be found in [15-19]

Due to the strong interdisciplinary nature of surgical robotics, it is challenging to define a distinctive classification that combines both technical features and clinical applications.

In the field's literature, many authors have attempted to categorise surgical robotic systems developed in the last three decades into specific groups [16, 18-22]. Surgical robots can be classified in different criterions according to *Taylor* [23]. These criteria based on the surgical robot's clinical applications, its role during the surgical operations, and the level of interaction with the surgeon.
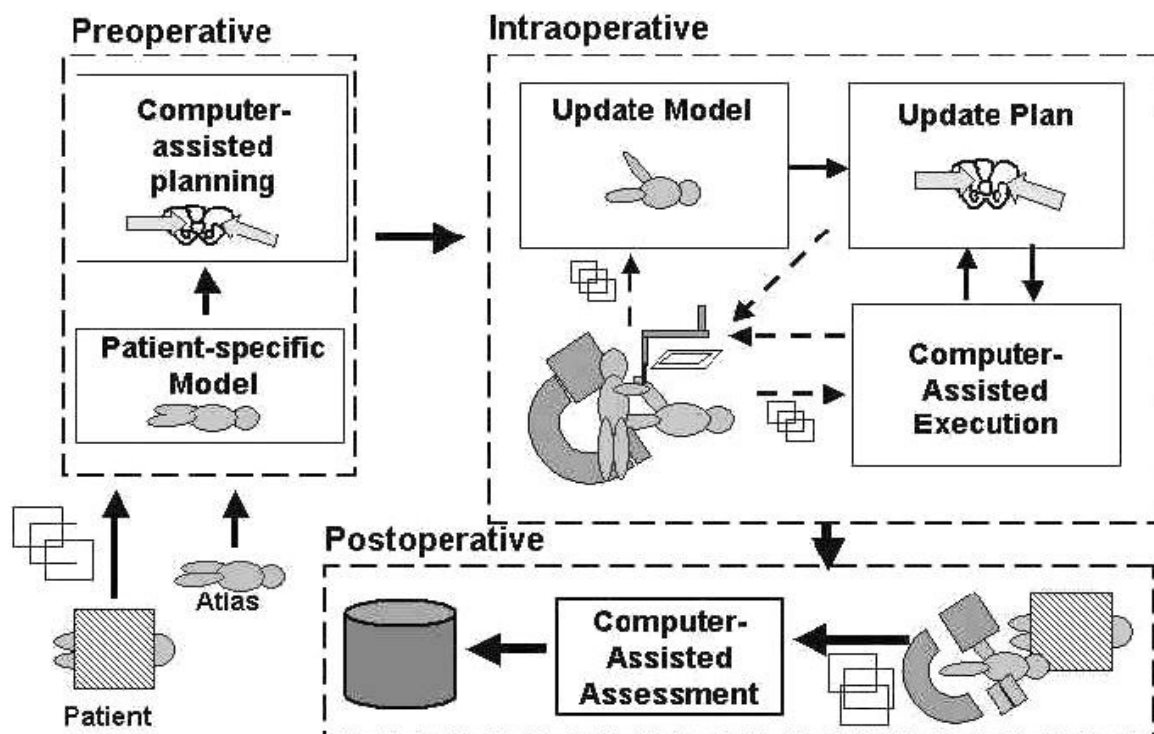
Figure 3: Information flow of Computer-Integrated Surgery (CIS) systems. The figure highlights the three main stages of the procedure: preoperative, intraoperative, and postoperative. (Figure source: R.H. Taylor (21))

A different classification has focused on the role of surgical robots within the broader perspective of Computer-Integrated Surgery (CIS), which may comprise successive stages, which include preoperative planning, intraoperative registration, and postoperative verification (Figure 3). CIS systems were divided into two families: surgical Computer-Assisted Design/Computer-Assisted Machining (CAD/CAM) systems and surgical assistants.

Samplers for both CAD/CAM and surgical assistant systems can be found in Appendix 1.1 and 1.2 respectively.

For the purpose of this thesis, and to provide the relevant background, the surgical robots were classified according to their level of interaction with the surgeon. The focus of this section will be on master-slave systems as it is the most representative systems that are relevant to the work carried in this thesis.

Surgical robots can be classified into three categories [21]:

I.   Semi-Autonomous Systems:

Preoperative planning along with graphical representation, obtained by an imaging device (e.g., CT, MRI) of the anatomy was employed to specify the tool path of the surgical robot operating in this category. It is followed by registering the locations of the anatomical structure and the robot. The task is then completed by the robot using position commands without any further involvement of the surgeon who can only stop the action for safety reasons. This type of surgical robots is applied to surgical procedures with well-constrained anatomical structures such as hard tissues and bones or with soft tissue such as the brain [21].

II.   Guided Systems:

These systems are operated directly by the surgeon in cases where high precision is required, such as microsurgery, ophthalmology, or urology. The surgeon interacts directly with the robot arm, which provides stable and precise tool movements. These systems are supported by force/torque sensors to sense the forces and torques applied by the surgeon's hands [20].

III.   Tele-operation or master-slave Systems:

Surgical robots are not designed to replace surgeons in the operating theatre. Surgeons, with their observational and decision-making skills, are still the key element for taking charge during surgeries. Surgical robots are established to support and enhance the surgeon's capability and not to replace them [24]. Master-Slave Systems (MSS) unable to move independently without guidance from the surgeon since the surgical robot replicates the motion of the surgeon's hands. As the action of the surgeon is physically separated from the robot, this control modality is considered as Tele-operation and has the potential for treating patients from afar. Since the surgeon is in control in most surgical robots, MSS are designed to provide an effective human-robot interface to perform procedures with high precision and

accuracy. In addition, these systems were built to be intuitive, simple and ergonomic, because most surgeons are not specifically used to working with robots.

The main components of MSS are the surgical console and the robot [10, 22]. The typical operation of Tele-operation system is described in Figure 4. At the surgeon's console, three-dimensional (3-D) visual information from the operation area is displayed. The surgeon moves the input device (the master), which is registered to the coordinate frame of the 3-D monitor, to produce position commands for the robot.
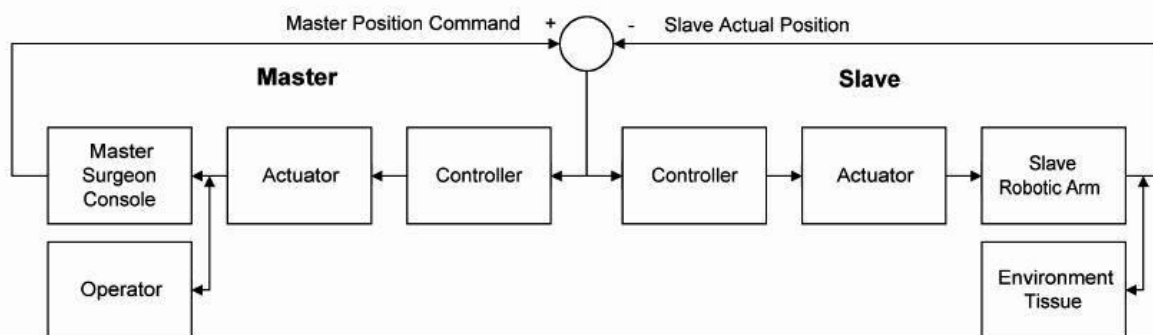
Figure 4: A block diagram of a typical Tele-operation system. The surgeon controls the movement of the robot (slave) via moving the user interface (master). (Figure source: J.E. Speich (19))

The controller transfers the positional commands to the surgical robotic manipulator (the slave), which is moved accordingly to the desired positions. To enable the surgeon to feel the forces between the tool and the tissue, some systems incorporate force feedback devices.

Since many MSS have been developed, I focused on innovative features, differences and state of the art technologies of some MSS.

The most common Tele-operated surgical system currently available on the market is the da Vinci surgical system. The main features of the system are as follows: The robot manipulator has 7 DoFs for positioning and orientation yielding natural manipulation of the tool. With many interchangeable end effectors, the tool can pass through small incisions. With a 3-D display receiving the visual information from the operating field through the stereoscopic cameras at the tip of the endoscope, the surgeon is allowed to have a 3-D image inside a patient body, and have natural handeye coordination while performing surgery. Additional features that come with the da Vinci master-robotic system are the ability to eliminate the surgeon tremors and motion scaling capability [6, 10, 22, 24]. However, limitations of the system include high cost and a lack of haptic and tactile feedback [10, 25].

The ZEUS Tele-operated surgical robot [11, 23] was developed in parallel to the da Vinci system. The main feature that makes ZEUS different from da Vinci is that its end effector has 5 DoFs. The ZEUS surgeon console has force feedback, an anti-tremor facility, motion scaling, and control of the slave with voice commands. Eventually, the ZEUS system was withdrawn from the market in favour of da Vinci in 2003.

In neurosurgery, *Hongo et al.*[26] have developed NeuRobot, a Tele-controlled system for microsurgery. Together with the slave micro-manipulator and the master device, the system comprises a 6 DoFs manipulator-supporting device and a stereo display monitor. The slave manipulator features three forceps and a 3-D endoscope. Each micro-manipulator is then remotely controlled during the procedure by 3 DoFs levers.

2.1.1 Benefits of Robot Integration in Surgery

The evolution of surgical robots was achieved through a number of consecutive generations. Many issues were improved from one generation to another [17, 27]; these include the invasiveness, accidental tissue damage and surgical dexterity. In this section, the advantages of robots integrated into surgery were presented.

The necessity of protecting humans from direct interactions with hazardous objects such as poisonous and radioactive materials was the main motivation of developing robots in industry [28]. Since the introduction of Tele-operator systems in the 1940's; robots have been used in various industrial applications and other areas such as space exploration, military application, oceanographic exploration, education, and currently surgery [18].

The concept of surgical procedures was significantly improved in the late 1980's with the development of Minimally Invasive Surgery (MIS). The MIS technique, which is based on inserting special instruments and vision devices into the body via small incisions, has helped the surgeon perform operations without placing their hands within the body [16]. This technique has been widely adopted and benefited the surgical procedures by reducing surgical trauma, recovery time, and hospitalisation cost [29]. However, MIS procedures were only applied to relatively simple applications due to substantial limitations compared to conventional instruments used directly by surgeons such as loss of wrist articulation, poor touch sense, and loss of 3-D vision [17, 22]. The involvement of robots in surgery was initially proposed to eliminate most of these impediments.

The advantages of robots in surgery often come from comparing their strengths and weaknesses to the human surgeon (Table 1). The main difference is that robots can precisely integrate a large amount of quantitative data through different sensors, hence being able to perform and repeat repetitive tasks with good stability and positional accuracy. On the other hand, surgeons are superior in combining various sources of qualitative information for making challenging decisions. Therefore, combining the human's advanced tactical thinking and decision-making with robot's high precision and accuracy into one system could provide great benefits to surgical procedures [21].

Table 1: Strengths and weaknesses of robots compared to human [18, 30]

	Strength	**Limitation**
Human	- Strong hand-eye coordination - Flexible and adaptable - Good judgment - Ability to use qualitative information - Task versatility - Dexterous (at human scale) - Many sensors with seamless data fusion	- Prone to physiological tremors and fatigue - Limited geometric accuracy - Susceptible to radiation and infections - Limited ability to use quantitative information - Limited dexterity outside natural scale
Robot	- Repeatability - Stability and good geometric accuracy - Manage multiple simultaneous tasks - Resistant to radiation and infection - Can use diverse sensors - Optimized for a particular environment - Spatial transformations handled with ease	- Poor judgment - Limited dexterity and hand-eye coordination - Expensive and large - Low versatility - Inability to process qualitative information

Surgical robotic systems are mainly designed to make possible surgeries that were otherwise technically difficult and impractical. The widely deployed surgical robots are the consequences of delivering real benefits. The most important one is the ability of surgical robot systems to significantly develop the technical skill of the surgeons by making the

procedures more precise, faster, and less invasive. Secondly, is the potential of a surgical robot system to support surgical safety, including improving the technical performance of complex procedures, on-line monitoring and information support; and preventing robots from moving tools in unsafe proximity to subtle anatomical structures. Finally, is the ability of surgical robots to promote consistency while captures detailed online information for every procedure.

The general improvements that made the use of robots feasible in surgery are described here. The robotic systems enhance dexterity by increasing the degrees of freedom which has greatly improved the surgeon's ability to handle instruments and, therefore, the tissues [31]. Filtering out physiological tremor through suitable hardware and software, and adjustable motion scaling has helped to increase precision as large hand movements can be converted to smaller tool motion [28]. Also, the simultaneous movement of robotic instruments and the surgeon's hands eliminates the counter-intuitive fulcrum effect observed in laparoscopic surgery [32]. Another advantage is the restoration of appropriate hand-eye coordination and an ergonomic position.

To further increase the safety of robotic surgical systems, the concept of Virtual Fixtures (VFs) for Tele-manipulation has been introduced by *Rosenberg* [33]. These can be described as perceptual overlays designed to reduce the workload of processing certain sensory modalities while performing a remote manipulation task.

In practice, two types of VFs can be generated: Forbidden Region VFs (FRVFs) and Guidance VFs (GVFs). FRVFs are used to keep the robot end-effector within a safety region defined pre-operatively by providing a strong reaction force when the operator reaches the surface boundary. GVFs are instead soft attractive forces aimed to guide the operator hand motion so that the robot end-effector follows a pre-defined virtual pathway. However, the haptic interface always leaves the operator in full control of the robotic manipulator [34]. Therefore, systems implementing VFs can be described as 'cooperative' or 'synergistic' control systems.

The concept of VFs in collaborative manipulation has also been advanced by *Davies et al.* [35], who introduced the so-called 'active constraints' by gradually increasing the haptic stiffness when the end-effector approaches the pre-defined forbidden region. The research group at *Imperial College London* developed the first active constraint robot for orthopaedic surgery known as Acrobot.

Recent progress in robotic surgery involves the integration of advanced imaging such as 3-D cameras. This technique, along with depth perception and controlling the stable visual field with increased magnification, has improved tissue features and further navigation clues [31, 36].

Also, specific design have been developed to maximise performance, including miniature robots, and articulated tools incorporating an additional degree of dexterity to allow great flexibility [37]. Many efforts have been devoted to the development of Tele-operated surgical systems where the surgeon can benefit from visual feedback at the master console, and highly dexterous slave manipulators [36]. Some surgical robots, such as da Vinci (Figure 5) [12, 38] can be used for a number of surgical tasks including cardiac, abdominal, and urologic procedures.
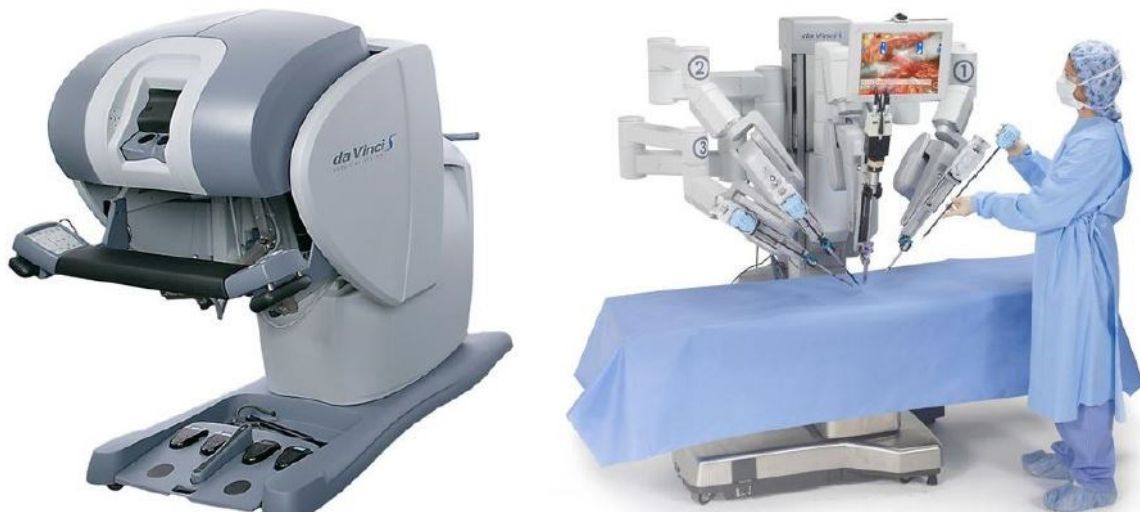
Figure 5: da Vinci surgical robot system. da Vinci S Master Console (left) with patient side Slave Unit (right). The surgeon sits at the master console and their hand motions are mapped to the miniature instruments on the slave. The large footprint of the system can be clearly seen. (Image source: Intuitive Surgical Inc.)

Other surgical robot systems are designed for specific surgical tasks, such as Eye-Rhas (Eye-Robot-for-haptically-assisted surgery) which is used for Vitreoretinal[1] Eye Surgery (Figure 6) [39, 40], and prostatectomy [5].

All these advantages of robots in surgery, from creating images with increased resolution, the increased degrees of freedom and enhanced dexterity, greatly enhances the surgeon's ability to identify and dissect anatomical structures, as well as to conduct microscopic operations.

---

[1] Specialized ophthalmic technique used in the surgical repair and or treatment of disorders that include retinal tears or detachment.
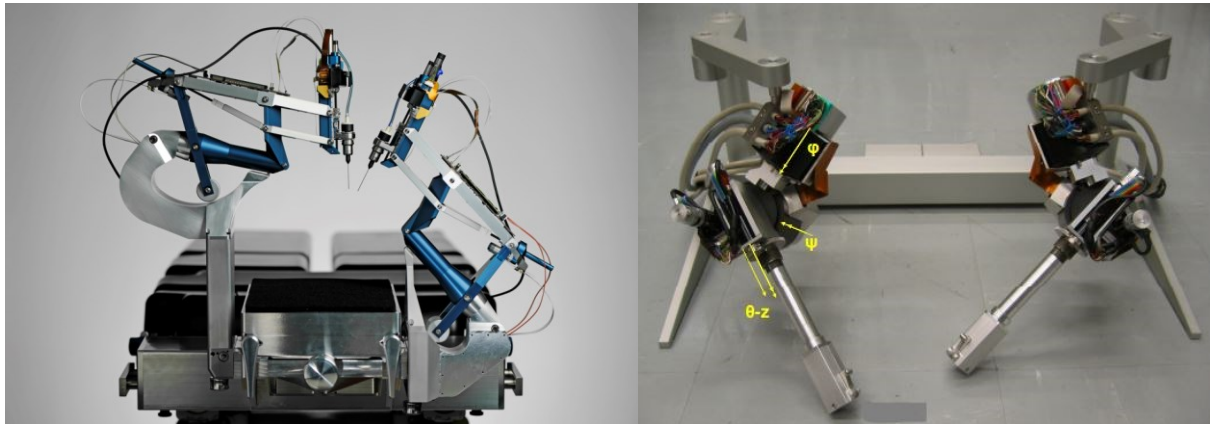
Figure 6: The Eye-Rhas system used for Vitreoretinal eye surgery robot. The master device (right) is two 5 DoFs haptic interface (φ, $\psi = \pm 45°$, Z = 30 mm, and $\theta = 360°$). The slave device (left) is a multiple instrument manipulators equipped to perform a complete intervention. The slave is adjustable to position the instrument manipulators over either the left or right eye. (Image source: H. Meenink (39))

2.1.2 Limitations and Technical Challenges

The above review introduces some of most successful surgical robotic systems, which have been integrated into the operating theatre and their effect in improving the surgeon's performance and patient outcome. However, the design of surgical robots has been related to the capabilities of industrial robots, therefore, their function is limited to provide precision cutting and tool holding and positioning. While the integration of autonomous navigation capability and the introduction of synergistic control systems has the potential to improve the clinical applicability and enhance the performance of the surgeon in terms of both accuracy and safety, their application is restricted to specific procedures with highly structured and static environments, due to the challenges of designing an active constraint which can adapt in real-time to the deforming tissue.

Master-slave systems may become the preferred control scheme due to their ability to overcome many of the issues related to the traditional approaches. The use of ergonomic user interfaces and computerised kinematic planning have reduced the fulcrum effect. In addition, tremor removal and motion scaling have led to the precise motion control of the device tip. Further developments in imaging and on-screen vision technologies have boosted the capabilities of the master console.

Despite the many advantages stated earlier, the lack of force control and haptic feedback are still the main weaknesses of master-slave systems [25]. Haptic sensing requires miniaturised sensors to be embedded in the surgical tool. Hence, implementing these sensors needs practical considerations of biocompatibility and sterilisation. For this reason, the current

research consideration has logically moved from haptic sensing to haptic rendering, which is the process of computing and generating forces in response to user interactions with virtual objects in real time [41]. However, due to the computational cost that is required for both graphics and haptic rendering in real time, this technique has not considerably improved since the launch of the da Vinci surgical system in 1999. Instead, the main innovative feature of the last version of the system has been associated with achieving better visualization in developing 3-D high definition (HD) cameras, and the integration of extra master console. Nevertheless, applications of the master-slave system remain limited, with an insignificant range of procedures. This is due to the limited reachable workspace of the rigid tools used for the procedures, which typically involve complex anatomical pathways.

Extending the benefits of surgical robots will require advances in mechanical design, sensing, and control systems, along with further miniaturization of actuation technology, which is essential for the development of versatile systems with greater flexibility. Advances related to control and manipulation fundamental to any multi-DoFs actuation mechanism were predicted. Recently, research in medical robotics has been trying to address these issues within the development of flexible robotic devices.

2.1.3 Flexible Robotic Devices: Medical Applications

As stated in previous sections, a key limitation of current surgical robotics is the restriction imposed by the use of rigid tools presented through a fixed point. As a result, the workspace of these tools is limited. Hence, the inability of rigid devices to follow curved pathways has limited the number and type of procedures suitable for robotics. To overcome this restriction, flexible tools can be used instead, and this section will present an overview of currently available flexible medical robotic devices. These devices can be classified depending on their medical application, such as endoscopy, cardiac intervention, laparoscopy, and orthopaedic surgery.

The difficulty of inserting the endoscopes through narrow, complex paths was the main consideration that led to the design of the active endoscope by *Ikuta et al.* in 1988 [42]. A schematic of the system is shown in Figure 7. The system comprises five segments, each of which is Ø13 mm, 40 mm in length and is capable of bending 60° in one plane. Pairs of shape memory alloy (SMA) coil springs arranged around a central stainless steel coil spring provide actuation. The SMA coils are indirectly cooled via a cooling water tube, located at the centre of the segments, to improve the system's speed safety. The device integrated with the

endoscope and, therefore, provides image feedback, but there is no passage of interventional instruments due to insufficient space.
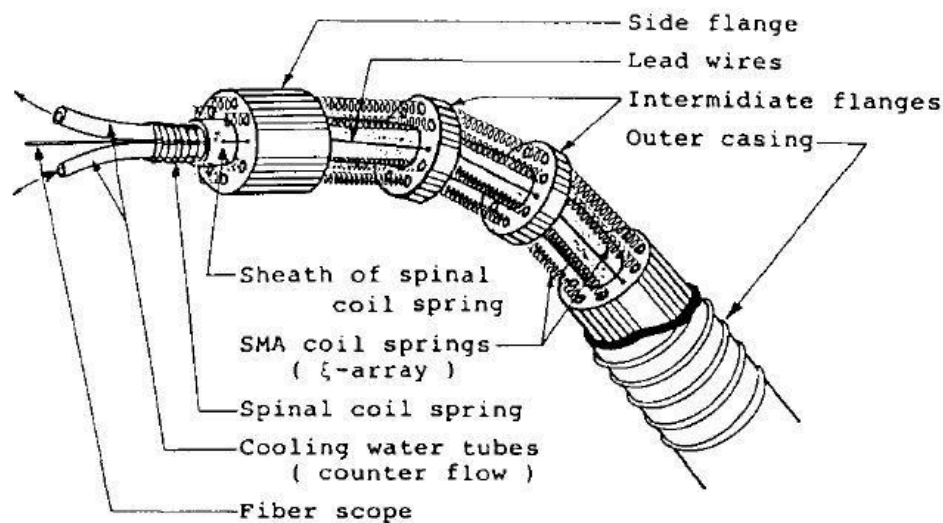
Figure 7: Configuration of the shape memory alloy actuated 'Active Endoscope' which provides five degrees of in-plane actuation from its proximal joint segments and two degrees of freedom at its distal segment. (Image source: *Ikuta et al.* (42))

Although the system represented many technological accomplishments, ultimately its applicability was limited due to the reduced number of DoFs and complications in accurately controlling the SMA actuators. Nevertheless, this medical robotic device represents one of the earliest flexible devices for medical applications.

The NeoGuide Endoscopy system from *Neoguide Systems Inc*. [43] has further explored the idea of an "Active Endoscope". The system (Figure 8), which is used for colonoscopy, features sixteen steerable segments, which follow the steerable tip through the colon.

Figure 8: The console of the NeoGuide Endoscopy System contains the video control, light, and insufflation functionality in addition to motors that control the segments in the insertion tube. (Image source: Neoguide Systems Inc. (43))

The highly dextrous system and provision of a Ø3 mm internal channel would be very suitable for flexible access surgery; however, the system ended up being long and heavy because it was designed for travelling the length of the colon.

The Hyper Finger remote system has been developed by *Ikuta et al.* [44] for laparoscopy. The system is one of the smallest master-slave robots in medicine. The finger size is Ø10 mm and has 9 DoFs. It comprises four links, connected together by universal joints, and a detachable gripper.
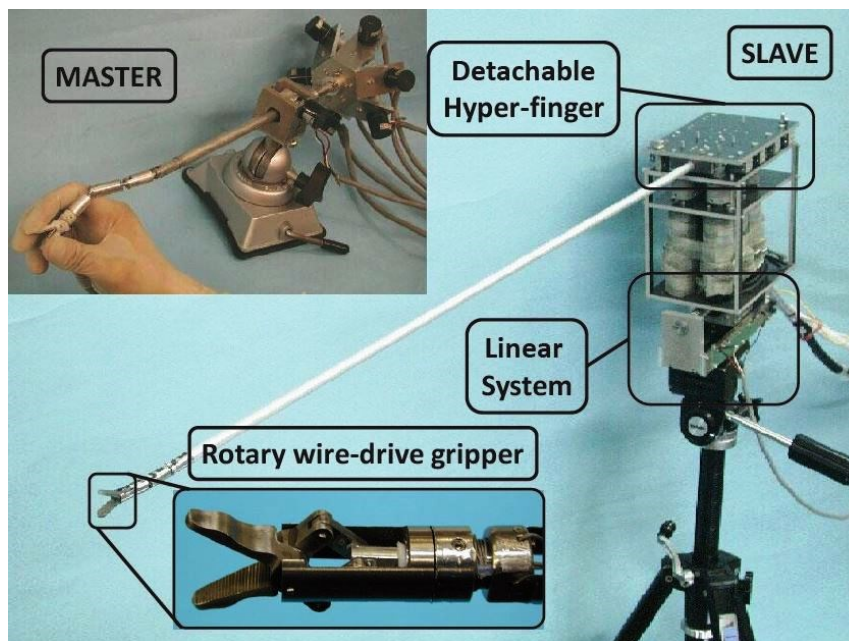
Figure 9: Clinical size prototype with 9 DoFs of the *Hyper Finger* system mounted on a camera tripod. (Image source: *Ikuta et al.* (44))

As shown in Figure 9, the slave manipulator is mounted on a stand featuring a system for linear positioning. The system also incorporates a compensation mechanism for the elongation of the driving tendons, which usually occurs due to frequent stress, and the mechanism, therefore, maintains positioning accuracy

A highly articulated robotic probe (HARP) was designed to enter the pericardial cavity and undertake therapeutic interventions under direct control [45, 46]. The probe (Figure 10), which is Ø12 mm and 300 mm in length, consists of two concentric tubes built with rigid cylindrical links connected by spherical joints. The probe is actuated with four cables and achieves a 7.5 mm radius of curvature. By alternating between rigid and flexible mode of both tubes, the HARP can arbitrarily move in three-dimensions. However, the inability of the joints to actuate independently and the limited bending degree of ±10° are the main drawbacks of the design.
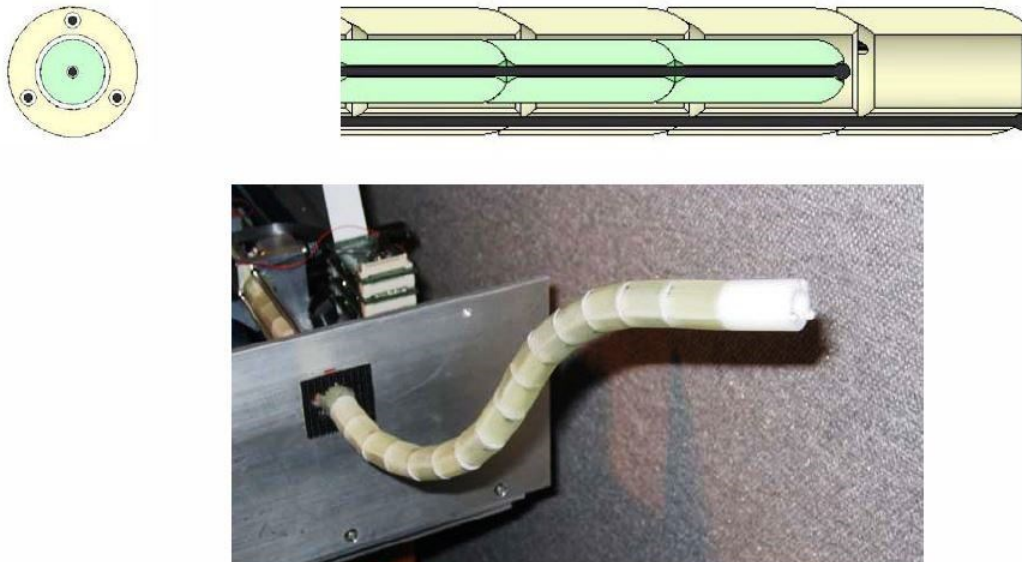
Figure 10: (Top) Front and cross sectional view of HARP showing inner (green) and outer tubes (yellow), and four actuating tendons (black); (bottom) the HARP demonstrating its ability to maintain an arbitrary 3-D shape (Image source: A. Degani (45))

Concentric-tube robots are used as a novel approach in cardiac intervention. Concentrically combined pre-curved elastic tubes constitute this type of robot actuation. *Dupont et al.* [47] studied different strategies for real-time control of robots.
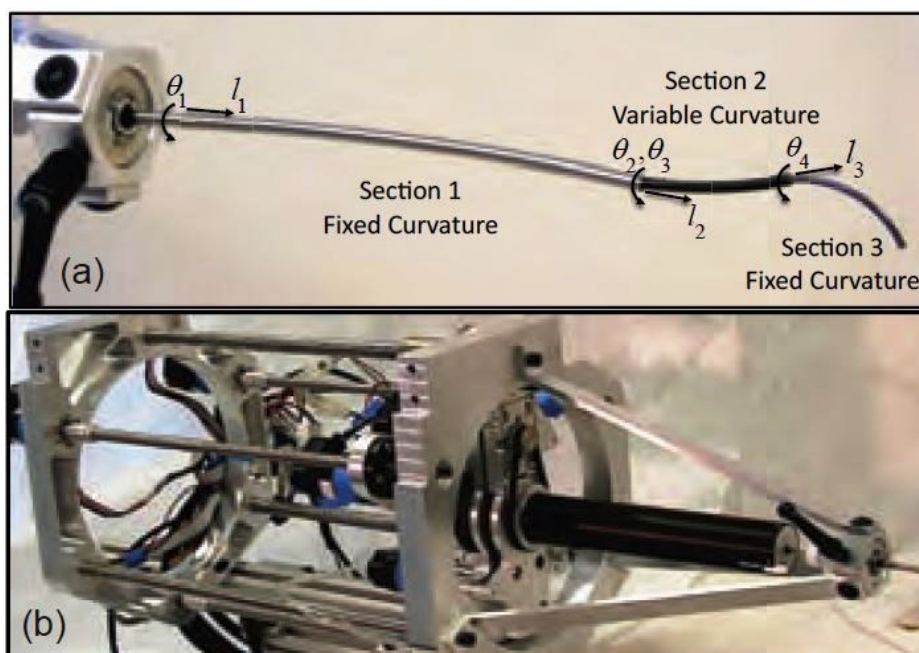
Figure 11: Concentric tube robot used in cardiac intervention. (a) Three section robot design. (b) Drive system. (Image source: *Dupont et al.* (47))

The group provided a framework for the design and kinematic modelling of concentric-tube robots (Figure 11) that enables accurate real-time position control. For such robots, the curvature along with the overall length of the robot can be varied by relative translation and

rotation of four pre-curved tubes, which are inserted inside each other, with respect to each other. The main drawback of this method arises from the complexity of the robot kinematic model, which increases with the number of embedded tubes and affects the accuracy of tip positioning.

The first robots of this kind comprised of two tubes were presented by *Okzawa* [48]. The group applied this method for the designing of novel steerable needle device for percutaneous interventions, which is a modification of the existing medical biopsy needles.
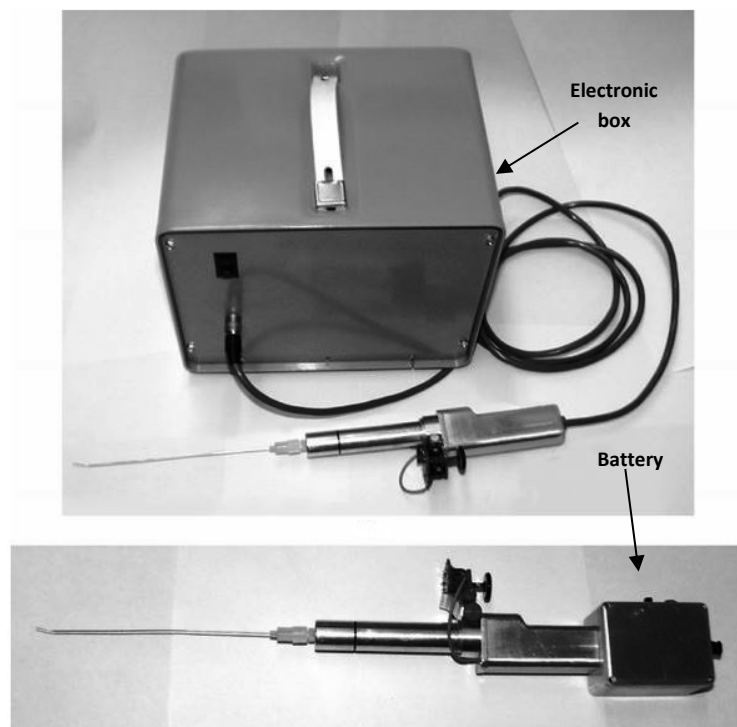
Figure 12: Two versions of the steerable needle system (top) the large separate electronics enclosure with linear dc power supply and (bottom) the miniaturized electronics with battery power mounted in the box attached to the base of the device. (Image source: Okzawa et al. (48)

The needle is actuated to the desired steerable direction via a motorised device. Two versions of the freehand steerable needle device have been built; one with a separate electronic enclosure box, and the other using battery power installed in a small box that is mounted directly on the handheld of the device (Figure 12).

The mechanism of the concentric tube robot was combined with the mechanism of a highly articulated robotic probe to form a hybrid snake robot for cardiovascular surgery by *Zenati et al*. [49]. Figure 13 shows the hybrid snake robot, which is comprised of a robotic probe and two, sets of pre-curved Ni-Ti tubes. These segmented tubes are longer than the probe and are combined by inserting them inside each other. These combined tubes can rotate with respect to each other to reach maximum curvature.
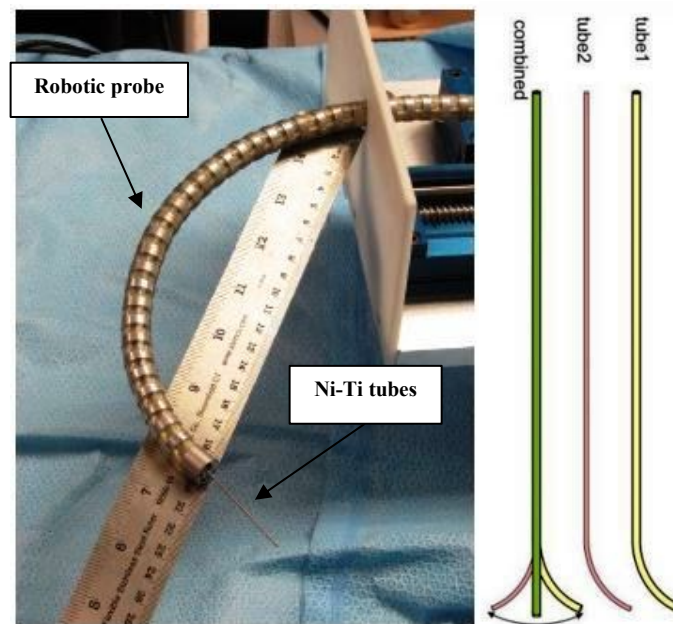
Figure 13: Hybrid snake robot, hybrid snake robot concept (top), pre-curved Ni-Ti tubes of the hybrid snake robot (bottom). (Image source: Zenati et al. (45))

A dextrous, active modular instrument devoted for minimally invasive coronary artery bypass grafting (CABG) surgery[2] was designed by *Salle et al.* [50]. The device, shown in Figure 14, is built with embedded brushless DC motors whose rotation is transformed to joint rotation, achieving actuation along 5 DoFs.
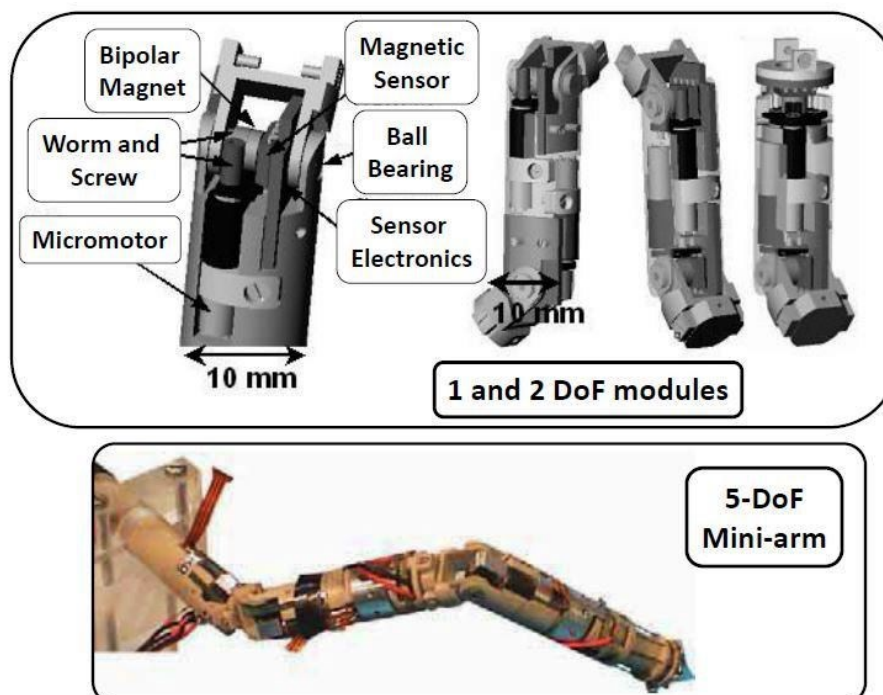
Figure 14: Optimal 5 DoFs dexterous instrument for minimally invasive CABG. It features five identical 1 DoF modules that can be connected to form different 2 DoFs configurations, also shown. (Image source: *Salle et al.* (50))

---

[2] The Coronary Artery Bypass Grafting (CABG) is a surgery of the arteries irrigating the heart muscle (the coronary arteries).

It has a 10 mm outer diameter enabling it to pass through the intercostal spaces. In addition, the device is integrated with hall-effect sensors to provide its position feedback. However, the device only features 5 DoFs and is optimised for CABG. Moreover, it does not provide any internal channels for the passage of instrumentation or control wiring.

Another approach of implementing embedded motors for actuation was used by *Peirs et al.* [51] in designing a miniature manipulator for integration in a self-propelling endoscope. The design consists of two serial modules, with each 1 DoF and 12 mm outer diameter, driven by electromagnetic motors with worm gear reduction.

The miniature manipulator, which is placed at the tip of the endoscope, controls the position and orientation of the tools and camera. A miniature prototype of a smaller diameter (Ø8.5 mm), featuring only 1 DoF was also designed (Figure 15b). However, the main disadvantage of embedded motor actuation is the requirement for a worm gear transmission system that significantly reduces the space at the joint, and thus limits its motion speed.
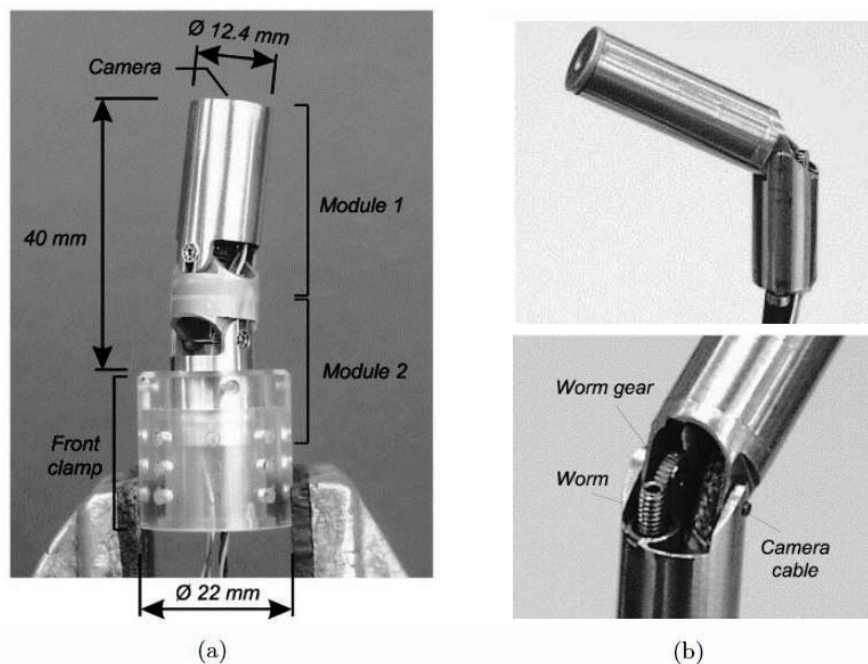
Figure 15: Miniature manipulator for integration in a self-propelling endoscope. (a) The 2 DoFs manipulator prototype integrated in the front clamp of the endoscope propulsion unit. (b) The miniature manipulator with 1 DoF, showing details of the worm gear reduction. (Image source: Peirs et al. (51))

The miniature manipulator, which is placed at the tip of the endoscope, controls the position and orientation of the tools and camera. A miniature prototype of a smaller diameter (Ø8.5 mm), featuring only 1 DoF was also designed (Figure 15b). However, the main disadvantage

of embedded motor actuation is the requirement for a worm gear transmission system that significantly reduces the space at the joint, and thus limits its motion speed.

Simman et al. [52, 53] developed a system for minimally invasive Tele-surgery of the throat. The system features a three-armed robot with distal dexterity units (DDU), each containing a detachable parallel manipulation unit (PMU) and a snake-like unit (SLU). The SLU provides the motion capabilities while the PMU provides high accuracy localized 3 DoFs motion at the tip of the DDU. The SLU provides dexterity by the continuous bending of its flexible segments, which is different from the systems, described previously that used articulated connections between rigid links. The prototype shown in Figure 16 has four super-elastic Ni-Ti tubes; one primary tube is located at the centre, and three secondary tubes are placed equidistant from one another and from a central primary tube.
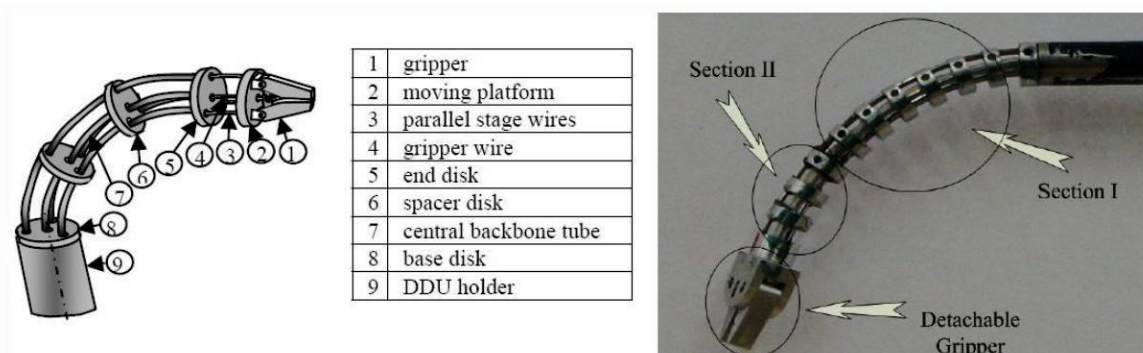
Figure 16: SMA based snake robot showing (left) schematic of internal components and (right) the actual device with two bending sections clearly marked. (Image source: *Simman et al.* (52))

The primary tube is attached to both a base and an end disk, and to several disks featuring holes to allow for the sliding and bending of the three secondary tubes, which are attached only to the end disk. The main disadvantages of the system are related to the difficulties in modelling and controlling the actuation of super-elastic Ni-Ti tubes, due to response time, friction and buckling. In addition, the robot is designed for manipulation tasks and does not feature internal channels through which to pass instrumentation.

A super-elastic Ni-Ti tube is also used by *Peirs et al.* [54] in designing a flexible distal tip for endoscopic robot surgery. The flexible tube shown in Figure 17 could bend from -90º to +90º in two directions (2 DoFs) by pulling on the cables running along its length. The significant advantage of the inner tube is that it allows the insertion of a flexible instrument without contacting the cables. The outer tube has been cut into a structure consisting of a series of rings connected by thin elastic joints to enhance the bending flexibility.
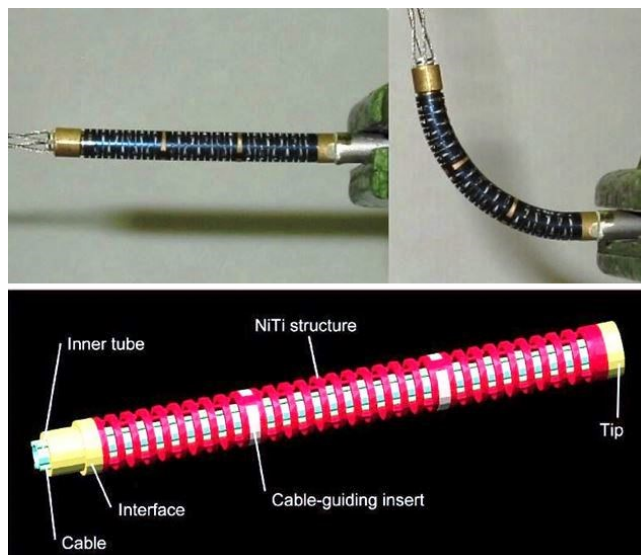
Figure 17: Flexible tip prototype in straight and bend position (top) and design of the flexible instrument tip (bottom) showing the position of inner tube within the structured Ni-Ti tube. (Image source: Peirs et al. (54))

A robotics system was developed by *Sekiguchi et al*. [55] to assist in Single Port Endoscopic Surgery (SPS). The study proposed a surgical endoscopic robot for SPS with dynamic vision control, the endoscopic view being manipulated by a master controller. The prototype robot (Figure 18) consists of a manipulator for vision control, and two surgical tool manipulators (gripping 5DOF's, cautery: 3DOF's) and one flexible endoscope. The diameter of the insertable component is approximately 30mm; the maximum bending angle is 45°.
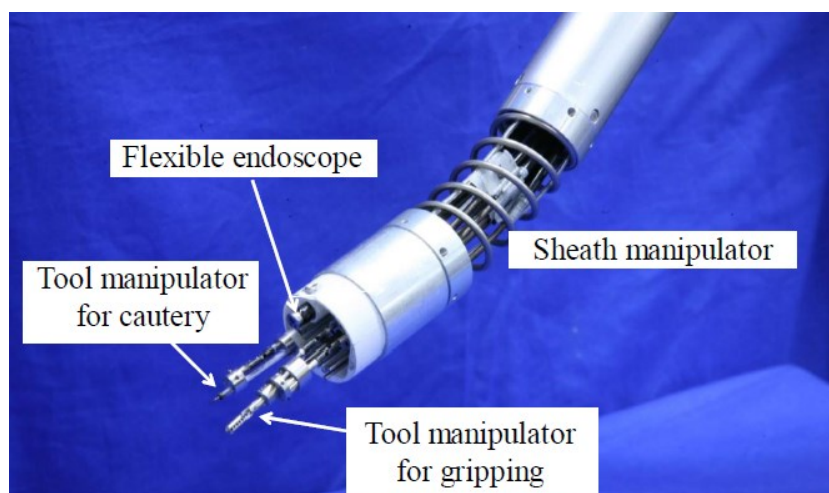
Figure 18: Enlarge view of the tip of the surgical endoscopic robot for SPS showing the insertable components (Image source: Sekiguchi et al. (55))

While many systems, which fit into the broad description of 'flexible medical robotic device', exist, none fulfils the requirements of a flexible surgical device for the application of spinal surgery as were described in Chapter 1. The purpose of such a device would be to access complex internal structures, reach the target object around the spinal column, and dissect

cancerous tissue. Existing systems either do not have the ability to cut tissue or are not used for spinal surgeries.

2.2   Water Jet Cutting Technology

The cutting high-pressure water has been used in industry for a long time. Lately, this technology has also found its application in the medical field. In general, Water-jet technology does not damage the surrounding tissues during the cut because it reaches only a low temperature; it enables high-precision cutting, leaves a clean cut as it instantly flushes out the debris and decreases bleeding at surgery. This section will introduce this technology and describe its principles, classifications, and medical applications.

2.2.1 Brief History

One of the first documented use of water jet technology was in the mid-1880s in hydraulic mining in which the collection of water from a stream was used to carry the coal away from the working surface of a mine [56]. Concurrent with the improvement of mining machinery, the water jet had been evolving for use as a method of rapidly cleaning surfaces. Initially, the water was driven at high speed using steam, but the cost and the system losses led to slow progression. With time, the abilities of the system improved, and pumps were developed to operate at steadily increasing pressures that allowed the jets to clean or cut through progressively harder materials.

A paper metering, cutting, and reeling machine was developed by *Fourness* and *Pearson* in 1933 [57]. The machine used a diagonally moving water jet nozzle to cut a horizontally moving sheet of continuous paper. In 1956, *C. Johnson* of *Durox International* [58] developed a method for cutting plastic shapes using a thin stream high-pressure water jet. Schwacha developed the first water jet system established for cutting hard materials in 1958. The system applied an ultra-high pressure liquid of 690 MPa using a pump to deliver a liquid jet that could cut high strength alloys [59].

In 1962 a pulsing water jet, operating at up to 345 MPa to cut metals, stone, and other materials was developed by *P. Rice* of Union Carbide [60]. In the mid-1960s, research by *Leach* and *Walker* determined the ideal nozzle shape for high-pressure water jet cutting of stone [56]. In the late 1960s, *N. Franz* and his colleagues in Michigan found that a very high-pressure jet could be used to cut through wood products precisely and at a high cutting speed. *N. Franz* also developed a method for producing a high velocity liquid jet [61], and created a

water jet nozzle with an orifice as small as 0.05 mm that operated at pressures up to 483 MPa [62]. In 1972, *Franz* worked with McCartney Manufacturing Company to install the first industrial water jet cutter. The equipment was installed in Alton Boxboard and led to the development of a new tool for manufacturing industry (Figure 19).

Figure 19: First water jet cutter that installed in Alton Boxboard by N. Franz. (Image source: KMT Water jet)

Flow Industries Ltd. also began to market industrial water jet cutting equipment. It was *Flow Industries Ltd.* who added sand to a pressurized cleaning system to give metal a white finish. After this, it was demonstrated that abrasive water jet systems could cut through metal and ceramics. From here, the water jet cutting industry took off.

A nozzle for producing high-pressure liquid as a coherent jet for fluid jet cutting was developed by *Chadwick et al*. [63]. The authors came up with an idea that improved the durability of the water jet nozzle by using corundum crystal[3] to form a water jet orifice, which has a geometry consisting of a straight-sided conical entrance section merging into a straight-sided cylindrical exit section. The development of the market from the mid-70s to the mid-80s was dominated by the use of ultra-high pressure and low rate operations. These systems were built around the use of intensifier systems, which were effective in a factory environment. However, the delicacy of the equipment, its sensitivity to water quality, and its high cost limited its penetration of the market. To overcome the disadvantages of the use of very high pressure, in 1986 the *British Hydrodynamic Research Association* had produced a means by which an abrasive could be injected into the flow line between the high-pressure pump and the acceleration nozzle [56]. This development allowed the use of much lower pressure to achieve acceptable cutting. Commercially viable abrasive water jet nozzles for precision cutting were produced by *M. Hashish* who invented the technology of modern abrasive water jet cutting, and also coined the new term 'Abrasive Water Jet' AWJ [64]. His

---

[3] Corundum is an aluminium oxide with a hexagonal crystal structure, commonly known as Ruby and Sapphire.

research team at *Flow Industries Ltd.* continued to develop and improve the AWJ technology and its hardware for many industries worldwide.
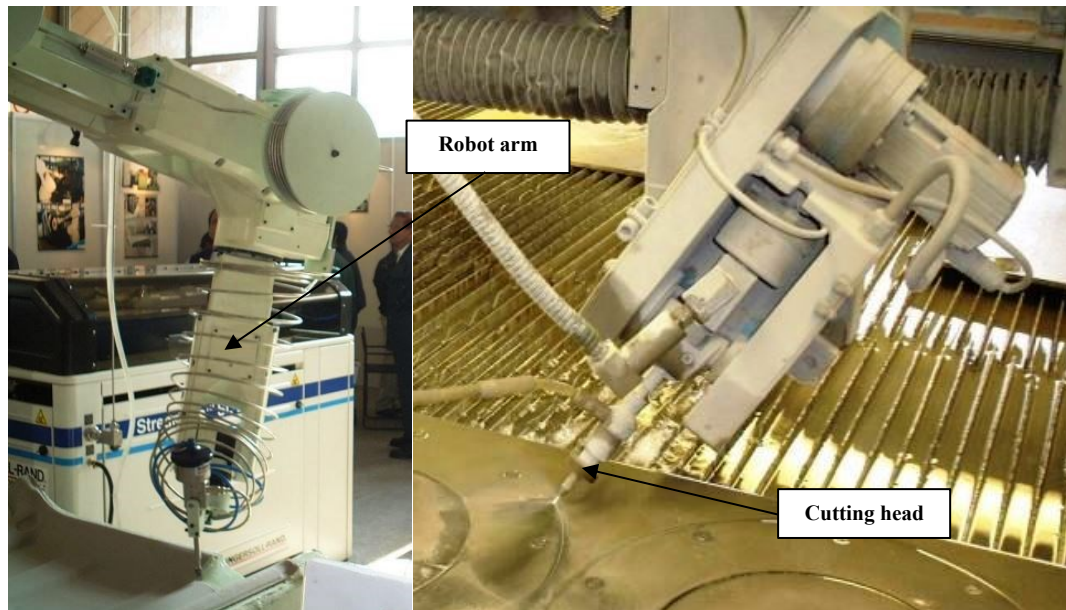
Figure 20: KMT Water jet system for automotive and mechanical engineering industry. The cutting head (water jet nozzle) is installed on a robot arm for trimming or cutting materials. (Image source: KMT Water jet (65))

In recent years, the use of water jets under pressure has become more common for a growing range of tasks because of these rapid developments. One of the recent advances in water jet technology is the 3-D cutting system, by *KMT* water jet systems [65], which is used to meet the complex requirements of material forming the automotive and mechanical engineering industries (Figure 20). In this system, the cutting head is installed on a robot arm and run along a 3-D workpiece for trimming material or cutting holes.

2.2.2 Principles and Classification

At its most basic, water flows from a pump, through plumbing and out through a cutting head (Figure 21). Every cutting technique is based on the input of energy into the material, in order to overcome the chemical binding present in the structure of the material. For instance, thermal cutting methods apply the energy of chemical reactions, electricity, or light to create high temperatures in order to melt the material at the cutting point. Mechanical methods utilize the kinetic energy of the moving tool or form ductile materials through the application of pressure [56, 65].

Water jet Cutting can be classified as a mechanical method. The energy of the rapidly moving jet is established and then applied to the workpiece causing micro-erosion. The cutting water

works as a cooling agent on the cutting edge, thus allowing for a very high quality cut. The main component of any water jet cutting system is the high-pressure pump.

Direct drive pumps provide large volumes of high-pressure water. However, their pressure ranges are limited. Their main area of application is in the areas where large cutting power without very good accuracy is required, i.e. in the construction industry, surface cleaning, material removal, etc.
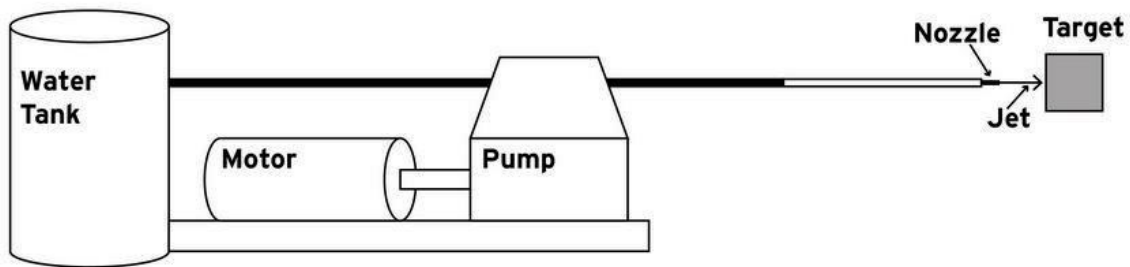
Figure 21: The components of typical high pressure water jet system. Pressurised water is generated by a pump and runs through a jet nozzle that focuses the jet towards the target. (Image source: D.A. Summers (56))

For cutting applications, so-called Intensifier pumps are primarily used. Their pressure is achieved using a variable displacement pump and subsequently multiplied by a typical factor of 20 in the reciprocating intensifier. The pressurised water is then transported through special high-pressure tubing to an orifice with various diameters. Orifice materials are usually sapphire, ruby, or diamond. Diamond orifices offer better reliability and an extended life (up to 1000 hours) than sapphire and ruby (50-100 hours), but their high cost has resulted in them making a limited impact on the water jet cutting market [56, 66].

At the orifice, the potential energy of compressed water is transformed into high kinetic energy of the water jet. According to Bernoulli's law the water jet velocity, *v*, can be estimated as:

$$v = C_D \sqrt{\frac{2P}{\rho}} \qquad (2.1)$$

Where, C_D is the coefficient of discharge (typically 0.9-0.98), ρ is the density of the water, and P is the water pressure.

The water jet, which emerges from the orifice, will generally have to travel some distance, known as the stand-off distance. This distance will cause some energy loss of the jet on the way to the target.

In most industrial applications, there are two kinds of high-pressure water jets: Pure/Plain Water Jet (PWJ) and Abrasive Water Jet (AWJ). A schematic drawing of both systems is illustrated in Figure 22.
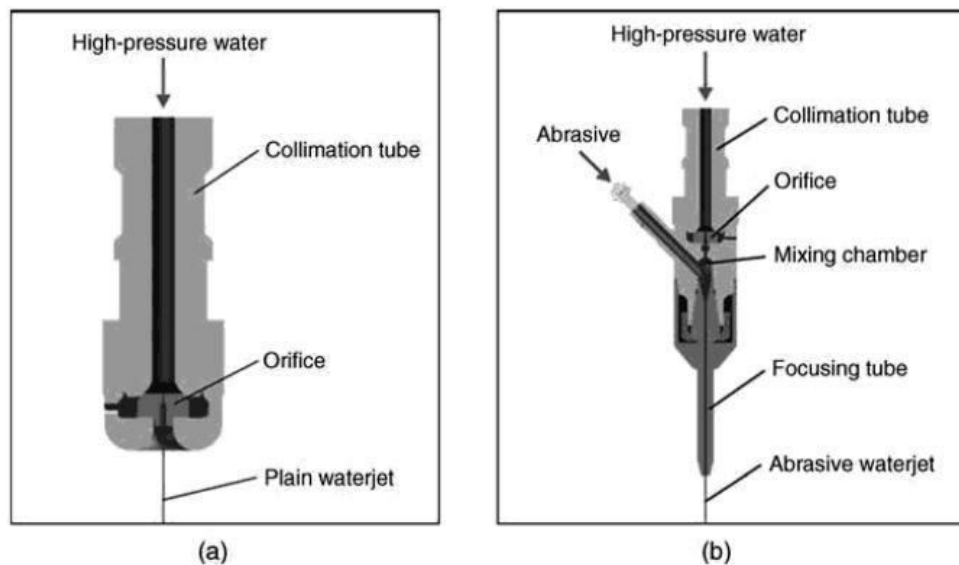
Figure 22: Cross section of plain water jet cutting head (a), and abrasive water jet cutting head (b). The basic difference between these two types is the addition of an abrasive medium in AWJ to increase the cutting ability of the water jet. (Image source: KMT water jet).

As mentioned previously, in plain water jets, the cutting material is removed by means of the fluid affecting the material with a high kinetic energy (Figure 21a). For the AWJ, the plain water jet generated in the orifice flows through a mixing chamber (Figure 21b) and generates a vacuum pressure, which allows the feeding of dry solid abrasives into the mixing chamber. Water, abrasives and air are then mixed, accelerated in a focusing tube. The main functions of the water in the AWJ cutting process are to accelerate the abrasive particles (mostly garnet and olivine[4]) and clear away the removed material.

A comparison between PWJ and AWJ has been experimentally studied by *J. Wang* [67]. This preliminary study was driven by the local meat processing industry to investigate the feasibility of cutting meat, meat with bone and bone. The study showed that the performance of an AWJ, using salt particles as the abrasives, showed an improved quality over the use of a PWJ as well as increasing the depth of cut significantly (Figure 23).

---

[4] Olivine is a group of rock-forming minerals found in earth's crust, and they are usually green in colour.
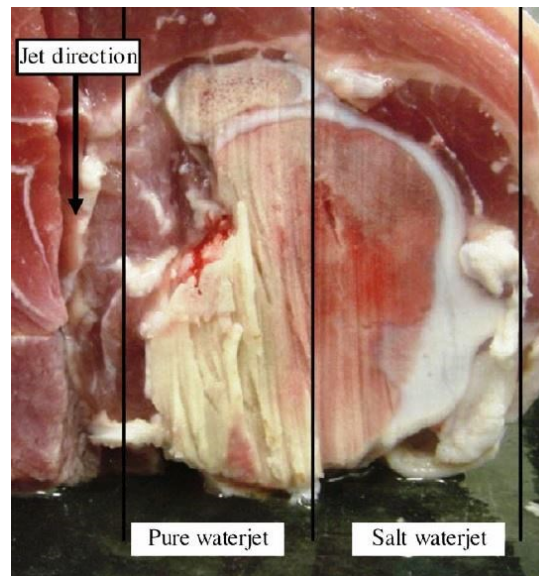
Figure 23: Comparison between pure water jet cutting and abrasive water jet cutting of pork with bone. The region cut by an AWJ depicts a smooth cut in contrast to that by a pure water jet. (Image source: J. Wang (67))

2.2.3 Medical Applications

As presented in the previous section, pressurized water jet cutting was originally developed to be used in the industry, particularly in the steel and glass industries where ultra-precise cutting is required.

In surgery, PWJs with a highly pressurised fluid are used to dissect organs. However, this type of system is not suitable for cutting cortical bone, as this procedure requires pressures of more than 80 MPa, which, for safety reasons, is unacceptable during surgery. Whereas the use of AWJs, where solid particles are added to the water jet, results in a substantial increase in the cutting efficiency with less pressure. However, the abrasives must be water-soluble and pharmacologically safe, such as disaccharides[5], sugar, amino acids, and salt [68].

The water jet technique was adapted in 1982 for medical applications by *Papachristou* and *Barters* [69] for the resection of the liver. They generated a jet of normal saline at a maximum pressure of 966 KPa using a standard agricultural electrically-driven spray system. This technique was further developed and modified by *Persson et al*. [70] and *Une et al*. [71]. They used a jet pressure of less than 5 MPa and a nozzle with a diameter between 0.08-0.2 mm for dissection of the liver (Figure 24). However, these initial attempts suffered from the defect of using a low-pressure (1.5-5 MPa) system with resulting reduced efficiency. In time, the system was improved and used for many surgical applications.

---

[5] Disaccharides are sugars or carbohydrates made by linking two monosaccharaides such as maltose and lactose.
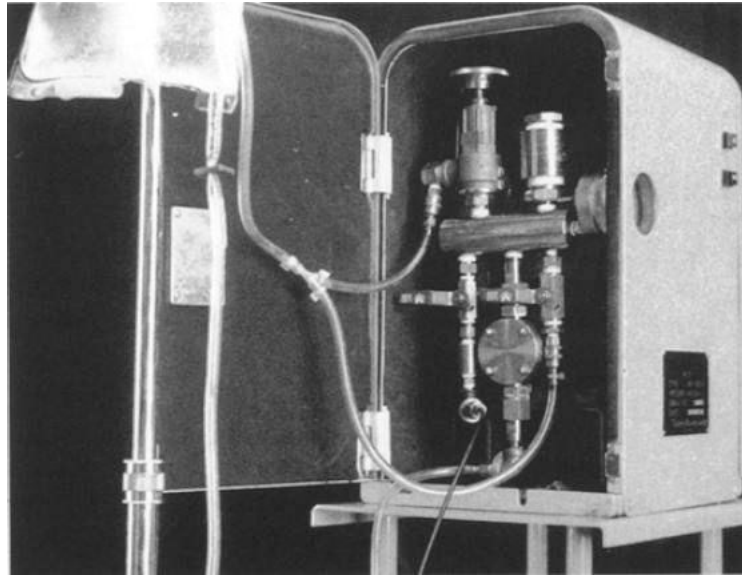
Figure 24: The water jet equipment consisting of a pressure-generating pump and a flexible hose connected to the hand piece. (Image source: Une et al. (71))

The dissection of the liver using a water jet instrument (Figure 25) is also described by *Bear et al.* [72, 73] by applying different jet pressures (20-100 MPa) and nozzle diameters (0.02 and 0.07 mm).
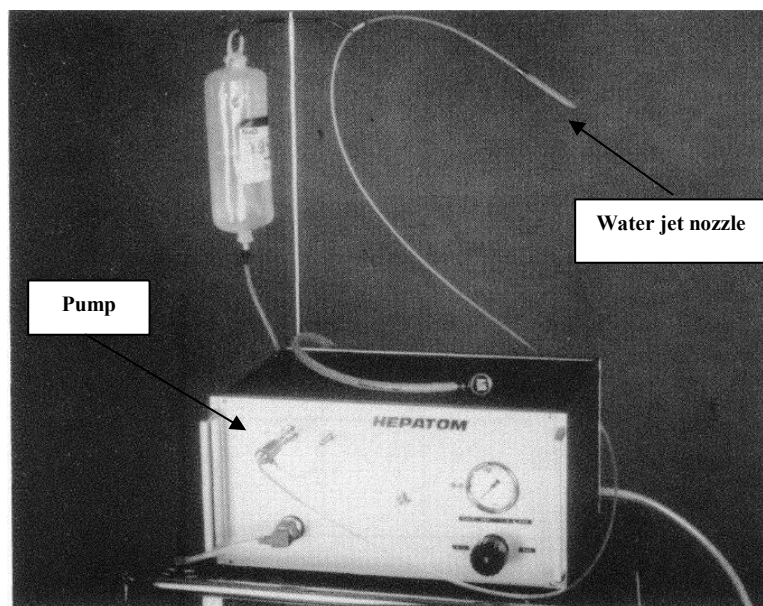
Figure 25: Photograph of the assembled dissector showing sterile water bag, pump, connecting tubing and nozzle. (Image source*:* Bear et al. (72))

R. Izumi et al. have designed a water jet dissector for hepatic resections in humans [74]. The water jet dissector consists of a handpiece connected to a control console via a flexible hose. The handpiece comprises a jet nozzle with an orifice of 0.1 mm diameter, which projects

physiologic saline at a maximum jet pressure of 5 MPa. The control console has a pressure regulator that enables the water jet to be directed accurately at an adjustable pressure, and on-off control is provided via a switch within the handpiece (Figure 26). A suction line is connected to a transparent hollow tip, which covers the jet nozzle, through which physiological saline, blood, and tissue fragments are removed.
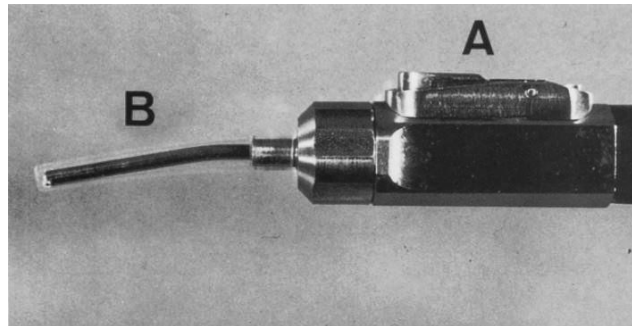
Figure 26: Surgical handpiece of the water jet surgical dissector with switch (A) to project a water jet. The water jet is projected through the nozzle (B). A suction line is connected to a transparent hollow tip which covers the nozzle. (Image source: Izumi et al. (74))

The efficiency of the Water jet system for hepatic parenchymal dissection was examined by *Vollmer et al.* [75]. The authors concluded that water jet dissection minimizes large blood volume loss.
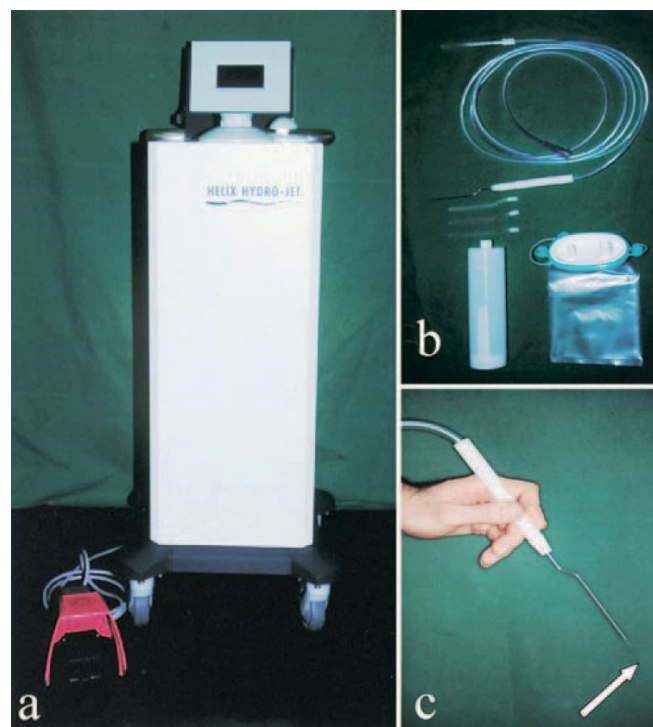
Figure 27: Photographs showing the water jet instrument (a) and its parts, (b) pencil like handpiece with arrow pointing to water stream emerging from the nozzle, and (c) suction parts. (Image source: Piek et al. (76))

In neurosurgery, the safety and the ease of handling in various procedures of a water jet dissection device were demonstrated by *J. Piek et al.* [76]. The water jet instrument, *Helix Hydro-Jet*, used by the group is connected to a pencil-like handpiece consisting of a fine nozzle that is 100 μm in diameter, and a surrounding suction tube (Figure 27). This device appears to be particularly suitable for the dissection of highly vascularized Glioma[6] or normal brain tissue.

An experimental study by *J. Oertel et al.* [77] of water dissection of 50 porcine cadaveric brains, using several nozzle types (80–150 μm) and several levels of water jet pressure (100–4000 KPa) showed that the water jet enabled very precise and consistent brain parenchyma dissection with vessel preservation under conditions corresponding to the clinical situation. In addition, this study shows an almost linear relationship between the water jet pressure and the depth of the dissection. Moreover, dissection characteristics of two different nozzle types (100 mm straight nozzle; 120 mm Helix nozzle) are compared by *J. Oertel et al.* [78] in order to analyse their potential for clinical application.

In order to conduct an endoscopic neurosurgery using a water jet, a handpiece (Figure 28) was designed by *J. Oertel et al.* [79]. This device was tested in 20 cadaveric porcine brains and in four patients; a reliable and accurate dissection of the ventricle wall was consistently achieved in the porcine brain with the new handpiece.
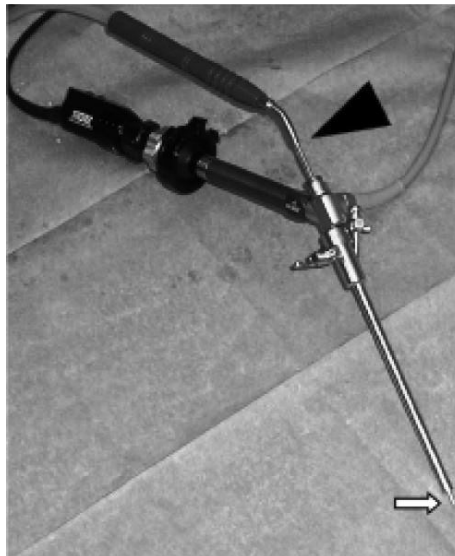
Figure 28: Photograph of the water jet handpiece designed by *Ortel et al*. (black arrowhead). The white arrow indicates the nozzle tip. (Image source: Oertel et al. (75))

---

[6] Glioma is a broad category of brain and spinal cord tumours that come from glial cells, brain cells that can develop into tumours.
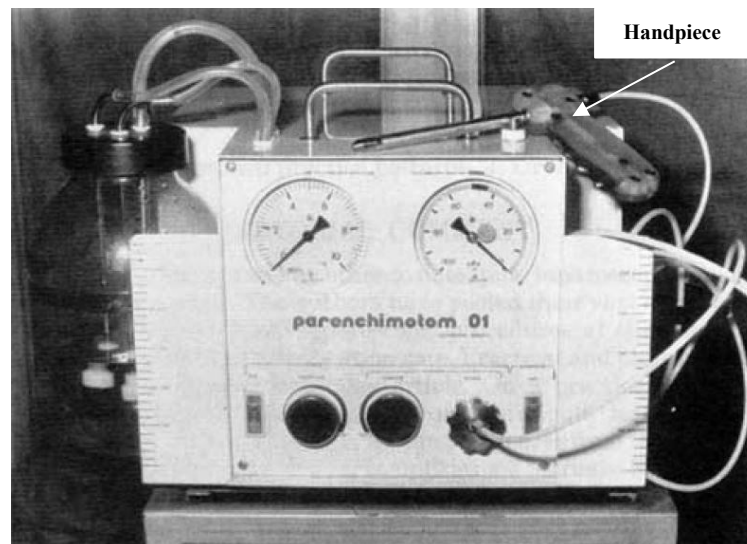
Figure 29: Water jet system designed by *Penchev et al.* The equipment consists of a pressure generating pump and flexible hose connected to the hand piece. (Image source: Penchev et al. (81))

Water jet dissection in renal surgery was first experimentally investigated by *J. Hubert et al.* [80]. This technique is then used by *Penchev et al.* [81] and *Basting et al.* [82]. *Penchev et al.* used a water jet with 2.5-3.0 MPa pressure and 0.3 mm nozzle diameter (Figure 29) to remove a well-encapsulated tumour of the lower pole of the left kidney and clean the renal parenchyma.
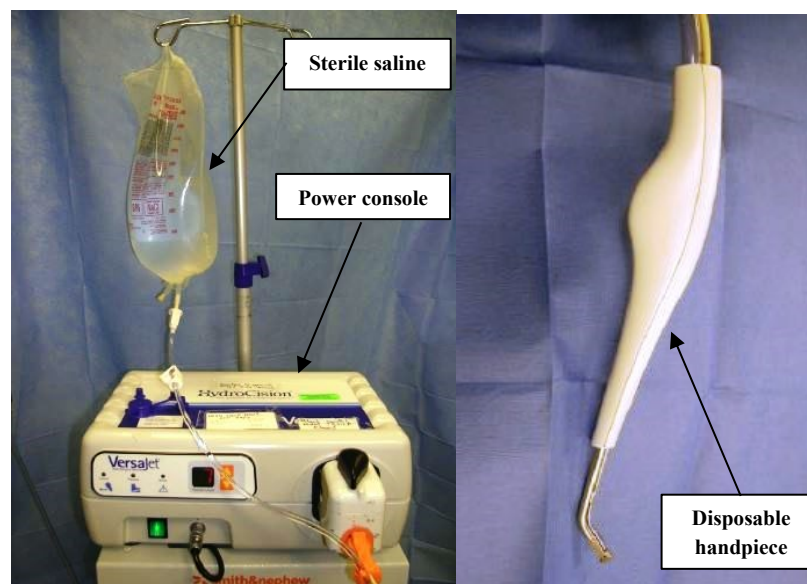
Figure 30: The Versajet™ hydrosurgery console (left). The system utilizes a reusable power console with foot pedal activation, disposable handpiece (right) and tubing assembly in conjunction with sterile saline. (Image source: Gurunluoglu (83))

In wound debridement, use of the water jet hydrosurgery system (Versajet™) provided by Smith & Nephew, Inc. (Figure 30) was examined in 15 patients with various wounds. The hydrosurgery system is a combination of a high-velocity water jet and a suction system which

permits the surgeon to hold and cut targeted tissue while aspirating debris from the site [83]. This system has also been promoted as an alternative to the standard surgical excisional technique for burn wounds [84].

In orthopaedic surgery, *Schwieger et al.* [68] investigated the cutting quality of an abrasive water jet on the cancellous bone and the viability of using a water jet in the implantation of endoprostheses and osteotomy. In this study, the water jet-cutting device (Figure 31) consisted of a pneumatic reciprocating plunger pump with a pressure that can be adjusted from 28-72 MPa using a pressure control valve. The abrasive was injected into the mixing chamber, which is then connected to a nozzle of 0.2 mm diameter. The study shows that the cancellous bone can be cut with an abrasive water jet and the accuracy was sufficient for the osteotomy.
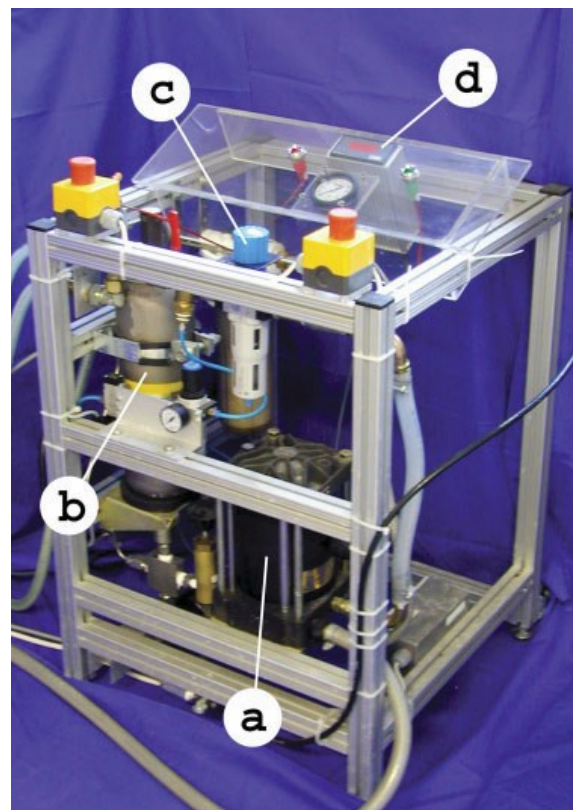
Figure 31: Water jet device with a reciprocating pump (a) and bladder accumulator (b). The water pressure can be adjusted with a pressure control valve (c). The water pressure is measured and displayed on a digital display (d). (Image source: Schwieger et al. (68))

Experimental cutting of porcine bones (Figure 32) using the abrasive water jet cutting system was conducted by *Hloch et al.* [85]. In this experiment, a pressure of 60 MPa was generated and a nozzle with a 0.33 mm diameter was used. The preliminary results showed that the quality of the surfaces created by abrasive water jet cutting is suitable for orthopaedic surgical procedures, such as total hip and knee replacement or for osteotomies.
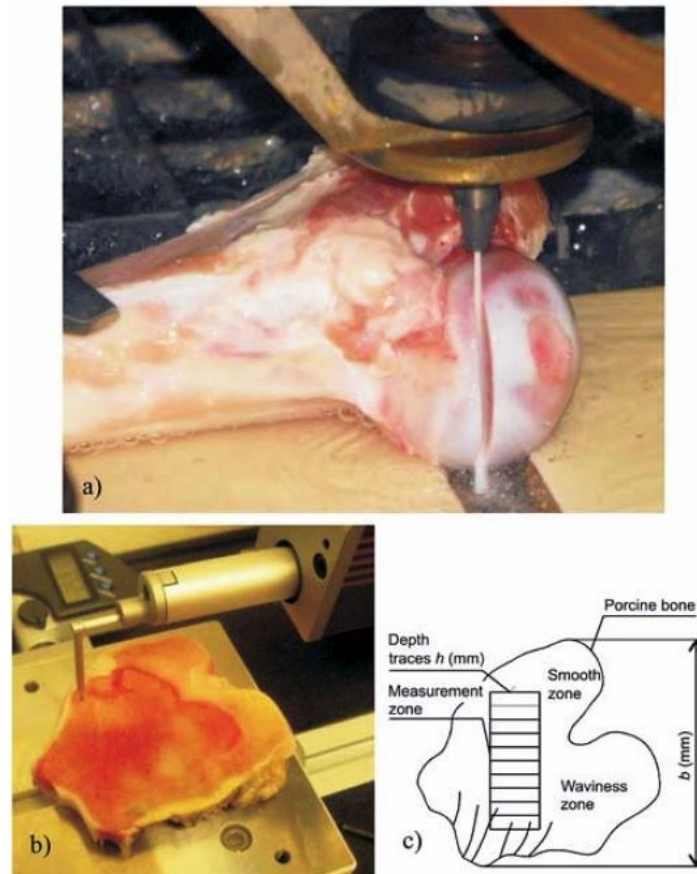
Figure 32: Experimental cutting of porcine bones using abrasive water jet cutting system (a), surface roughness measurement (b), measurement traces *h* mm(c). (Image source: *Hloch et al.* (85))

2.2.4   Advantages and Disadvantages of Water Jet Technology

Water jet technology offers several important advantages compared to traditional machining methods and other more recent machining techniques such as laser cutting and ultrasonic machining. Water jet can be used to cut almost any kind of material such as steel, ceramics, composite materials, stone, glass, etc. with a high cutting speed [66]. Materials up to 300 mm and 500 mm can be cut with a water jet at 400 MPa and 600 MPa respectively. It has a relatively small cutting width (kerf), typically about 0.5-1.2 mm, which contributes to the material savings. Water jets have no thermal effect on the workpiece material, and also have no thermal or chemical reaction products. The cutting head has no direct contact with the workpiece, which results in low cutting and reaction forces, hence, the workpieces do not need to be heavily clamped, enabling a very fast implementation from drawing board to cut piece. The water jet cutting system is a multifunctional tool that can be used for cutting, drilling, milling, and cleaning with one tool. It can be robotically controlled to give the system the capability of machining forms with complex geometries.

These advantages caused the rapid spread of the application of water jet technology in the aircraft and automotive industries, military hardware production, medical procedures, and many other fields.

One of the main disadvantages of water jet cutting is that a limited number of materials can be cut economically. While it is possible to cut tool steels, and other hard materials, the cutting rate has to be significantly reduced, and hence the time to cut a part can be very long compared to other methods. Because of this, water jet cutting can be relatively costly.

Another disadvantage is that very thick parts cannot be cut with water jet cutting and still hold dimensional accuracy. If the part is too thick, the jet may dissipate, and cause it to cut on a diagonal, or to have a wider cut at the bottom of the part than the top. Taper is another problem with water jet cutting in very thick materials. Taper is when the jet exits the part at a different angle than it enters, and can cause dimensional imprecision. Decreasing the speed of the head may reduce this, although it can still be a problem [86, 87].

2.3 Conclusion

In this chapter, a brief overview of existing medical robotic systems, flexible robotic devices, and water jet technology were provided. The principal part of the chapter is about flexible robotic devices and water jet technologies that could potentially be utilised in any new design. While many systems, which fit into the broad description of 'flexible medical robotic device', exist, none of these devices was used in flexible spinal surgeries. The purpose of such a device would be to reach internal targeted structures at the interior side of the spinal column, and cut cancerous tissue. Existing systems either do not have the necessary tool to dissect internal structures or do not have the ability to navigate between and around the complex bones of the spinal column.

As such, any potential flexible surgical robot would be required to incorporate the following features:

- Flexible probe: has the ability to access from the posterior side of the spinal column and bend around to reach the interior side of the spinal column.
- A surgical cutting tool: has the ability to dissect internal tissues, and has the ability to integrate with and follow the guides of the flexible probe.
- A robot platform: allows positioning of the surgical cutting tool to remove cancerous tissue.

Each of these features has been addressed in the design of the flexible surgical robot, and was described in the following chapters. The design of the flexible probe to be described in Chapter 3 contains a distal tip that is able to bend around the spinal column via a pull-bend mechanism. Chapter 4 will present the design of a flexible surgical drill, and Chapter 5 will describe the design of the flexible water jet system. The mechanical design of a parallel robot manipulator with 6 DoF will be represented in Chapter 6. The platform contains a fixed top, which is connected to a mobile base via six extensible linear actuators. Chapter 7 describes the control and haptic of the parallel robot platform. Firstly, however, in Chapter 3 the preliminary design of the flexible surgical probe prototype will be investigated.

3   The Preliminary Design of the Flexible Surgical Probe Prototype

In the previous chapter, the use of actuation devices in medical applications and the current actuations have been discussed. In this chapter, a flexible probe prototype will be described that is able to access from the posterior side of the spinal column. The flexible probe must be able to navigate between the transverse processes of the spinal vertebrate, bending into a J-shaped configuration to reach the interior side of the spinal column and carry out tissue resections. This chapter covers in detail the first attempt to design a flexible surgical probe. At the beginning a full analysis of the design process analysis of the concept will be presented, then of the subsequent fabrication process. There follows a further analysis of the mechanical testing of the probe, will revealing the forces required to actuate it, supported by a description of computational modelling and simulation undertaken. Finally, there is an examination of the experimental testing of the probe, examining its drilling performance as well as its bending capabilities.

3.1   Design Process and Analysis

In this project, interviews with our spinal surgeon collaborator showed significant uncertainty in the desired features and requirements of such a device, despite the overall need being firm. Therefore, a series of exercises to narrow the design scope were first conducted, which then led to prototyping and testing as a means to refine the final features and reduce technical risk. Envisioned application of this model is iterative and proceeds through several phases for small-scale testing and review to be broadened up for entire system analysis. It allows for evaluation of risk before proceeding to subsequent project phases.

Initially, the design of the system was approached through transforming the customer requirements into the system development by applying a simple pairwise analysis and a Quality Function Deployment (QFD) method to scope the features of the first prototype.

The pairwise comparison method is a tool to rank a set of decision-making criteria and rate the criteria on a relative scale of importance [88]. Its process begins with compiling a list of items (attributes) which can be any aspects involved in the design. These items are then compared to each other in terms of achievement of objectives. In our case, the desirable

criteria or customer requirement for our design is based on a feedback from our spinal surgeon collaborator, which includes:

- Flexibility: a flexible device that has the ability to navigate around the corners of complex bones such as the spinal column.

- Dissections: the device must have the ability to cut through cancerous tissues.

- Size: the device must be miniaturised to be able to access through small incisions surrounded by vital tissues and reach the desired locations in the body.

- Practical: the assembled parts of the device need to be installed / dismantled easily by the surgeon as well as to ensure the comfortable use of the device during the surgical procedure.

- Visualization: the device should be mounted with a camera in order to perform surgery where the operation field is almost invisible.

- Cleaning: flushing water during the surgery to clean the operation field.

- Clearing: removing the water and debris constantly to clear the operation field.

- Tele-operating: perform the operation from the physician's workstation, allowing a doctor to control the procedure from a comfortable sitting position.

- Force feedback: improve the performance of robot-assisted surgery by providing the surgeons with a sense of touch or force information.

- Safe to surrounding tissue: the device must not damage the tissues that are not involved in the surgical procedure. The damage could be in the form of sharp edges, high temperatures, or uncontrolled cutting.

Figure 33 shows a complete pairwise ranking for the flexible drilling system. The next step of the design process was to apply the Quality Function Deployment (QFD) method, which is the method that transforms the customer requirements (voice of the customer) into the system development. This process begins by taking the attributes with their weights from the pairwise analysis and places it in the customer requirement column in the QFD 1 (Appendix 2.1). In this stage, customer requirements are translated into measurable technical requirements. It focuses on identifying those with the highest-ranking matrix; these are bending capacity, control the movement, sharp end, and diameter. This stage is followed by QFD 2 (Appendix 2.2) in which the technical requirements are converted into compliant Design Solution Requirements (functions). The preferred solutions (tools) that resolve the technical requirements are: flexible tools, cutting tools, and direction control tools.

67
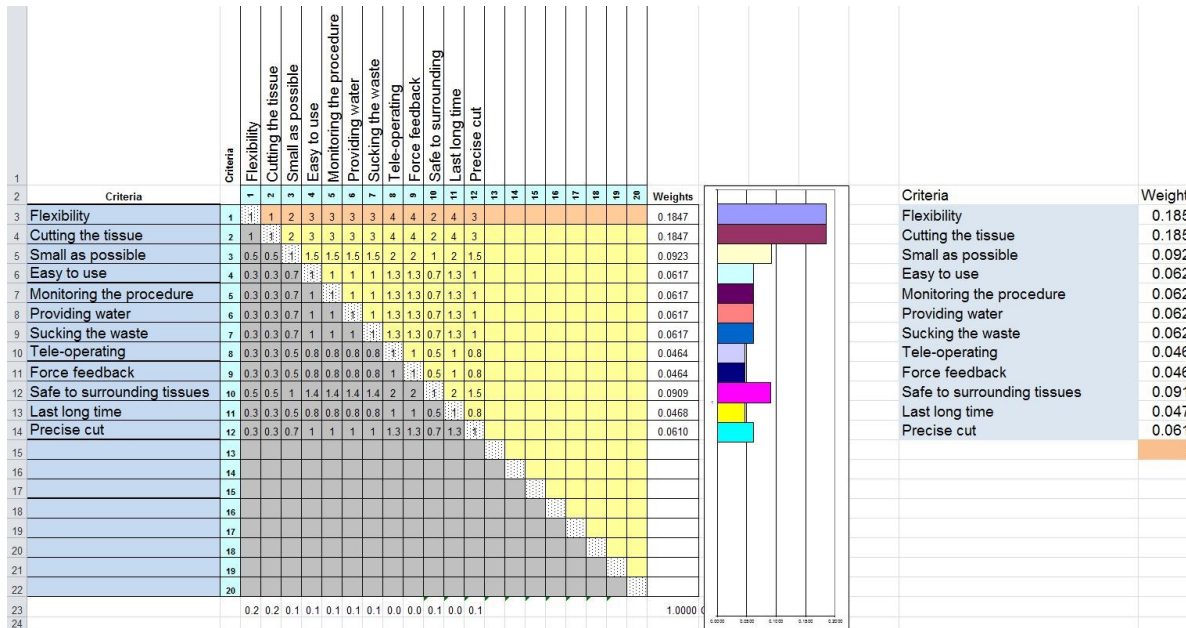
Figure 33: Pairwise analyses, the spread sheet for Pairwise comparison method is set up such that the comparison needs to be completed for the first row of the table (Orange row). The spread sheet is also set to weight these attributes in a normalise scale
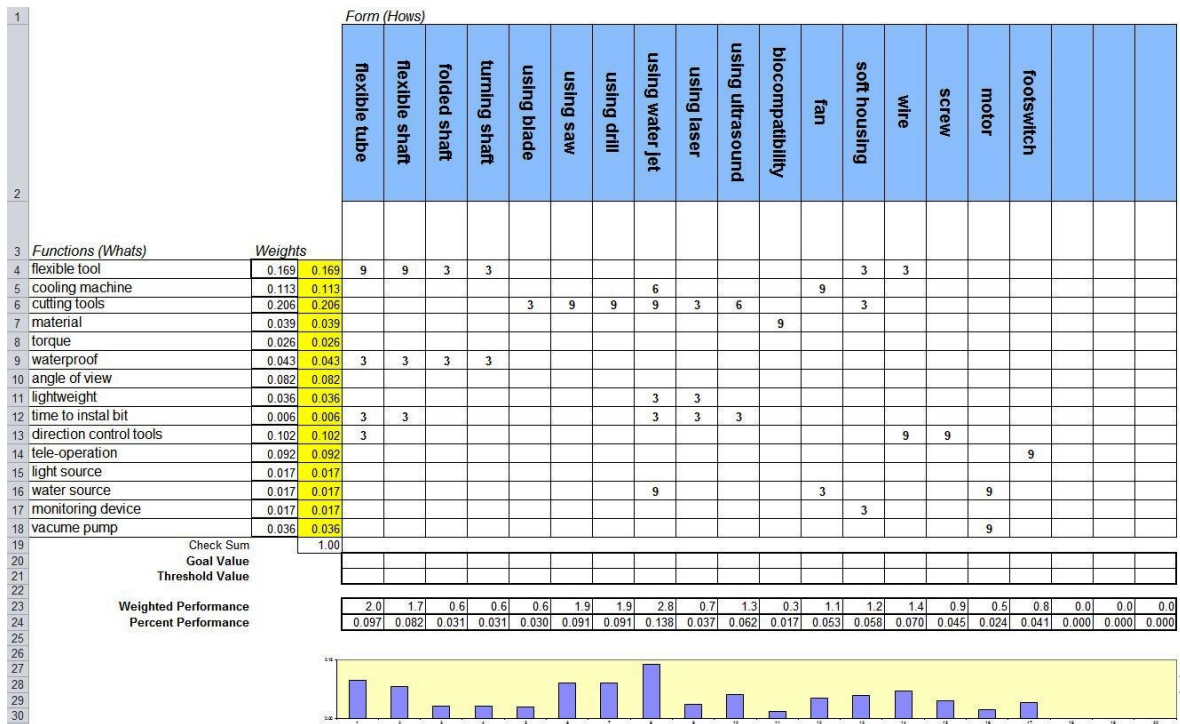
Figure 34: The final step of the Quality Function Deployment analysis (QFD 3), the bottom chart shows the level of priority of each set of design options.

Figure 34 shows the last step of the design process of our first prototype (QFD 3) in which the design solution requirements are transformed and linked to a specific form of the system that been developed. This displays and predicts detailed parts of the first prototype such as a flexible tube, flexible shaft, and wire.

68

The features identified as being important to this particular device are as follows:

- Using a flexible shaft for the transmission of motion and power around the corners.

- Using a flexible tube for housing and bending the flexible shaft.

- Using wire or micro- cable to pull/bend the flexible tube and control the direction.

- Using a water jet or drill to dissect the tissue.

3.2   Manufacturing and Assembling Process

Based on the outcomes, the first generation design was focused principally on delivering a flexible cutting tool, with additional features to be designed around this constraint. To reach this goal, some of the design features had to be sacrificed at this stage, such as the size of the tip, while features like the pulling-bending technique can be completed at this stage. However, the desired miniaturized size of the flexible tip could be reached by a redesign of the end housing part such that the connection of the full function's units would not disturb the bending of the flexible shaft.   The first prototype was comprised of the following components:

I.   Flexible Shaft

One of the extreme limitations of a solid shaft is that it cannot transmit motion or power around corners. A flexible shaft may often be an economical solution for transmitting motion around corners [89].

The construction of a flexible shaft is shown in Figure 35. The cable is made by twisting several layers of a wire around a central core such that the torsional deflection is approximately the same for either direction of rotation.
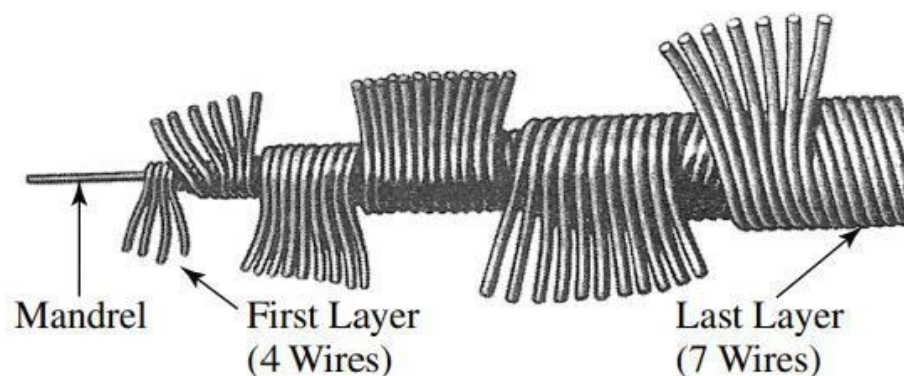
Figure 35: Construction details of the flexible shaft, several layers of wires are twisted around the central core. (Image source: Shigley (85))

Two flexible shafts were specially designed and manufactured to meet our requirement (*S. S. White Technologies Inc.* UK). The flexible shafts (Figure 36) were made using steel wires and have the following characteristics:

- Shaft 1: a Ø3 mm flexible shaft with 150 mm length and fitted on both ends with Ø3 mm/12 mm long male solid shaft.
- Shaft 2: a Ø4 mm flexible shaft with 200 mm length and fitted on both sides with Ø3 mm/12 mm long male solid shaft.
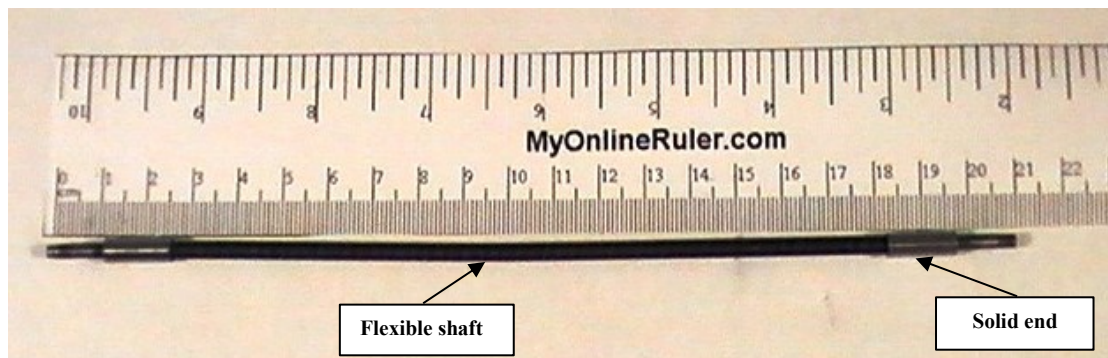
Figure 36: The flexible shaft that used in the construction of the flexible probe. The flexible part of the shaft is attached from the both ends with solid parts that used to be attached with the drill and drill bit.

The shafts are threaded from both ends enabling the attachment of the drill bit and drill motor shaft engine. Also, a Ø2.8 mm groove with 0.40mm width has been made at both ends of the shaft for placing Ø3 mm external Circlips for the retention of the bearings.

II. Flexible Tube

Initially, it was proposed to use a super elastic Nitinol (Ni-Ti) tube as a part to accommodate and bend the flexible shaft and its components, but the high cost of such tube to be used in the manufacturing of the first prototype has driven us to think about alternatives. Therefore, based on a bending requirement of at least 90°; three stainless steel compression springs (*Lee spring Ltd.)* with an external diameter of Ø15.239 mm were used, one with a free length of 63.5 mm, and the other two with a free length of 31.750 mm.

III. Pull-Bend Technique

A Ø0.26 mm fine stainless steel Micro-cable (*Ormiston Wire Ltd.)* was used to pull-bend the flexible part of the prototype. The pulling mechanism consists of a rectangular cross section comprised of two U-shape panels (Figure 37). The panels are closed by a tiny block, which contains a centred Ø2mm hole used as a path for a Ø2 mm stud (tensioning screw). The stud

is then attached to a miniature '+' shaped nut, which sits freely in the panel and is attached to the pulling wire (micro-cables).
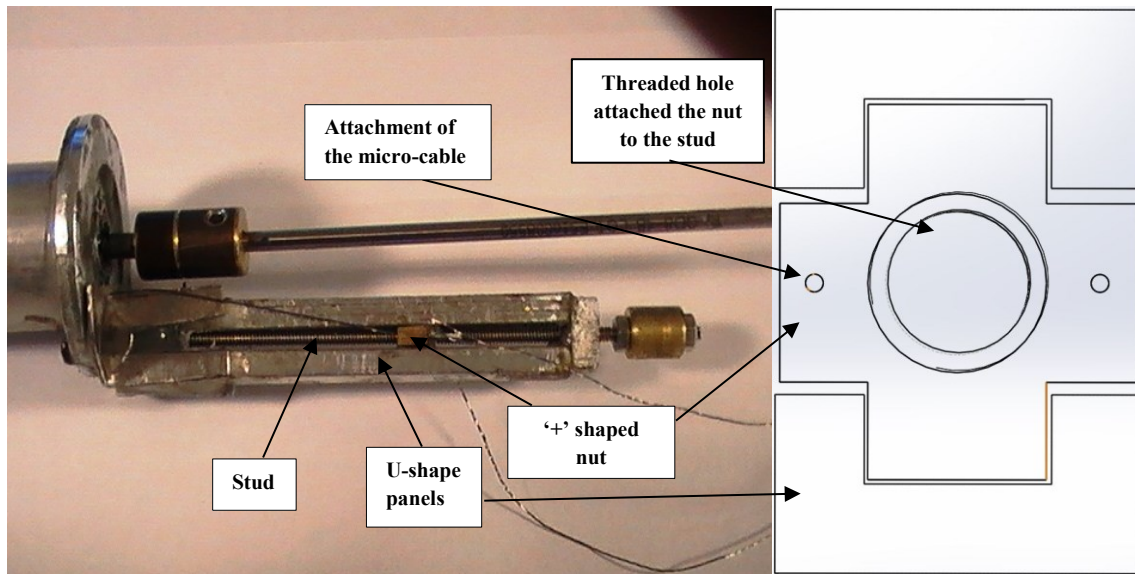
Figure 37: Pull-bend mechanism (left), the '+' shaped nut is attached to the stud and contained by U-shape panels. (Right) an engineering drawing of cross- sectional view showing the position of the nut within the panel.

IV.　　Drill Bit and Engine

An electrical drill (*BOSCH-GSR-18VE-2 Professional*) was used. This drill can perform with two speeds: 40 and 130 rpm. Also, the drill bits of an existing high-speed surgical drill (*Medtronic*) were used.

3.3　　Assembling and Bending Mechanism:

The details of the entire flexible drilling prototype are shown in Figure 39. The three compression springs were attached to each other via two cylindrical middle connections made of Aluminium (Figure 38). These connections were initially made to avoid the flexible shaft from attaching the springs while bending/drilling that could damage the flexible shaft. They were embedded with bearings (*SKF-W628/4-2Z*) to allow a smooth rotation of the shaft that goes through them, and Ø0.5 mm holes were made thorough them to serve as a path for the micro-cables. Then, both ends of the springs were attached to the flexible shaft using two specially designed Aluminium end housings. These were made using a Computer Numerical Control (CNC) machine to enable the integration of devices such as tubes for the flushing water, suction of debris, and cameras. These housings were fixed with bearings (*SKF-W637/3-2Z*) to allow the rotation of the shaft, and could be secured in the desired position by an external circlip.

71
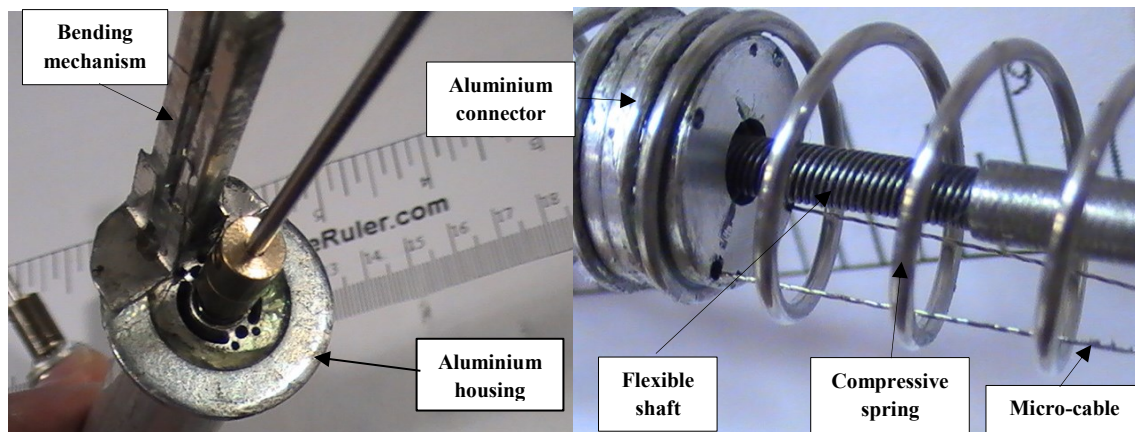
Figure 38: Assembled parts of the prototype, the attachment of the bending tool to the one of the end housing (left), and the attachments of the spring to the mid connector and the positions of the flexible shaft and the micro-cable (right)

The original *Medtronic* drill bits were resized and redesigned to be fixed to the flexible shaft using small connections (Ø6 mm *x* 12 mm length) and 3 mm grab screw. The pull- bend mechanism is attached at the surface of one of the housings using a 2 mm screw.

ITEM NO	PART NUMBER	DESCRIPTION	MATERIAL	QTY.
1	BEARING'S HOUSING	BEARING'S HOUSING		1
2	BEARING'S HOUSING	BEARING'S HOUSING		2
3	COMPRESSIVE SPRING	COMPRESSIVE SPRING		1
4	BEARING'S HOUSING	BEARING'S HOUSING		2
5	BEARING	BEARING		2
6	COV1	BEARING COVER		2
7	BALL			30
8	COV2	BEARING COVER		2
9	COMPRESSIVE SPRING	COMPRESSIVE SPRING		2
10	BEARING'S HOUSING			1
11	FLEXIBLE SHAFT			1
12	B27.8M - 3FM1-3	CIRCLIPS		2
13	CH	CONTROL PART		1
14	nut	+SHAPE NUT		1
15	screw,L	LONG STUD		1
16	con1	CONNECTION		1
17	con2	CONNECTION		1
18	drilCON	DRILL CONNECTION		1
19	grabscrew	GRAB SCREW		2
20	screw,S	TINY SCREW		1
21	drillbits	DRILL BITS		1

Figure 39: A detailed engineering drawing show the entire parts of the flexible surgical drill prototype. The pull-bend mechanism is highlighted in a circle.

In addition, Araldite extra strong rapid adhesive was used for the part attachments excluding the one that was attached with a screw. As the stud is turned clockwise or anticlockwise, the freely placed nut attached to it will slide up or down respectively. As a result, the micro-cable attached at one end to the nut and at the other end to the tip, was pulled up or released down accordingly, causing the flexible part of the prototype to bend.

3.4   Performance Simulation

A Finite Element Modelling (FEM) analysis of the prototype has been developed using the Solid Works computer-aided design software. This study was performed to analyse the stresses on the prototype parts during the bending process. In addition, the simulation was used to calculate the maximum deflection (δmax) of the flexible prototype under certain applied forces.

In order to perform a computer simulation, there were a number of input parameters needed to carry out the simulation study. The prototype was designed with certain parts derived experimentally based on theories and testing. One of the main parameters that had to be obtained was the Elasticity (E) of the probe, which was unknown in our case. To calculate E, mechanical tests were performed using the principle of cantilever bending. The experiment was approached in two ways:

a)   Using electromechanical testing systems (*INSTRON 3366*), the machine was set to compress (10 mm/min) at one end of the prototype while the other end is fixed (Figure 40-top). This test enabled us to directly calculate the compressive load (N) versus compressive extension (mm) (Figure 40- bottom).

The result shows that the compressive load of 0.115 N deflected the prototype by 50 mm, and then the Elasticity (*E*) is calculated theoretically using the deflection of beam formula as shown below:

$$\delta = \frac{PL^3}{3EI} \tag{3.1}$$

Where *P* = load (*N*), *L* = length (*m*), *E* = elasticity (*N/m²*), *I* = moment of inertia (*m⁴*), *δ*=deflection (*m*). In our case, *I*= 3.97×10^{-12} m⁴, **δ**= 0.05 m, *P*= 0.115 N , *L*= 0.14 m, therefore, *E*= 552.9 MPa.

However, the load capacity of the electromechanical testing systems (INSTRON 3366) that used in this test was very big (10Kn) which is poorly sensitive to our flexible prototype. This caused a non-linearity of the data shown in Figure 40 and could lead to imprecise output data. Hence, the manual mechanical testing was carried out.
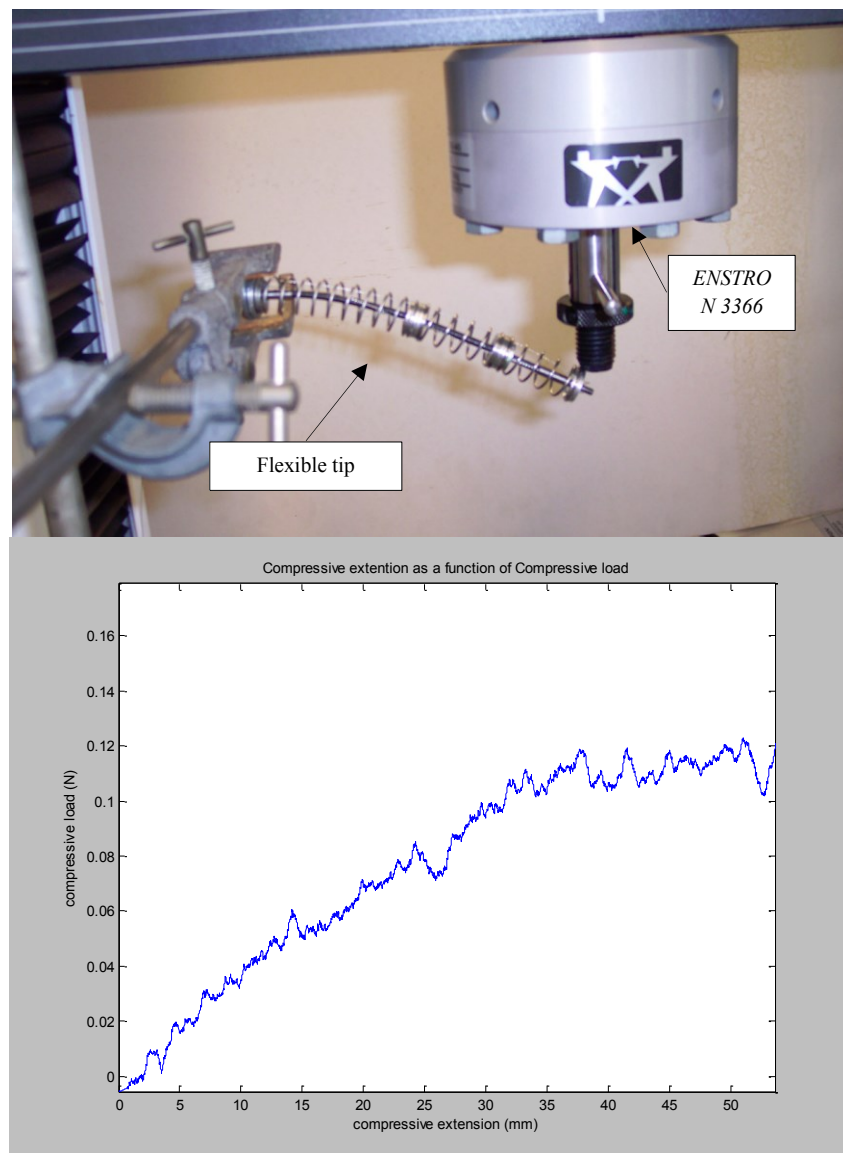
Figure 40: Electromechanical testing of the prototype, (top) INSTRON 3366 testing system, (bottom) testing results depicting the relationship between the compressive loading and compressive extension

b)   Using a manual bending test by fixing one end of the prototype and placing masses (5-75 g) at the other end (Figure 41- top). These masses were then converted to weight in newtons (N). Figure 41- bottom shows the relationship between the weights (N) versus deflection (mm) in x and y directions. The flexible probe prototype comprises of a number of connections attached to each other by compressive springs, and a flexible shaft runs thoroughly. Each part of this construct is prone to a different reaction when the load is increased each time. This led to some odd non-linearities appeared in the result shown in Figure 41.

The table of results (Appendix 3) shows that the compressive load of 0.735 N is deflecting the prototype by 65 mm. The Elasticity (E) of the probe is calculated theoretically using equation (3.1) as shown previously. This test results in Elasticity (E) =3207. 6 MPa.

The elasticity value of 3207.6 MPa was then used as an input for our simulation study alongside other properties of the material such as density (7000 Kg/m^3) and Poisson ratio (0.3).
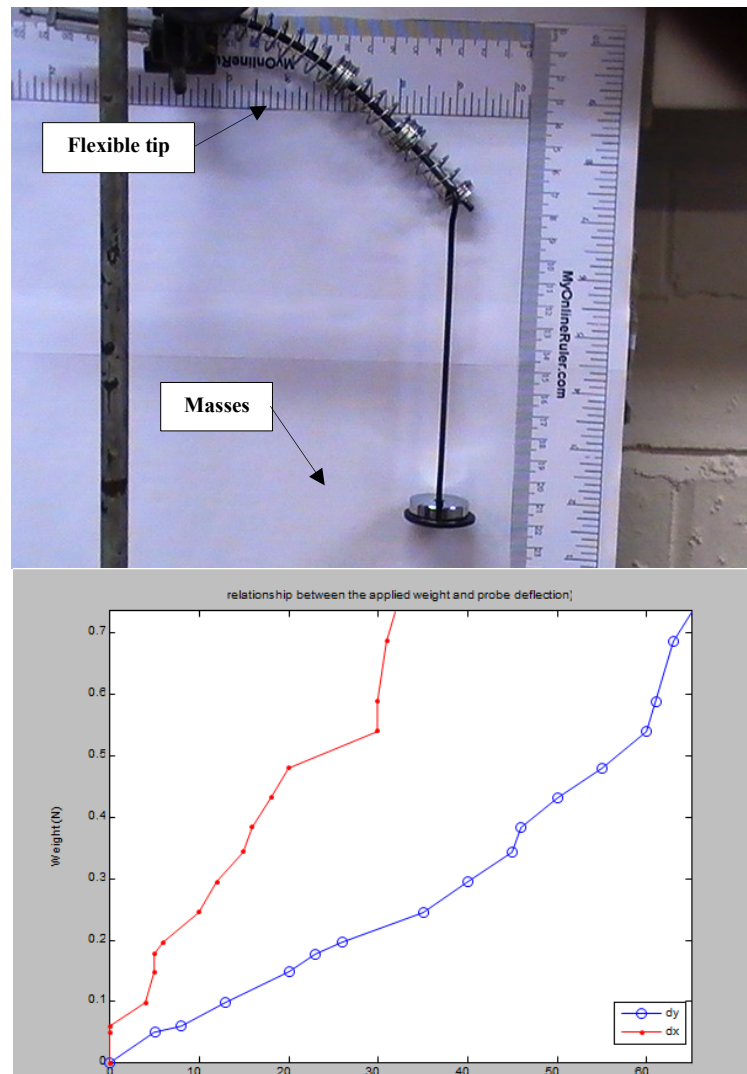
Figure 41: Manual testing of the prototype, (top) placing masses at one end, (bottom) testing results representing the relationship between the applied weight and probe deflection.

It was assumed that the flexible part of the prototype was pinned at one end and was free at the other end. The finite element modelling was determined by applying incremental forces (0.5-3 N) at the tip of the flexible prototype (free end) and calculating the resultant displacement. The study shows that a force of 0.75 N would deflect the flexible tip by a maximum of 68.2 mm (Figure 42-left) and a maximum Von Misses stress of 38 MPa (Figure 42-right).
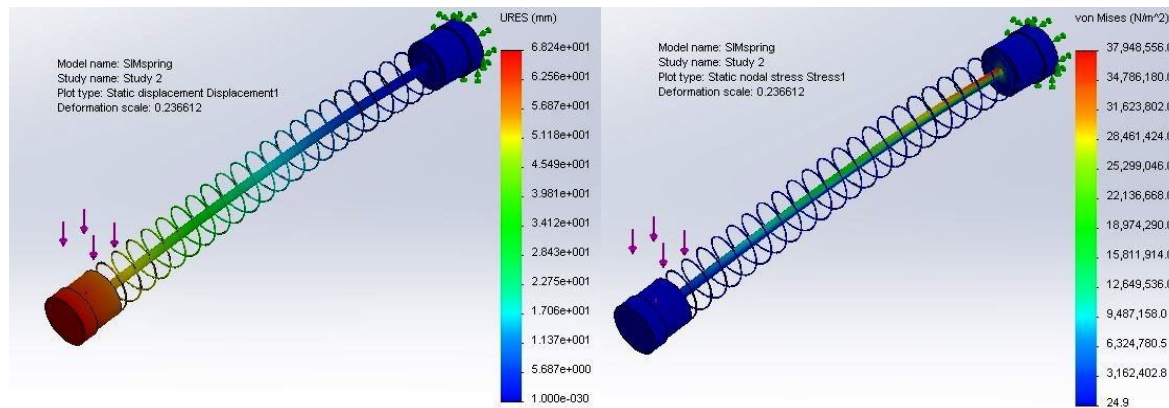
Figure 42: FEM study of the flexible probe prototype shows maximum deflection (left), and maximum Von Misses stress (right)

The study was also conducted for a modified flexible probe prototype (explained in the next section) with the addition of a rigid tube that was implemented into the original design to achieve a J- shaped configuration of bending with angulation >90°. The study showed the effect of the additional tube upon the deflection level of the flexible part at the same applied forces. The simulation of the modified probe showed that a force of 0.75 N deflected the flexible tip by a maximum of 33.5 mm (Figure 43-left) and a maximum Von Misses stress of 14 MPa (Figure 43-right).
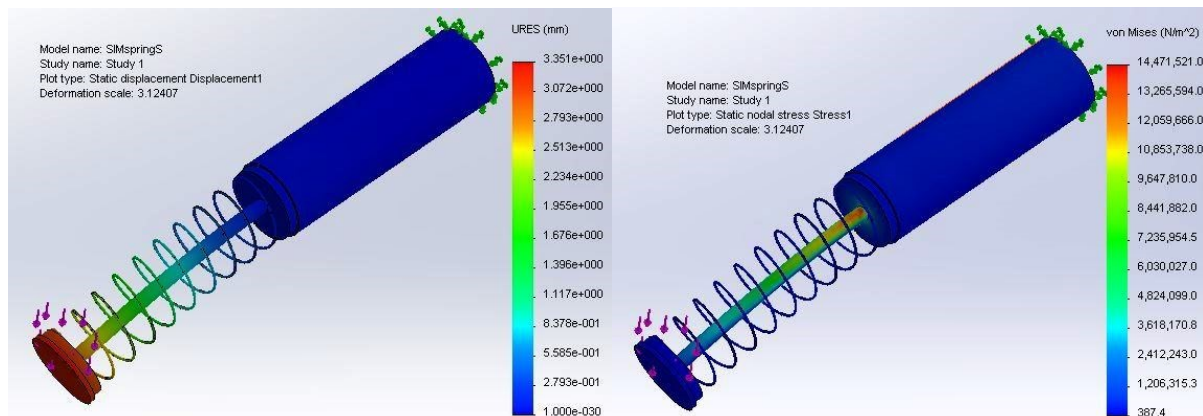
Figure 43: *FEM* study of the flexible probe prototype with additional tube shows maximum deflection (left), and maximum Von Misses stress (right)

Once incremental forces were applied to both designs, the resulting displacement and von Misses stresses were recorded. Figure 44 illustrates the linear relationship between these three outcomes with different levels of deflections and stresses under same applied forces.
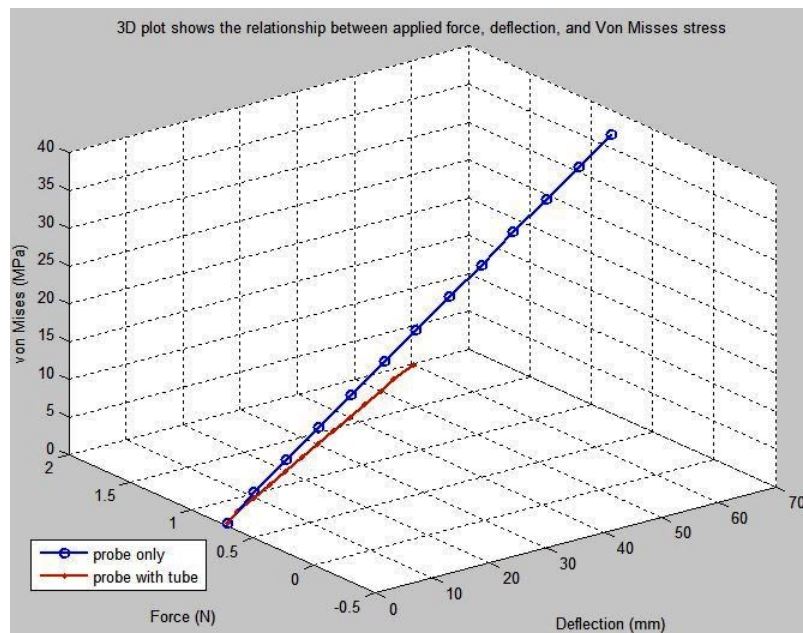
Figure 44: 3-D Plot shows the linear relationship between applied force, deflection, and Von Misses stress for both flexible probe prototypes (with/without rigid tube)

The performance testing shows the behaviour of the flexible probe under various bending forces. Also, it provides the angular displacement of the flexible probe under certain forces.

3.5   Testing and Analysis

3.5.1 Degree of Angulation

The then-current design of the flexible tip prototype showed that the entire tip assumed a curve form when the micro-cable is pulled by the pull-bend technique with a roughly C-shape configuration, at an angle of 55° from its principal axes (Figure 46a).
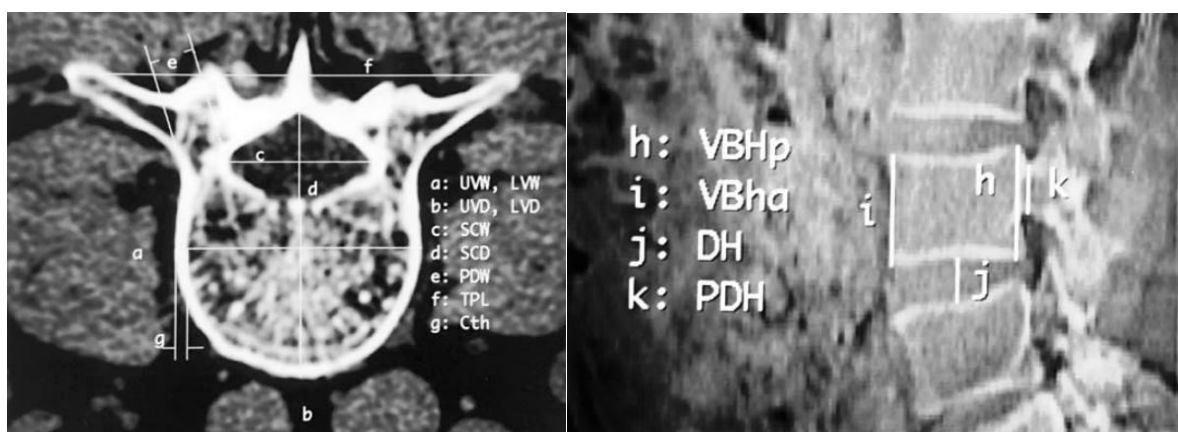
Figure 45: A cross-sectional image (left) and a lateral computed tomographic (CT) (right) of the fourth lumbar vertebral body (*UVW* upper vertebral width, *LVW* lower vertebral width, *UVD* upper vertebral depth, *LVD* lower vertebral depth, *SCW* spinal canal width, *SCD* spinal canal depth, *PDW* pedicle width, *TPL* transverse process length, *Cth* cortical bone thickness, *VBHp* vertebral body height posterior, *VBHa* vertebral body height anterior, *DH* disc height, *PDH* pedicle height). (Image source: S.H. Zhou (90))

In order to virtually visualise the device and its position within the body, particularly around the spinal column, an image tracing analysis was performed using Solid Works software. Initially, a cross-sectional image of the fourth lumbar vertebral body in a 47-year-old male subject [90] (Figure 45) and an image of the flexible tip (Figure 46a) were imported to the solid works software.
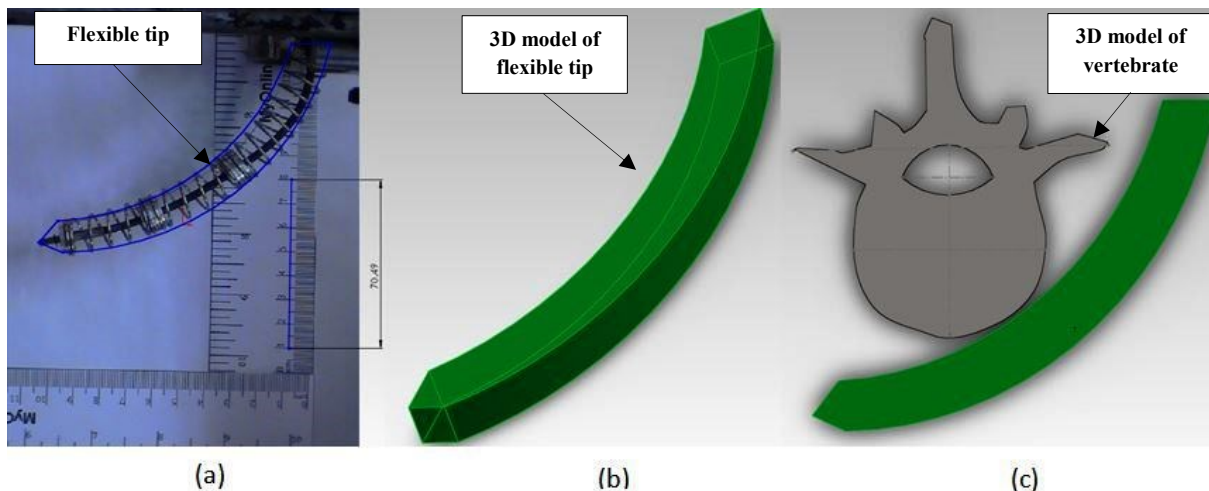
Figure 46: Image trace analysis of the flexible probe, a) transfer an image of the flexible probe to SolidWorks software, b) obtain actual size of the flexible probe and converted to a solid part, c) a solid part of the a human vertebrae, which is obtained from an image, is then compare with flexible probe.

These images were re-sized to the actual dimensions of the vertebrae, and then converted to 3-D solid parts using image tracer (Figure 46b, c). Consequently, the 3-D parts were assembled together and compared to each other. Based on the shape of the bent flexible tip, the analysis showed that in order to reach the bottom of the vertebrate, the flexible tip must access the body from an incision that was far from the vertebrate and, therefore, that could damage the surrounding critical tissues (Figure 46c).

According to the surgical requirements set by the surgeon, the whole flexible tip is not required to bend continually, as the form during surgical access must be straight to reach a certain point and then the tip needs to bend around at an angle of >90°. In order to meet these needs and solve the problem, an Aluminium tube of inside diameter of Ø13.5 mm and outside diameter of Ø15 mm with a length of 65 mm was added to the assembly (Figure 47a). The tube was attached at one end to the inner surface of one of the end housings using Araldite adhesive, and the other end was attached to one of the middle housings using a grub screw. The tube has been implemented to hold the first compressive spring (long spring) such that it remained rigid while the rest of the tip was bending.

The image tracing analysis was applied to the new design using the same previous technique. The analysis shows that when the micro-cable was pulled, a J- shaped tip was formed with angle > 90°. The images show that the flexible tip accesses the field with a straight route from a point that is closer to the spinal column. After reaching the desired depth, the flexible tip then can go around the vertebral body to reach the operation target (Figure 47c).
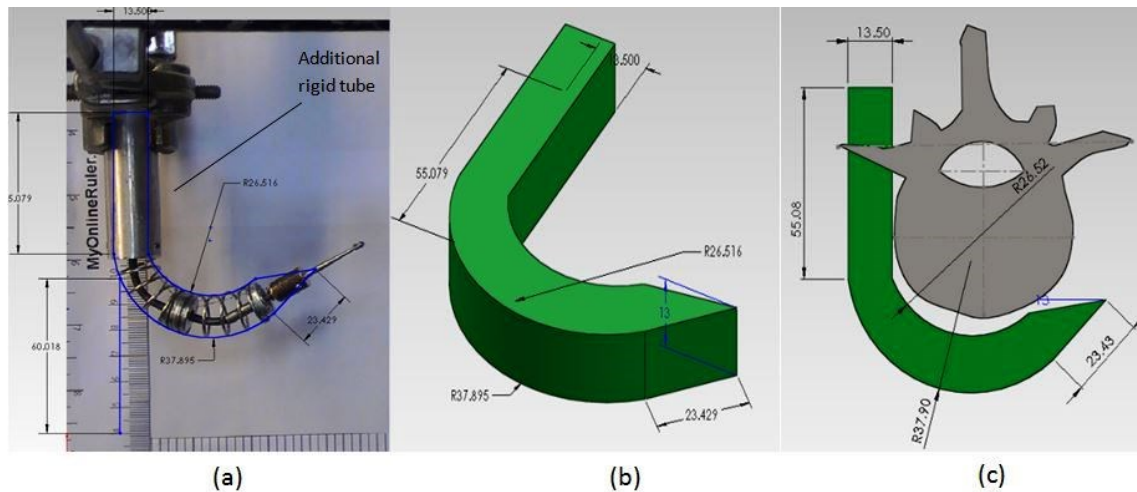
Figure 47: Image trace analysis of the flexible probe with added rigid tube, (a) obtain real size of the flexible probe, (b) convert the image of the flexible probe to solid part, (c) comparing the flexible probe with actual size vertebrae.

3.5.2 Drilling Performance

A simple experimental apparatus was set up to test the drilling performance of the second prototype. In this test, two experimental setups were used:

Setup 1: the experimental setup consisted of the modified prototype with flexible shaft 1 (section 3.2-I), a *BOSCH-GSR-18VE-2* Professional electrical drill with drilling speed of 400-1300 rpm, clamps, and a piece of wood (as the object). The drilling was performed with L- and J- shape bending of the flexible tip (Figure 48).
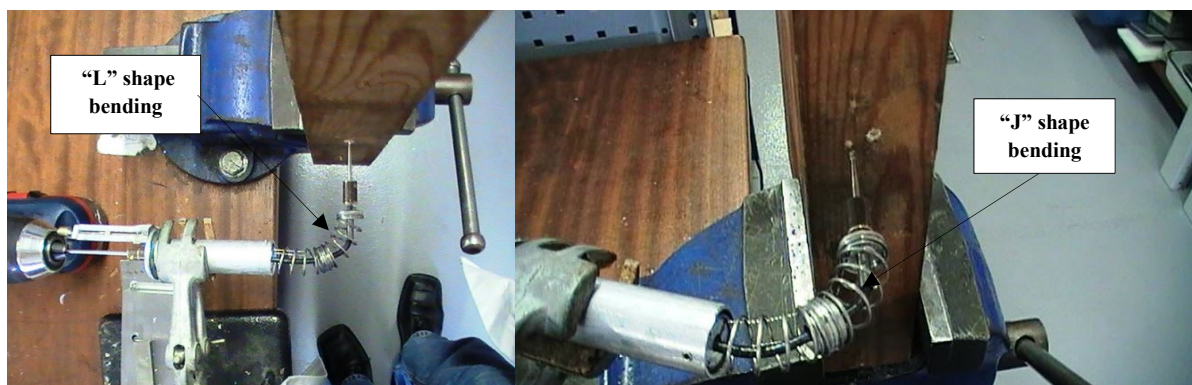
Figure 48: Drilling performance testing, with L-shaped (left) and J- shaped (right) bending of the flexible tip. A block of wood was used as a target object.

Setup 2: the experimental setup consisted of the modified prototype with flexible shaft 2 (section 3.2-I), a *BOSCH-CB8 700-2RE-701W* electrical drill with drilling speed of 48000 rpm, clamps, and lamb femur (as a target object). In this test, drilling was conducted with a straight configuration probe (Figure 49).
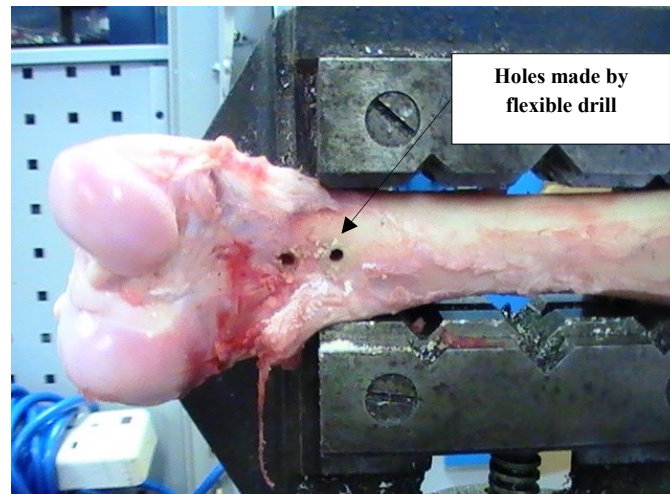
Figure 49: Holes made by the flexible drill on lamb femur with a straight configuration of the flexible probe.

3.6   Discussion and Conclusion

The purpose of this chapter was to introduce a new flexible surgical probe design suitable for navigating around corners, which can address some of the challenges outlined in Chapter 1. The key challenge addressed by this chapter is that of Challenge 1 and 2 - Design and construct a miniaturised flexible device that can be integrated with a surgical tool, and has the ability to go around corners with minimum angulations of 90° and cut tissues. The modular surgical probe design described here is capable of this, and its functioning principles shown to be significant advantages in the following chapters.

The chapter started by addressing the key elements required to construct a tool that is a proposed solution to this particular clinical problem. This was done by identifying the desired criteria based on clinical issues identified by the surgeon. Then, this information was analysed by using pairwise and QFD methods, in which the final requirements for designing the device were specified. Although this study helped in visualising the required features of the device, it is not a feasibility study and it is prone to change depending on the availability and practicability of the specified features.

 The initial idea of choosing a flexible drill as a method of cutting is to modify the surgical drills that are currently used in the operating theatre and find engineering solutions to the

complications that such drills face during the spinal surgeries. Hence, some parts of the first prototype were manufactured and assembled with the use of alternative, less costly materials, such as using compressive spring instead of Ni-Ti tube, just to prove the concept.

The modelling side of this chapter established the principles of designing the flexible surgical probe in terms of both the size and the required degree of angulation. This was successfully done by simulating the real dimensions and shape of the vertebrate. This significantly helped, when the probe was placed around the vertebrate, to determine the size and angulation of the designed flexible probe. However, the work of this chapter revealed important issues related to the stability of the probe during its operation.

During the test with both setups mentioned above, the drill bit kept moving off the pre-marked target point, which prevented the drill bit from contacting the target object at the desired point. Also, a wobbling of the flexible tip was observed. Although these defects were superficially resolved by either holding the tip by hand or initiating a notch on the object before the start of drilling, it remains a primary drawback that had to be solved.

To completely damp any vibration generated by the prototype and perform support free drilling with high effectiveness, consideration was given to replace the compression springs, used to accommodate the flexible shaft in the prototype, with a metallic flexible positioning and holding arm (Figure 50). This arm can be positioned in various angulations and can then be locked when the required position is reached. Therefore, this technique will eliminate most of the vibration or movement off target produced by the prototype.

In conclusion, following the preliminary development and testing of the flexible surgical probe, it is clear that while functional, in its current configuration the instrument is not yet ready to provide constant flexibility and perform controlled cutting. It, therefore, does not fit the overall design goals of the flexible surgical probe and new system architecture and design is required to more specifically target the challenges outlined in Chapter 1. To deal with these challenges, while incorporating the lessons learnt from the preliminary design of the flexible surgical probe prototype, a flexible retraction instrument was designed. This new design will be described in Chapter 4.

Figure 50: Flexible positioning and holding arm (Image source: Mediflex Surgical Products)

4   Flexible Surgical Mechanical Drilling System

In the previous chapter the first flexible drilling probe prototype has been designed, modelled, fabricated, and experimentally tested. The analysis revealed some drawbacks related to the unbalanced behaviour during drilling. However, the preliminary design established the principles of the bending technique that was used in the design of the new flexible probe prototype. To prevent the previous problems, the new prototype was proposed to be a flexible probe that is able to bend to a rigid J- shaped configuration. The weaknesses of the previous probe design were identified, and the design was refined. The new device was built with the capacity to completely bend through a J- shaped configuration.

Unlike the design of the first prototype in which the drilling unit was permanently built within the flexion unit for a flexible surgical probe, the new prototype consisted of two separate units, the flexion unit and the drilling unit. The two units were combined to form a flexible surgical device that can bend up to J- shape configuration and dissect tissues around the corners of the spinal column.

4.1   The Flexion Unit

The flexion unit is a surgical Retraction Instrument with a Ø5 mm adjustable articulated tip, and a working length of approx. 250 mm. The metal section of the system, made with 1.4301 Surgical Steel, is comprised of a shaft, with a proximal end, a distal end, a channel extending through the proximal and distal end, and a handle, made with Polyphenylsulfone (PPSU) Plastic-type material, over the proximal end shaft. A tensioning screw is located on the proximal shaft (Figure 51).

A retractable lower distal tip section comprises a series of links held together by a cable (1.4305 Steel), and the links are tightened to form a predetermined adjustable shape. When the cable is not tensioned, the distal tip section links lie in a loosely formed semi-straight shape. Links are tightened by turning the tensioning screw until the lower distal tip section is formed into the desired semi-rigid, curved shape at the desired angle, within the functional limitations of the device. The surgical retraction instrument was manufactured by *NEWCO Surgical Ltd*. as they were contracted to build the device.
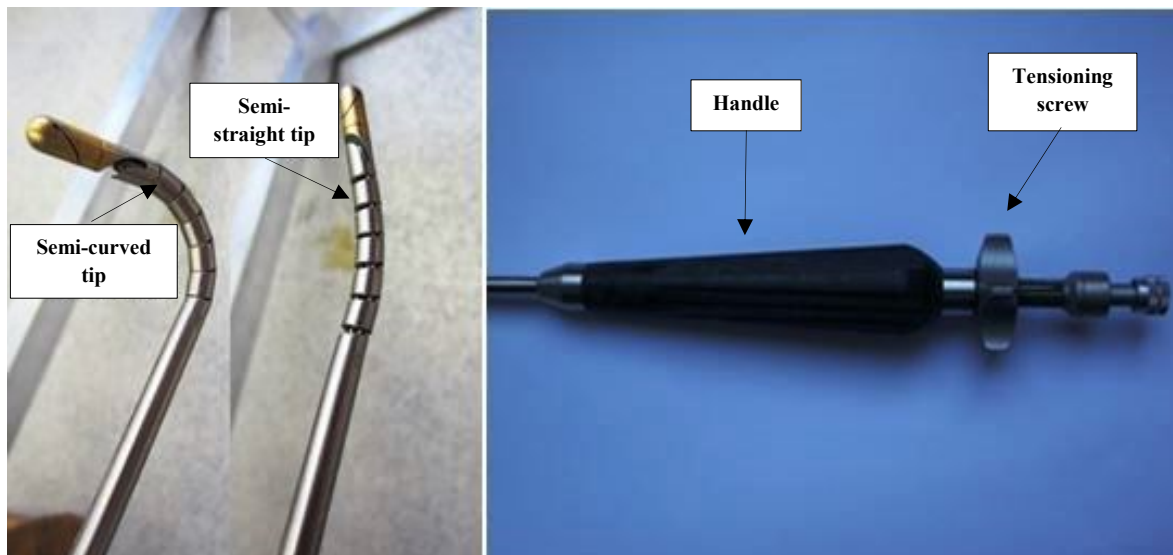
Figure 51: The flexion unit. (Left) a retractable lower distal tip fully tensioned and fully released. Proximal end with the attachment of tensioning screw (right).

4.1.1 Flexible Distal Tip: Angulation Principles

In this sub-section, the work principles of the flexion unit, including an analysis of the degree of angulation, will be described. Some assumptions were made to produce the drawings that make the analysis simpler without affecting the working principles of the flexion unit.

The distal end of the Flexion tool is shown in Figure 52. Condition (1) shows the tool with zero tension loads through the actuation cable (AC). Condition (2) shows a moderate amount of tension applied to the AC. The tip is comprised of multiple segments or links (ML) of the hollow round shaft (R). The links are defined by a series of slots (SL) cut into the shaft (R), such that only a small proportion of the shaft remains (RS), and all of the slots are aligned at the same angular displacement along the principal axis of the shaft. The remaining shaft material at the slots retains the overall tubular form of the shaft, but allows it to flex in a single plane, which coincides with the shaft principal axis.

The enlarged view of the multiple links is shown in Figure 52- right. As the cable AC is tensioned, it pulls the anchor point (AP) in the end link (EL) closer to the shaft (R), which induces the multiple links (ML) to pivot approximately around point PP. These pivot points occur on each multiple link ML, and are due to flexing of the remaining parts of the shaft at points RS.
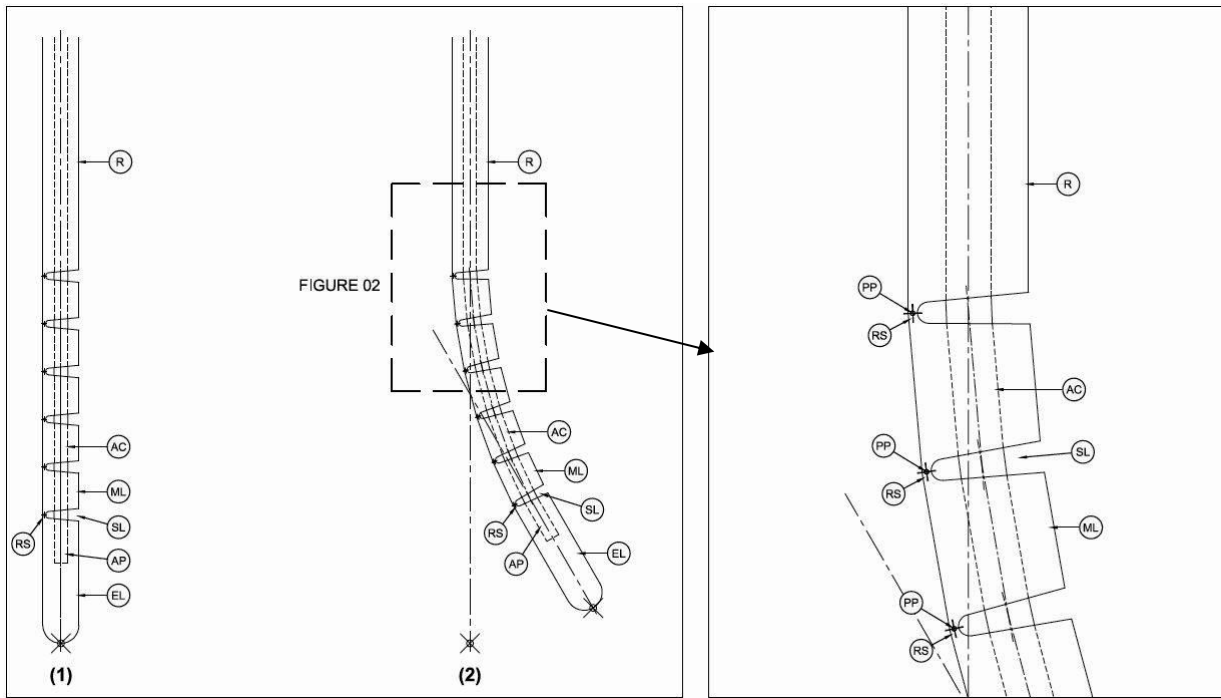
Figure 52: Bending of tool's flexion tip. (Left) tool with zero tension load (1) and moderate amount of tension applied (2), (right) enlarged view of the multiple links.

Figure 53 shows the ascending stages 1 - 5 of distortion of the distal end, with displacements relative to the zero-tension position (1) noted for stages 2 – 5 as the tension in the actuation cable (AC) increases. The plots of the motion of the distal end shown presuppose that the distortion is uniform along its length, i.e. each multiple link moves in the same manner relative to the other links. The varying radii of the arcs formed by the distorting distal end as a whole are also noted.
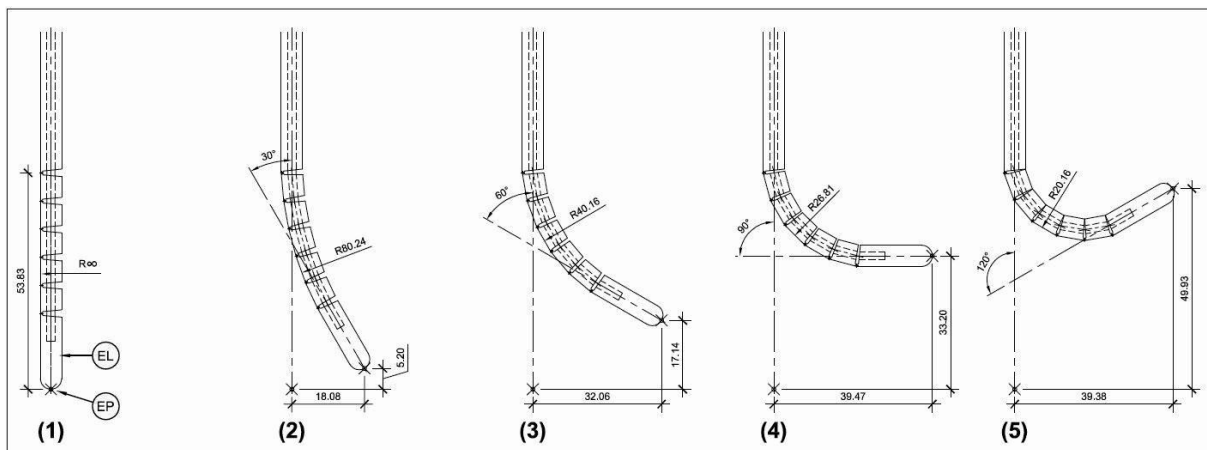
Figure 53: Stages of bending the flexion distal tip showing the angulation degree for each ascending stage.

At zero tension in the actuation cable, the radius is, in theory, infinite, i.e. a straight line. However, in practice the pivot points (PP) between each section of the multiple links (ML) exhibit a degree of plasticity, presumably due to small frictional forces acting on the

85

actuation cable (AC) as it passes through the shaft (R), meaning the radius is always less than infinity.

The mapping of the end point (EP) of the end link (EL) as the tension in the actuation cable (AC) increases is shown in Figure 54. The path of the end point is an arc of approximate radius 42 mm.

Hence the equation of the position (x, y) of the end point (EP) will be derived from the standard form of the equation for points of a circle $(x^2 + y^2 = r^2)$, where r is the radius of the circle.
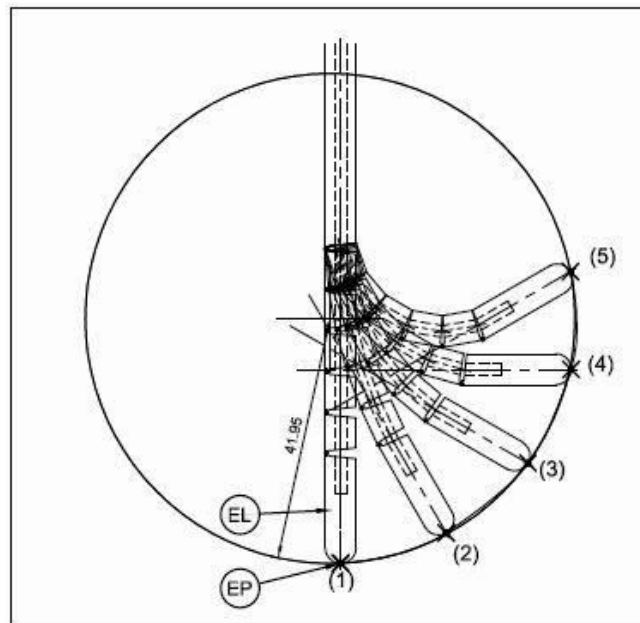
Figure 54: The mapping of the flexion tip. As the tension in the actuation cable increases; the path of end point (EP) of the end link (EL) forming an arc of approximate radius 42 mm.

4.2 The Drilling Unit

The drilling unit is comprised of two Ø3 mm flexible shafts, FS1 and FS2 (see section3.2-I), with 112 mm length and fitted from both ends with Ø3 mm rigid shafts with 12mm length. The shafts are threaded from both ends, enabling the attachment of the drill bit and the drill drive shaft. An electric drill (*DREMEL 800*) with a flex shaft attachment was used to rotate the flexible shaft (Figure 57). The speed range of the *DREMEL 800* drill is 5,000- 35,000 rpm similar to the surgical drills that are currently used in operating theatres (*Medtronic Ltd.*). In addition, an existing surgical drill bit from *Medtronic Ltd.* was used.

4.3   The Prototype: Assembling Process

The flexion and drilling units were integrated together via two connectors. Both connectors were made of brass and embedded with bearings that allow the rotation of the FS1, and features for the attachment of the retractor (Figure 55-left). One of the connectors (Con1) has been designed such that it connects the end of the FS1 to the articulated tip of the surgical retractor.
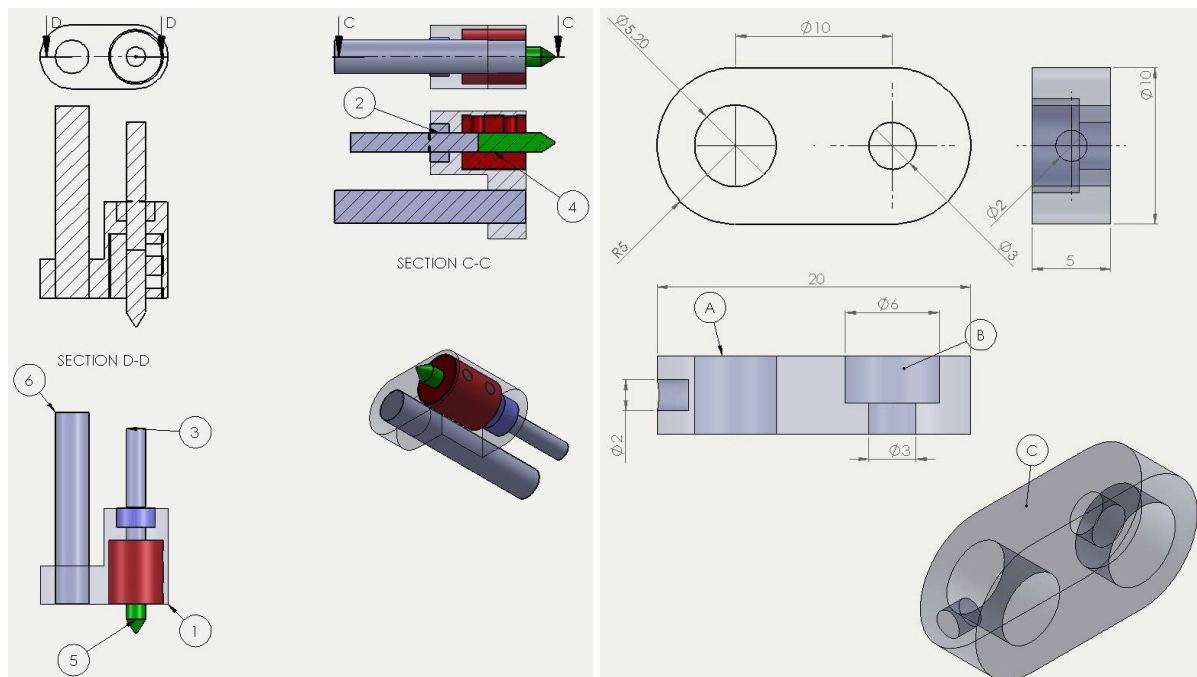
Figure 55: Engineering drawing of the flexible drilling system's connectors: (left) the connector for several parts, (1) the body, (2) bearing, (3) flexible shaft, (4) rotary coupling, (5) cutting burr, (6) retractor, (right) connector that attaches the solid part of the retractor to the other end of the flexible shaft, (A) path of the solid part of the retractor, (B) the position for the bearing that surrounds the flexible shaft, C-connector body.

The second connector (Con2) has been designed to attach the solid part of the retractor to the other end of the FS1 (Figure 55-right). The FS2 is attached from one end to FS1 at the second connector via an Aluminium flexible coupling, secured via a setscrew. The other end of the FS2 is attached directly to the drill engine. The entire assembly is fixed to an aluminium bracket that can be adjusted to align the device horizontally or vertically (Figure 56). As the retractor's tension, screw is turned clockwise or anticlockwise; the flexible part of the retractor will bend or straighten respectively. As a result, the integrated drilling system will bend accordingly and follow the curved path of the bent retractor.

The first assembly of the flexible drilling system (described above) was initially tested by bending the tip of the surgical retractor while running the drill motor
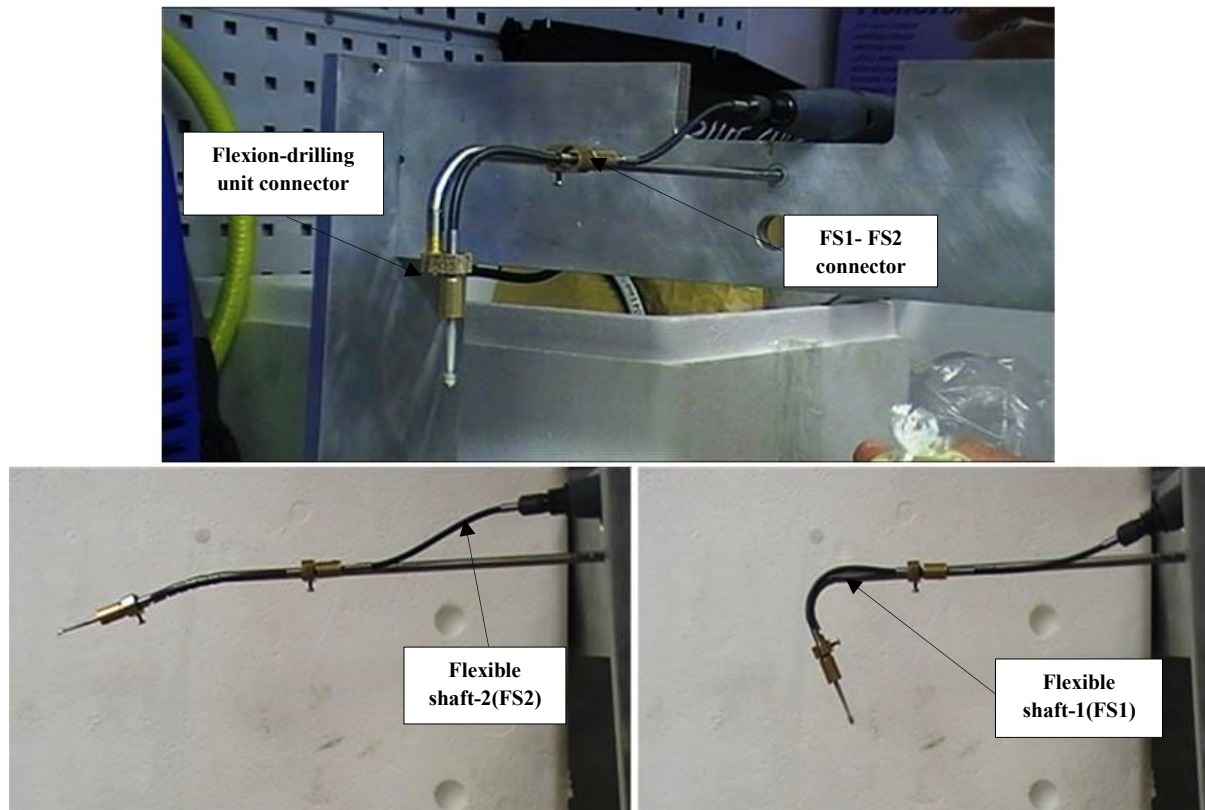
Figure 56: An assembled first flexible surgical drill prototype. (Top) the entire prototype mounted on an aluminium bracket, (lower left) pre-tensioning configuration of the prototype, (lower right) fully tensioning configuration of the prototype.
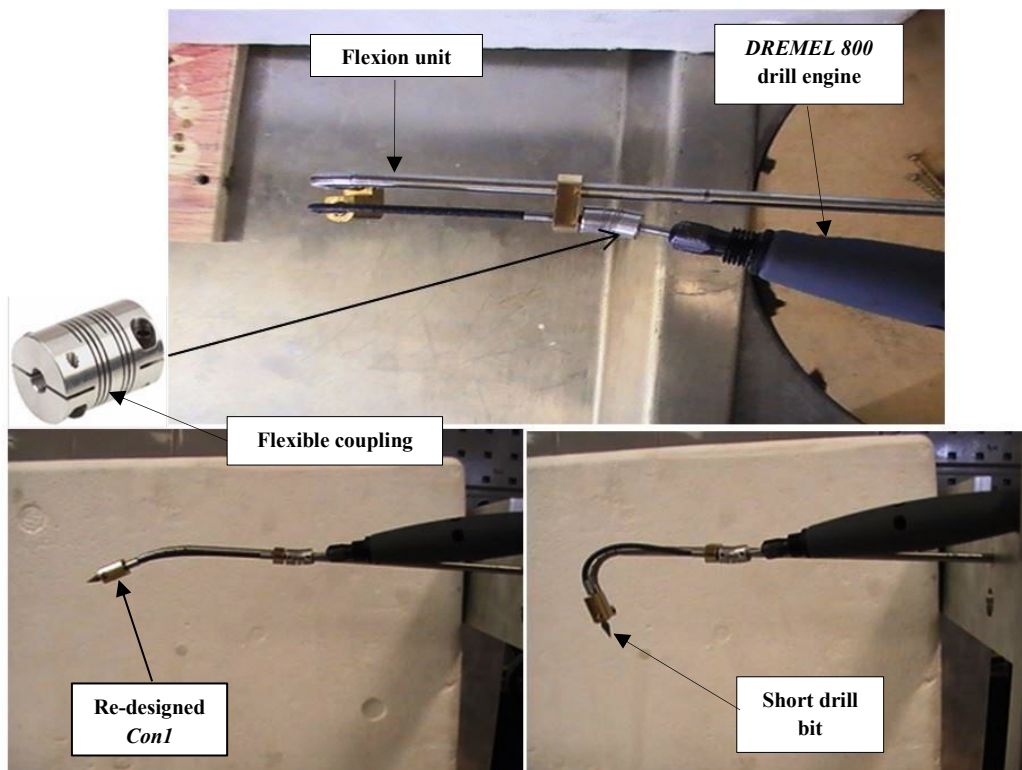
Figure 57: Re-designed flexible drilling prototype. (Top) position of the flexible coupling that replaced FS2, (lower left) pre-tensioning probe with the attachment of new Con1, (lower right) fully tensioned probe with the addition of new shorter drill bit.

The test revealed two problems that could affect the performance and the accuracy of dissecting tissues around the spinal column. Bending the tip of the retractor shows that the tip of the bit is positioned far from the targeted point of cutting around the spinal column. This defect was solved by re-designing Con1 and using a shorter drill bit. The second defect was a noticeable vibration of FS2 that affected the stability of other parts of the system. The solution was to remove FS2 and connect the drill motor directly to the FS1 via a flexible coupling. The flexible coupling was also used to align the drill engine parallel and away from the solid part of the retractor (Figure 57).

4.4   Experimental Testing and Results

4.4.1 The Position and Degree of Angulation

According to the surgical requirements set by our collaborator surgeon, the prototype was designed such that the surgical access must be straight to reach a certain point and then the tip needed to bend around at an angle of 90° from its principal axis.
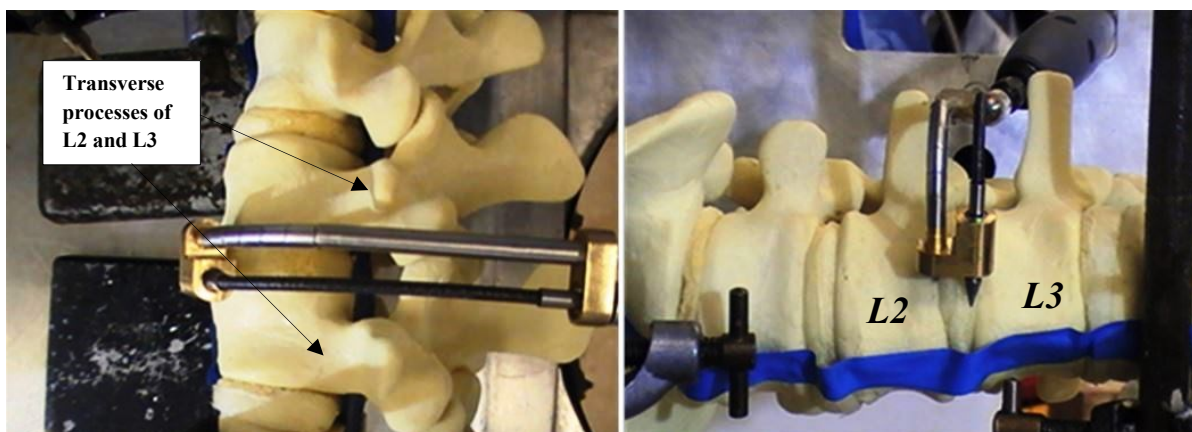
Figure 58: Test of the position of the flexible drill, (left) position of the flexible drill between the transvers processes, (right) position of the flexible drill between L2-L3 and reaching the lower mid line of the vertebrate body.

Therefore, it was important to achieve the requirement set by the surgeon and to test the flexible drill in vitro using a human model. To conduct the test, a model of a human lumbar spine (*London Bone Company*) was used. The flexible drill was inserted between L2 and L3 of the lumbar spine model. Figure 58 shows the insertion of the flexible surgical drill between the transverse processes of L2 and L3.

Figure 59 shows a side view along the spinal column of a gradual move of the flexible drill from the insertion point to the end point where the full curve of a J- shaped configuration is reached.
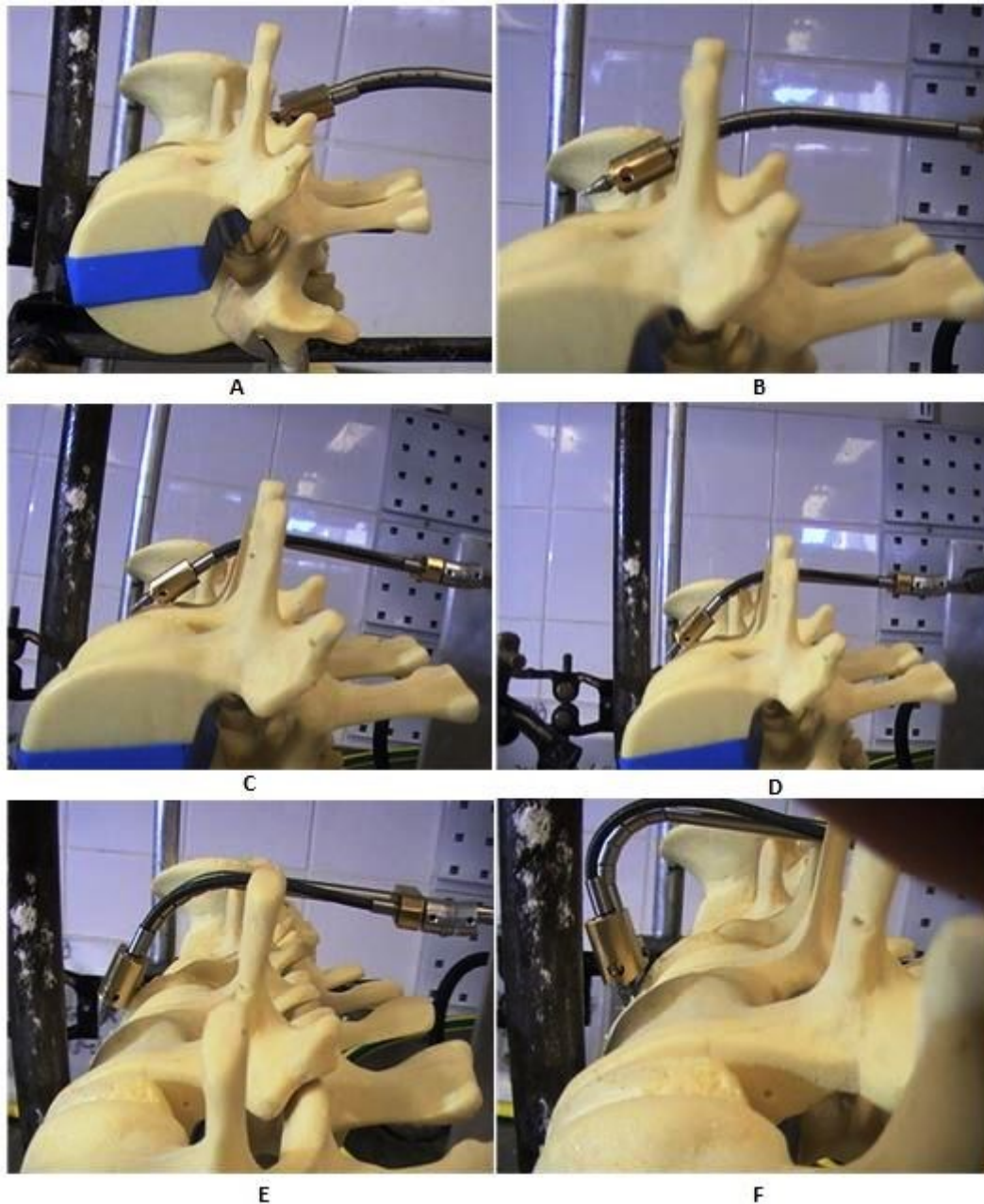
Figure 59: Side view of the flexible drill from the point of insertion in between L2-L3 to the point of reaching the interior side of the vertebral body, A-F respectively

The procedure of the insertion the flexible drill was done by moving the probe whilst simultaneously turning the tensioning screw, thus bending the tool in a form corresponding to the vertebral body shape. Figures 60-62 show the front, back, and top views of the flexible drill moving gradually around the lumber spine vertebrate.
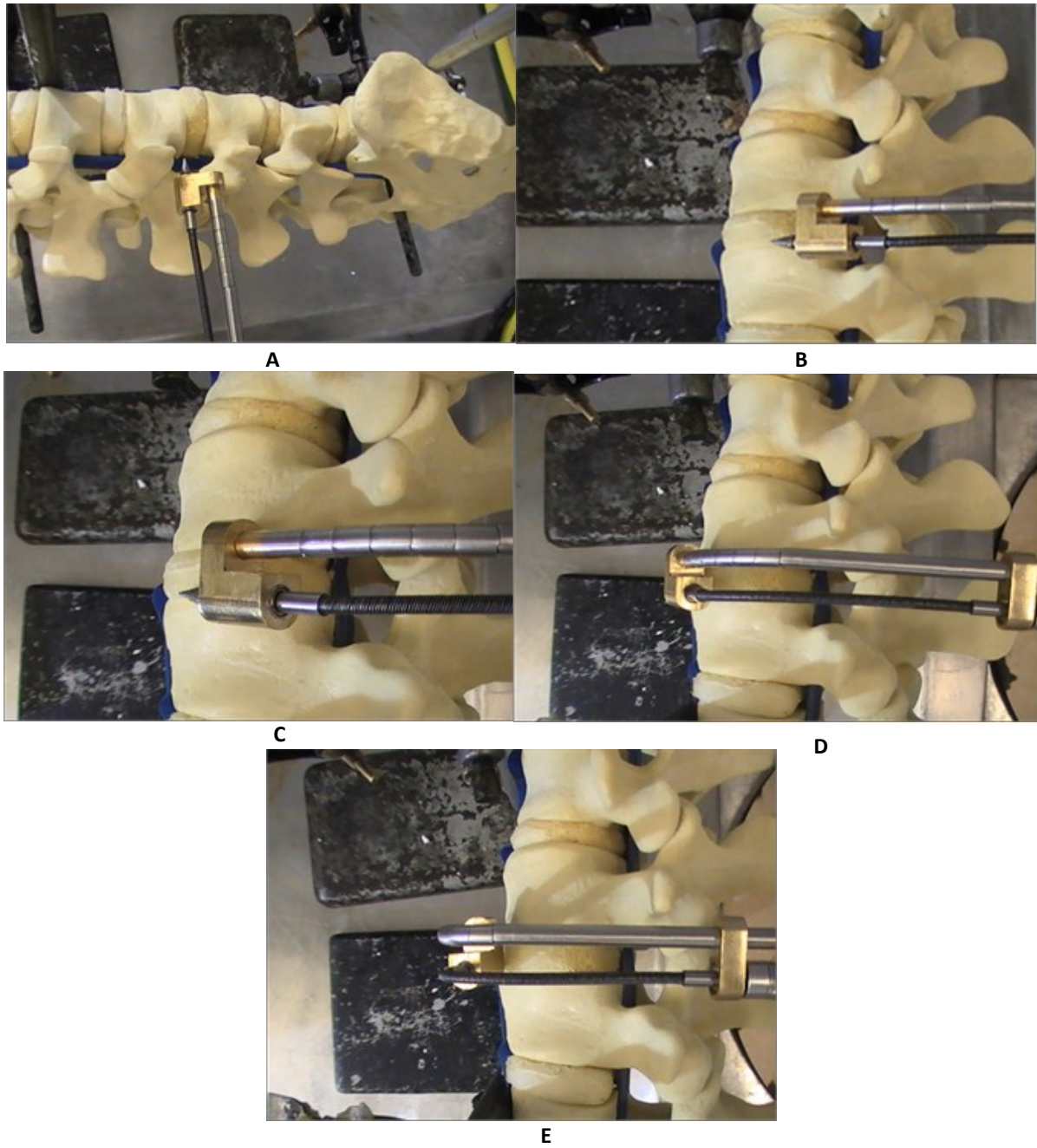
Figure 60: Top view of the flexible drill from the point of insertion in between L2-L3 to the point of reaching the interior side of the vertebral body, A-E respectively
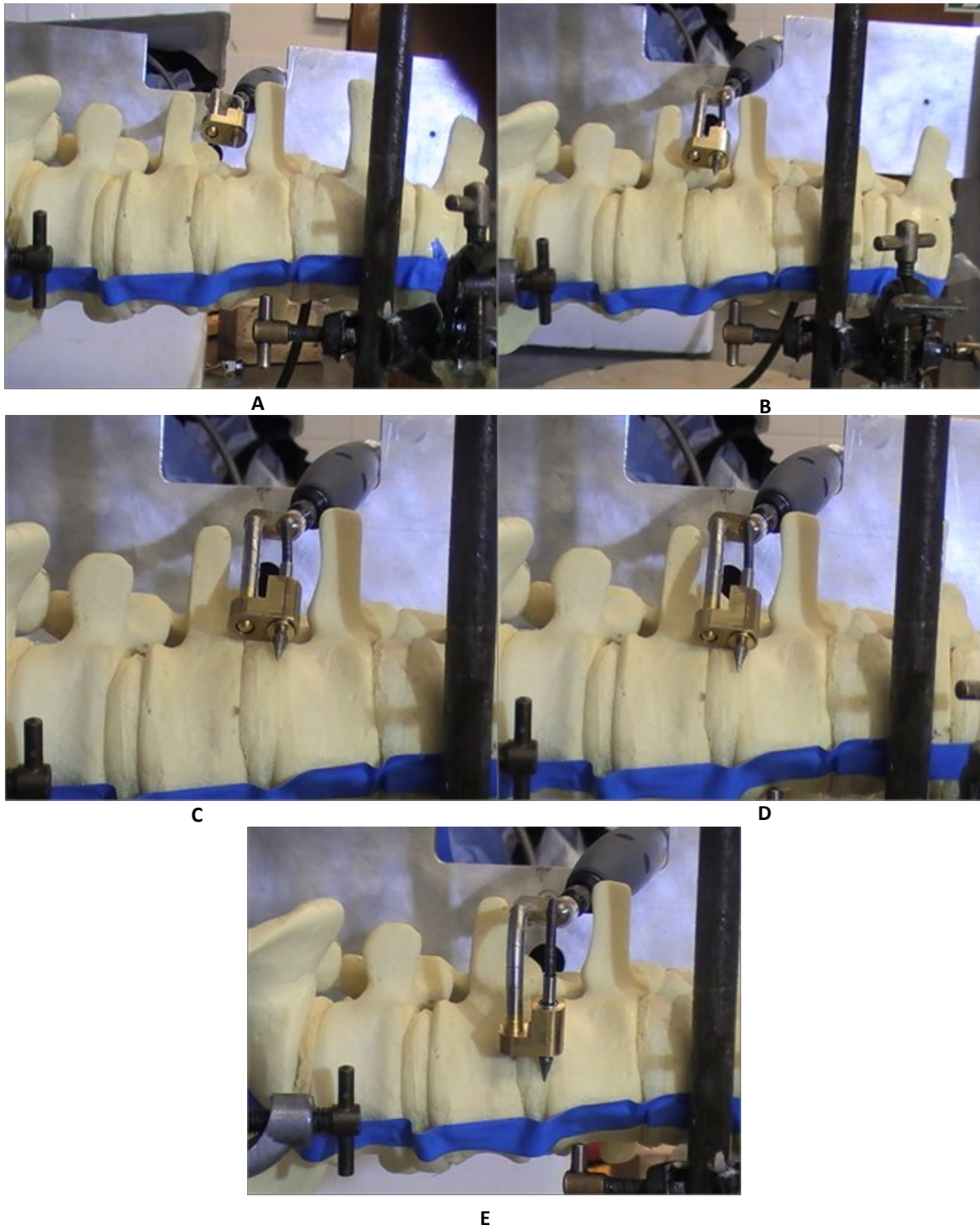
Figure 61: Front view of the flexible drill from the point of insertion in between L2-L3 to the point of reaching the interior side of the vertebral body, A-E respectively
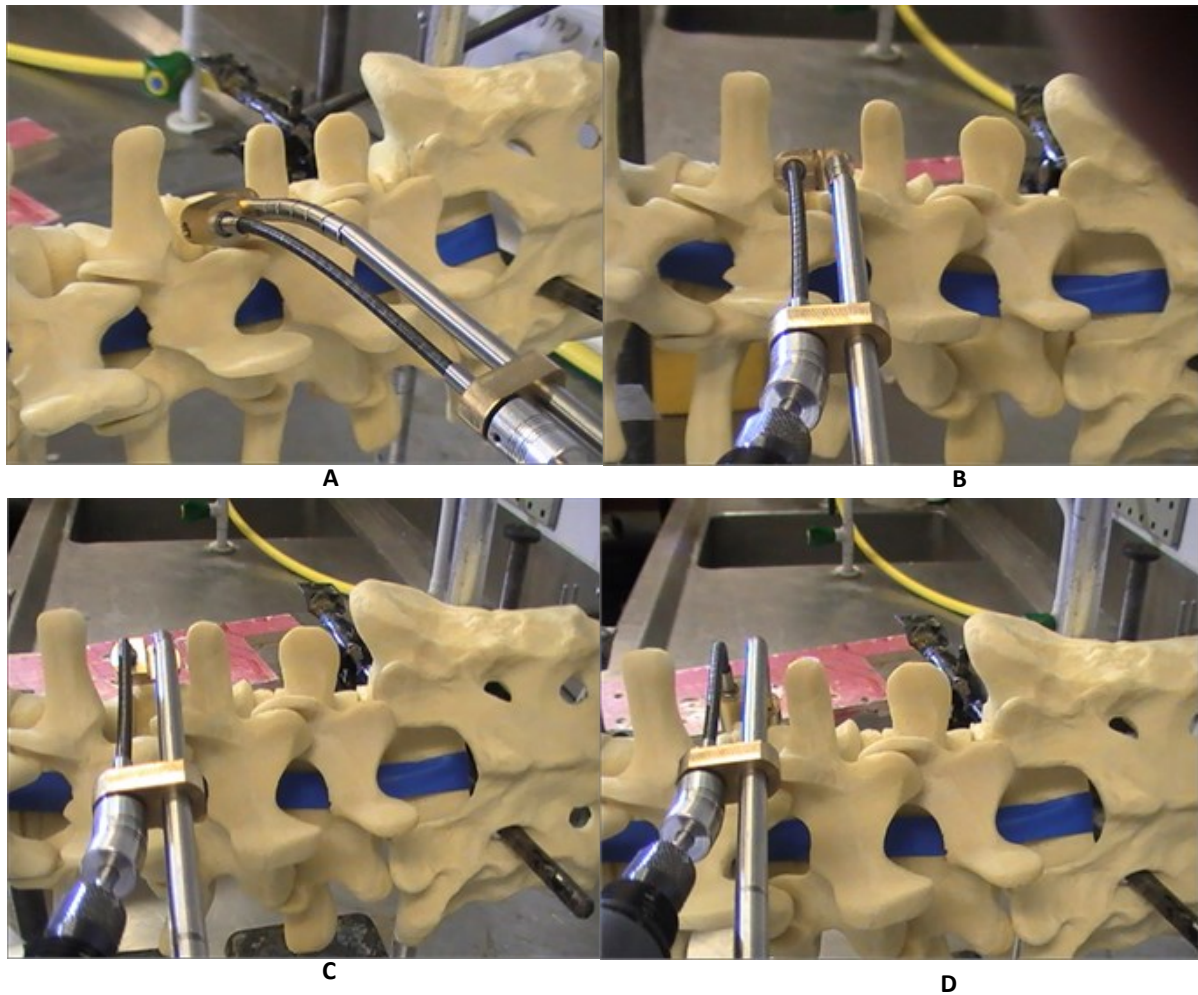
Figure 62: Back view of the flexible drill from the point of insertion in between L2-L3 to the point of reaching the interior side of the vertebral body, A-D respectively

4.4.2 Drilling performance

An experimental apparatus has been setup to test the ability of the flexible surgical drill system to drill. The flexible drilling system prototype and an electrical drill (*DREMEL 800*) were attached to a holding aluminium bracket. A human femur bone model (Figure 63) was used as an object fixed by clamps.

The speed range of the drill used in this test was 25,000-30,000 rpm matching the speed of actual surgical drills used in the operating theatre. The experimental result showed that the prototype under a J-shaped configuration bending is able to cut a line through the bone model as well as drilling holes, with depth equal to the length of the drill bit, (Figure 63) smoothly and fast.

Figure 63: Experimentally testing the performance of the flexible surgical drill system, (left) experiment setup, (right) holes made by the flexible drill.

4.5   Discussion and Conclusion

This chapter focused on finding solutions to the drawbacks appearing in the design of the first flexible probe prototype. With the benefit of the functional principles that were obtained from designing the first prototype, the design and manufacturing of the flexible probe (flexion unit) was successfully achieved in this chapter (Challenge 1). The new probe has satisfied all the clinical requirements set in the discussion with our contributing surgeon, these include: a linear form conducive to straight entering through an incision, and the bending to a J- shaped configuration, allowing the probe to reach the operation target at the interior side of the spinal column. The probe also becomes a hook-shaped solid structure that reduces vibration and gives stability to the device while drilling.

A detailed angulation analysis was conducted to explain the work principles of the flexion distal tip and measure the degree of angulation through varied stages of bending. The study was based on assumptions to simplify the drawings and introduce the concept clearly.

The flexion unit was successfully integrated with the mechanical drilling unit (Challenge 2). Together, they complete the flexible surgical drill system. This system was experimentally tested to prove its feasibility in terms of positioning and drilling. With reference to Figure 57, the system was thoroughly tested demonstrating the movement of the flexible drill from the point of entering the body to the point of reaching the anterior side of the spinal column. Moreover, the drilling was also carried out successfully, but with repeating the test and extending the drilling time, some defects begin to appear.

Two main drawbacks were observed during the test. One is that a slight wobble is generated in the entire system that emanates from the second flexible shaft (FS2) attachment. This defect has been solved by removing FS2 and replacing it with a flexible coupling as

described in section 4.3. The other drawback is that the first flexible shaft (FS1) gets hot as the drilling continues, which affects the mechanical properties of the flexible shaft and can lead to damage. As the flexible shaft used in the device is relatively short (112 mm length), so under full bending, the shaft is prone to a high-tension force. Therefore, it was proposed, as future work, to use a flexible drill extension in which a long flexible shaft can be used with less tension force.

In conclusion, the work of this chapter has established promising first principles for the design of flexible surgical drills that can be used in spinal surgery. A flexible shaft with more appropriate material properties could achieve better results and deliver a novel and extremely useful surgical tool.

5   Flexible Water Jet Cutting System

The experimental work and analysis of the flexible mechanical drilling system, described in the previous chapter, has revealed a number of mechanical defects that affected the accuracy and performance of the system; these include wobbling and an unwanted increase in the shaft's temperature at high shaft rotation speed. To overcome this, an alternative and effective method of cutting that is appropriate to our surgical application with the possibility of using our current flexion unit is designed.
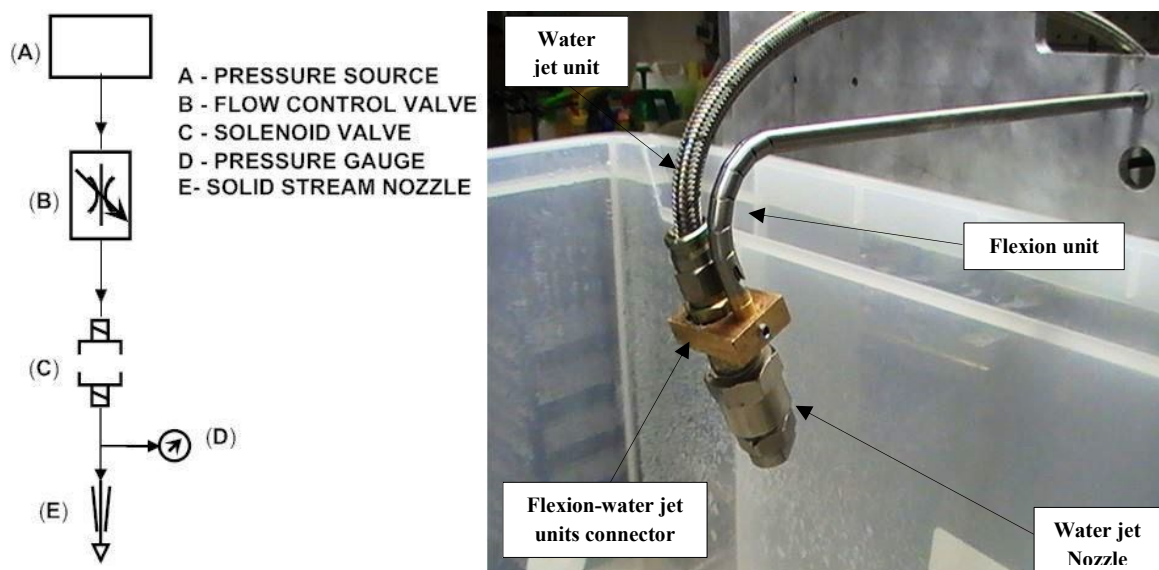
Figure 64: Schematic of water jet system comprised of five main elements (left). Integration of the water jet unit with the flexion unit via connector (right)

Water jet technology was reviewed in Chapter 2. The review showed that the performance and the depth of water jet cut when using AWJ is improved over the use of PWJ. However, AWJ is mostly used to cut hard materials/tissue with relatively complex head/nozzle. The target application of this project was to dissect soft cancerous tissue; therefore, PWJ is preferred over AWJ with simple head/nozzle.

This chapter is a description of the first prototype of a flexible water jet cutting device and the feasibility of a pure water jet to dissect or drill holes in various animal soft tissues. The prototype consists of two integrated units (Figure 64): the flexible unit (described in section 4.1) and a water jet-cutting unit.

5.1   Operating the Pure Water Jet System

The main components of the pure water jet system consist of a high-pressure pump, flow control valve, solenoid valve, pressure gauge, reinforced flexible tube, and high-pressure solid stream nozzle. The current prototype was set up using a standard, commercially available domestic garden DIY-pressure washer. This pressure washer was then connected to a solenoid valve, which essentially acts as an on-off switch, allowing the flow of the water to be controlled using the Novint Falcon haptic enabled controller (Chapter 7). This is then connected to a variable flow valve, which controls the pressure and rate of the flow, followed by a pressure gauge, to monitor the pressure of the flow (Figure 65). All end connections are 1/4" BSP threaded.
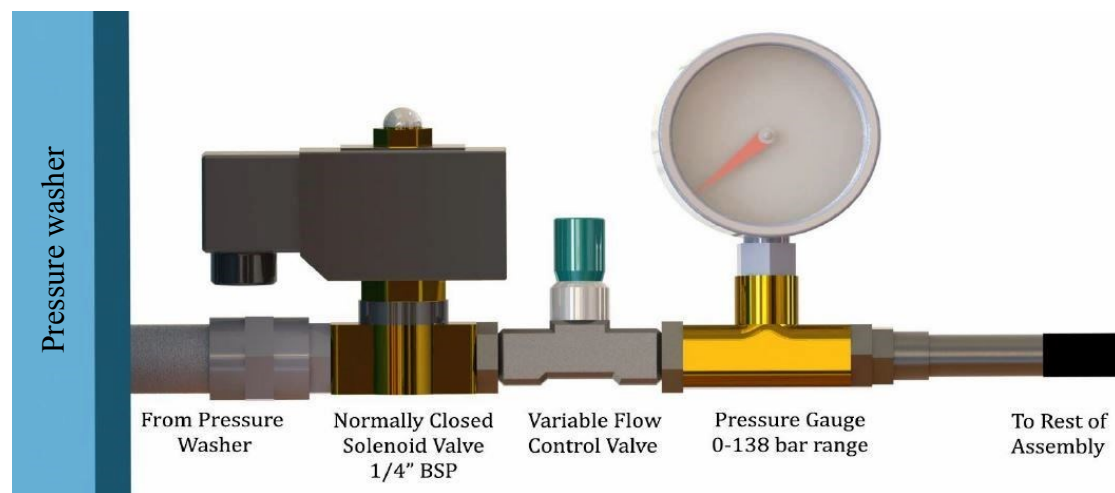
Figure 65: Water jet system configuration. Pressure washer acts as a source of a high pressure water flow. The pressurised water is then moves via number of main parts of the system that control and monitor the flow of water.

The pressure washer used is the *Nilfisk C110.4-5 X-Tra* Pressure Washer, which operates with a positive-displacement (PD) reciprocating pump, powered by a motor in the washer body. These types of pumps work on the basis of displacing liquid from the suction to the discharge part of the cycle with each revolution of pumping elements, usually plungers, pistons or diaphragms. As the suction cavity expands, liquid flows from the inlet valve into the pump cavity, and liquid discharges from the cavity once the cavity is collapsed. PD pumps supply the flow at a rate that does not vary much with pressure and viscosity, thus for that reason they are suitable for pressure washer applications. Pressure washers usually operate using reciprocating plunger pumps that operate on the following basis: The inlet valve allows water to enter into a cavity. A rotating swash plate then moves the piston up and down, pressurising the water through the cavity. Pressurised water is then discharged through valves to the nozzle.

The *Nilfisk C110.4-5 X-Tra* Pressure Washer has a rated water pressure output of 7.5 MPa, with a maximum output of 11 MPa. This produces a flow rate of 5.2 liters per minute (L/min) carrying water at a maximum temperature of 40˚C. The pressure washer is then connected to a brass, normally closed solenoid valve (*Connexion Developments Ltd*). The solenoid valve is connected to the AC mains and acts as a switch to control the flow. It has a maximum operating pressure of 12 MPa, and is able to transport media with a maximum temperature of 120˚C. It was also supplied with Polytetrafluoroethylene (PTFE) seals, to prevent leakage.

Normally closed solenoid valves contain an electromagnetically activated valve that is usually closed when no current flows through it. Upon inducing a current, the electromagnet field is activated and the valve is pulled upwards, causing the valve to open and thus the medium can flow through the valve. The output of the solenoid valve is then connected to a pressure gauge, connected at the bottom using a 1/4" BSP thread. Two nozzles were made, with orifice diameters of 0.85 mm and 0.6 mm.

The different parts are all connected using standard brass fittings. A synthetic Nitrile Butadiene Rubber (NBR) hose with one wire braid reinforcement (*Completely Hydraulic Ltd*) was used to connect the various parts of the system. This hose with Ø5 mm inner diameter had a maximum operating pressure rating of 25.5 MPa with an operating temperature range of -40˚C to 100˚C.

5.2   Water Jet Nozzle: Design and Fabrication

In 1952, *Rouse* and his colleagues undertook the first major study of water jet nozzle design [56]. The study was concerned about the design of a nozzle to improve the performance of firefighting monitors. This was followed by a study carried out by Leach and Walker [91] with the jet operated at higher pressures, principally for cutting rocks. However, most effective overall design of a nozzle was suggested by *Nikonov* and *Shavlovskii* [56] which was developed for hydraulic monitors.

The design of the nozzle used in the surgical water jet system was principally based on the simplicity of the design suggested by Nikonov and Shavlovskii, which influenced two key aspects of the design. Firstly, the fluid acceleration section, or conic angle, with the channel linearly narrowed at an angle of 13°. Secondly, the throat, or straight section, which is about 2-5 times the diameter of the nozzle size (orifice) (Figure 66).
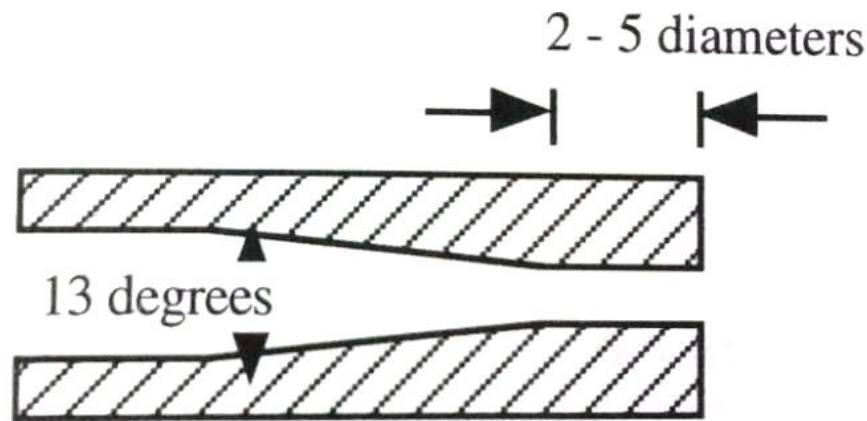
Figure 66: The fluid acceleration section and the nozzle throat of the Nozzles design *by Nikonov and Shavlovskii.* (Image source: Summers (56))

The length of the straight section is 2 mm, which is about three times the orifice size while the acceleration section is 37°. This angle was increased due to the relatively low pressure used; the work of Nikonov and Shavlovskii indicates that the conic angle is inversely proportional to the pressure and proportional to the fluid velocity.

Figure 67: Tools used to fabricate the solid stream nozzle. (Top) carbide burr cone used to machine the conical angle, (bottom) carbide micro-drill bit used to machine the throat of the nozzle.

The primary aims when designing the nozzle in water jet cutting systems is to maximise jet momentum towards an object, as well as creating a solid stream shape for the output jet for fine cutting results. Two solid stream nozzles with 0.6 mm and 0.84 mm diameter were made. Figure 68 shows engineering drawings of the 0.6 mm diameter nozzle, which is made of a brass material. The throat section of the nozzle has been fabricated with the use of carbide micro-drill bits with 0.6 mm diameter. The acceleration channel has been fabricated with the use of a carbide burr cone (Figure 67).

The input side of the nozzles is ¼" threaded to fix the nozzles to the reinforced flexible tube.
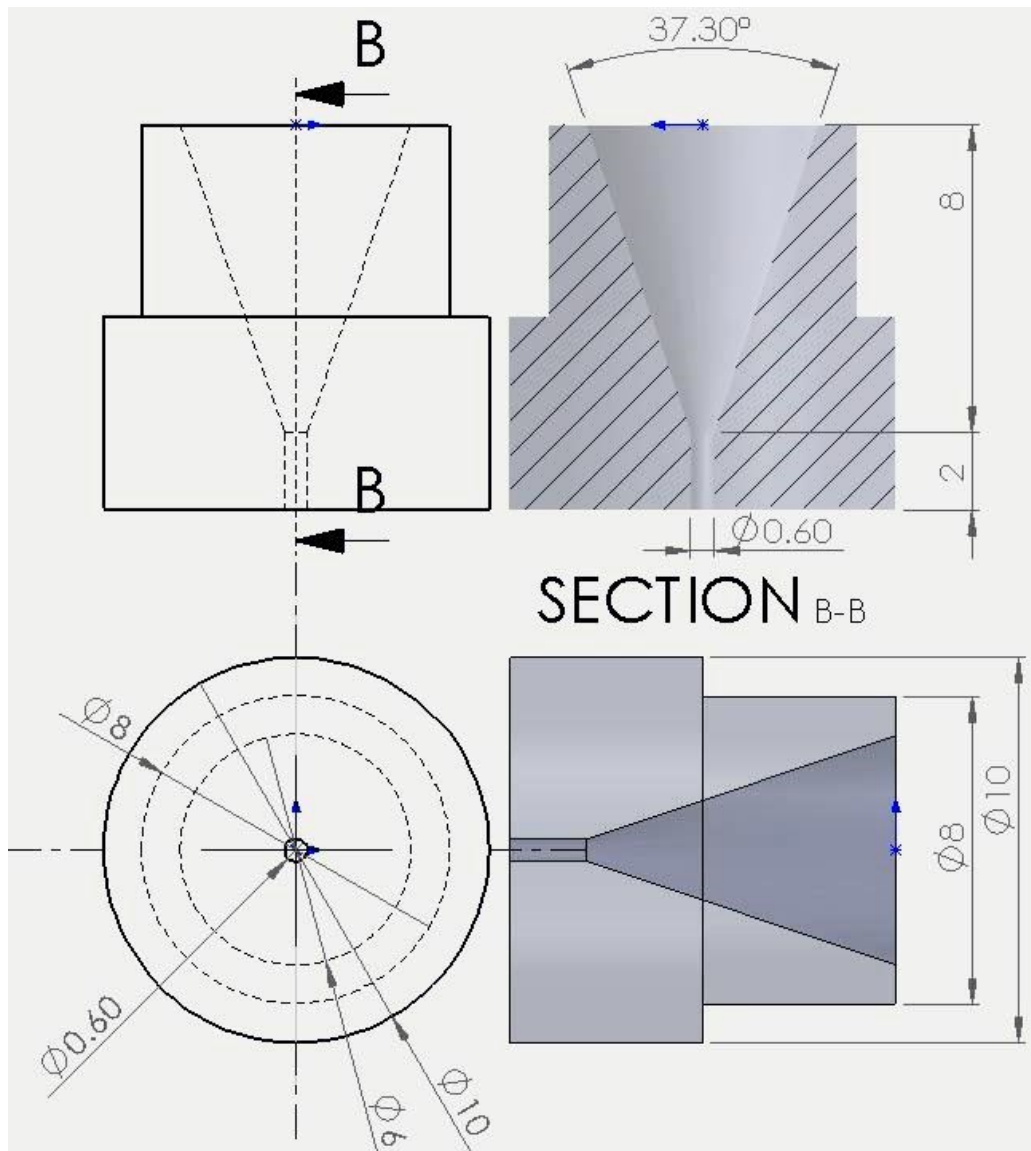
Figure 68: Engineering drawing of the 0.6 mm orifice diameter solid stream nozzle with a 2mm throat (section B-B).

5.3   Water Jet Unit: Experimental Testing

The water jet unit was experimentally tested to examine the capability of the output jet to cut or dissect soft tissue. The system was tested under pressure of 10 MPa generated by the pressure washer to push the water through the Ø0.84 mm high-pressure solid stream nozzle. Prior to performing tissue cutting, an excessively diffuse spray pattern of the output jet was noticed (Figure 69). This pattern could significantly affect the performance of the cut in terms of the accuracy and control of the procedure. Hence, further tests were conducted to investigate output jet pattern by experimentally measuring the jet velocity.

Figure 69: Initial testing of the water jet unit**.** An excessively-diffuse spray pattern of the output jet was noticed under 10 MPa

To do this, discharged water from the nozzle was collected over 20 s to calculate the mass flow rate $\dot{m}$ (see Appendix 4). The calculation shows that the velocity of the output jet (V) is very high (V=127 m/s). In addition, air bubbles were observed in the water jet after immersing the nozzle into a flask filled with water. It appeared that a turbulent flow was being generated at the entrance of the nozzle caused by the high-pressure flow applied by the pressure washer. Unfortunately, the flow control valve used in the setup of the system has little affected in terms of changing the level of source pressure. Therefore, the aim of the next step was to reduce the applied pressure down to about 4-5 MPa, in order to obtain a solid stream water jet pattern out of the nozzle, with the aim of given more precise and controlled cutting.
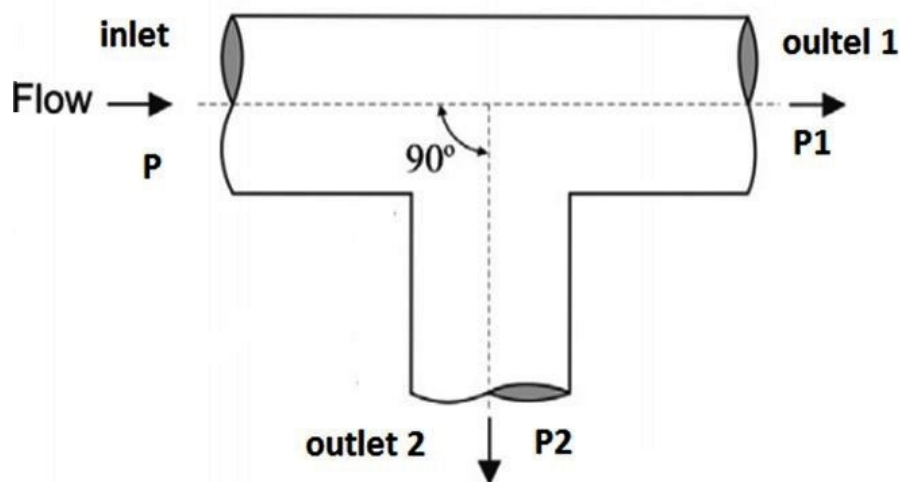
Figure 70: 90° T- branch arm, inlet flow is divided to form two outlets. The amount of fluid discharged from one of the outlet will affect the flow of the other outlet, hence affecting the pressure. (Image source: Kundu (92))

101

The direct solution to the problem was to use a pressure control valve to reduce the pressure from 10 MPa down to about 4 MPa. These types of valves are not common because of the big range difference, and they are very costly. Therefore, the fluid mechanics theory of T-junction flow [92] was applied (Figure 70).

The source flow is divided with a 90° T- branch arm in which the pressure on the nozzle is reduced by discharging a controlled amount of water (Q) from a second output. Hence

$$Q = Q_1 + Q_2 \qquad\qquad (5.1)$$

Experimentally, a flow control valve was placed as outlet 2 (Figure 71A) to control the amount of discharged water at outlet *2* and therefore control the amount of water discharged at outlet 1, hence minimise or maximise the pressure at the solid stream nozzle that was fixed at outlet 1.

Implementing the T- junction greatly modified the pattern and the pressure of the outlet jet, and hence the shape of output jet could be controlled by discharging a controlled amount of water (Q2) from the flow control valve (Figure 71B).
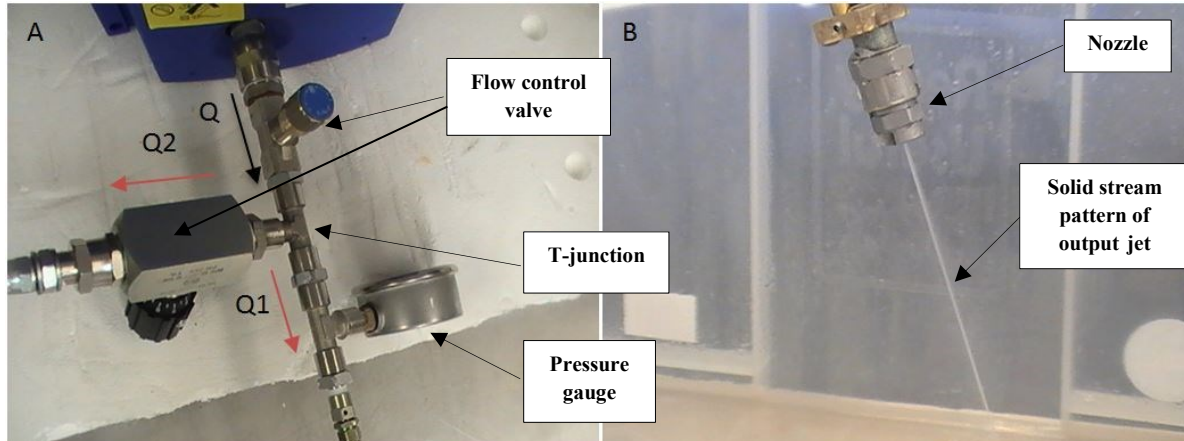
Figure 71: Experimental testing of water jet unit, (A) the addition of T junction and second flow control valve, where Q_1 and Q_2 are the amount of discharged water via output 1 and output 2 respectively. (B) Improved jet pattern at the outlet of the nozzle.

After modifying the water jet unit and achieving a solid stream output jet, the unit was then used to carry out cutting on various animal tissues. The cutting performance was dependant on the duration of the cut and type of tissue. However, the water jet unit was effectively cutting through any type of soft and semi-hard tissues with an applied pressure of 3-8 MPa (Figure 72).
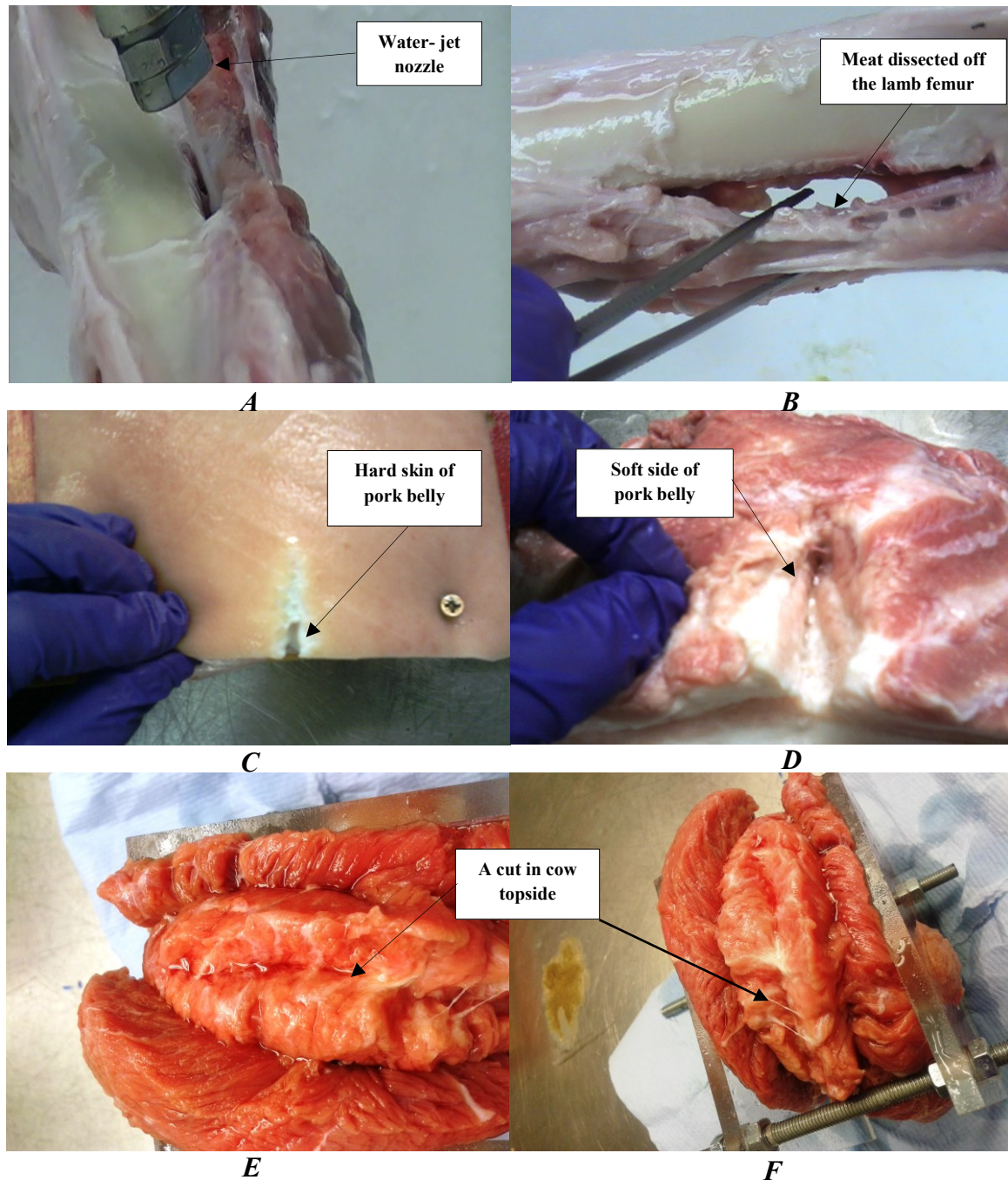
Figure 72: Experimentally cutting animal tissues using pure water jet system. (*A, B*) on lamb femur, (*C, D*) on pork belly, and (*E, F*) on cow topside

5.4   Water Jet Flow: Simulation and Analysis

Before assembly with the flexion unit, the water jet unit was tested separately to ensure it operated smoothly. This step confirmed the safety of the electronics on-board the surgical robot, as problems such as leakages would be contained within the water jet system. The water jet was set up in the exact configuration as discussed in the prototype section. The aim was to obtain quantifiable parameters of the actual system so that appropriate calculations can be carried out. The values obtained can then be compared with the predicted values gained

from the calculation and flow analysis simulation. Hence, the first test was to measure the flow rate (Q) and pressure of the water jet (P). The flow rate and pressure were expected to vary based on the discharge flow valve opening. This was done by measuring both variables at every 0.25 revolution of the valve knob from fully closed to three revolutions. Table 2 and Figure 73 summarises the results of the test.

Table 2: Experimental and calculated results obtained to specify various parameters of the water jet unit.

Revolution (*turn*)	Pressure *P* (*bar*)	Volume (*L*)	Time (*s*)	Flow rate *Q* (*l/min*)	Mass flow rate $\dot{m}$ (*kg/s*)
0.25	50	0.233	10	1.403	0.0233
0.5	43	0.198	10	1.193	0.0198
0.75	36	0.18	10	1.084	0.0180
1	30	0.168	10	1.0120	0.0168
1.25	24	0.145	10	0.8734	0.0145
1.5	21	0.142	10	0.8554	0.0142
1.75	19	0.137	10	0.825	0.0137
2	15	0.13	10	0.783	0.0130
2.25	14	0.12	10	0.723	0.0120
2.5	12	0.116	10	0.699	0.0116
2.75	11	0.11	10	0.6626	0.0110
3	9.5	0.108	10	0.6506	0.0108
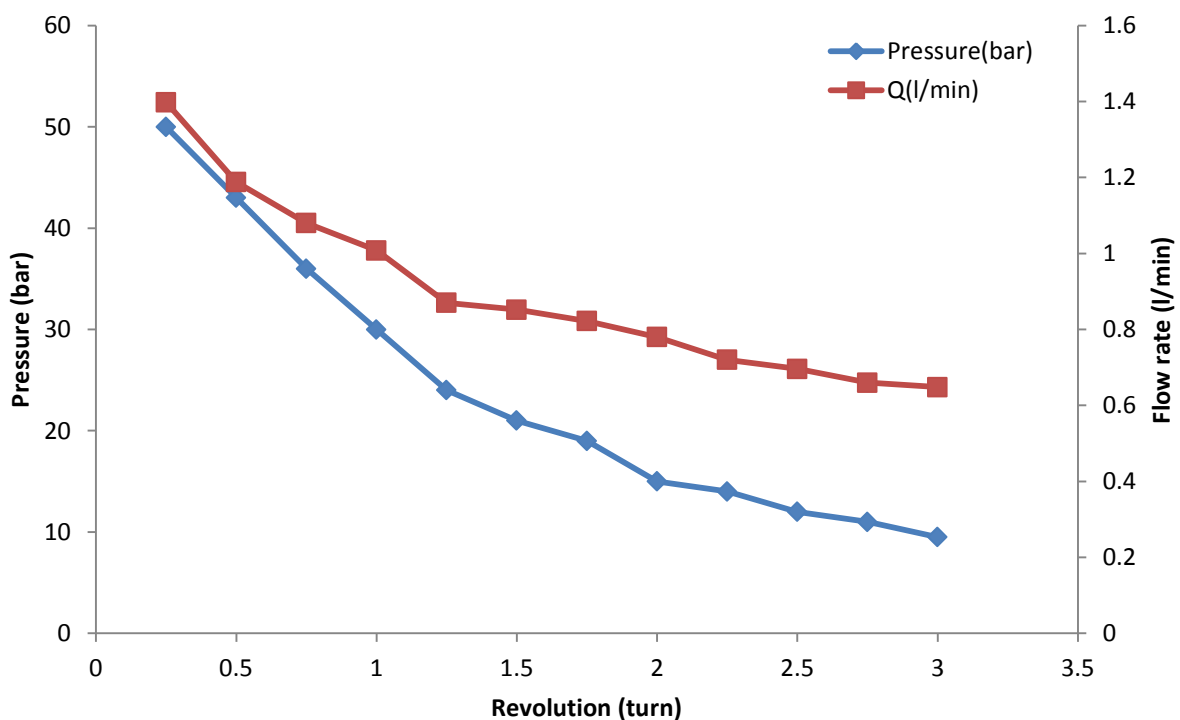
Figure 73: Plot shows the relationship between flow pressure (*P*) and flow rate (*Q*) of the water jet unit at every 0.25 revolution of the discharge flow valve knob.

Flow rate Q is a measured volume of the fluid discharged from the nozzle per unit time. Experimentally, we varied the revolution by an incremental 0.25 turn of the valve and the water was collected over 10 s. Water flow rates were calculated using the formula:

$$Q(m^3/s) = \frac{V(m^3)}{T(\sec)} \tag{5.2}$$

Multiplying this by the density ρ of the fluid gives us the mass flow rate:

$$\dot{m}\ (kg/s) = \rho(kg/m^3)Q(m^3/s) \tag{5.3}$$

The experimental outcomes are also used to calculate the momentum flow rate (F) which is the force applied on an object by the water jet as follows:

The exit area of the nozzle (orifice) is $A = \pi r^2$

Where, r is the radius of the orifice. With a known area, A, and flow rate, Q, we can calculate the velocity of the flow, v

$$v\ (m/s) = \frac{Q(m^3/s)}{A(m^2)} \tag{5.4}$$

Another approach of calculating the velocity of the flow is to apply the following formula using the known outlet pressure P and density of the fluid ρ.

$$v = C_d\sqrt{\frac{2P}{\rho}} \tag{5.5}$$

Where C_d is the coefficient of discharge, this is the ratio of the actual discharge to the theoretical discharge. Generally, the range of the coefficient for an orifice is 0.9-1.0. For conservative results, a value of 0.9 was used for all calculations (Appendix 5).

Consequently, we calculate the momentum flow rate F applying:

$$F(kgm/s^2) = \dot{m}\ (kg/s)v(m/s) \tag{5.6}$$

Table 3 and Figure 74 shows the values of the momentum flow rate F calculated by applying equations 5.2,3,4,6 and its relationship with flow velocity v respectively.

Since C_d takes into account the shape of the orifice and allows for the possibility of vena contracta, calculating the velocity of flow, using (5.5) will not give the same result as (5.4)

precisely. In addition, the exact momentum of the jet will depend on the flow profile in its cross-section, and this will not be uniform due to viscous effects in the nozzle, and jet spreading due to entrainment of the air around the jet through viscous interaction. Hence, the result is an approximation.

Table 3: Calculated velocity (v) and momentum flow rate (F) obtained from applying equations 5.2,3,4,6.

Revolution (*turn*)	Flow Velocity *v* (*m/s*)	Momentum flow rate *F* (*kg m/s^2*)
0.25	83.21	1.939
0.5	70.71	1.400
0.75	64.29	1.157
1	60	1.008
1.25	51.79	0.751
1.5	50.71	0.720
1.75	48.93	0.670
2	46.43	0.604
2.25	42.86	0.514
2.5	41.43	0.480
2.75	39.29	0.432
3	38.57	0.417
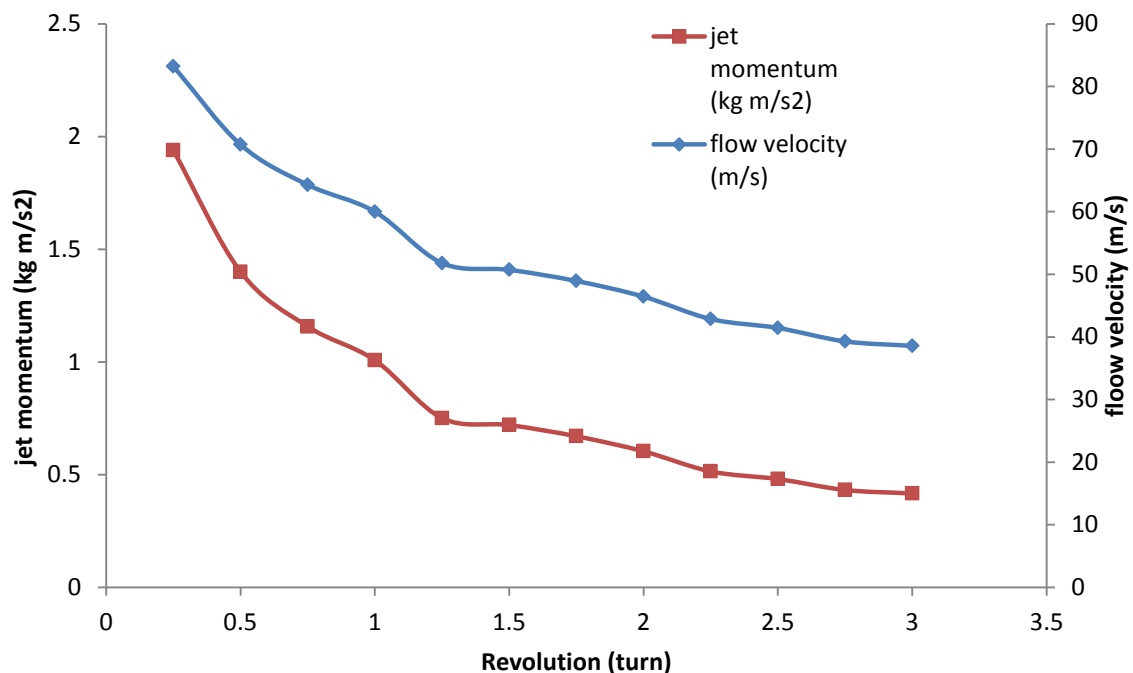
Figure 74: Plot shows the relationship between flow velocity (*v*) and momentum flow rate (*F*) of the water jet unit at every 0.25 revolution of the discharge flow valve knob .

A flow simulation was conducted to measure the flow parameters at the nozzle. Using Solid works flow Simulation, the flow of water in both nozzles of Ø0.6 mm and Ø0.84 mm orifice diameter with an inlet pressure of 5 MPa was studied (Figure 75). The simulation study of the water jet flow in the 0.6 mm nozzle shows values of flow velocity close to those calculated from experimental outcomes.
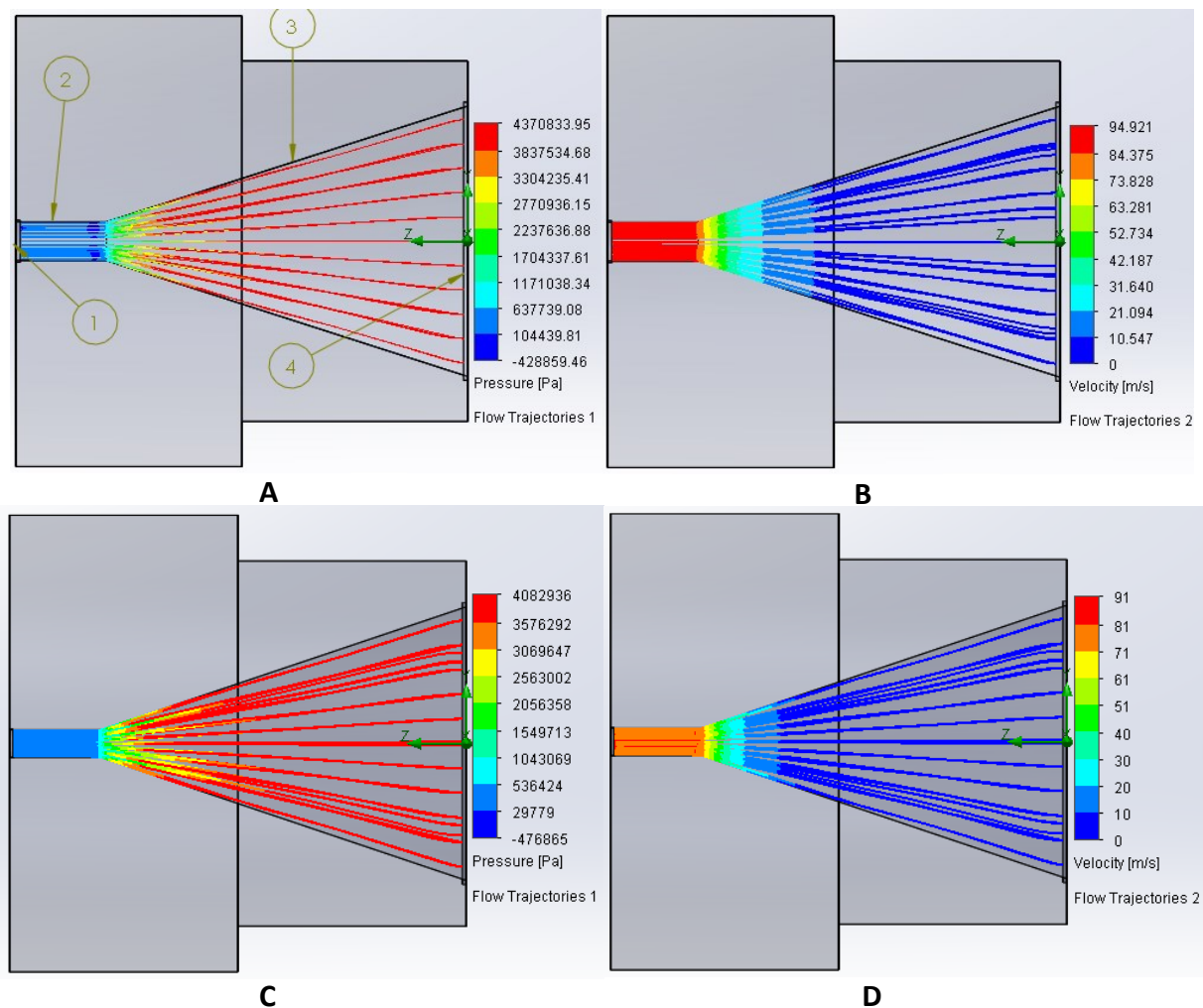
Figure 75: Flow simulation analysis shows the pressure and velocity distribution for Ø0.84 mm diameter nozzle (A, B respectively), and Ø0.60 mm diameter nozzle (C, D respectively). Where 1-jet outlet/orifice, 2-nozzle throat (straight section), 3-conic angle (fluid acceleration section), 4- jet inlet.

Also, the simulation revealed the effect of the orifice diameter on the flow velocity. The simulation shows that increasing the orifice diameter would increase the output jet velocity, and hence, the momentum flow rate, which is the forces applied by the output jet on an object.

5.5   The Depth of Water Jet Cut: Measure and Control

Despite the advantages of implementing a water jet system to cut tissues in a surgical environment, there is a risk of the jet cutting through the target tissue, and then going on to hit the underlying tissues and damaging them. Therefore, it is critical to be able to measure and control the depth of water jet cut, and hence the depth was experimentally measured. In this test, cow topside was used as an object, which was fixed between two clear Perspex sheets. The Perspex sheets have a hole at the centre and were held together with steel studs and nuts to adjust the space between them, according to the size of the object (animal tissue).

The holes at the centre were used to apply the water jet that was used to drill through the object (Figure 76).
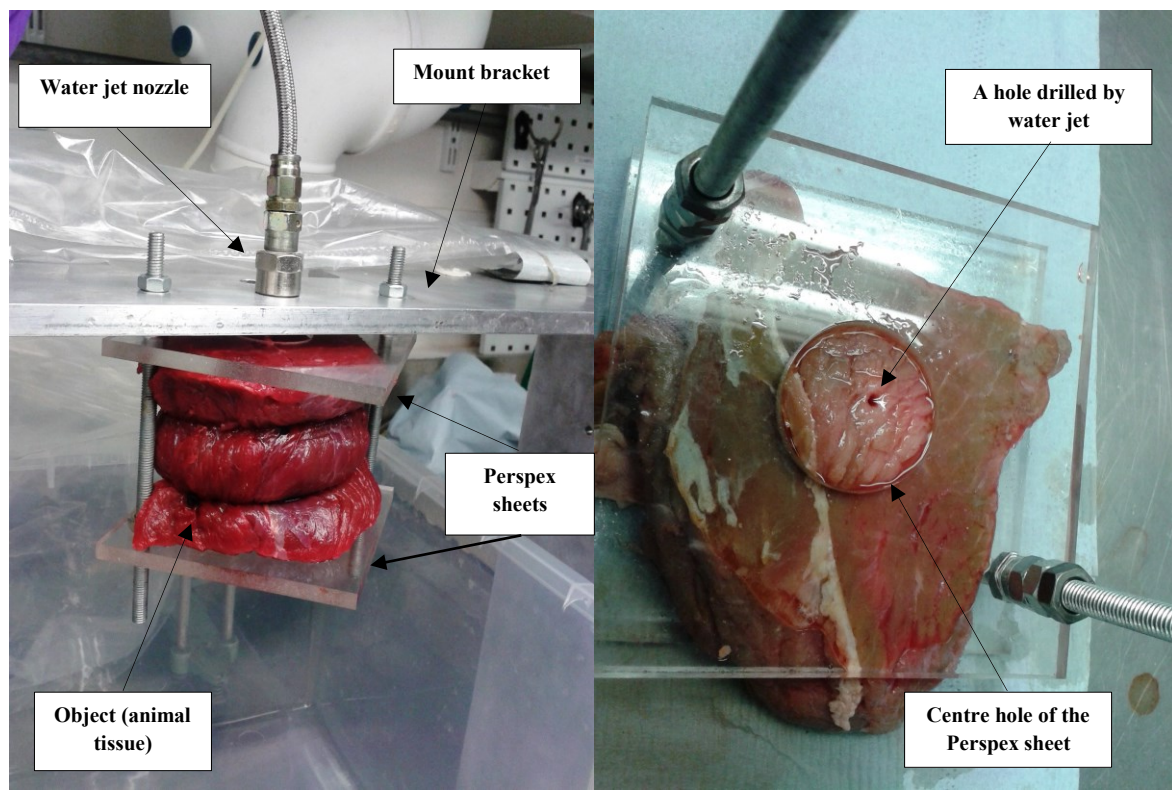
Figure 76: Experimentally measuring the depth of the water jet cut. Experimental setup (left), and a hole drilled by the water jet on an animal tissue (right).

All of the parts are then fixed on a bracket that is used as a reference point for the depth-measuring device. The depth of cut was measured using a digital calliper with a blunt needle fixed on the tip of the calliper. The water jet cutting process result depends on several process parameters; the most important for plain water jet cutting are: water pressure, orifice diameter, nozzle stand-off distance, and the duration of the cut.

These parameters were varied and the resultant depth of the water jet cut was measured. The first test was conducted to test the effect of the pressure on the depth of cut by varying the source pressure (10-25 bars), whilst keeping the nozzle stand- off distance constant at 3.9 mm (Figure 77). The test was carried out over a 5 s period of applied water jet. Secondly, the stand- off distance of the water jet nozzle was varied (3.9-23.3 mm) for a selected set of pressures (10-25 bar) that were kept constant over the same period of applied water jet (Figure 78).
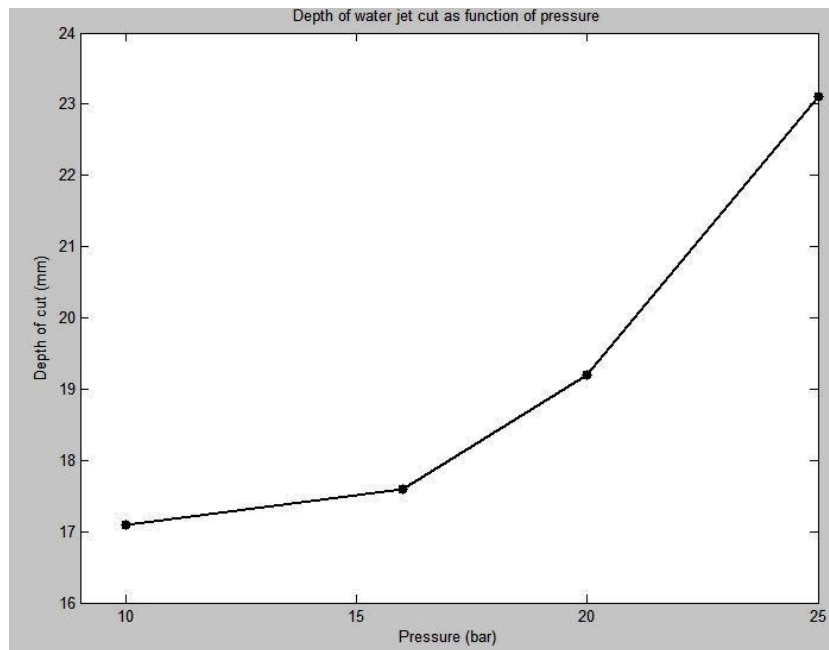
Figure 77: The depth of the water jet cut as a function of pressure with 3.9 mm nozzle stand-off distance and 0.84 mm orifice diameter over 5s duration of applied jet.
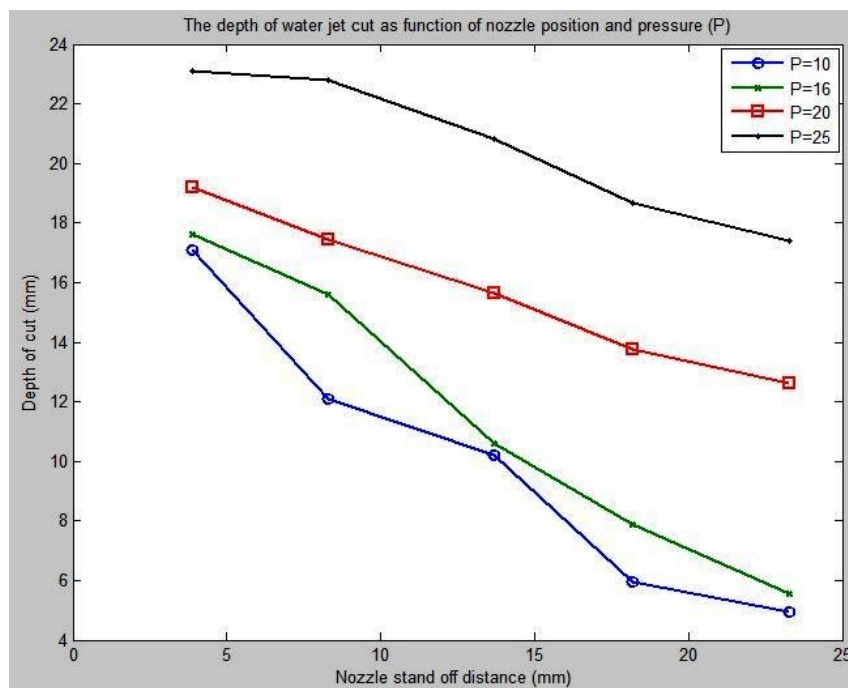
Figure 78: The depth of the water jet cut as a function of nozzle stand-off distance with 0.84 mm orifice diameter, applying various set of pressures over 5s duration of applied jet.

The last test was conducted to explore the effect of the nozzle's orifice diameter and time of cut on the depth of water jet (Figure 79). Two sizes of orifice diameters were used (0.6 mm and 0.84 mm); the water jet applied for a period of 5s intervals (5- 50 s) with a nozzle stand-off distance of 3.9 mm and 20 bar of applied flow pressure.
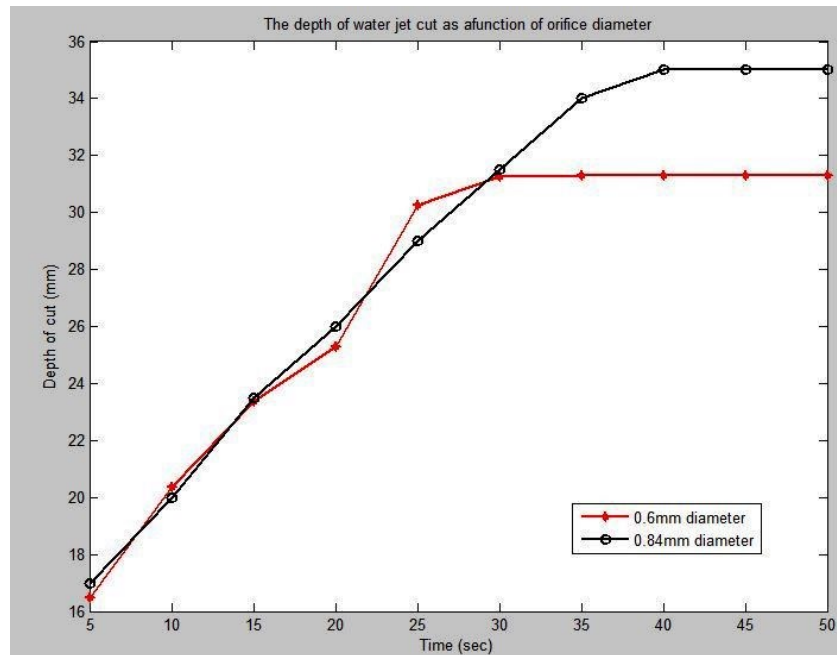
Figure 79: The depth of water jet cut as a function of nozzle's orifice diameter and the duration of applied water jet under flow pressure of 20 bars.

5.6   Discussion and Conclusion

A new flexible surgical system was presented in this chapter. The first prototype of the flexible water jet-cutting device has been designed and constructed such that it can be combined with the flexion unit, described in Chapter 4, to complete the flexible water jet system.

The prototype was set up using a standard, commercially available domestic garden DIY-pressure washer. This inexpensive pressure washer was chosen for the setup of the prototype to test the feasibility of using pure water in the dissecting of soft tissue. The flow of pure water through the solid stream nozzle was controlled by determining the flow pressure levels. The flow pressure levels were determined by adjusting both the variable flow control valve and the amount of discharged water. A better method of controlling the pressure level would be the use of pressure valves. However, the relatively high cost and poor availability of existing pressure valves that are able to control the pressure in the range of 0-100 bars pushed us to apply a fluid dynamic theory of a 'T-junction'. This theory was practically applied and the experimental dissection of various soft tissues has been successfully conducted. Ranges of flow pressures that fulfil the requirement of smooth surgical procedures have been obtained.

The experimental testing also produced measurable parameters of the actual system. The values of these parameters were compared with the values obtained from a Computational Fluid Dynamic (CFD) study that gives important information about the flow properties through the nozzles.

The most critical issue regarding the use of the water jet cutting tools in surgery is the method of controlling the depth of cut such that it does not affect (damage) the surrounding tissues. Hence, significant experimental testing was conducted. In these tests, the most important parameters that are involved in the pure water jet cutting process have been tested. The parameters, including water pressure, orifice diameter, stand-off distance of the nozzle, and duration of the cut were all measured in relationship to each other using two different nozzle sizes.

The experimental result showed that the depth of the water jet cut is significantly dependent on the various parameters. The depth of cut is directly related to the source pressure, duration of the cut, and nozzle diameter. The depth of cut is inversely related to the stand-off distance. As a result of undertaking the previous experimental tests and analysing the outcomes, we are now able to define the depth of water jet cut, or the jet effective length in which it starts to cut the tissue, for certain known parameters; these include orifice diameter, stand-off distance, source pressure, and duration. The most consistent parameter that affects the depth of water jet cutting depth is the duration of applied water jet. The experimental data (Figure 79) show that a constant increase in application duration gives a constant increase in the depth of cut. The data show that an interval of 5 s increase in duration results in an interval 3 mm cutting depth. Therefore, controlling the depth of water jet cut can be done by controlling the cutting duration. However, the effectiveness of the above parameters is dependent on the type and the mechanical properties of the target tissue such as the tensile strength, compressive strength, modulus of elasticity and hardness. A variation in any of these properties will lead to change the strength of the material and thus the resistance to a water jet. Therefore, it would be necessary to specify/establish the properties of targeted tissue in order to apply the water jet system in surgical environments safely.

A proposed method of combining the experimental results of defining the effective length of water jet cut with a haptic control of the entire system will be presented in Chapter 7.

111

6 Parallel Robot Manipulator for Spinal Surgery

The significance of implementing robots in surgery was presented in Chapter 1 supported by an extensive literature review. A great deal of work has been carried out towards implementing robots in the surgical theatre, and the field of surgical robots seems more promising as technology progresses. This is a consequence of the greater dexterity and higher accuracy that robot-assisted surgery delivers by means of eliminating human error. As a result, the rate of success of surgery rises through increased fidelity hence minimizing trauma to the patient.

This chapter will present the design of the parallel robot, which is developed to act as a guide and provide the desired position and orientation of the flexible surgical tool. The parallel robot is envisioned to be integrated with a number of units (explained in previous chapters) to form a surgical robot system. The focus of the chapter will be mostly on the mechanical aspects of the design, leaving the implementation of control and haptic feedback to be described in Chapter 7.

 In addition, all the relevant background theory will be introduced. This includes the fundamentals of parallel robot types and design, a comparison with other forms of robot platforms, and applications of parallel robots that are used to position the surgical tools in medicine.

6.1 Parallel robots

A parallel robot is a mechanical system that uses computer-controlled closed chains to support an end-effector. To give an understanding of the significance and importance of the development of mechanical aspects of the parallel manipulators, this introductory section presents a brief survey of the field of parallel robots. This review will also allow for the later assessment and evaluation of the design of a surgical parallel platform.

The review, in the form of a literature survey, starts with a reference to the history and uses of parallel platforms. This is followed by presenting the general fundamental principles of such

platforms, compared to other robot manipulators, and closing with its uses in medical applications.

6.1.1   The Origin of Robots and Parallel Robots

Historically, the word robot was first used in 1921 by *Karel Čapek* in his book *Rossum's Universal Robots*. The concept of the industrial robot was patented in 1954 by *George Devol* [93] who described how to create a controlled mechanical arm which can perform tasks in industry.   In 1961, *Unimation Inc.* installed the first industrial robot [94] and since then many robots have been put to work in the industry around the globe.
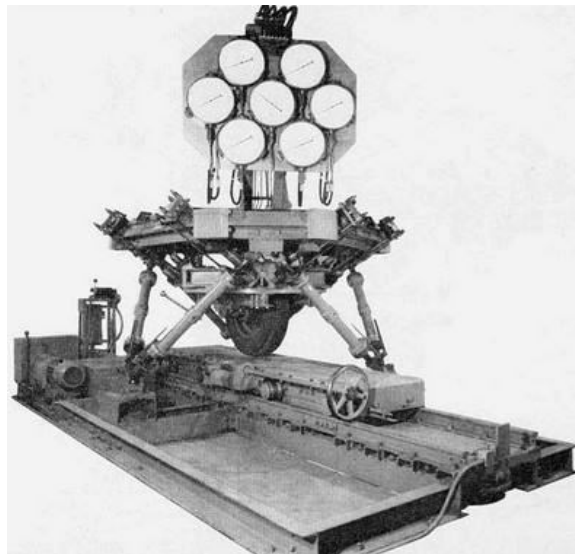
Figure 80: The first octahedral hexapod, the original Gough platform, was built in 1954. (Image source: *Merlet* (99))

 In 1928, *J.E. Gwinnett* applied for a patent [95] for his invention of a 3 DoFs spherical motion platform for use in movie theatres which was, possibly, the beginning of parallel robots [96]. A decade later, *W.L. Pollard* [97] invented a new parallel robot for automated spray painting. In 1947, the most common parallel robot, the octahedral hexapod, was invented by *E. Gough* who established the basic principles of a mechanism with a closed-loop kinematic structure to address tire problems associated with aircraft landing loads [98, 99]. The machine was built and was operational in 1954 (Figure 80).

While the work of *Gough* remained unknown for many years [96], in 1962 *Suliteanu* and *La Valley* had filed a patent application for a 6 DoFs antenna support consisting of three stands [100]. Also, in 1965, *E. R. Peterson*, filed a patent application for an octahedral hexapod with double-ball joints [101]. *Peterson's* application was, however, preceded by a few months by the patent application of *K. L. Cappel* of the *Franklin Institute*. *Cappel's* motion

simulator was the first ever flight simulator (Figure 81) based on an octahedral hexapod which became one of the most important patents in the history of parallel robots [102].
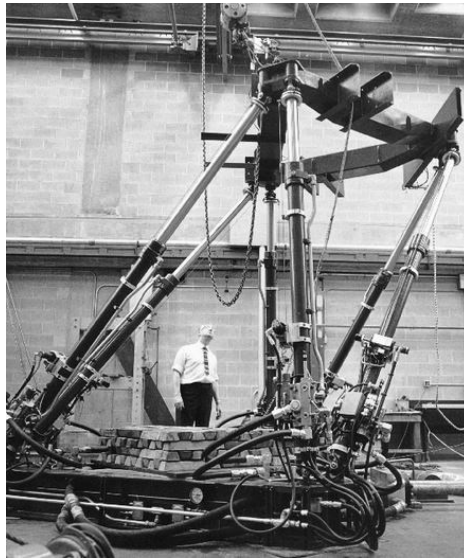
Figure 81: The first flight simulator based on an octahedral hexapod pictured in the mid-1960s. (Image source: Cappel (102))

In 1965, a mechanical engineer, *D. Stewart* proposed a mechanism with six telescoping legs for use as a flight simulator [103]. His parallel mechanism (Figure 82), however, is different from the octahedral hexapod configuration. Confusingly, hexapod robots are often referred to as "*Stewart platforms*".
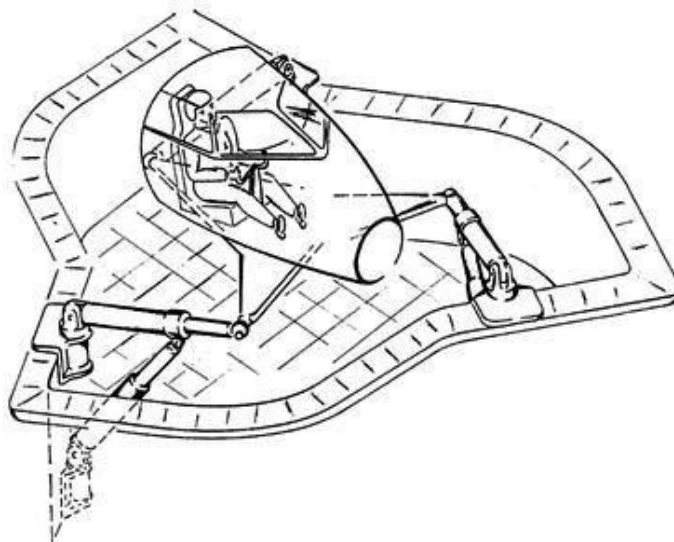
Figure 82: Schematic of the original "Stewart platform" used as a flight simulator. (Image source: Stewart (103))

Stewart's paper had a remarkable impact on subsequent development in the field of parallel robots despite the fact that he was neither the inventor of the octahedral hexapod nor the pioneer of today's six-legged flight simulators [96].

Figure 83: The first ever Delta robot, developed in 1985. (Image source: Clavel (104))

After a period of being largely ignored by industry and academia, the popularity of parallel robots suddenly began to rise in the 1980's. Since then, many novel and truly innovative designs have been proposed. The most successful parallel architecture was the Delta robot (Figure 83) designed by *R. Clavel* in 1985 [104].

6.1.2 Parallel Manipulators: Principles

A robot manipulator is an electromechanical system in which a rigid body (the 'end effector') can move with respect to a fixed base [94, 99, 105]. The motion of a rigid body in space termed a 'degree of freedom' (DoF), can be in translation (i.e. linear movement) or rotation, with maximum of six degrees of freedom (6 DoFs).

These 6 DoFs are three translational motions along the Cartesian axes *x, y, z*, and three rotational motions about the axes($\theta x, \theta y, \theta z$) or roll, pitch, and yaw (Figure 84) [106].

Robot manipulators or mechanisms are usually constructed from a number of rigid bodies (links) connected to each other and to the base via various types of joints. The number of the links, which are connected in pairs, and the type of the joint, which is the connective element between the links, determine the number of DoFs. Joints allow restricted relative motion between two links. Table 4 [107] describes some of the common joints used in robotics.
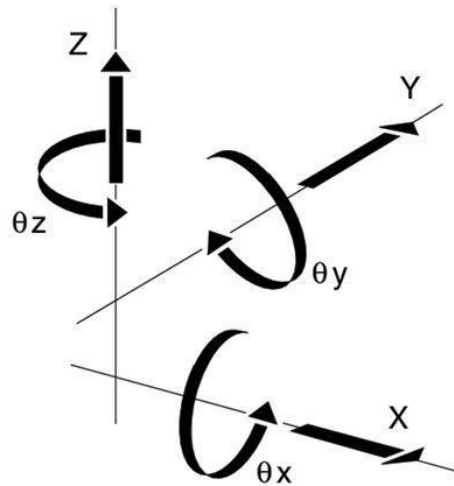
Figure 84: The representation of 6 DoFs where X, Y, and Z are the three translational motions and $\theta x, \theta y$, and θz are the three rotational motions. (Image source: Newport ESP Technology (106))

Robot manipulators can be classified according to their motion characteristics (planar, spherical, and spatial), kinematic structure (serial, parallel, hybrid), or by the number of degrees of freedom.

In this thesis, the robot manipulators will be classified according to their kinematic structure.

Table 4: Some of common joints used in robotics (Table source: Maplesoft (107))

Name of joint	Representation	Description
Revolute		Allows relative rotation about one axis.
Cylindrical		Allows relative rotation and translation about one axis.
Prismatic		Allows relative translation about one axis.
Spherical		Allows three degrees of rotational freedom about the center of the joint. Also known as a ball-and-socket joint.
Planar		Allows relative translation on a plane and relative rotation about an axis perpendicular to the plane.

Serial robots are constructed from an open-loop kinematic chain and are the most common type of robot used in industry.

The serial chain consists of a number of rigid links connected by joints forming a mechanical arm structure (Figure 85) [108]. A large workspace is the main advantage of serial manipulators, whereas their low stiffness (caused by their open kinematic structure), high relative mass, and positioning errors are the main drawbacks.
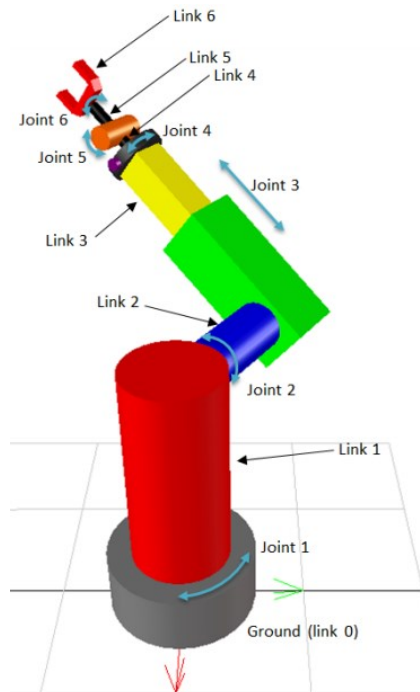
Figure 85: The construction of Stanford serial manipulators. Mechanical arm is constructed from several links connected by joints. (Image source: Maplesoft (108))

Parallel robots are made from a number of closed-loop chains whose moving platform is linked to the base by several independent kinematic chains. This is a generalised definition of parallel robots. Taking into account their mobility, chains and number of actuators; parallel robots can, therefore, be defined according to *Merlet* [99] as follows:

"A parallel robot is made up of an end-effector with n degrees of freedom, and of a fixed base, linked together by at least two independent kinematic chains. Actuation takes place through n simple actuators".

Their positional accuracy, lighter construction, and high structural stiffness are their main advantages. Their major disadvantages are limited workspace and the mechanical limit of the passive joints of their links.

Parallel manipulators can be classified according to the number of DoFs of the platform. It is known that the number of DoFs of a rigid body in space cannot exceed six; hence, the number of DoFs of a parallel mechanism can be any number between two and six.

117

Parallel manipulators with 6 DoFs are the most common manipulators; these are generally composed of six legs that can be arranged to produce various architectures. One of the most frequently used in various application is the *UPS* (Universal- Prismatic- Spherical) chain robot, which is usually called a Stewart platform (or more correctly *Gough* platform), 6-6 (six joints on the base and six joints on the mobile platform) robot (Figure 86) [109], or hexapod.
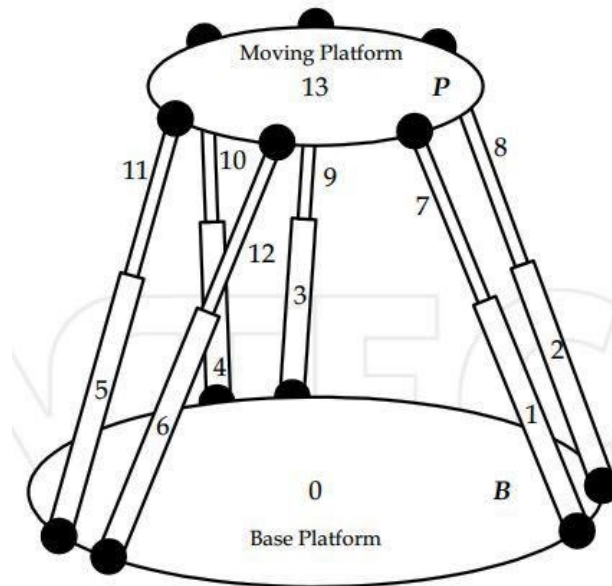
Figure 86: A sketch of the 6-6 manipulator where the fixed base platform is connected to the moving platform via six extensible linear actuators. (Image source: A. Akbas (109))

This manipulator has been considered by many researchers, such as *Sreenivasan et al.* [110], *Nguyen et al.* [111], *Lee* and *Shim* [112], and others. Other configuration of 6 DoFs parallel manipulators are 6-4 robot [113], 6-3 robot [114], 5-5 robot [115], 5-4 robot, 4-4 robot [116], and 3-3 robot [117, 118].

6.1.3 **Parallel versus serial manipulators**

Parallel manipulators present numerous advantages over serial manipulators in certain applications. In parallel manipulators, several links connect the end effecter to the fixed base; thus, any load is shared between these links. Hence, for given mass and size, they carry greater load capacity than serial manipulators. The deformation of the127 parallel platform, even under high loads is reduced because the links only experience compressive or tensile loads, but no shear forces or bending and torsion moments [119, 120]. In addition, parallel manipulators generally have very low inertia due to their designs, which typically have all of the actuators in or near the base. Hence, a higher bandwidth can be achieved with the same actuation power.

A number of links (or legs) are coupled in parallel from the base to the Tool Centre Point. All drive motors/gearboxes can then be located on the fixed base, enabling drilling, welding, or tapping with greater accuracy and repeatability. This architecture makes parallel robots more lucrative for many practical applications, where improved robot performance beyond that of serial manipulators is required. Parallel robots are basically more accurate than serial robots because their errors are averaged (instead of added cumulatively as with serial robots), due to many parallel links as well as the closed loop architecture.

Other advantages of parallel manipulators over serial manipulators are: higher structural stiffness, reduced sensitivity to certain errors, easier controlling and built-in redundancy via inverse kinematics. However, parallel manipulators generally have a smaller and less dexterous workspace. The causes vary depending on the configuration, but are generally due to link interference, the physical constraints of universal and spherical joints and the range of motion of actuators. They can also suffer from platform singularities, which is when a particular overall geometric form is achieved where the platform may instantaneously loss or gain one or more DoFs; it loses either overall stability or 'locks-up'. Table 5 lists a comparison between parallel and serial manipulators [119].

Table 5: Comparison between parallel and serial manipulators (Table source: Y.D. Patel (119))

	Type of manipulator	
	Parallel manipulator	Serial manipulator
Type of manipulators	Closed loop	Open loop
End effectors	Platform	Gripper
Natural description	In Cartesian space	In joint space
Location of actuators	Near the immobile base	On the links
Inertia forces & stiffness	Less and high respectively	High and less respectively
Design considerations	Structure, workspace considerations, singularities, link interference	Strength and stiffness considerations, vibration characteristics
Preferred property	Stiffness	Dexterity
Use of direct kinematics	Difficult and complex	Straightforward and unique
Use of inverse kinematics	Straightforward and unique	Complicated
Singularity	Static	Kinematic
Direct force transformation	Well defined and unique	Not well defined; may be non-existent, unique or infinite
Preferred application	Precise positioning	Gross motion

6.1.4 Parallel robot for medical applications

Robots are gradually entering the medical field with systems such as the da Vinci or Zeus robots (mentioned in section 2.1). Parallel structures are also playing a role in this evolution.

Figure 87: Laboratory setup of the *CRIGOS* robot to simulate a puncture of a cystic cavity into the femoral head. (Image source: Brandt et al. (121))

In orthopaedics; *CRIGOS* system, presented by *Brandt et al.* in 1999 [121] as a Compact Robot for Image-Guided Orthopaedic Surgery. In this system, a compact parallel robot was equipped with a software system to assess the surgical intervention as well as supervision of the robotic device (Figure 87). One of the key components of the *CRIGOS* system is the ability of the compact robot to support the surgeon in achieving a better accuracy of intraoperative execution in a less invasive way.

Girone et al. [122] presented the '*Rutgers Ankle*' orthopaedic rehabilitation interface, comprised of a Stewart platform structure controlled by an electronic interface (Figure 88). The *Stewart* platform design allows the control of forces and torques in 6 DoFs and movement throughout the ankle's full range of motion. The platform's actuators are double-acting cylinders with a stroke length of 100 mm and maximum force of 133 N. During the rehabilitation exercise, the Stewart platform robot supplies forces to the patient's foot. Position sensors were attached in parallel with each cylinder; they are linear potentiometers in which their resistance are measured and converted into linear displacements by the controller.

A 6 DoFs force sensor is placed between the shoe harness and the top platform and is used to measure forces at the user's foot in real-time. The host PC in a database, which can be accessed remotely via the internet, records the platform's movement and output forces. The '*Rutgers Ankle*' has been used in clinical trials for patients with Grade I and II inversion sprain, and bimalleolar[7] fractures [123].
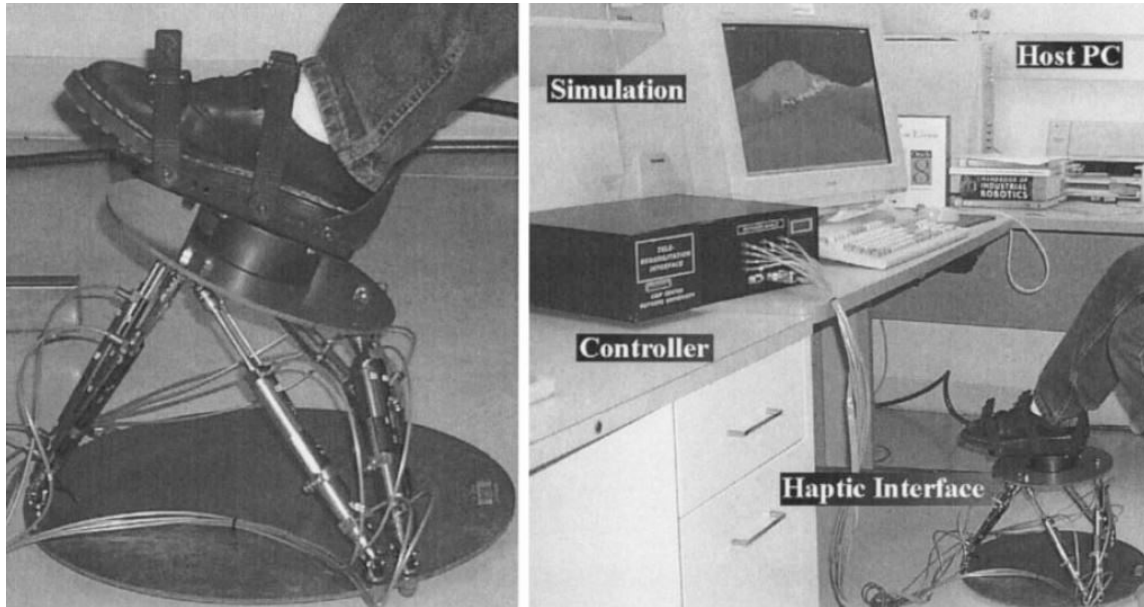
Figure 88: The "Rutgers Ankle": a Stewart platform robot supplies forces to the patient's foot during the rehabilitation exercises (left). (Right) the system view comprised of Stewart platform haptic interface, electro-pneumatic controller, and the PC host computer. (Image source: Girone et al. (122))

Two of the *Rutgers Mega-Ankle Robot* (RMA), a larger version of the original *Rutgers* Ankle force feedback device, was used by *Boian et al.* [124, 125] to model the walking surface geometry and condition.

The RMA robots are fixed on the floor beside each other, and the patient's feet are secured on top of them (Figure 89). Walking is simulated by moving the platforms back and forth similar to stepping on a treadmill. A large display in front of the patient was used to project a graphic display of simulated environment. Due to the limited work envelope of the system and control algorithms, a preliminary study on healthy subjects indicated that walking speeds on the simulator were significantly slower than normal over-ground walking.

---

[7] A fracture of the lower tibia which affects the internal (medial) and external (lateral) malleolus

Figure 89: General view of the mobility simulator (left) and The Rutgers Mega-Ankle robot (right). The system simulates walking by moving the platforms back and forth similar to the stepping on a treadmill. (Image source: Boian et al. (124))

Another device for ankle rehabilitation was designed by *Onodera et al.* [126] using a *Stewart* platform mechanism to measure and assist the motion of a human ankle joint in 6 DoFs. The platform's six linear actuators were pneumatic cylinders with assembled potentiometers mounted between stationary and mobile plates, leg and footplates respectively, via ball joints (Figure 90). Control of the motion of the ankle joint in 6 DoFs was achieved by adjusting the length of the linear actuators, by changing the air pressure within the cylinders.
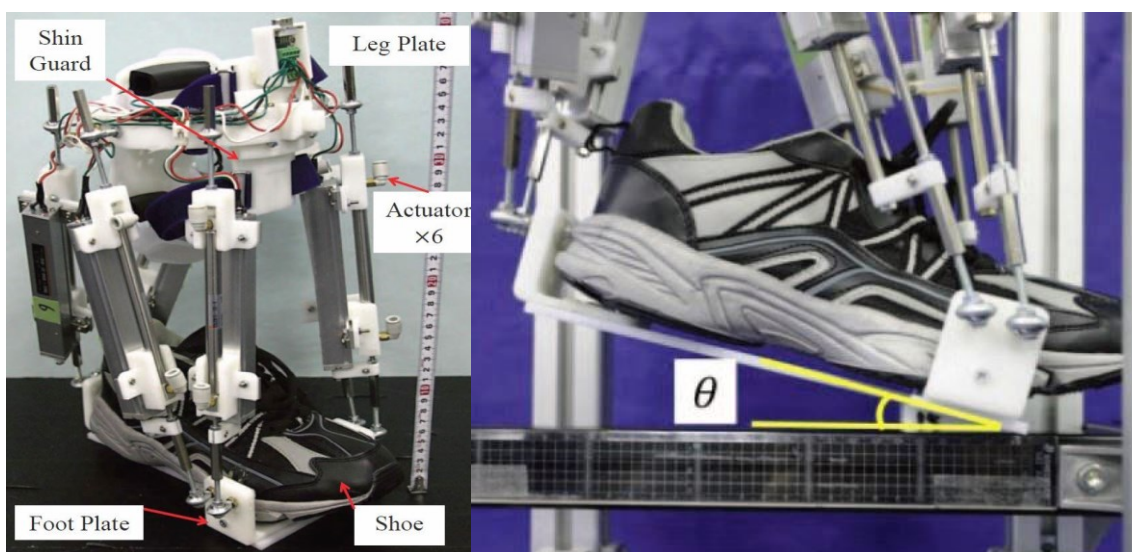
Figure 90: The Stewart platform-type ankle-foot assist device (left) and the device with arbitrary posture (Planter Flexion). Six linear actuators are mounted between two plates fixed on the leg and foot. Two linear actuators are mounted behind the Heel and the other four linear actuators are mounted on both sides of the foot. (Image source: Onodera et al. (126))

A parallel manipulator robot was implemented on a traction table by *Lin et al.* [127] for a femoral fracture reduction in a clinical environment. In the clinical setup, the patient is positioned on the traction table with a flexed knee. The platform's immobile base, which is a solid disk, is attached to the centre pole of the traction table (Figure 91).
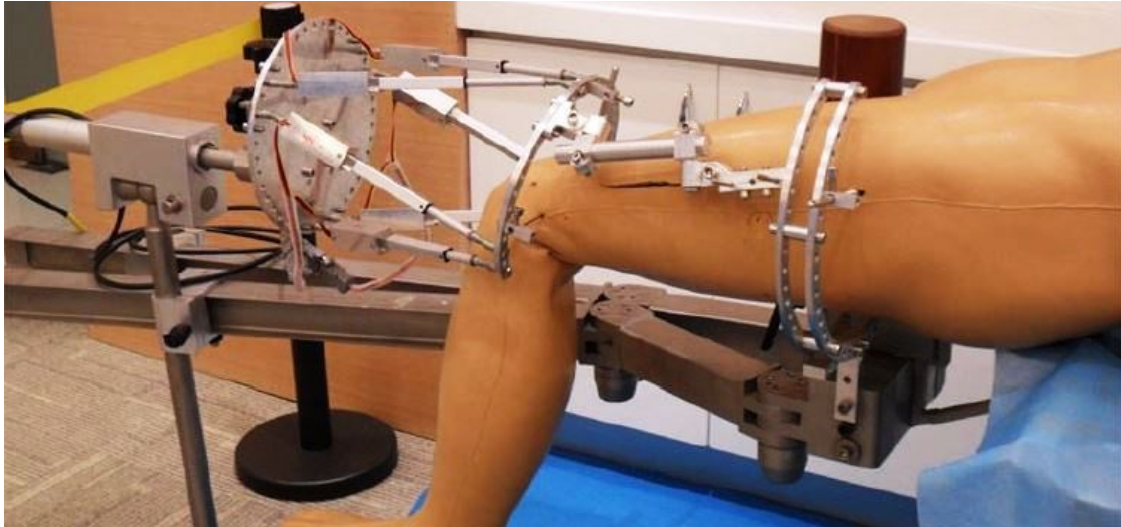
Figure 91: Configuration of Parallel manipulator robot (PMR) implemented on traction table for femoral fracture. The solid disk side of PMR and the proximal femur of the patient can be treated as one rigid body. The distal femur, fixed to the 2/3 circular ring platform, will perform the 6 DOF movement. The alignment and reduction algorithm is based on the restoring the pre-fractured limb length and mechanical axis principle. (Image source: Lin et al. (127))

Barkana developed an orthopaedic surgical robotic system called OrthoRoby [128]. The system was developed to be used in bone-cutting operations. The *OrthoRoby* consists of a parallel construction robot and a cutting tool (Figure 92).
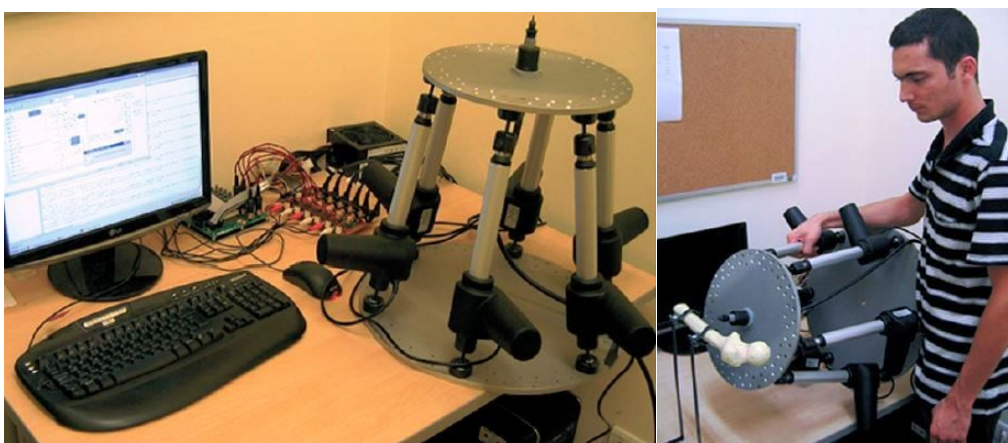
Figure 92: *OrthoRoby* robotic system (left), consists of parallel robot controlled by PC and control card, which is developed to drive the DC motors (actuators) of the robot, *OrthoRoby* within bone-cutting operation (right). (Image source: Barkana (128))

The parallel robot consists of two circular plates connected by six linear actuators having a stroke of 150 mm and maximum force of 600 N generated by each actuator. Encoders

attached to the actuators determine the position of the robot. A control design was established for *OrthoRoby* system, consisting of preplanning and the post-operation phases. The control architecture helps the surgeon to decide the proper cutting operation and automatically modify the execution of the cutting task.

In spinal surgeries, a parallel robot was developed by *Tian et al.* [129] for the replacement of the cervical artificial disc. The robot was implemented to replace the fixture system used in such surgery (Figure 93). Two types of joints were used in the design of the robot; universal and spherical joints, connecting the six linear actuators to the fixed platform and moving platform respectively. Six brush-type DC gear motors developing 400 N of force at the ball screw drive the linear actuators. For the purpose of the system, the robot is equipped with a bone-milling device, which is powered by a brushless DC motor. The entire active parallel robot system is then mounted on a passive serial support with 3 DoFs.
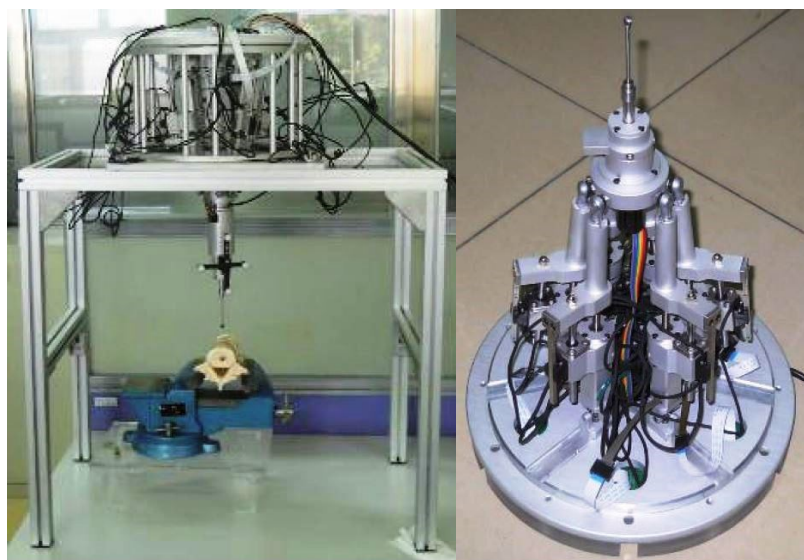
Figure 93: The entire robot system (left), the parallel robot is attached to the support which has the 3 DoFs adjustment movement such as front and back, left and right, up and down. The active parallel robot is equipped with a milling device which actively mills bone according to the preoperative grinding planning (right). (Image source: Tian et al. (129))

A miniature parallel robot for the positioning and orientation of a drill or needle in spinal and trauma surgery is designed by *Shoham et al.* [130]. The robot, called MARS (MiniAture Robot for Surgery), has 6 DoFs and mounts directly on the bone close to the surgical site via its fixed base. Its primary function is to position and orient the targeting guide to a precise preoperatively defined location and lock itself there, hence it is not designed to perform the surgical operation itself.
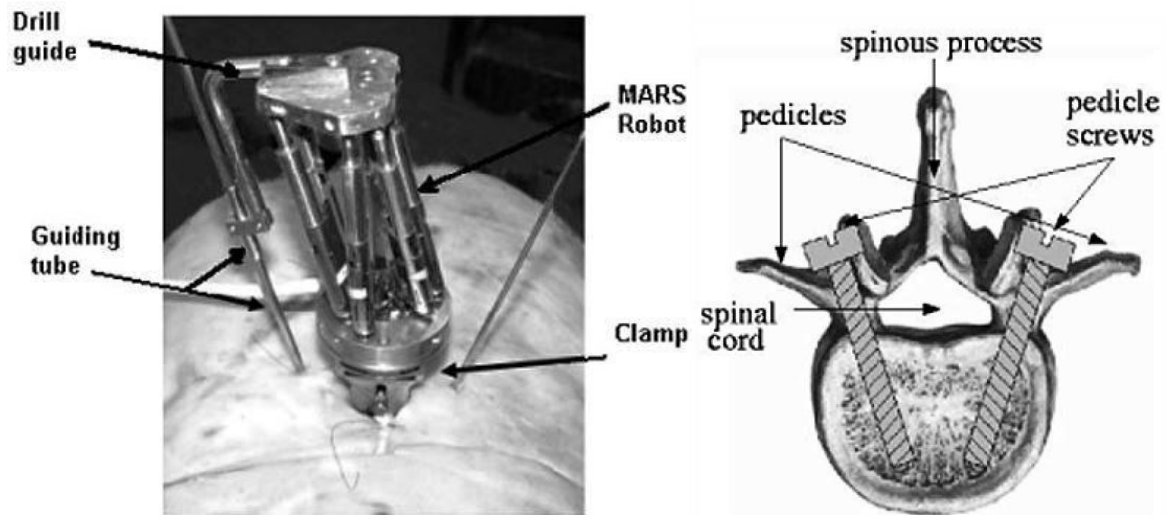
Figure 94: The *MARS* robot in a spinal procedure (left), a K-wire is inserted into pedicles in a minimally invasive approach. Diagram showing an axial view of a vertebra with two pedicle screws inserted (right). (Image source: Shoham et al. (130))

The authors have applied MARS in two clinical applications: pedicle screw insertion in spinal fusion (Figure 94), and distal locking in closed intramedullary nailing (Figure 95).
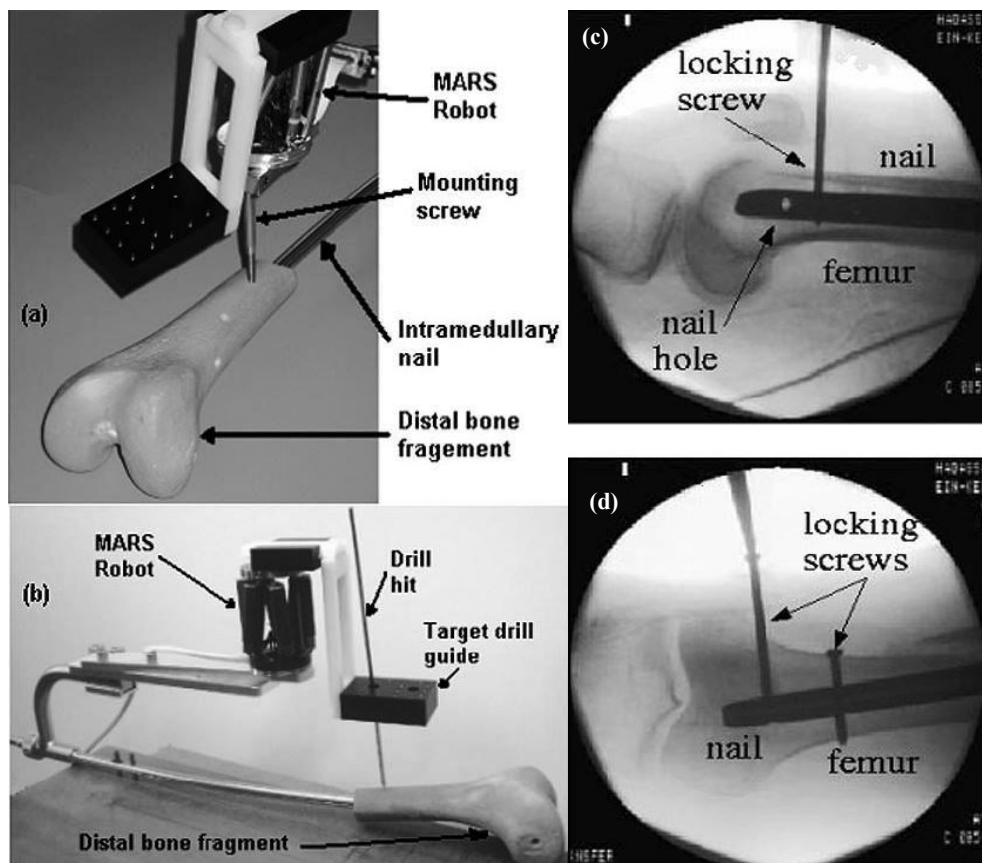
Figure 95: Photograph of the *MARS* robot mounted (a) on the femur (b) on the nail head, and X-ray fluoroscopic images showing (c) the distal part of the femur and the intramedullary nail with two distal locking nail holes, (d) the intramedullary nail with two distal locking screws. (Image source: Shoham et al. (130))

The authors have applied MARS in two clinical applications: pedicle screw insertion in spinal fusion (Figure 94), and distal locking in closed intramedullary nailing (Figure 95).

The miniature size and small workspace are the main advantages of the MARS over other existing surgical robots. Such benefits make the robot easier to integrate in the operating room and safer than larger robots. Moreover, mounting the robot right on the bone eliminates the requirement for additional hardware for bone motion tracking or patient immobilization.

Subsequently, the pioneered work of *Shoham et al.* [130] in introducing a bone-attached parallel robot for orthopaedic and spinal procedure, presented previously, was the motivation for developing bone-attached parallel robots for knee arthroplasty (Figure 96) by *Wolf et al.* [131, 132], and *Plaskos et al.* [133].
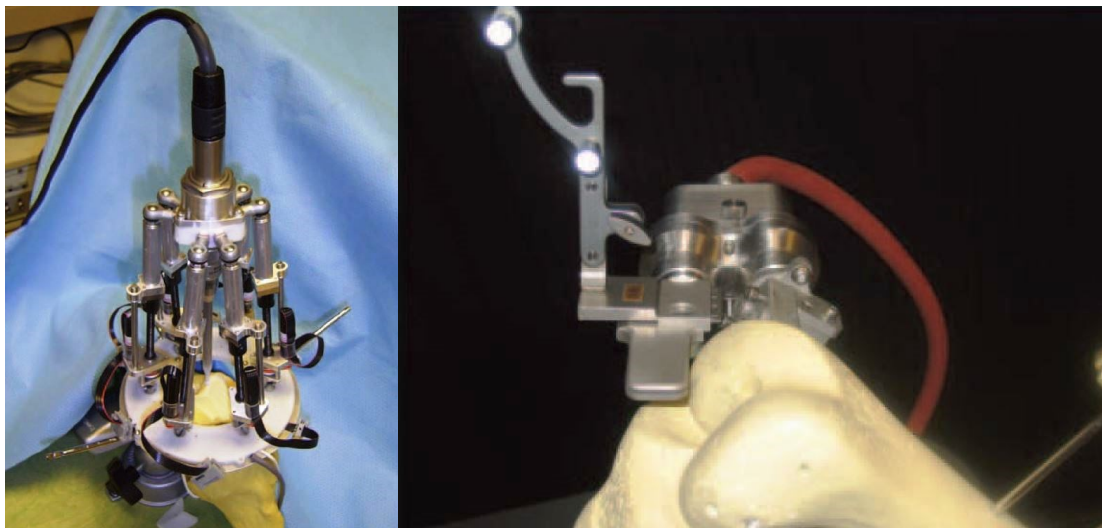
Figure 96: Bone-attached parallel robots for knee arthroplasty. (Left) miniature bone-attached robotic system (MBARS) by Wolf et al. (131), and (right) Miniature bone-mounted robot for minimal access total knee arthroplasty (TKA) Plaskos et al. (133)

Also, a bone-attached miniature parallel robot frame for Automated Image-guided Microstereotactic (AIM) was developed by *Kratchman et al.* [134]. The AIM frame was applied for percutaneous cochlear implantation[8]. The robot is based on a typical classical *Stewart Gough* structure and is actuated by six linear piezoelectric motors, with each motor enclosed in an aluminium fixture with a linear encoder forming a prismatic joint. Screw rotation causes linear translation of the motor housing, which is attached to a ball joint on the robot's top platform (Figure 97).

---

[8] Cochlear implant is electronic device that can restore hearing to individuals who have severe or total hearing loss.
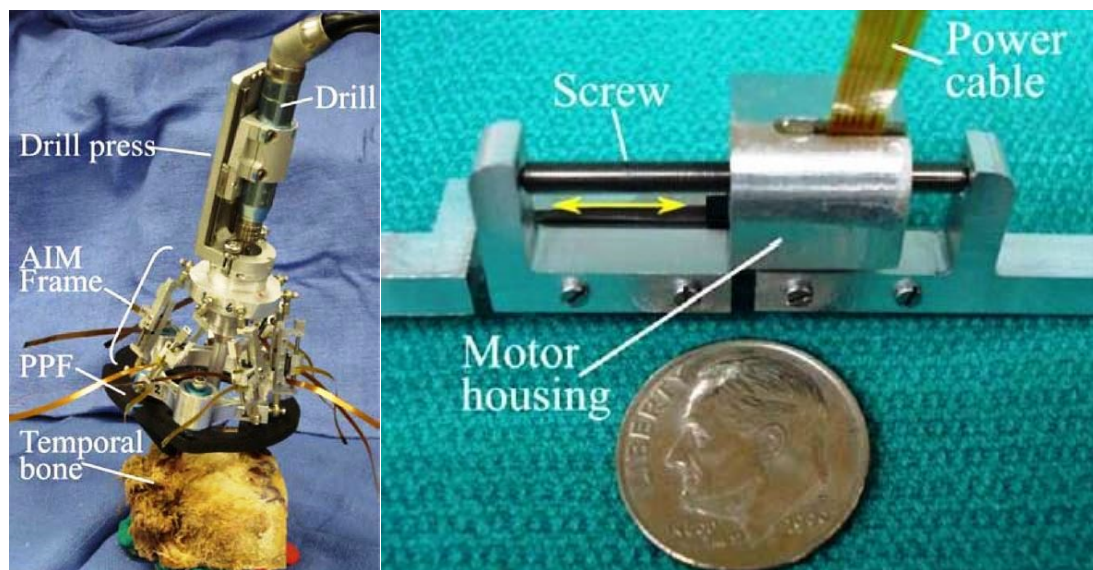
Figure 97: *AIM* Frame with surgical drill attached (left). During surgery two tools will be attached: a drill press and a cochlear implant insertion tool. One of six motor-actuated prismatic joints (right). A screw rotation causes linear translation of the motor housing, which is attached to a ball joint on the robot's top platform. (Image source: Kratchman et al. (134))

A drill press and cochlear implant insertion tool are attached to the top platform. A bushing that supports the drill bit up to the skull entry point, preventing drill bit stroll during drilling, is attached to the bottom of the same plate. The advantages of bone-attached parallel robots are that they are less obtrusive in the operating room; they do not require head fixation or optical tracking, as well as high stiffness and accuracy of the parallel robot itself.
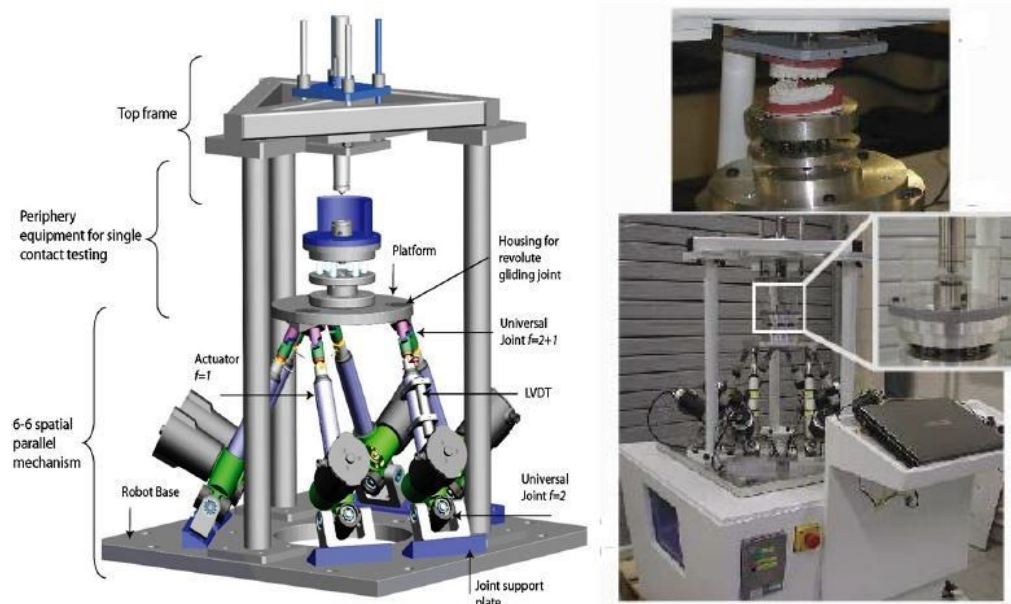
Figure 98: Virtual dental simulator: (left) assembly of simulator, (right top and bottom) Dental Mastication Robot. (Image source: Raab et al. (135))

A dental wear simulator, based on 6-6 parallel mechanism and the kinematics of human jaw, was presented by Raab et al. [135, 136] The construction of the robot (Figure 98) , which is based on the well-known Stewart-Gough platform, was used to replicate mechanical wear formation on dental materials and components, such as individual teeth, crowns or bridges. An appropriate physical mechanism for the robot was built such that it capable of accurately reproducing mandibular movements for a range of different chewing patterns and force profiles.

In neurosurgery, a parallel surgical robot for precise skull drilling was developed by *Tsai* and *Hsu* [137] to be applied in stereotactic neurosurgical operations. The feed carriage of the drilling device is mounted on the parallel surgical robot, based on a 6 DoFs structure (Figure 99). A position controller, carrying the feed carriage and the drill, to the predefined drilling position with the correct orientation automatically, controls the parallel surgical robot. In their work, the authors present the inverse kinematics, motion simulation, and geometric design parameters of their surgical robot.
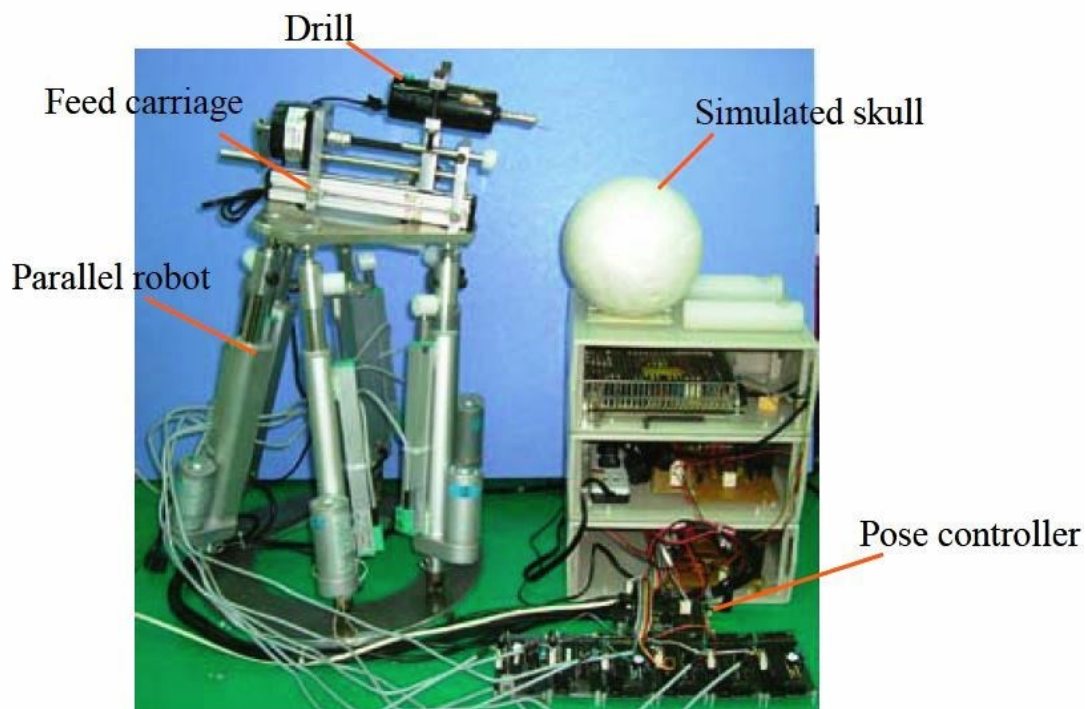
Figure 99: The working prototype of the parallel surgical robot for precise skull drilling. The feed carriage of the bone drilling device, which has one translational degree of freedom, is mounted directly on the parallel surgical robot. The pose controller controls the parallel surgical robot, carrying the feed carriage and the drill, to the predefined drilling position with correct orientation automatically. (Image source: Tsai and Hsu (137))

A robotic surgical device "*Evolution 1*", from *Universal Robots* (Figure 100), Germany, has been designed particularly for micro-neurosurgical and micro-endoscopic applications [138].

For its precise movement in 3D-space, the hexapod robot was selected with an absolute positioning accuracy of 20 μm. The mobile platform was designed such that different types of the surgical instrument could be integrated via a universal adapter. The robot is mounted to a compact mobile framework that needs to be pre-positioned to overcome the small working range of the robot. Once the robot is in an appropriate position to carry out the intervention, the framework is locked and the procedure then performed by the robot only. A rigid ventriculoscope with an outer diameter of 6 mm has internal multi-channels for insertion of various instruments. The system's functions such as the start-up procedure and robot speed control are controlled through a touch screen user interface, whilst the intra-operative active vision-guided steering of the robot itself is performed with a joystick device. The main consideration in the design of "*Evolution 1*" as a holding and positioning device for the endoscope was to carry out very smooth and slow motions inside very critical anatomical regions. Despite the safe procedure performed by the neuroendoscopic system, the range of the robot motion of 30° restricted the use of the robot in endoscopic procedures where larger ranges of motion are required.
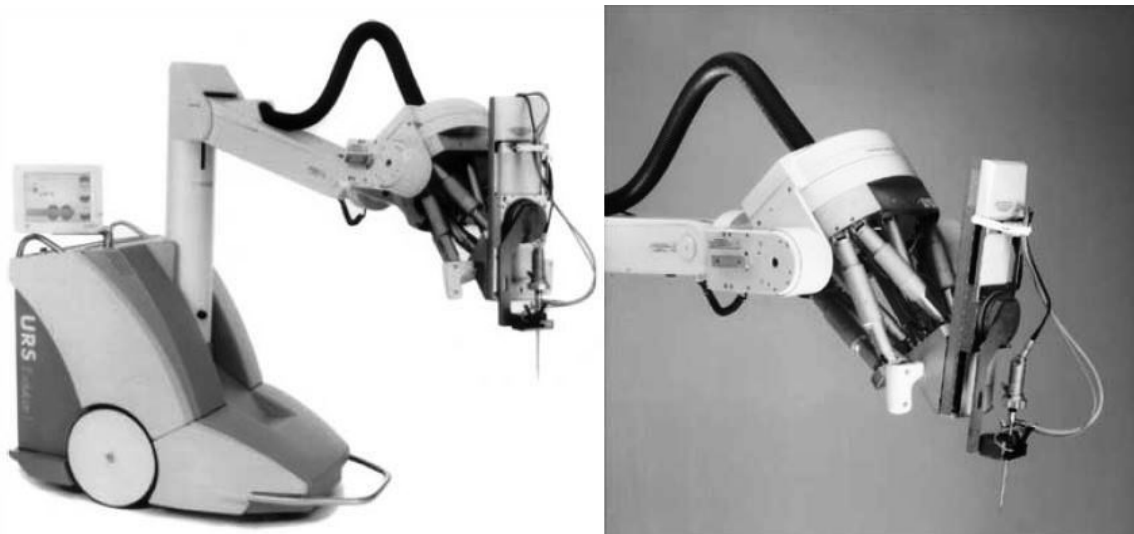
Figure 100: URS '*Evolution 1*' precision robot with 7 actuated axes, a universal instrument interface, a mobile pre-positioning system, including the control computer rack, and the touch operated graphical user interface (left). A hexapod robot, which consists of a fixed and an articulated mobile platform (right) (Image source: M. Zimmermann et al (138))

In eye surgeries, a robotic system for retinal micro-vascular surgery was developed by *Yu et al.* [139]. The 11 DoFs robot system includes a 6 DoFs *Stewart-Gough* platform, a 2 DoFs differential wrist, and a 3 DoFs actuator for deployment of stent and bridge vessel separators.

The parallel robot has a Ø52 mm moving platform and a Ø80 mm base platform and a centre height of 150 mm. The stent deployment robot attaches to the parallel robot via a quick-changeable tool (Figure 101). Both the parallel robot and the stent deployment robot have

been designed using ball-screws and preloaded apex screws to provide control precision accuracy within 5 μm. The robot design also includes the intra-ocular deployment of a custom-designed Optical Coherence Tomography (OCT) probe.
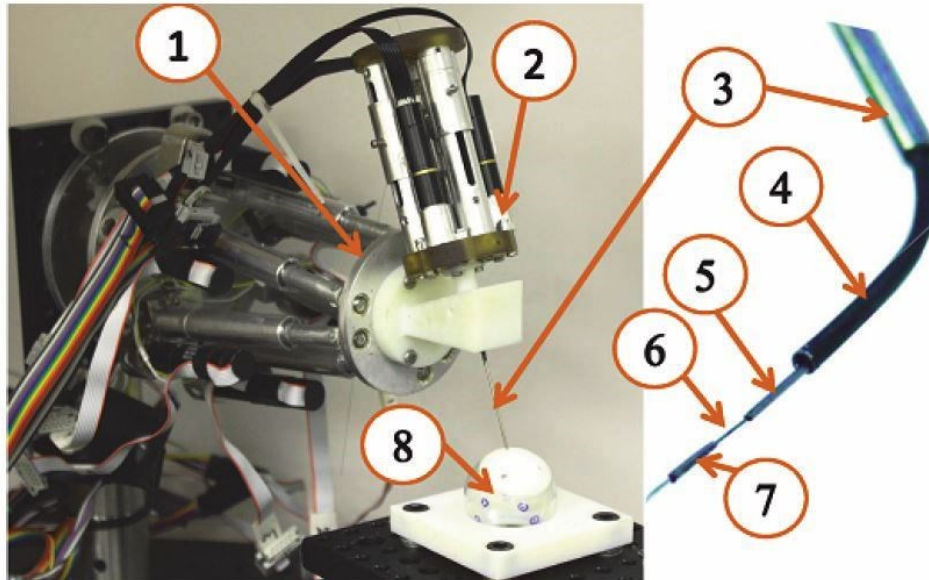
Figure 101: Stent actuation robot. (1) Parallel robot moving platform; (2) stenting robot; (3) robot stem; (4) angle adjustment tube; (5) stent pushing tube; (6) guide wire; (7) stent; (8) eye model (Image source: Yu et al. (139))

A novel microsurgical system for vitreoretinal surgery[9] [140] was developed by *Nakano et al.* [141]. This particular surgical procedure is challenging for the surgeon due to the restrictions of tool manipulation, hand tremor, and the delicate nature of tissues such as the retina. The microsurgical system consists of master-slave robot manipulators, an optical system, and a 3-D view of the microscope via high definition (HD) display (Figure 102).

Both arms of the user using 7 DoFs in each of them, 3 DoFs for each translation and rotation, and 1 DoF for grasping control the master part of the robot.

Motion information provided by the surgeon is recognised, scaled down, and transmitted to the slave part by the master robot. The unique condition of the vitreoretinal surgery, which requires a manipulator that must be precise, compact, and achieve pivotal motion was the motivation for selecting a parallel construct slave robot.

---

[9] A sub-specialty of ophthalmology involving the treatment of all retina diseases including age-related macular degeneration, retinal detachment, macular holes, and diabetic retinopathy
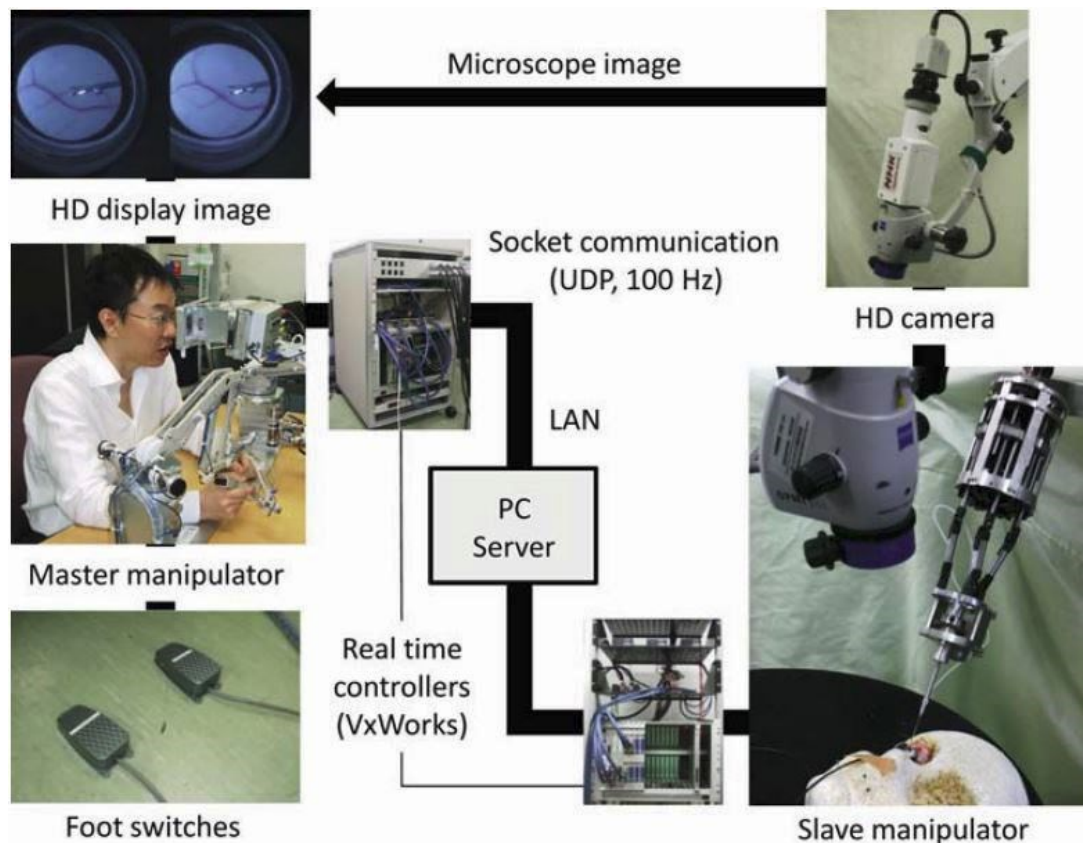
Figure 102: Overview of the microsurgical system for vitreoretinal surgery. The system consists of two manipulators (master and slave) controlled by the real-time controllers and a high-definition (HD) display provides a 3-D view of the microscope. (Image source: *Nakano et al.* (141))

Despite the use of a 6 DoFs slave robot, which provides 3 DoFs for each translation and rotation, the authors have separated the rotational DoF around the tool by placing a rotational mechanism, on the end-effector. This addresses the limitation in the rotational movement around the tool due to the interferences that are likely to occur between the links with the rotational displacement. Using a microscope, the evaluation experiments of positioning stability and accuracy showed a predicted physiological hand tremor for the surgeons performing the procedure manually using the microsurgical system, which is barely observed. However, it observed that the hand tremor was not reduced by a motion-scaling factor of 1/40 and the time for a tracing task by the system was about five times longer than the manual procedure.

6.1 The Design of the Surgical Robot Platform: Overview

The principles of the mechanical design of the parallel manipulator are based on a structure (Figure 103) [142] patented [143] by our manufacturing contributor, *Paul Harkin* of *Form Changing Structures*, a UK based company [144] whose mission is to develop designs for structures that change their form.
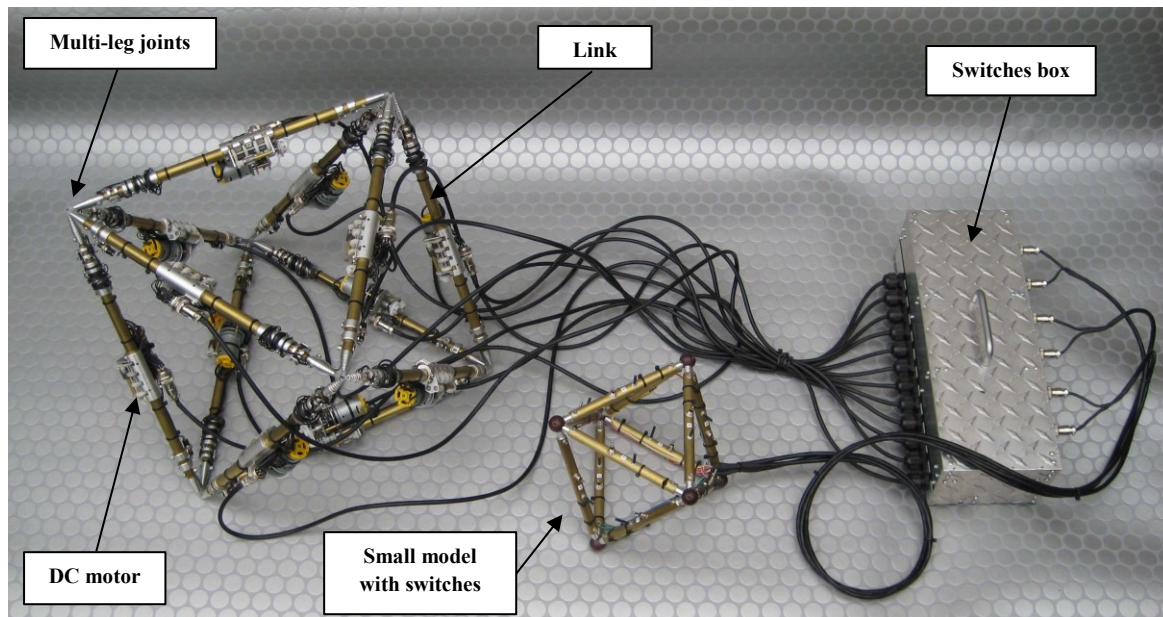
Figure 103: Form changing structure designed by Paul Harkin. Multi-links were attached together at the ends via passive, free-rotation, multi-leg joints. A DC motors were used for extending and retracting the actuators, and they assembled at the middle of the actuators. These motor were powered manually using switches. Note that this form changing structure has no base or top platform and the links were attached to each other. (Image source: imeche. Org (144))

With reference to Figure 104, both of the surgical cutting tools (T) need to be positioned and moved around the dorsal parts (e.g. the vertebral cavity VC) of patient (P), who would be laying facedown during the surgical procedure.

The tools could be hand-held and manipulated by a surgeon, but there is an intrinsic problem with fatigue in the human hand during longer length procedures [18]. To overcome this, a parallel manipulator robotic platform, which is also called the octahedral platform [145] (OP), has been designed that acts as a mount for the tools (T), and produces the desired range of movements. The octahedral platform is a 6 DoFs parallel manipulator, which is comprised of a fixed top (FT), and a mobile base (MB), connected by six individually powered extensible linear actuators (LA) or '*legs*'. The linear actuators are configured in an octahedral arrangement, commonly known as a Stewart Platform. This configuration was chosen over a

serial manipulator because it produces an inherently more stable end effector position. The octahedral platform is intended to be suspended from a rigid structure (RS) located above the prone patient (P).
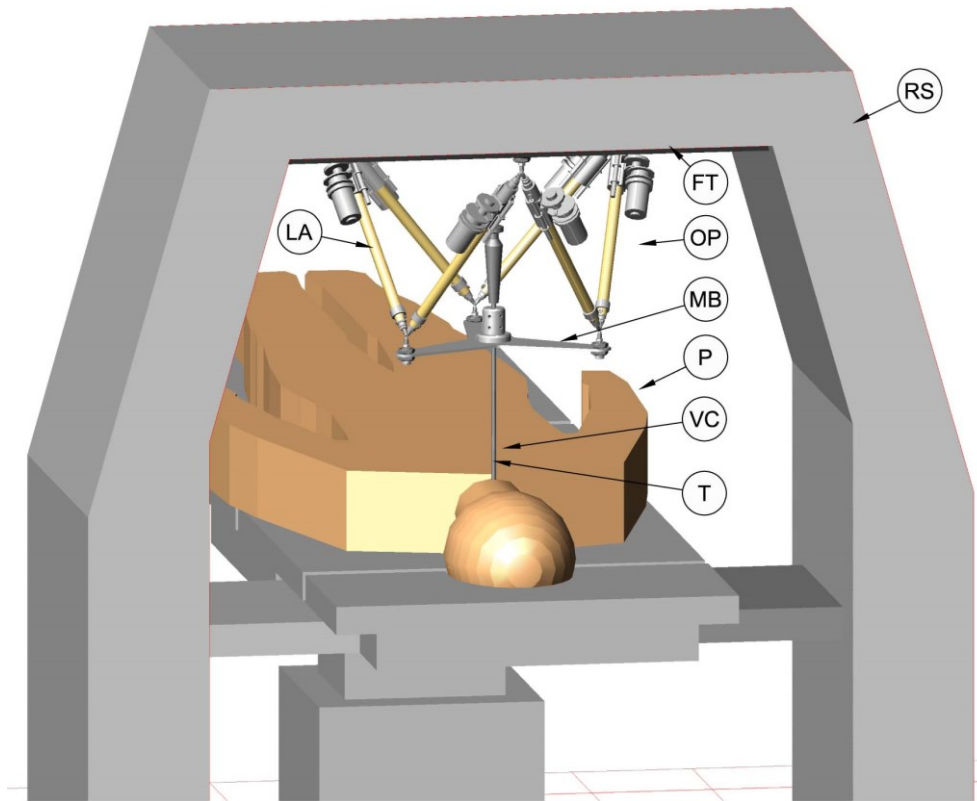
Figure 104: An illustration of the assembled surgical robot device installed in an operating theatre environment. (T) Surgical tool, (VC) vertebral cavity, (FT) fixed top, (LA) linear actuators, (MB) mobile base, (P) patient, (OP) octahedral platform, and (RS) rigid structure.

6.2   Design Specifications

6.2.1 Range Of Movement and Working Envelope

The vertebral cavity (VC) containing the spinal column (Figure 105) of a typical prone adult patient (P) has a cross-sectional area of very approximately 60 mm width and 80mm height, and an average length of approximately 700 mm.

However, with reference to Figure 1 (Chapter 1) it will be seen that the tumours that are the device's target are typically less than approximately 100 mm in length along the axis of the spinal column. Therefore, it was decided that the surgical cutting tool (T) needs to access a section of the vertebral cavity only approximately 120 mm in length, rather than the full 700 mm of the spinal column. This helped to simplify the mechanism, and prioritised end effector accuracy within a smaller working envelope.
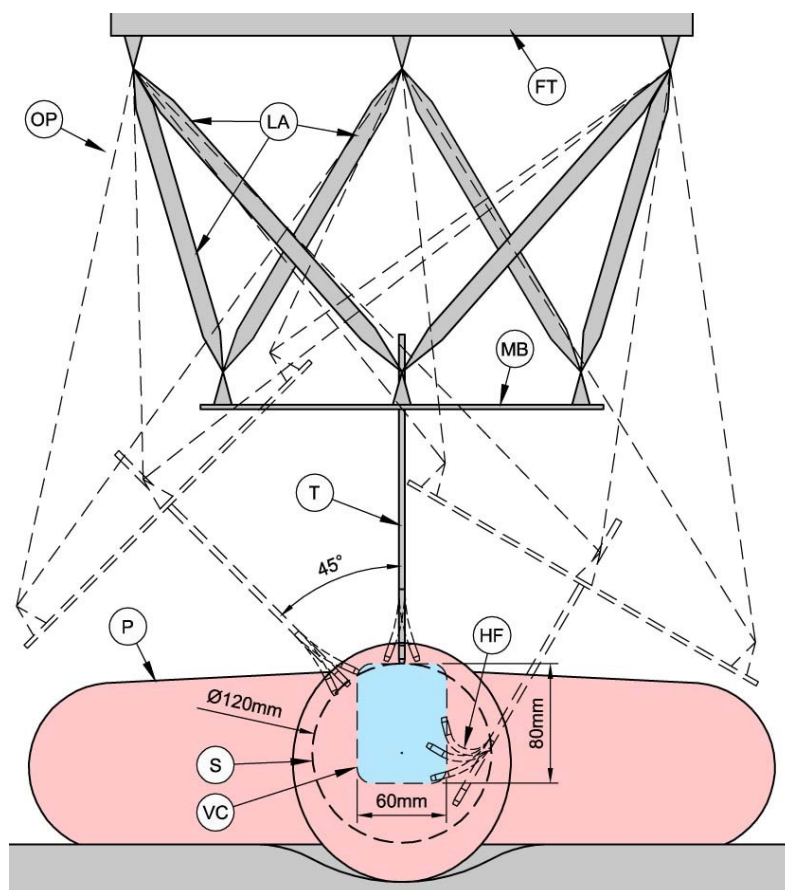
Figure 105: Surgical tool (T) working envelope relative to vertebral cavity (VC). (FT) fixed top, (LA) linear actuators, (MB) mobile base, (HF) hook-like form, (P) patient, (S) approximate sphere, and (OP) octahedral platform.

Taking the spinal column as being very approximately cylindrical in form, and based on the dimensions as above, the end-effector working envelope was established as an approximate sphere (S) of Ø120 mm. Based on the ability of the flexion system to assume a hook-like form (HF) around the spinal column, the platform was configured to give an angular displacement of ±45° from the z-axis, thus giving the surgical tool complete access to all sides of the spinal column.

6.2.2   Fixed support structure

The robot manipulator was designed such that it will be suspended from a fixed structure located above the patient. This requirement is a consequence of the prone, facedown posture of the patient during the surgical procedure. The structure of the suspension system simply has to provide three rigid attachment points for the topmost triangular face of the octahedral robotic framework.

The aforementioned practical limits on the range-of-movement for the robotic framework (an approximate sphere (S) of Ø 120 mm), and the consequence of having to reposition the support structure to enable access to as much of the length of the vertebral cavity as possible

(700 mm in length), result in the need to consider how the support structure itself is configured, i.e. fits around the patient (Figure 108).

6.2.3   Configuration of the surgical platform

There are two possible configurations of the surgical platform:

1. Mounted from a fixed structure above the surgical table (e.g. suspended from the ceiling of the operating theatre), possibly in the form of rails that run parallel to the patient's spine, to allow the robotic framework to move along them.

2. An independent floor-bearing structure that straddles the operating table, i.e. a trolley in the form of an inverted *U*-form, that could fix to the table, and then move relative to it as needed along the length of the patient's spine.

6.3   Surgical Robotic Platform: Detailed Design

Based on the aforementioned octahedral configuration, and to create a device that was considerably lower-cost than those that are commercially available, a simplified design of the platform was developed for the moveable mounting platform for the surgical tool.

6.3.1   Linear actuator

For the variable-length linear actuators, or legs, a relatively simple single-portion extension configuration was used, sometimes referred to as 'telescoping'. This configuration was preferred over multiple-portion extension devices; these are normally used when the retraction/extension ratio needs to be greater than 1: 1.7. Typical applications for multiple-portion extension devices are for long-span crane booms that must be relatively compact when transported, or retractable radio aerials. For any given method of powered extension/retraction, their design tends to be more complex than for single-portion actuators.

With reference to Figure 106, the single-portion actuator comprises only two main groups of components: an outer, cylindrical '*barrel*' (B) and a corresponding inner '*piston*' (P). The ratio of the fully-retracted/fully-extended length of the whole assembly should be 1:2. However, this is only a theoretical ratio, as it is usually a slightly lower ratio (typically 1: 1.7). This is due to their typically being portions of the overall length of the actuator that do not fully retract into the barrel (e.g. seals/collars, or fixed-length connecting joints), and the need to prevent the piston from fully emerging out of the cylinder, i.e. there must always be a certain overlap of the lengths of the two components at the point of maximum extension.
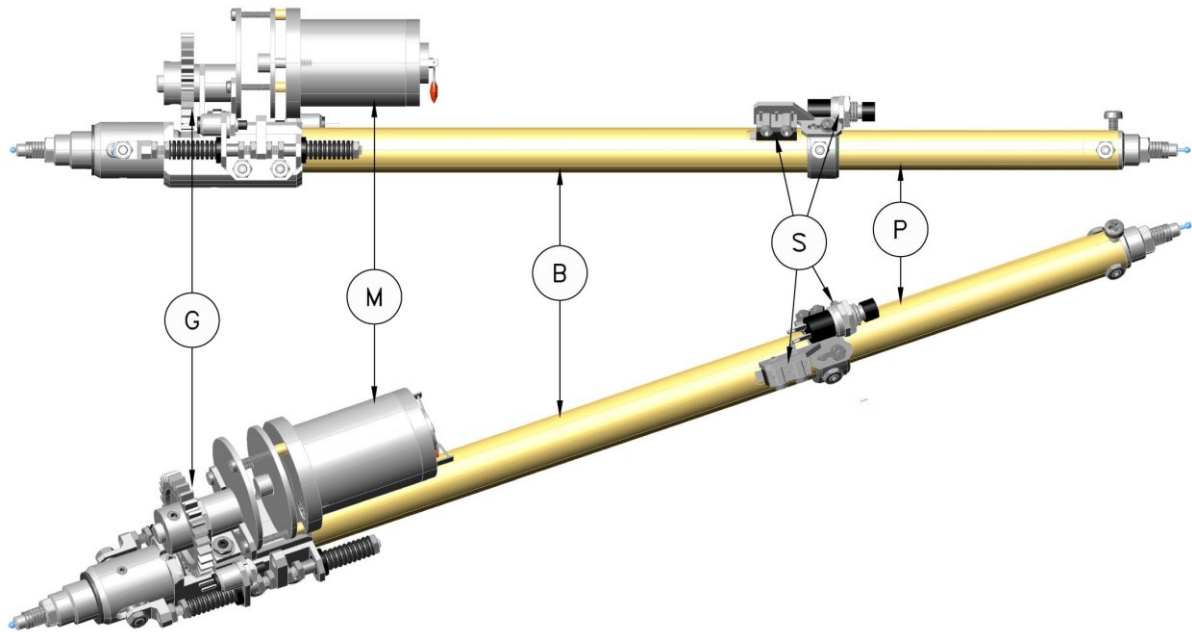
Figure 106: Variable length linear actuator. (P) Piston, (B) barrel, (M) motor, (G) gear, and (S) switch.

The 'stroke' of a linear actuator is the variation in length of the whole assembly as it goes from maximum retraction to maximum extension, i.e. accounting for any portions of the design that are either fixed in length/do not fully retract, and/or any overlap at maximum extension.

For mechanical actuators, such as for those using a rotating lead screw mechanism, the powered extension of the first portion via a lead screw is very straightforward; it simply requires the screw to engage in an internal thread as part of the extending portion

In our prototype, the lengths when fully retracted/ fully extended are approximately 270 mm and 450 mm respectively, i.e. a ratio of approximately 1:1.7. A single lead screw mechanism, powered by a DC motor (M) via a gear assembly (G), produces the linear movement.

6.3.2   Prismatic Bearings

For mechanisms where a lead screw is used, it is necessary to incorporate measures to prevent rotation of the various portions of the actuator relative to each other along the axis of the lead screw. Otherwise, there might be tendency for the rotation of the lead screw to simply rotate the portion intended to be extended/retracted, due to friction between the lead screw and the internal thread. This can be avoided by using a '*key*' in one of the portions, which engage/slides within a 'keyway' or slot within the other portion. This permits the actuator portions to move relative to each other along their shared principle axis, but not

rotate around it, in other words, it acts as a 'prismatic' bearing or joint. Figure 115 shows an 'exploded' engineering drawing of a complete 'leg' with all sub-components.

6.3.3   Maximum extension / minimum retraction sensors

These are switches (*S*) incorporated into the design of the linear actuators (Figure 110), which act as motor cut-out devices at the point of maximum extension or retraction, primarily to prevent the drive mechanism from breaking components when the mechanical limits of the actuator stroke are reached.

6.3.4   Measurement of Linear Extension

Rotary encoders are installed (Chapter 7) on the motor/gearbox shaft, as a means of measuring the revolutions of the motor, and hence calculate the extension/retraction of each actuator.

6.3.5   Connector Joints

To connect the linear actuators/legs to the stationary/fixed top and lower mobile base, existing octahedral robotic surgery platforms typically utilize two degree-of-freedom pivot joints. These are robust, but not concentric at the end vertices of the adjacent legs. Primarily to simplify the kinematics, near-concentric (within 1-2 mm), passive, free-rotation, multi-leg joints [143] are used. These were originally developed for use in variable-geometry space frames.

The joints (Figure 107) consist of a number of sub-assemblies (SA), which each connect to the ends of the linear actuators (LA), or legs, and the mobile base (MB). A flexible, slightly elastic cord (C) passes through each subassembly. The cord is precisely adjusted via a threaded mechanism (TM) to pre-tension it. The tips of the sub-assemblies are hollow barrel forms (HB), through which the cord passes, and the ends of the cords are tightly intertwined with each other. The pre-tensioning of the cord pulls the ends of the nylon barrels together, thus allowing free rotational movement, but resisting the primarily tensile and compressive forces imposed by the legs.
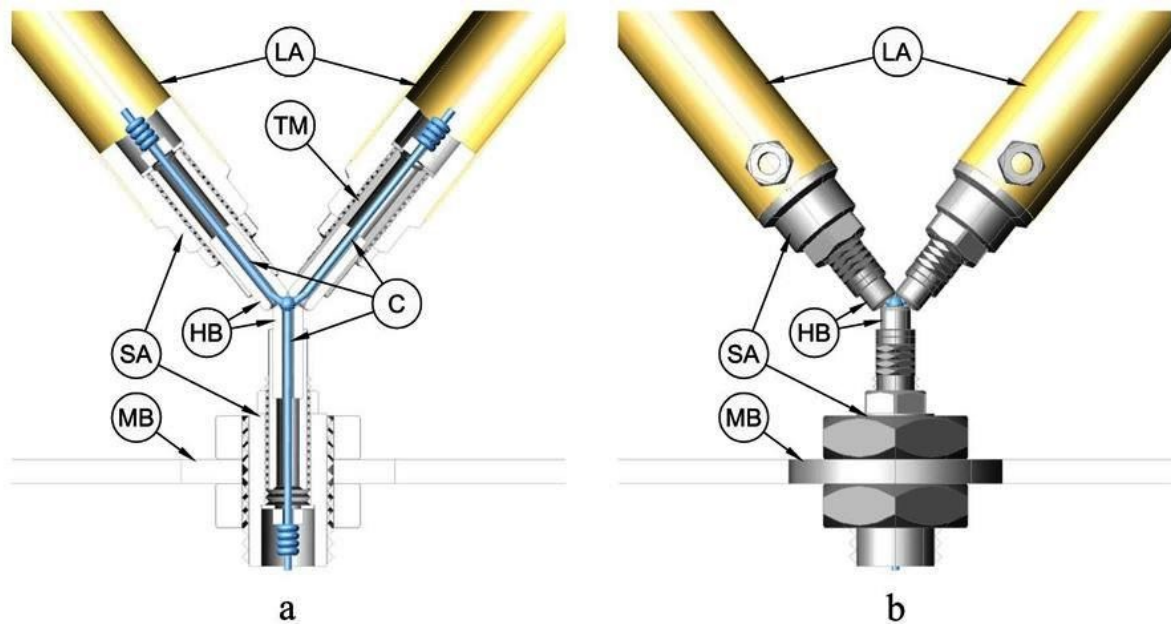
Figure 107: Connector joint assemblies, shown in (a) section and (b) side view. (SA) sub-assemblies, (LA) linear actuators, (MB) mobile base, (C) elastic cord, (TM) threaded mechanism, and (HB) hollow barrel.

6.3.6   Lower Plate

The form of this component has been determined by the need to make it as rigid as possible, whilst at the same time minimising the visual obstruction it creates for the operator/surgeon (Figure 108).
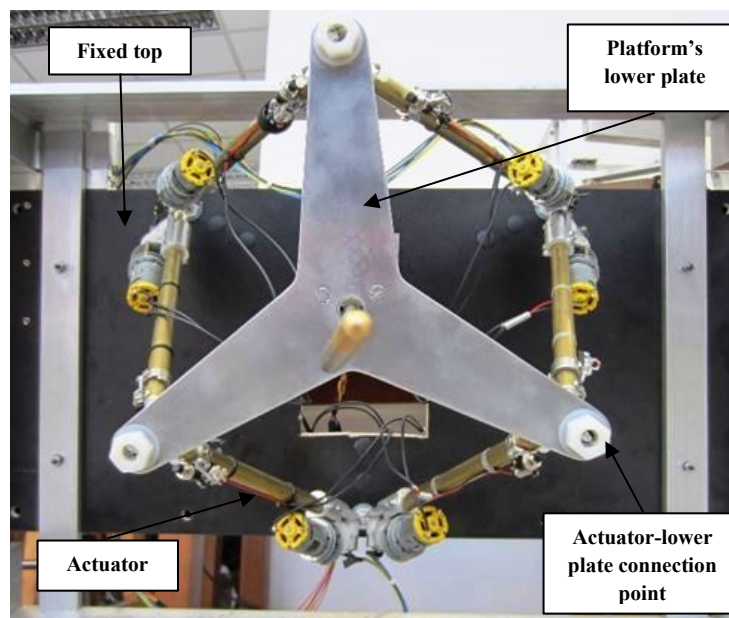
Figure 108: Top view of the completed surgical robot. The 6 extensible actuators are connected to the platform's lower plate at one end and to the upper fixed top from the other end. Each pair of actuators was connected to one point.

6.3.7   Load sensors

In addition to the components of the parallel platform listed above, a load sensor (Figure 109) has been fully designed. Each of these sensors, which are intended to be installed onto each of the linear actuator in the next stage of development, is configured as a piston that slides along the principle axis of the linear actuator, constrained by adjustable opposing pairs of compression springs. Via the activation of adjustable switches, these sensors will measure the tensile and compression forces acting upon the linear actuator.
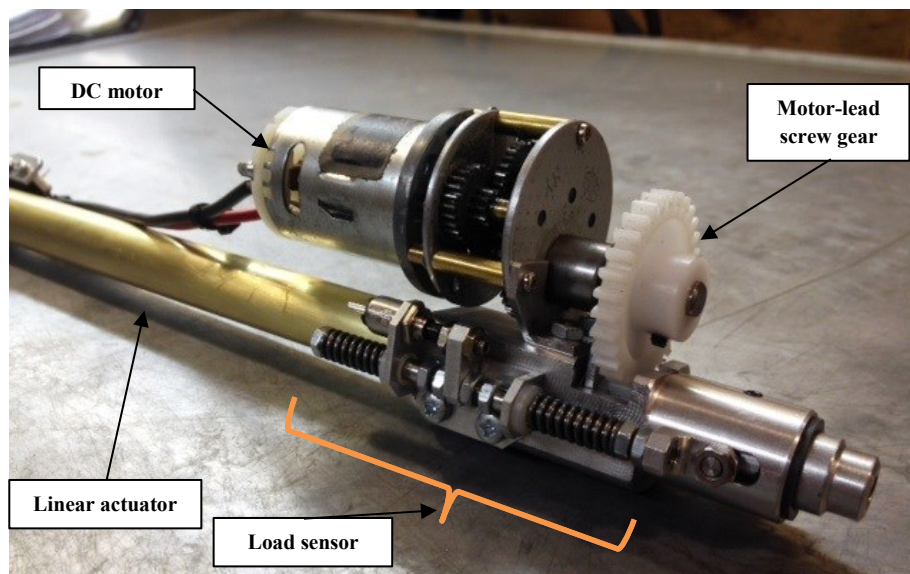
Figure 109: The implementation of the load sensor to the linear actuator

6.3.8   Materials

Due to the overall change in length of the actuator, it has several components that act as bearings, both linearly and rotationally. For the main lengths of the actuator portions that extend/retract, brass was chosen as it has a relatively low tendency to 'gall' when used in sliding contact with other metals. Collars that act as interfaces/bearing between the brass portions, and revolute bearings were fabricated in stainless steel (SAE grade 304), due to it being a reasonably hardwearing material and having good bearing properties. The 'nuts' of the leadscrew mechanism were originally fabricated in stainless steel, but these had a tendency to jam the leadscrew mechanism, due to even quite minor manufacturing misalignments. They were therefore refabricated in nylon 6 (Polycaprolactam), a material commonly used in mechanical bearing applications, which overcame the jamming problem.

During the detailed design and fabrication process, care was taken wherever possible to ensure components that move relative to each other presented bearing surfaces that were

perpendicular to the primary direction of any imposed load. This would minimise the frictional forces between the two components, and reduce wear.

For other, non-moving components, such as various brackets and the main mounting block, which connects the motor/gearbox assembly to the brass actuator portions, aluminium was chosen for its easy machining properties and low relative weight. See Figure 111 for all moving/non-moving components of the complete link 'leg'. All materials, including fasteners/fixings, were chosen to have high corrosion resistance in their as-supplied form.
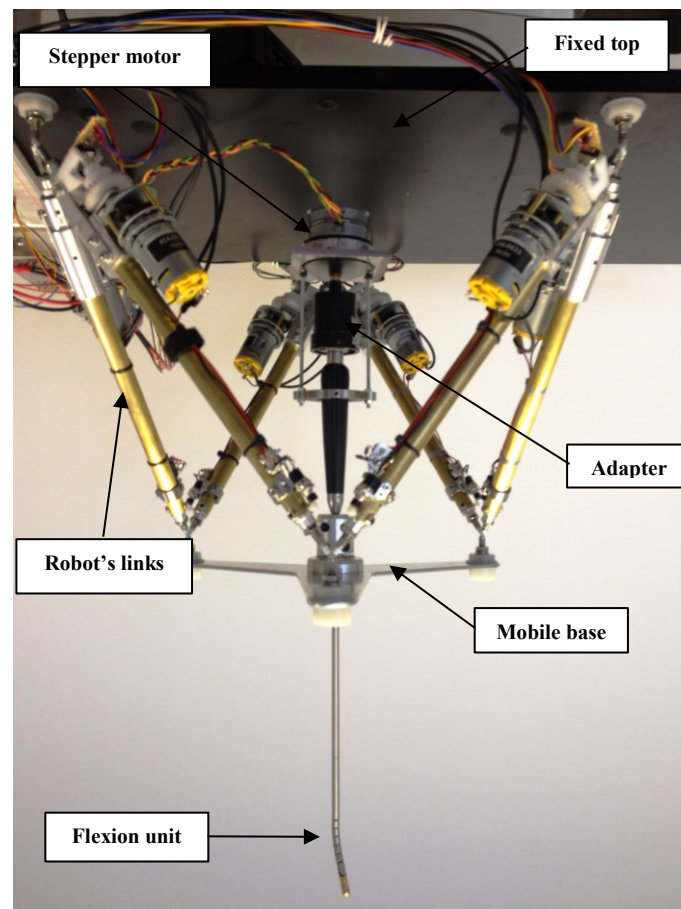
Figure 110: The complete parallel platform with the integration of flexion unit. Six extensible links are connecting the mobile base to the fixed top. The flexion unit is installed at the mobile base at one end and connected, at the other end, to the stepper motor via an adaptor for automatic actuation of the flexible probe.

After completing the design and fabrication of all components, the parallel platform was built and the flexible unit was assembled to the end-effector (Figure 110). The implementation of all necessary hardware (electronics components) and software (programming algorithms) required to operate the parallel platform will be described in Chapter 7. In addition, a haptic feedback method will be applied to further support controlling the movement of the surgical platform
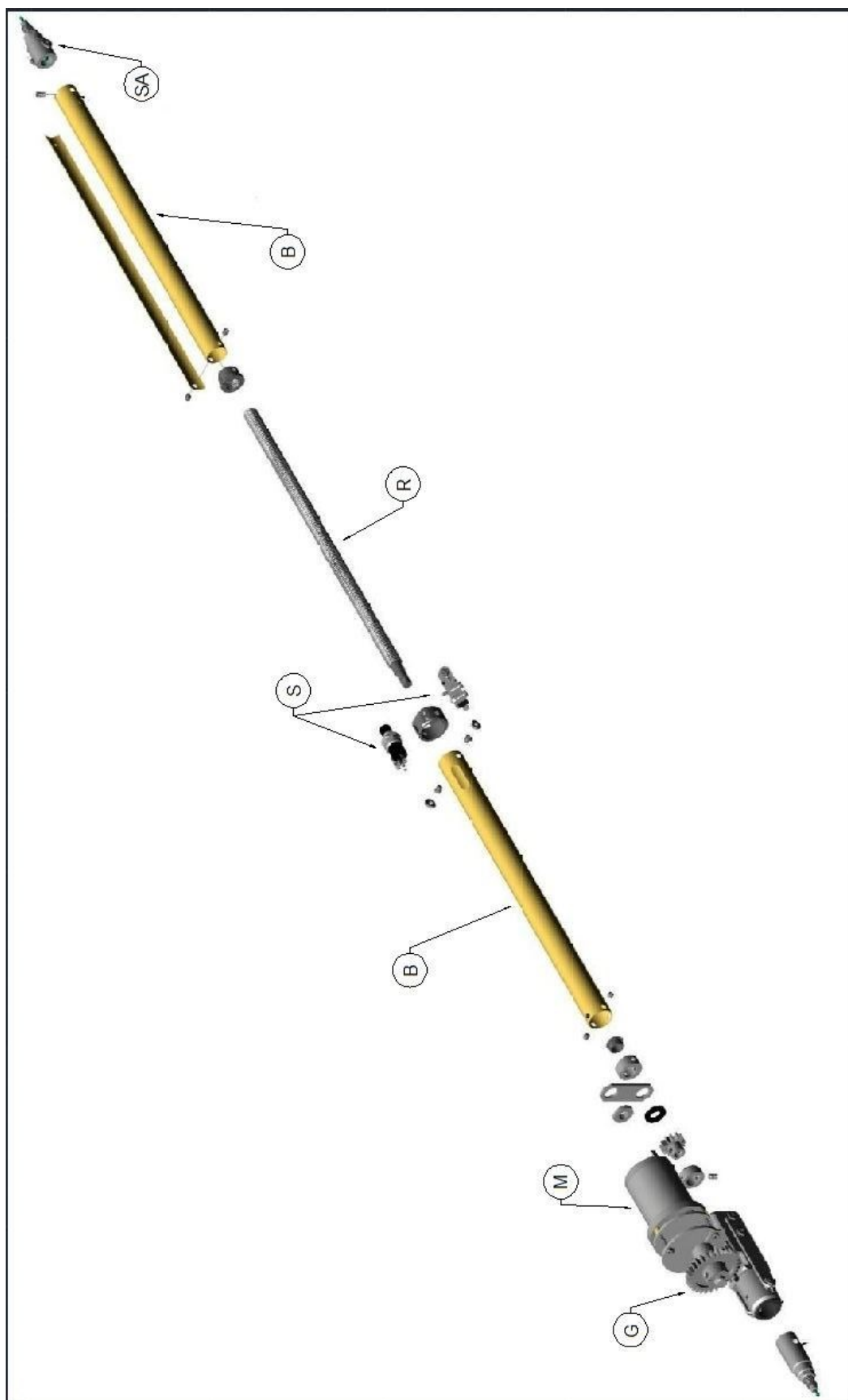
Figure 111: An isometric view of an expanded plot of the linear actuator: (G) gear, (M) motor, (B) barrel, (S) switches, (R) rod, and (SA) SA) sub-assemblies.

6.3 Positioning and Actuating of the Surgical Probe

Positioning the surgical flexible probe around the spinal column using the positioning and guide capabilities of the robot platform was conducted in vitro. With reference to Figure (112), using rigid tool, which is currently applied in operating theatre for the application of spinal surgeries, has little effect on cancerous tissues appears at the interior side of the spinal column. The figure illustrates using the non-flexible cutter to show an inability to remove tissue.
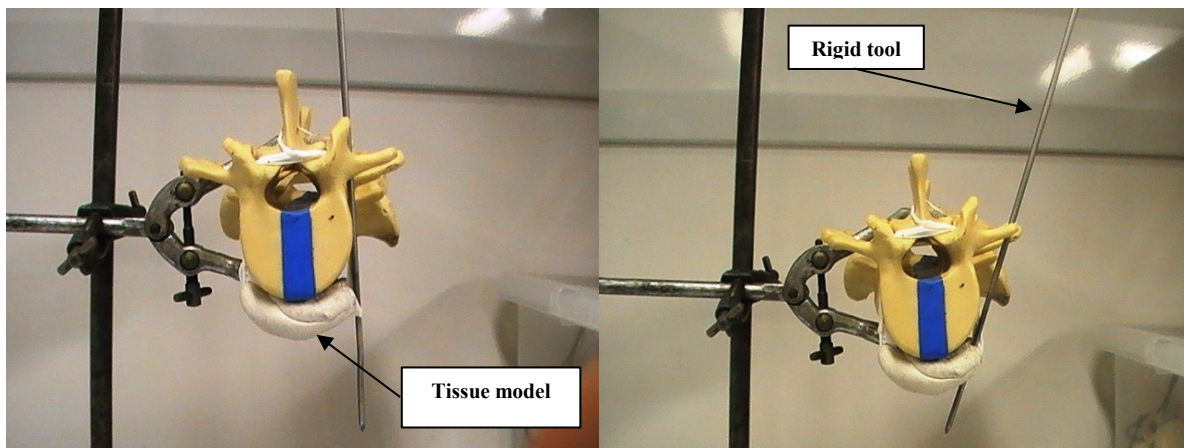
Figure 112: Using rigid tool for the dissection of cancerous tumour (white) around the spinal column in vitro, (left) straight access, (right) angled access.

Figure (113) demonstrate the insertion and the bending of the flexible surgical probe, developed in Chapter 4, which has the ability to bend around corners. The guide and support of the 6 DoFs robot platform is also shown in Figure 113, this support has added multiple bending configurations to the flexible probe, hence surgical tool, to approach the desired surgical field and completely remove the cancerous tumour.

A graphical illustration describing the concept of developing a flexible surgical probe for the application of spinal surgery is shown in Figure 114-right. The figure shows the area on the interior side of the spinal column that can be reached using the capabilities of an integrated robot platform and flexible surgical probe, which result in removing the entire cancerous tumour. This illustration was compared to approaching same procedure using a rigid surgical tool. Figure 114-left shows the limited effect of rigid tools of reaching around the spinal column. Most of the cancerous tumour will be remained and a second invasive surgical procedure will be required to remove the remaining of the cancerous tumour, which is always a challenge to the surgeons and causes risk to the patients.
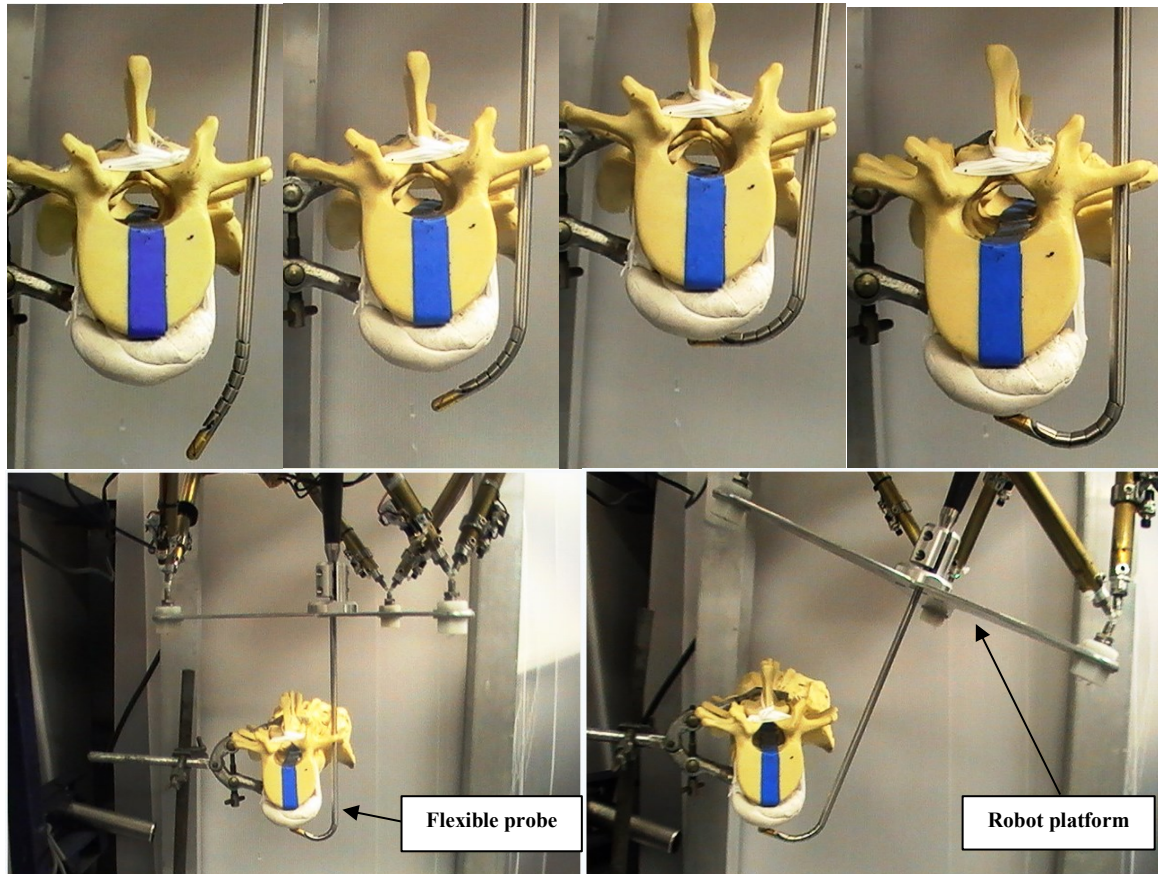
Figure 113: In vitro illustration of using flexible surgical robotic probe around the spinal column. Steering of the flexible surgical probe around the spinal column (top-left to right). The guide and support of the robot platform in positioning the flexible probe to reach the desired target with straight configuration (bottom-left) and angled configuration (bottom-right)
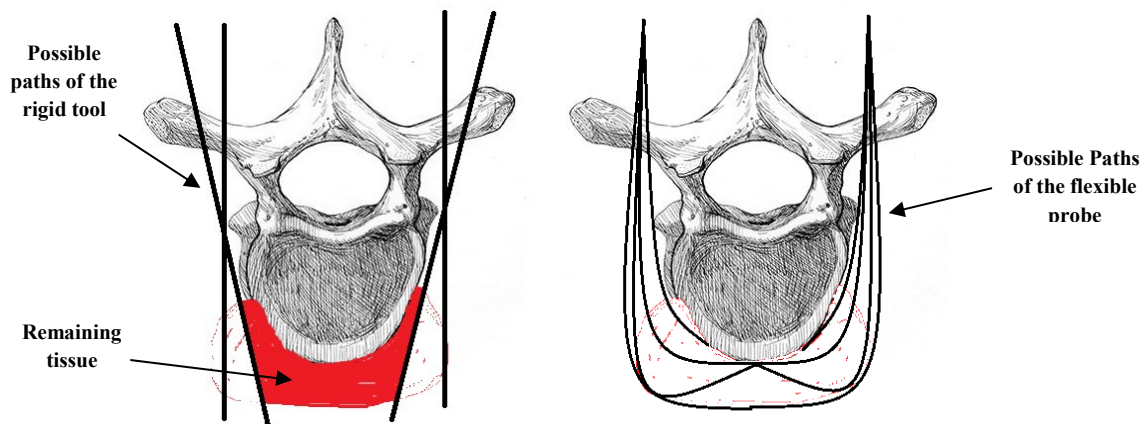
Figure 114: Demonstrating the concept of flexible surgical robotic probe in spinal surgery. (Right) multiple positioning configurations achieved by the combination of the robot platform and the flexible probe, cancerouce tumour removed completely. (Left) two possible configurations of using rigid tools for similar surgical application, most of the cancerous tumour was remained at the interior side of the spinal column.

The use of flexible surgical robotic probe would safely remove the cancerous tissue surrounding the spinal column at the first attempt without the need for an additional invasive surgical procedure. This would significantly reduce trauma, time of recovery, and cost compared to using rigid surgical tools.

143

6.4   Modelling the robot Platform Using SimMechanics

This section will describe the initial modelling of the proposed prototype design of the robot platform, which was conducted at an earlier stage of this project. This section will only introduce the modelling of the physical plant of the robot platform. The control and trajectory modelling of the physical plant was adopted from creating a Stewart platform model performed by *J.Wendlandt* [146].

The design of the surgical platform is based on the classic Stewart platforms (parallel manipulator) used in many applications (section 6.1.4) for positioning objects. The surgical platform has an exceptional range of motion and can be accurately and easily positioned and oriented. The platform provides a large amount of rigidity, or stiffness, for a given structural mass, and thus provides significant positional certainty. In this section, the behaviour of the surgical platform is demonstrated using SimMechanics to model the mechanical components of the system. Figure 115 show the complete surgical platform model.
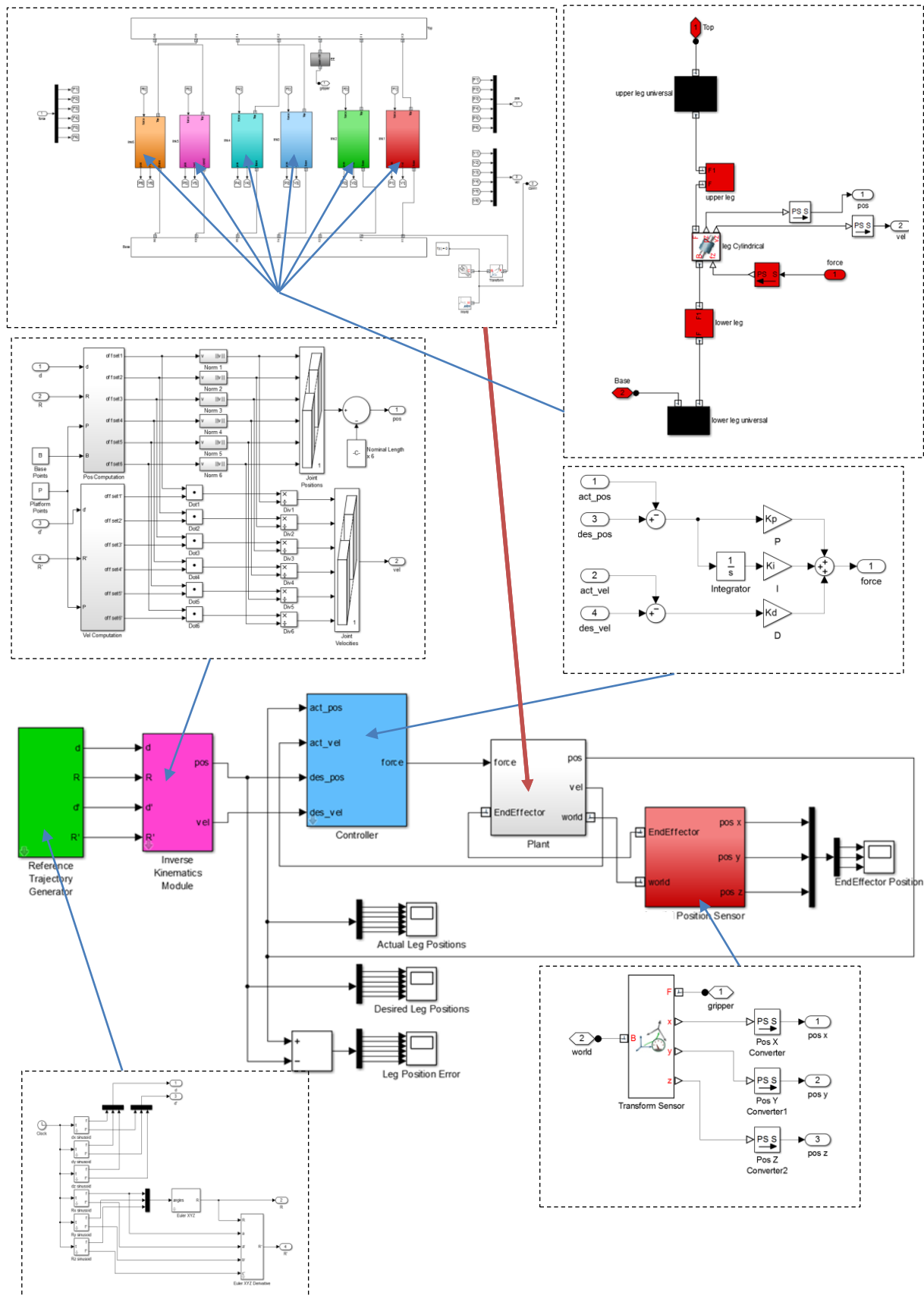
Figure 115: The complete surgical platform model. The physical plant is connected to the controller model, which is encompassed of inverse kinematics and trajectory models, to perform simulation. The model is also connected to several displays representing positioning data.

6.4.1   Modelling the Physical Plant

The platform model is moderately complex, with a large number of mechanical constraints that require a robust simulation. The full assembly is a parallel mechanism consisting of a mobile platform connected to an immobile base and defined by at least three stationary points on the grounded base connected to the legs.

The platform used here is connected to the base at six points by universal joints as shown in Figure 116. Each leg has two parts, an upper and a lower, connected by a cylindrical joint. Each upper leg is connected to the mobile platform by another universal joint.

The platform assembly parts were built in SolidWorks CAD software. After modelling a simplified motion platform, CAD translation tool is used to transform geometric CAD assemblies into Simulink block diagram model. The CAD translation tool first exports the assembly model from CAD platform into the physical modelling file with *xml* extension. The physical modelling file is then imported into Simulink, creating a SimMechanics model (Figure 117).
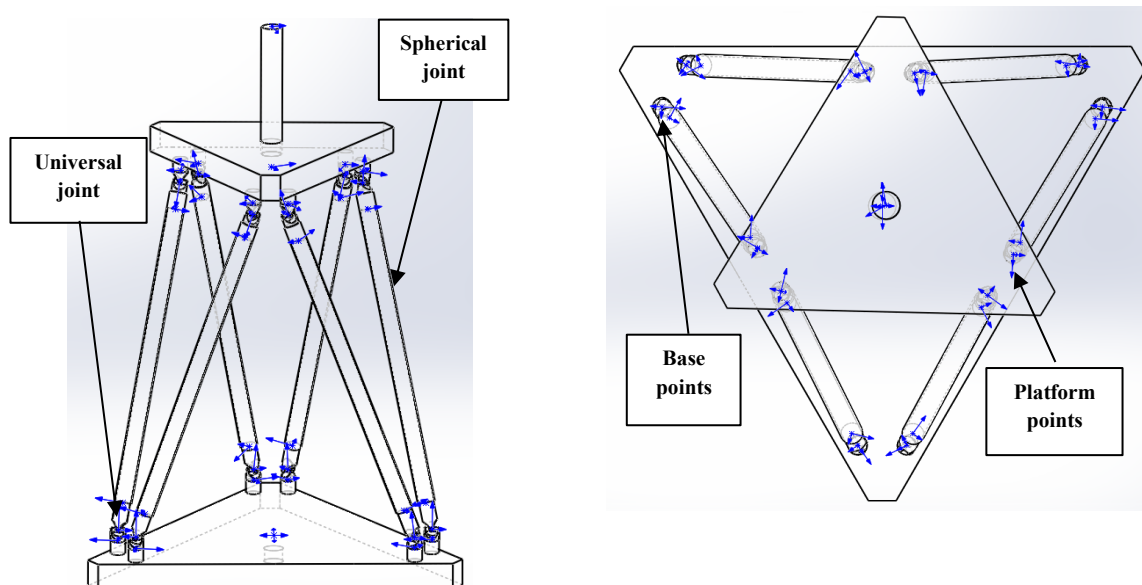
Figure 116: SolidWorks drawing of the surgical platform showing the legs attachment points, spherical and universal joints

Figure 117: The sequence of CAD to SimMechanics transformation

The imported *xml* file was then converted to a SimMechanics block (Figure 118).
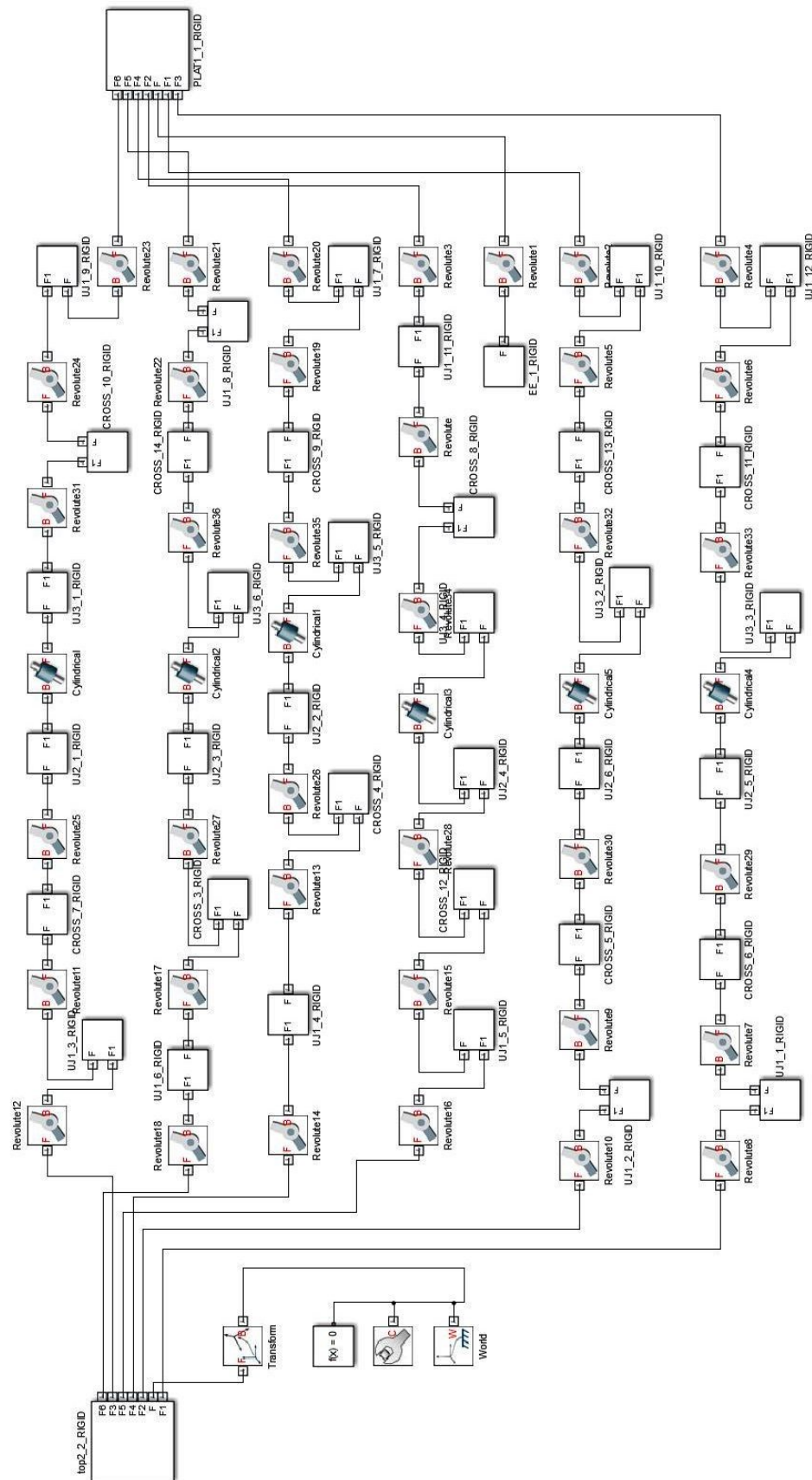
Figure 118: SimMechanics blocks network representing the physical modelling of surgical platform. Each line connecting the top plate to the base represent the joints and the links that built to complete each leg construction.

The Plant subsystem (Figure 119) is obtained by using the SimMechanics toolbox to re-arrange the model shown in Figure 122 into several subsystems.
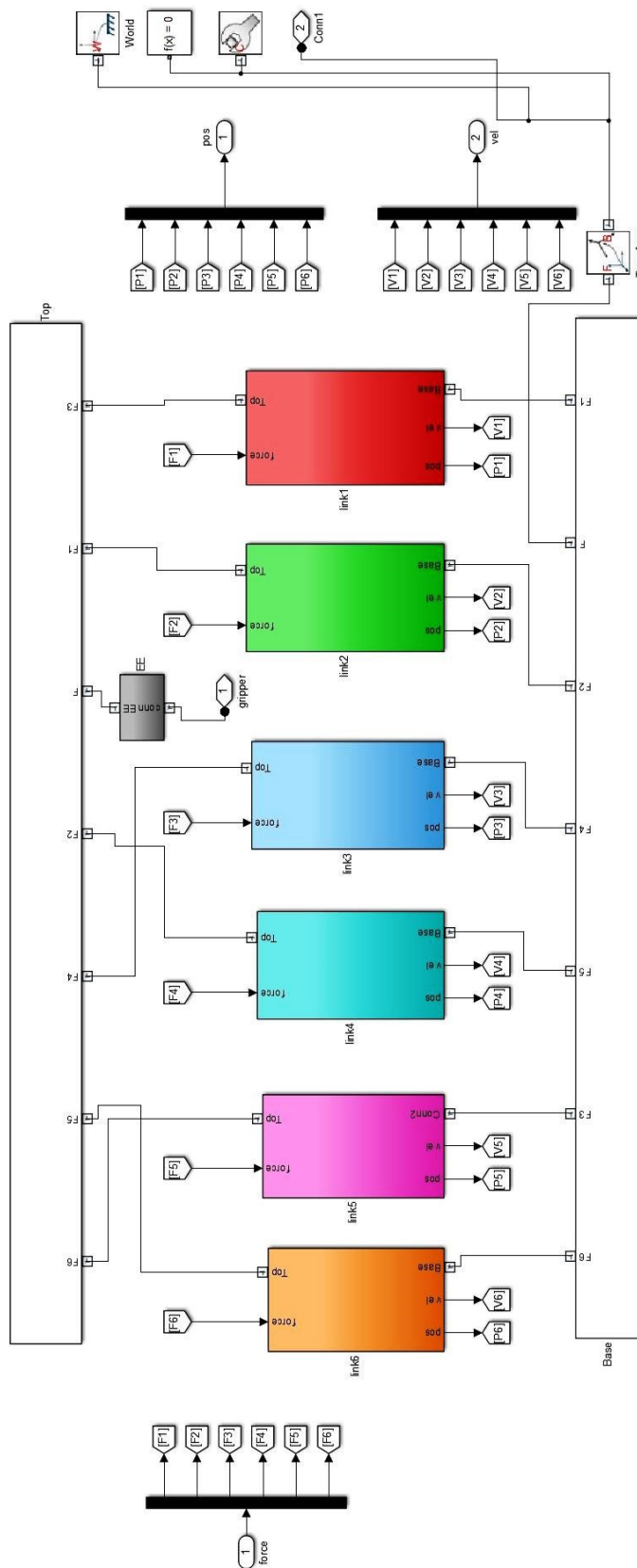
Figure 119: The plant subsystems. Each subsystemcontains the element of building each leg, which connects tope plate to base

The mechanical components of the Platform consist of a top plate, a bottom plate, and six legs connecting the top plate to the bottom plate. The overall system has 6 DoFs. Each leg subsystem (Figure 120) contains two bodies connected together with a cylindrical joint. The upper body connects to the top mobile plate using a universal joint, and the lower body connects to the base plate using a second universal joint.

Linear actuation of the platform is accomplished by varying the lengths of the legs. To move the legs, we use Simulink-PS convertor block, which converts the Simulink input signal to a physical signal. This convertor is used to control the translational degree of freedom of the cylindrical joint. (The rotational degree of freedom is unconstrained). A force signal will be created and used for actuation, rather than using the displacement. This enables us to create a more realistic model of the platform. PS-Simulink convertor, which converts the input Physical Signal to a Simulink output signal, is also used for sensing the length of the leg. The PS-Simulink convertor is used to extract the position and velocity, which will be used by the controller.
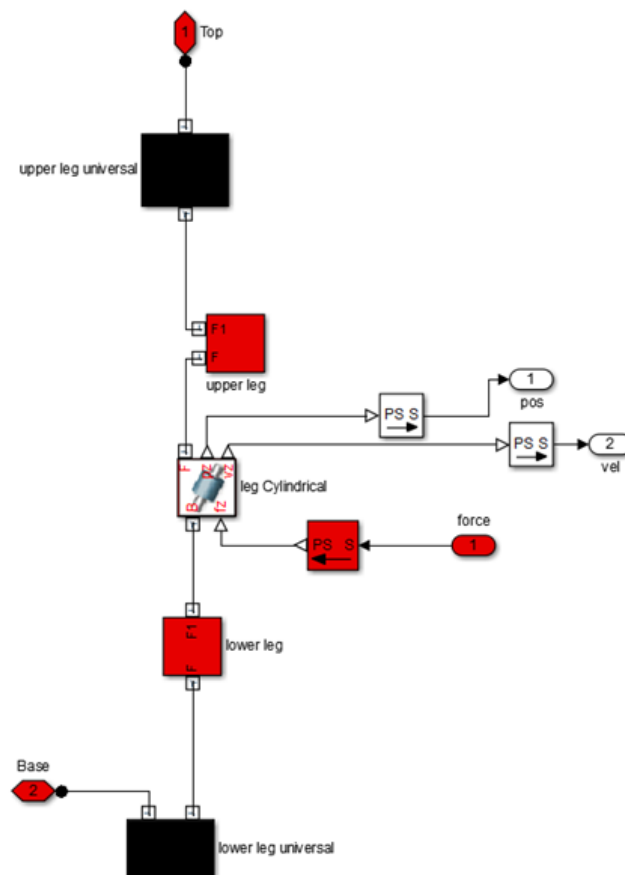
Figure 120: Leg subsystem. The upper and lower legs are connected to the top and base respectively, via universal joints. These two legs were connected to each other via cylindrical joint.

6.4.2   Modelling the Controller

The basic goal of the controller is to specify the desired trajectory of the top plate in both position and orientation. The desired trajectory to the corresponding trajectory in the legs is then mapped using inverse kinematics. Finally, a PID (proportional-integrator-derivative) controller was used for each leg to command the leg to follow the desired trajectory. In this way, we calculate the leg lengths given the position and orientation of the end effector (top plate).

In order to control the robots for desired motions kinematic and dynamic equations of the system should be known. Firstly, the inverse kinematic solution is computed. It is needed to find leg lengths to move the moving platform to its desired position and orientation according to fixed platform (inverse kinematics). The Simulink model of the inverse kinematics of the surgical platform is shown in Figure 121.
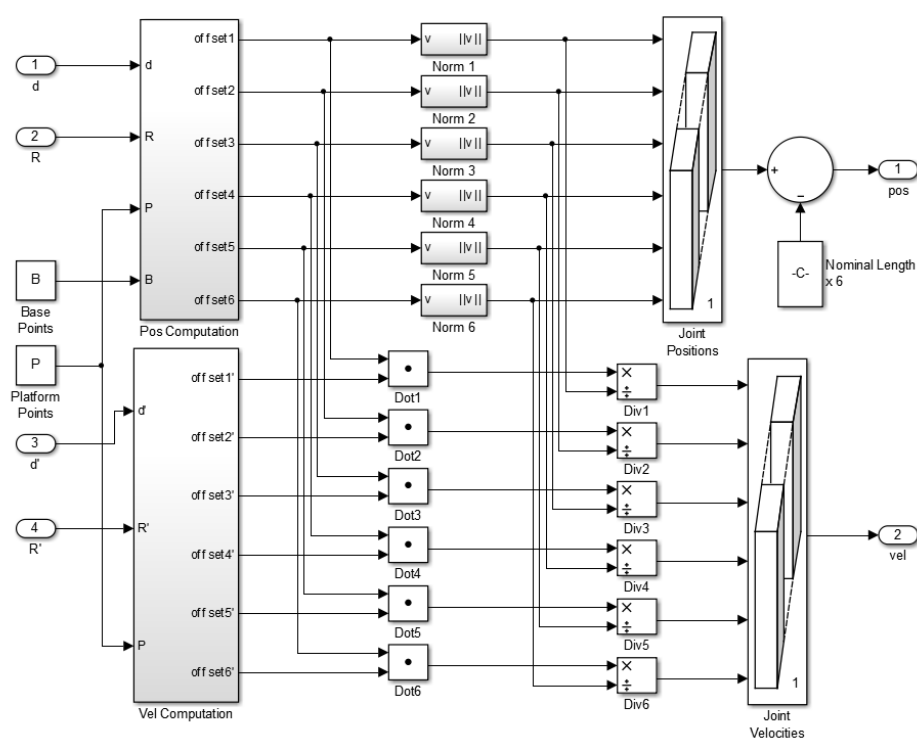
Figure 121: The Simulink model of the inverse kinematics of the surgical platform. Given a desired dynamic state of a platform manipulator specified by a 3-D rigid transformation from the mobile frame to the base reference frame, and the first time derivative of this transformation, this block computes the positions and velocities of the prismatic primitives of the six cylindrical leg joints necessary to achieve the desired dynamic state. (Image source: J.Wendlandt (146))

The control system consists of two sections: the leg trajectory and the PID controller. The leg trajectory generates the desired leg lengths for each time step. It starts with a desired rotation and position of the top plate and calculates the desired leg lengths to achieve this.

I.   Trajectory Generation

The leg trajectory generates the desired leg lengths for each time step. It starts with a desired rotation and position of the top plate and calculates the desired leg lengths to achieve this.

For step inputs, the leg lengths obtained from inverse kinematics solution input to an independent position control system for each motor. This movement is defined in the joint space. In order to move the robot along a straight line, a trajectory-planning algorithm is developed. Thus, it can be determined a start and stop times of the motion besides desired position and orientation inputs.

The set of Simulink blocks generates a reference trajectory in terms of linear position and three orientation angles, as a function of time is illustrated in Figure 122. The reference trajectory provided uses sinusoidal functions of time to define the rotational and translational degrees of freedom. Whatever comes out of the Top Plate Reference, the subsystem Leg Reference Trajectory assumes the translational position/three-angle form for the top plate. The rest of the Leg Reference Trajectory subsystem transforms these 6 DOF's into the equivalent set of 6 DOF's expressed as the lengths of the six platform legs. The reference trajectory output of the subsystem is a six-vector of these leg lengths.
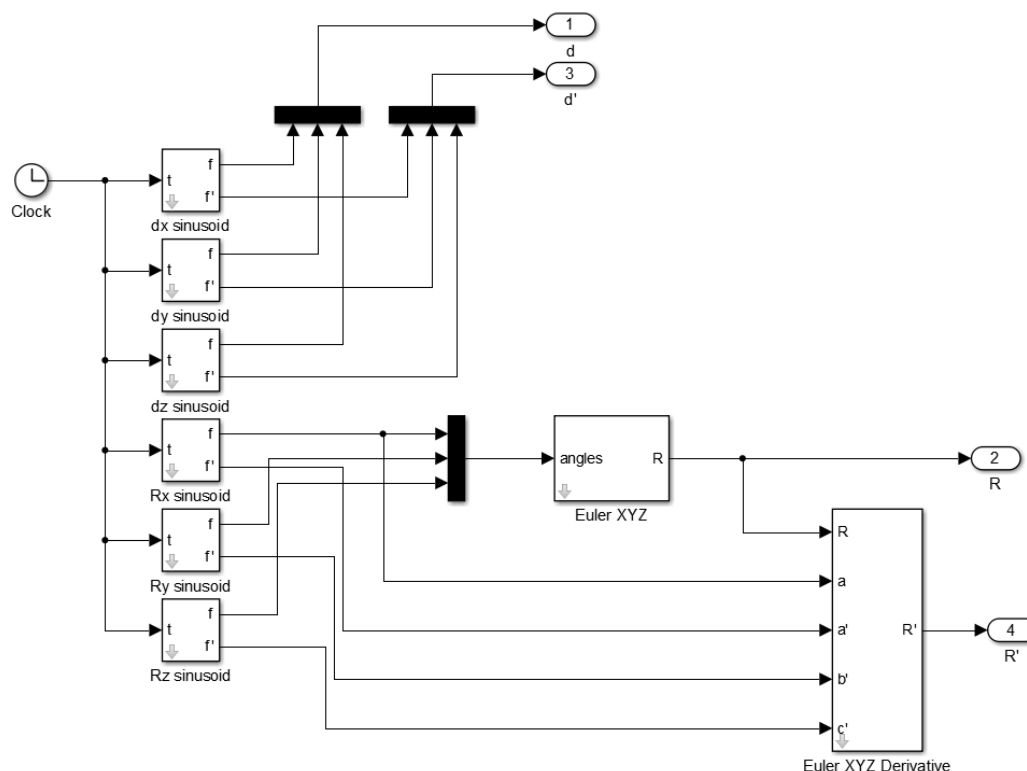
Figure 122: The reference trajectory provided uses sinusoidal functions of time to define the rotational and translational degrees of freedom. The rest of the Leg Reference Trajectory subsystem transforms these six degrees of freedom (DoFs) into the equivalent set of six DoFs expressed as the lengths of the six platform legs. The reference trajectory output of the subsystem is a six-vector of these leg lengths. (Image source: J.Wendlandt (146))

The actuating force on leg r is a function of the motion error. The error requires finding the instantaneous length of each leg from the positions of that leg's top and bottom connection points. The motion error is the difference of the desired or reference length of the leg and its instantaneous or actual length:

$$Error = E_r = reference\ length\ of\ leg - actual\ length\ of\ leg$$
$$= L_{traj,r}^{(t)} - \left| (R.P_{t,r}) - P_{b,r} \right|$$

The reference length $L_{traj}(t)$ is given as a function of time by the output of the Leg Reference Trajectory subsystem. The vectors $p_{t,r}$ and $p_{b,r}$ are defined in Figure 123. The orthogonal rotation matrix R specifies the orientation of the top plate with respect to the bottom.
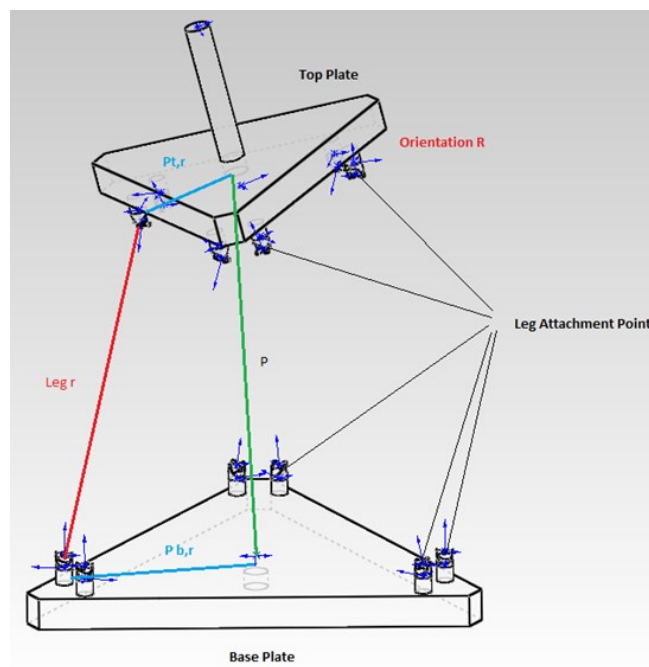
Figure 123: Defining the length of the platform leg

II.   PID (Proportional-Integrator-Derivative) Controller

PID control is one of the classical control methods and widely used in the industrial applications. The difference between the set point and the actual output is represented by the e (t) error signal.

In this modelling, the surgical platform model uses a simple *PID* controller (Figure 124) and Joint Sensor blocks to measure motion. The simplest implementation of trajectory control is

to apply forces to the plant proportional to the motion error. *PID* feedback is a common form of linear control.

A PID control law is a linear combination of a variable detected by a sensor, its time integral, and its first derivative. This robot platform's PID controller uses the leg position errors E_r and their integrals and velocities. The control law for each leg r has the form:

$$F_{act,r} = K_p E_r + K_i \int_0^t E_r \, dt + K_d (dE_r/dt)$$

The controller applies the actuating force $F_{act,r}$ along the leg. The proportional, integral, and derivative terms tend to make the legs' top attachment points $P_{t,r}$ follow the reference trajectories by suppressing the motion error.
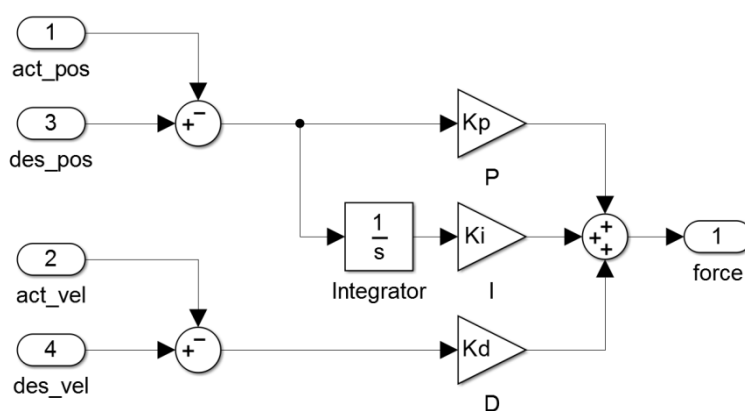
Figure 124: Simple PID controller. The input to this controller is the actual leg position and velocity and the desired leg position. Then an error is formed in the position and a force based on the gain and integral of the error is created. (Image source: J. Wendlandt (146))

6.4.3   Output Data (Workspace)

The output data on the behaviour of the surgical platform system are obtained graphically and numerically and displayed in the MATLAB workspace via position sensor block (Figure 125). This block contains sensors that sense the position of the X, Y, and Z of the end effector.
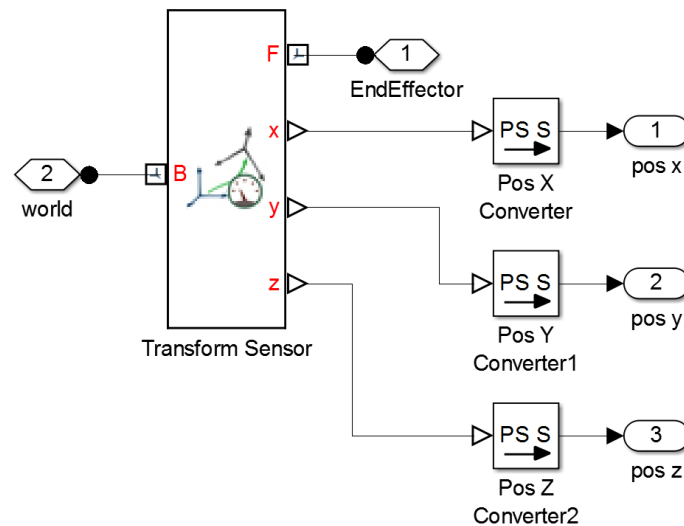
Figure 125: Position sensor measures the time-dependent relationship between two frames. A transform sensor senses this 3-D varying transformation, and its derivatives, between the two frames. (Image source: J.Wendlandt (146))

6.4.4   Simulation and Data Analysis of the Surgical Platform System

After modelling the surgical platform system with Simulink, SimMechanics, and SolidWorks, the design of the surgical platform is validated by simulating the system. Selecting Simulink and Start initiated the simulation in the model menu bar. Immediately after starting the simulation, the graphical representation of the platform is shown in MATLAB mechanical explorer, which is replicating the platform that is built into SolidWorks (Figure 126).
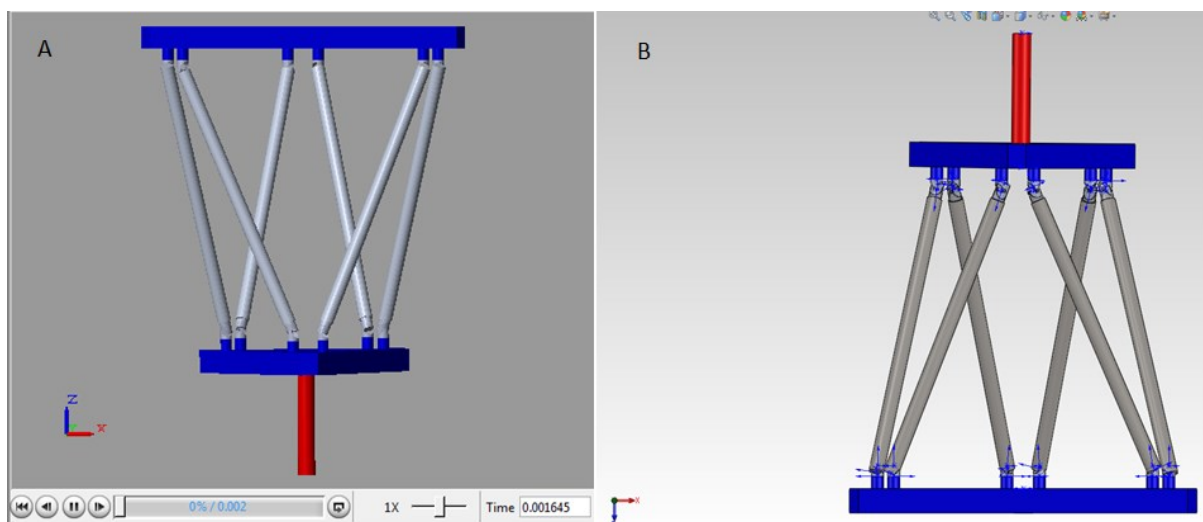
Figure 126: The graphical representation of the surgical platform in (A) MATLAB mechanical explorer, and (B) SolidWorks

During the simulation, we can view signals with the Scope block. Figure 127 shows the x, y, and z values of the position of the Body block representing the end effector moving over time as the model simulates.
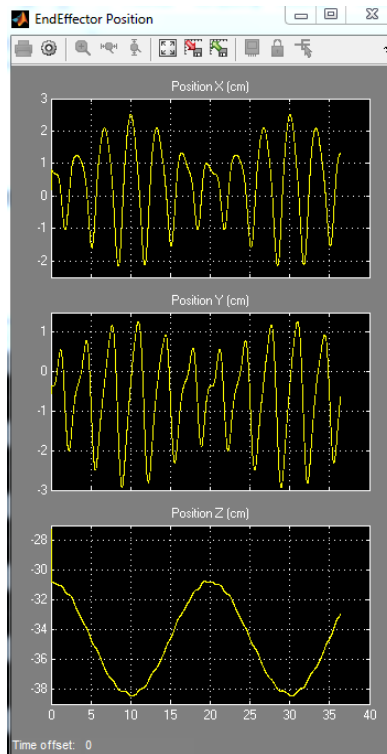
Figure 127: The platform's end effector position displayed by the scope block. The figure shows the position of the end effector as a function of time

The numerical data of the end effector position (X, Y, and Z) obtained in MATLAB workspace variables is used to plot a 2-D/3-D representation of the end effector path (Figure 128) and volume (Figure 129).
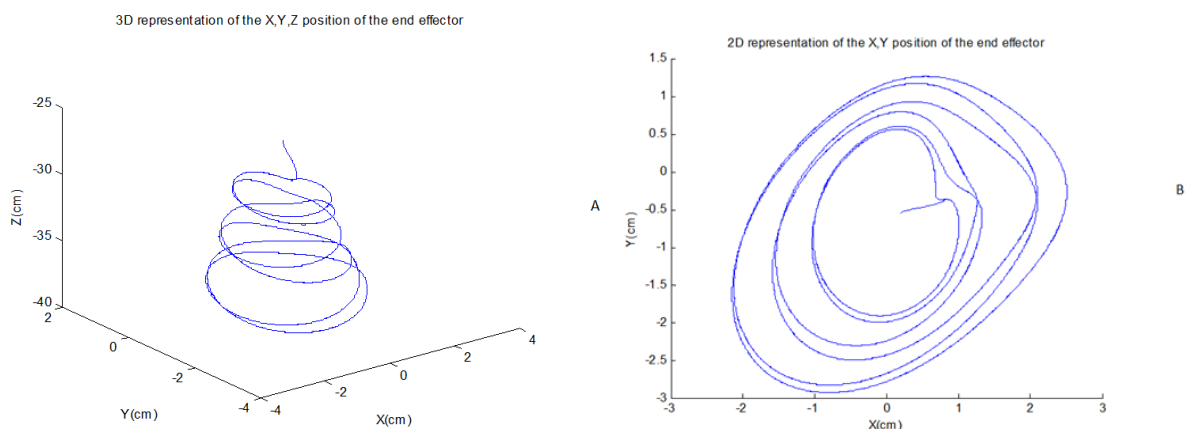
Figure 128: A plot representing the end effector path in A) 3D and B) 2D
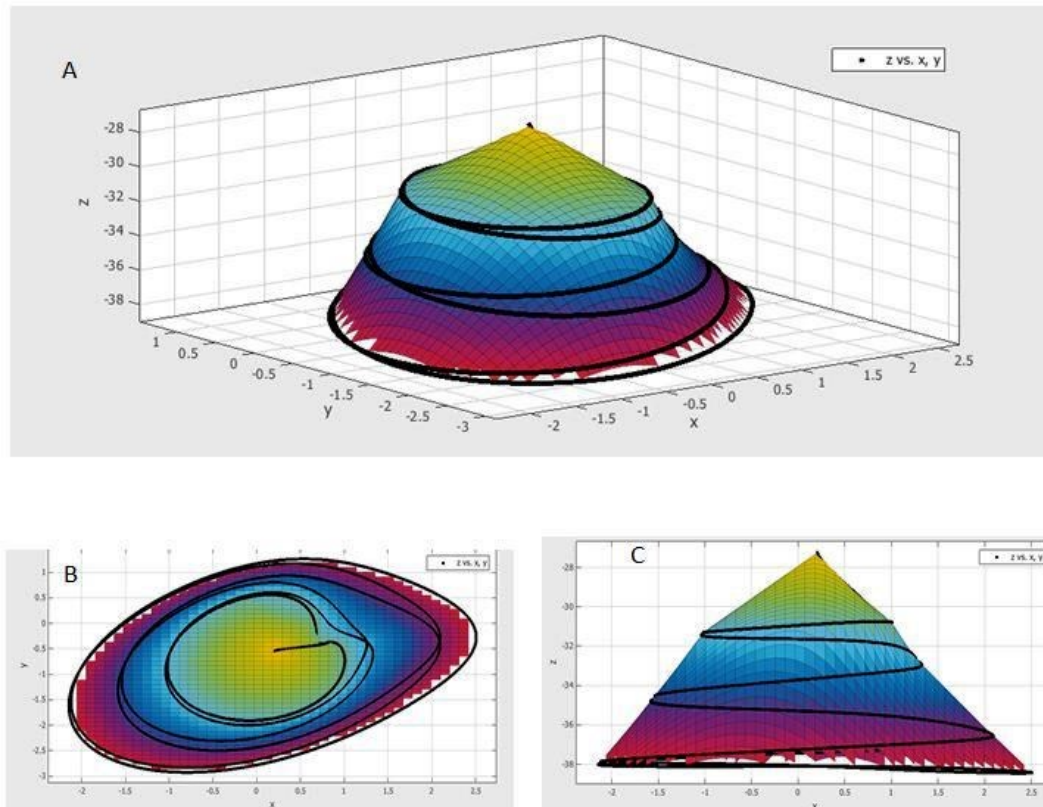
Figure 129: Plot representing the end effector volume in A- 3D, B- 2D (x, y view), and C- 2D (x, z view)

6.4   Discussion and Conclusion

In chapter 2, the benefits of the integration of robots with surgical tools have been discussed. This combination has added many benefits to the operating theatre by supporting the surgeon during challenging, complicated procedures. These include increased accuracy, stability, and repeatability. These advantages are the main reasons behind implementing a robot to our surgical flexible tool.

Because of the 'powered' nature of our flexible surgical tool, by means of either mechanical drill or fluid high-pressure pump, the handheld use of the tool is prone to vibration and fluid impact force. Consequently, this leads to control difficulties during critical operation procedures. Hence, implementing a robot was vital to ensure a safely performed surgical task by increasing the stability and, therefore, the accuracy of the tool.

Within the different robot structures, there are also advantages and disadvantages that determine the suitability of a certain robot structure for a particular task. The high accuracy and stability of a parallel robot performing in a small workspace led to it being designed,

manufactured, and integrated into our flexible surgical device, as it is the most suitable robot for our surgical application.

Principles of designing the surgical robot were adopted from a *Form Changing Structure* designed by *Paul Harkin*, our technical collaborator. The original design that was comprised of multiple extensible links, with each containing three telescopic tubes powered by a DC motor assembled at the centre of the link, was substantially re-designed to be more appropriate for our application. Modification/ re-designing and development has turned this form changing structure into a parallel platform with a fixed top and mobile base, connected via six extensible legs, each comprising two telescopic tubes powered by a DC motor that was attached to one end. The re-designing process has simplified the structure so it can be installed in an operating theatre and can be controlled remotely.

Designing a flexible probe with multi-DoFs is generally complicated, in terms of mechanical constructions, and increases the size and instability of the probe. Instead, implementing the parallel robot has added 6 DoFs to the tool's 2 DoFs. These 8 DoFs produce a workspace that has access all around the spinal column, with a less complicated and more stable tool. In addition, assembling the entire robot into a portable rigid structure that can be positioned at any point along the principal axes of the spinal column gives the tool more freedom to be close to the surgical area no matter where the cancerous tumour appears.

The robot platform built using high-speed geared DC motors, coupled to a lead screw mechanism via spur gears, to extend and retract the platform's legs. While cost effective, the DC motors are inadequate in actuating the lengths of the legs in a timely manner. This gives rise to many problems related to controlling the movement of the tool, as we will see in chapter 7. Instead of DC motors, pneumatics or linear actuators could be used. These actuators have desirable response times and may still deliver sufficient accuracy and holding torque for the surgical application. Furthermore, the robot should be encased in a fitted polymer jacket to protect the electrical components during operation. The jacket can be disposed after every operation and the probe can be autoclaved post-op to ensure that no cross contamination occurs.

An initial modelling of the parallel platform using solid works in conjunction with MATLAB SimMechanics and Simulink has established primary principles of the behaviour of the robot and the control system.

In vitro examining the positioning and actuating the surgical flexible probe around the spinal column has shown the positioning and guide capabilities of using the robot platform. This was compared to the use of a rigid tool, which is presently applied in operating theatre for the application of spinal surgeries. The test shows the amount of cancerous tissue that could be removed using either tool. It was demonstrated that using the flexible probe could remove most of the tissue at the interior side of the spinal column while using a rigid tool could result in most of the tissue remaining in the position.

7 Flexible Surgical Robot System: Control and Haptic Feedback

7.1 Introduction

As technology progresses, the field of medical robotics seems more and more promising, with a lot of work being done towards implementing robots in the surgical theatre (Chapter 1). Robot-assisted surgery promises greater dexterity and higher accuracy by minimising human error and invoking countless other methods of surgery, which are enabled by the incorporation of the processing power of a computer. Surgical robots are primed to increase the rate of success of surgery through increased fidelity, hence minimizing trauma to the patient, but it is postulated that there is limited clinical success due to the lack of force and tactile feedback presented to the surgeon [147]. It is found that surgeons using robotic surgical probes to operate find that the absence of feedback eliminates tactile cues, masks force cues and, in some cases, leads to an increase in intra-operative injury [148, 149]. Hence, it is clear that the widespread adoption of surgical robots will only be possible if a solution is found to arguably the biggest problem with surgical-robotics, the absence of touch.

Generally haptic technology or haptics is defined as simulated touch interactions between robots, humans, and real, remote, or simulated environments [150]. In the context of surgery, the absence of the surgeon's ability to feel the surgical environment via robots is the greatest complication that prevents the widespread use of the surgical robot. The haptic technology aims at addressing this problem by enabling robots to generate *kinaesthetic* (force) and *cutaneous* (tactile) feedback for the user.

Kinaesthetic haptic is defined as a form of sensory substitution whereby a robot generates force feedback simulating touch interactions with the patient, transmitting critical information about the surgical environment to the surgeon and thereby assisting him in performing a specific surgery using a robotic manipulator safely and successfully. Kinaesthetic haptic positional feedback control will henceforth be referred to simply as "*haptic feedback*". The haptic feedback scheme will be implemented on two fronts: guidance constraints and regional constraints. Guidance constraints refer to the process of generating force feedbacks in a

pattern to guide the user through a predetermined path. Applications of this technique, to assist surgeons in navigating robotic surgical probes along convoluted pathways inside the human body (now commonly being done with the use of passive control), imposes many limitations on the effectiveness of the surgery. Regional constraints refer to restricting of the position of the surgical probe to only operate within a predefined active space. This is important in constraining the degree of motion of the probe within the surgical environment and to avoid causing accidental damage to the patient through over-actuation.

The work of this chapter was carried out with the contribution of *J. Chan*, an undergraduate student in the Mechanical Engineering Department at Imperial College London.

The overall goal of this chapter is to develop and test a working positional control structure that incorporates haptic technology in a flexible surgical robot (designed and fabricated in chapter 6). The target surgery that is used as an example in this analysis is an operation on the lower lumbar vertebrae.

7.2   Overview

The word haptic was first introduced by psychophysicists in the early 20th century to describe their studies of human touch-based perception and manipulation [151]. In robotics, significant research work began in the 1970s and 1980s focusing on manipulation and perception by touch [152]. In the early 1990s, computer haptics began to emerge, just as computer graphics enables the display of simulated objects to humans in an interactive manner. This followed by the instigation of a haptic interface, in which the information is presented by exerting controlled forces on the human hand.

The theory of active constraints was first considered by *B. Davies* of *Imperial College London* as an aid to safety, during the development of a robot for a prostatectomy resection that was first clinically applied in April 1991[153]. This '*mechanical*' constraint was further developed to provide accuracy and motion constraint for orthopaedic knee replacement surgery. Three zones were defined for bone resection (Figure 130). In the safe zone *I*, the active constraint robot is designed to be moved freely by an operator. When the cutter is moved towards the cutting boundary and enters the transition zone *II*, the power of the motors is switched on to provide motion constraint for the cutter. In this case, the active constraint control sets the stationary position command in the direction of the normal, in an outward

direction towards the boundary. This control concept is similar to that of an active robot that prevents the cutter from entering the forbidden zone *III*.
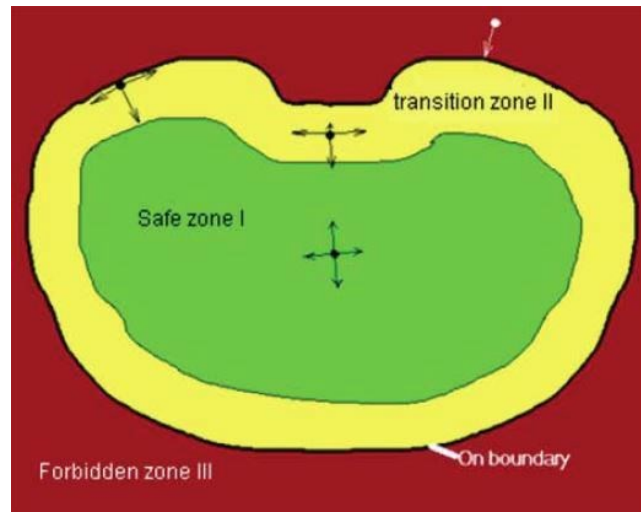
Figure 130: Constraint zones defined for bone resection by B. Davis. The tool is allowed to move freely by the operator within the safe zone. At the transition zone the motion will be constrained as the tool moved towards the boundary were the active constraint control sets the stationary position command. (Image source: B. Davis (153))

A useful example of constrained control in surgical assistant robots is explained and documented by *A. Kapoor, et al.* at the *Johns Hopkins University* [154]. In their report, the team identified five basic geometric constraints that are relevant to surgical robots: stay on a point, maintain a direction, prevent plane-penetrating, move along a line and rotate around a line. Complex linear and non-linear optimisations were compared and contrasted about accuracy and loop-time performance. The group also highlighted the usefulness of implementing constraint regions depending on the surgical task as illustrated in Figure 131.
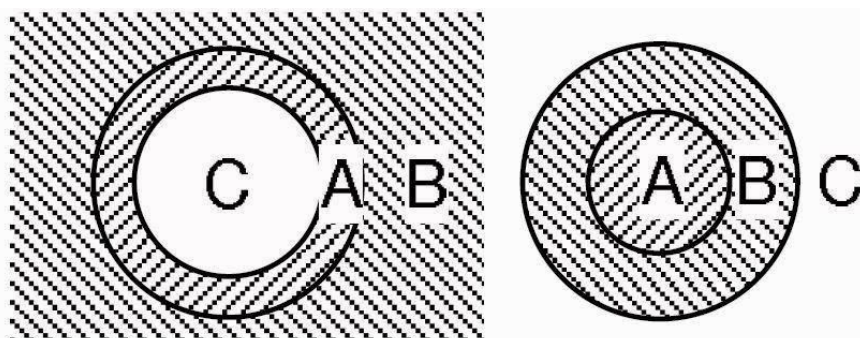
Figure 131: Constraint regions depending on surgical task: A- Preferred region, B- Safety region, C- Forbidden region. (Image source: A. Kapoor, et al. (154))

An example of regional constraint haptic implementation is presented by *M. Scheint et al.* [155] where a study of invariance control in trajectory supervision and haptic rendering was conducted. In their paper, three different methods of collision avoidance were highlighted: the virtual force method [156], escape velocities [157], and artificial potential fields [158]. In

this paper, invariant control was implemented to assist in trajectory guidance and haptic rendering.

The kinematics and dynamics of 6 DoFs platforms have been extensively covered by many researchers [110, 112, 113, 116, 118], and others. These papers discussed the various methods used to determine solutions to forward-kinematics, inverse-kinematics and dynamic system loading problems associated with the *Stewart* platform type robot. *Lagrange* formalism and the *Newton-Euler* method appear to be the most common methods adopted to formulate a solution [159]. Various methods were used to solve the kinematics of the parallel robots such as tetrahedron approach [160], and the exact algebraic method [161].

Most of these methods, however, induce a very large computational burden on the system and questions have been raised as to their suitability in the real-time implementation. Alternative methods incorporating simplifying assumptions that greatly reduce the computational load have been explored. *S. Lee, et al.* [162] found that since the Stewart platform has a relatively small workspace it was possible to approximate the coefficient matrixes of the dynamic equations to be constant. This introduced a small modelling error of about 10% while successfully reducing the computational load significantly. However, oversimplification of the system could lead to large errors and invalid results.

There has been extensive research done on the implementation of kinaesthetic haptics and the formulation of kinematic solutions to the Stewart platform type. However, there have been limited studies done in the context of the haptic control of flexible surgical probes incorporating positional actuation via a Stewart platform type robot, as is the case in the project, which is the main subject of this thesis. Hence, this chapter aims to borrow promising ideas from similar, more studied applications and work to augment, make relevant, and implement these ideas in our target application.

7.3   Methods and Methodology

This section aims to detail and discuss the methods and preferred methodology adopted in this project, in order to develop and test a working positional control structure that incorporates haptic technology in a flexible surgical robot. Having conducted a thorough literature review, it was found that although there were not any studies done specifically on flexible surgical probes incorporating kinaesthetic haptic feedback, there was a small amount of work done on each separate component of the project. Hence, it was decided to adopt the

techniques and approaches that seemed most promising in all the literature, and incorporate them, to as far an extent as it was practical, into the experiment. The necessary resources used in this chapter will be described. This will include all hardware, software, software add-ons, plug-ins and, finally, the coding that was used.

7.3.1 System Hardware

I. Parallel manipulator with *6 DoFs*

The project developed and constructed a 6 DoFs 3-3 parallel robot platform. Details of the robot platform can be found in Chapter 6.

II. Flexible Articulating Surgical Probe

This is the end effector in the system and is fixed to the mobile plate of the *6 DoFs* Platform. The flexible surgical probe is the only part of the machine that is designed to enter the human body during surgery. It is the operating point and has a functional head attached to it. Details of the Flexible Articulating Surgical Probe can be found in Chapter 4.

III. Haptic Enabled Controller

Kinaesthetic haptics (force feedback) is generated on the user-side controller through the implementation of the 3 DoFs Novint Falcon [163] haptic enabled controller. There was then a need to obtain an additional 3 DOFs inputs from a separate device since the Novint Falcon only inputs 3 DoFs.
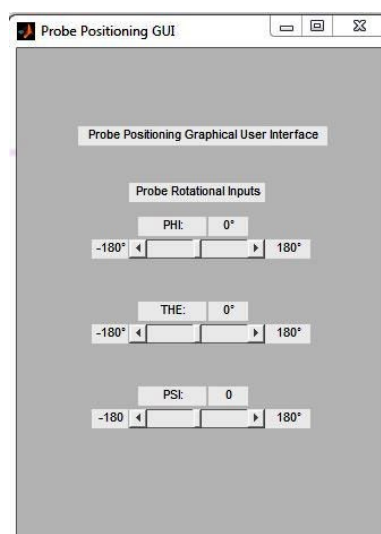
Figure 132: Screen capture of the probe positioning GUI that constructed to control the probe's rotational inputs

To solve this issue, a Graphical User Interface (GUI) was generated in MATLAB to control the three rotational input values, leaving the Novint to control the three translational inputs. This developed GUI is shown in Figure 132.

Through this, we were able to fully control 6 DoFs of the robot manipulator. The Novint Falcon consists of three arms, positioned equidistant from each other, to collect positional coordinate inputs. Each arm is also connected to a force generating motor. The software is then used to mimic forces through these motors, evoking the sense of touch in the user's hand. The controller also features four programmable buttons, which can be set to operate specific features of the robot.

IV.   Microcontroller and Associated Electrical Driver Circuits

An *Arduino Mega 2560 Rev 3* microcontroller was used to control all electrical components in this system. Coding for this microcontroller is done in Arduino language, which is based on C/C++. Three L293 motor integrated circuits (IC) are used to drive the single DC motors attached to each of the six platform legs. Further rotary encoders were connected to each of the six motors via a custom-made adapter provide positional feedback information regarding each leg (Figure 133-left). A single ULN2003a transistor array was used to control a unipolar stepper motor, which was connected to the flexible probe (Figure 133-right). A computer was used to run MATLAB, which served as the main processor in the setup.
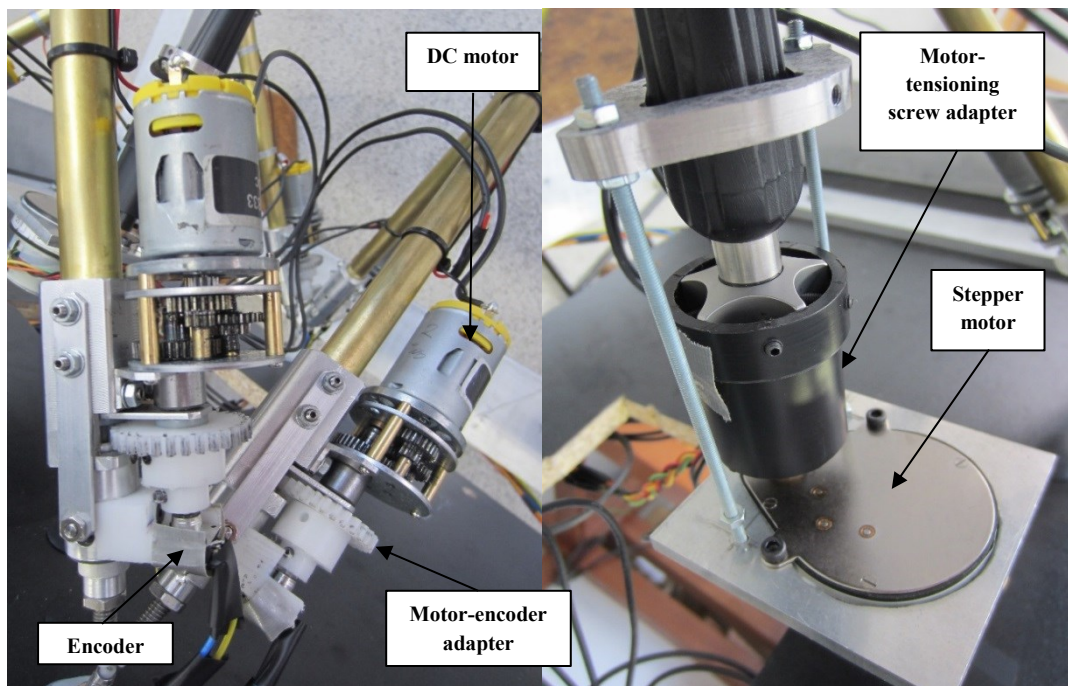
Figure 133: The installed motor-encoder units on the platform legs via motor-encoder adapter (left). The stepper motor attachment to the probe tensioning screw via motor-tensioning screw adapter (right)

7.3.2 System Software

I.   *Arduino IDE*

The *Arduino IDE* software allows the user to program, compile and upload C/C++ code onto an Arduino microcontroller. The *Arduino Mega 2560 Rev 3* used in this project is programmed using this software.

II.   **MATLAB R2013a**

Calculating the kinematics of the robot platform required quite significant computational power. Hence, it was necessary to include a computer in the system, running MATLAB software.

III.   *Novint Falcon* **Driver**

The haptic enabled controller, the Novint Falcon, reproduces forces through the controller to mimic the virtual environment. The computer determines the magnitudes and orientations of the forces reproduced by the controller. This set of drivers provided by *Novint Technologies Inc*. allows the computer to converse with the hardware.

IV.   *SIRSLAB Haptik* **Library**

Siena Robotics and Systems Lab group developed a very useful haptic library that can be used with a large array of haptic devices including the Novint Falcon. This library, "*Haptik Library*", acts as a hardware abstraction layer and successfully provides uniform access to haptic devices. The software is written in C++, which can be used with MATLAB and Simulink. This serves to enable programming of the Novint Falcon through MATLAB.

7.4   Position Control – Robot Manipulator

The Novint Falcon Haptic-Enabled Device controller allows user inputs of up to 3 DoFs and enables mechanical force-feedback to pass back to the user. The structure of the code used to process this user input into meaningful motion of the platform is shown in Figure 134 and was written in MATLAB. The program logic starts with defining global variables, assigning input, and output pins. After that, the main loop is started where the program continues to read the positional input from the Novint Falcon and controls the motors to adjust the six respective leg lengths, making them shorter or longer as necessary, to achieve the desired position of the end effector. The program using a formula based on inverse kinematics,

making use of the rotational matrix and positional matrix, calculates the target length of each leg. A feedback loop is created within the position control using six encoders, one on each leg. A home flag is used to datum the legs at the start of the program so that the program registers the initial position of the base. The length of each of the six legs of the platform is then represented by the readings of the encoder relative to this home position value.

To operate the water jet/operational head on the surgical device, the user will only have to press a button on the controller. A separate button was also programmed to control the amount of curvature of the surgical device. It was apparent that it was necessary to establish a link between the Novint Falcon and MATLAB and then onto the Arduino platform. This was achieved using a series of serial communication, bridging codes and plugins as detailed in Section 7.3.2. Implementing this resulted in the formation of a functional link which allows for seamless communication transcending, the various platforms.
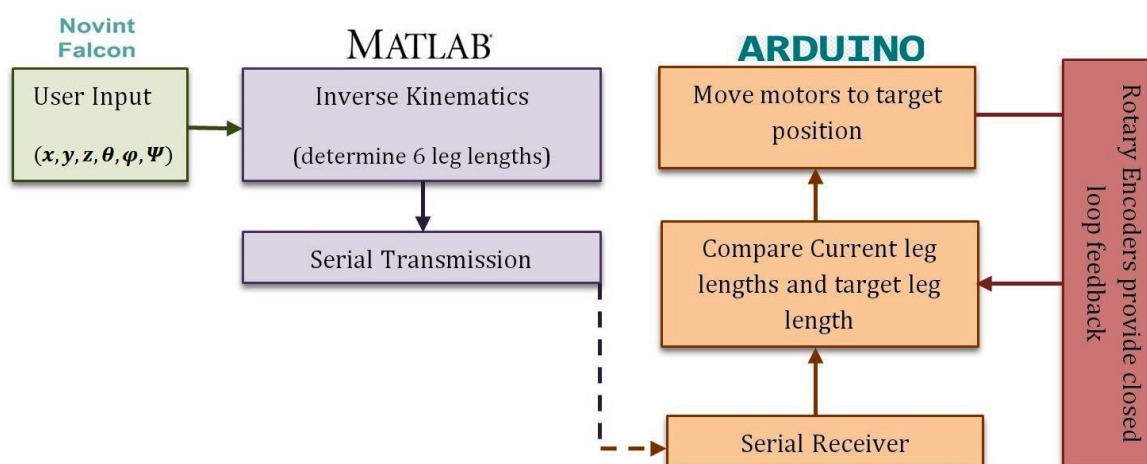
Figure 134: Code structure used to process the user input (Novint Falcon) into meaningful motion of the robot platform. Global variables defined by the user input are sent to the PC running MATLAB, which is used to determine the length of the six legs. The Arduino board is implemented to control the output functions of the system.

7.4.1 Inverse Kinematics

As illustrated in the positional control loop logic discussed in Section 7.4, the position of the end-effector is specified by the input controller. In this case, the user specifies the orientation and position of the flexible probe in 6 DoFs. It is then necessary to calculate the required leg lengths of each of the six platform legs in order for the Stewart platform to impose the desired orientation of its end-effector. This backwards calculation is known as inverse kinematics. Based on the studied literature [117, 159], it was possible to formulate the inverse kinematic relations for the 3-3 Stewart platform which was built. What follows will be a brief

description of the *Euler's* equations used to solve this system. For convenience, the important notations used here are presented in Table 6.

Table 6: Description of the notations used in the calculation of the inverse kinematics

Symbol	Physical Description
φ	Rotation about X-axis
θ	Rotation about Y-axis
Ψ	Rotation about Z-axis
R	Rotational matrix
P_i	Attachment point of leg i in the top plate
P	Position of the top plate relative to the base plate
B_i	Attachment point of leg i in the base plate
L_i	Nominal length of leg i

The configuration of a 3-3 robot platform can be seen in Figure 135. There are a total of six pairs of concentric spherical joints; three on the top $B_1=B_6$, $B_2=B_3$, and $B_4=B_5$ and three on the end effector $P_1=P_2$, $P_3=P_4$ and $P_5=P_6$. In order to progress further into the analysis, it is important to define two separate coordinate systems; the fixed Cartesian coordinate system X, Y and Z which are attached to the base and has its origin at the centre of the base, and the end-effector coordinates system x, y and z attached to the end-effector with its origin located at the geometric centre of the top plate.
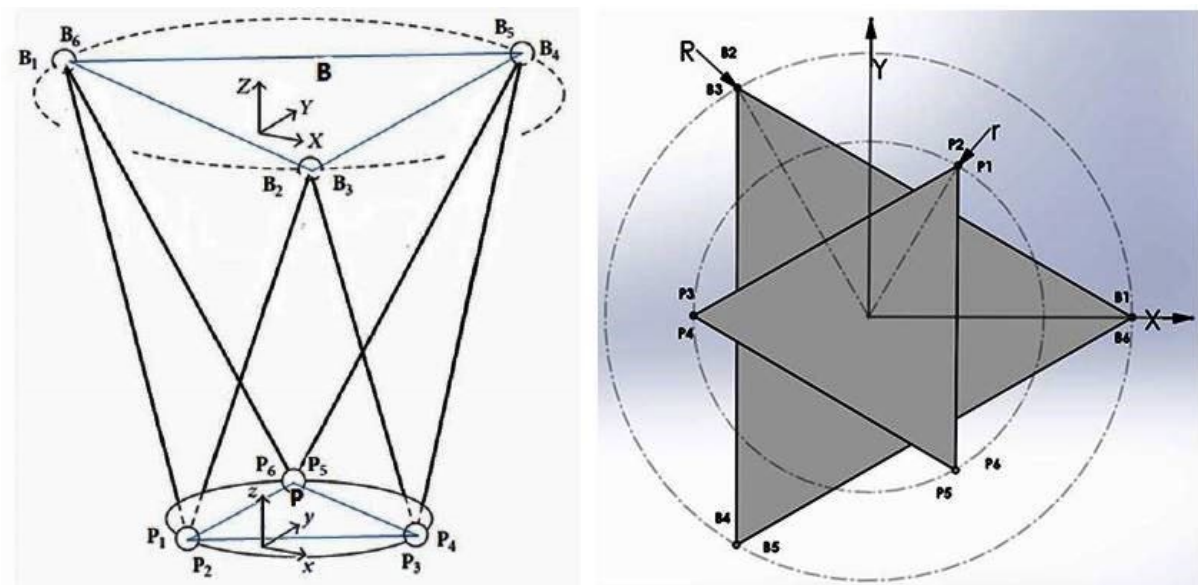
Figure 135: Diagram of a 3-3 robot platform. Isometric view (left) and plan view (right) shows the attachment points of the six links to the fixed top (B) and to the moving platform (P).

The position of the end-effector is denoted by P and given by the expression:

$$P = \begin{bmatrix} x \\ y \\ z \end{bmatrix} \tag{7.1}$$

The orientation of the end-effector can be denoted by using the *Euler* representation which is, in simple terms, three successive relative rotations: rotation of angle φ about the *X*-axis, rotation of angle θ about the *Y*-axis, and rotation of angle Ψ about the *Z*-axis. The overall rotational matrix R can be expressed by the multiplication of the above three basic rotation matrices.

$$R = R_Z(\Psi)R_Y(\theta)R_X(\varphi)$$

$$R = \begin{bmatrix} \cos\Psi & -\sin\Psi & 0 \\ \sin\Psi & \cos\Psi & 0 \\ 0 & 0 & 1 \end{bmatrix} \begin{bmatrix} \cos\theta & 0 & \sin\theta \\ 0 & 1 & 0 \\ -\sin\theta & 0 & \cos\theta \end{bmatrix} \begin{bmatrix} 1 & 0 & 0 \\ 0 & \cos\varphi & -\sin\varphi \\ 0 & \sin\varphi & \cos\varphi \end{bmatrix}$$

$$R = \begin{bmatrix} \cos\Psi\cos\theta & -\sin\Psi\cos\varphi + \cos\Psi\sin\theta\sin\varphi & \sin\Psi\sin\varphi + \cos\Psi\sin\theta\cos\varphi \\ \sin\Psi\cos\theta & \cos\Psi\cos\varphi + \sin\Psi\sin\theta\sin\varphi & -\cos\Psi\sin\varphi + \sin\Psi\sin\theta\cos\varphi \\ -\sin\theta & \cos\theta\sin\varphi & \cos\theta\cos\varphi \end{bmatrix} \tag{7.2}$$

It follows from the kinematics of each leg that the closed loop position vector equations are given by:

$$L_i = \begin{vmatrix} L_{ix} \\ L_{iy} \\ L_{iz} \end{vmatrix} = \|RP_i + P - B_i\| \tag{7.3}$$

Where P_i and B_i are given by the expressions:

$$P_i = \begin{bmatrix} P_{ix} \\ P_{iy} \\ P_{iz} \end{bmatrix} = \begin{bmatrix} r_p \cos(\lambda_i) \\ r_p \sin(\lambda_i) \\ 0 \end{bmatrix} \tag{7.4} \qquad B_i = \begin{bmatrix} B_{ix} \\ B_{iy} \\ B_{iz} \end{bmatrix} = \begin{bmatrix} r_B \cos(\Lambda_i) \\ r_B \cos(\Lambda_i) \\ 0 \end{bmatrix} \tag{7.5}$$

Where r_P and r_B are the radiuses of the points to the centre and λ_i and Λ_i are:

$$\lambda_i = \frac{(i-1)\pi}{3}, \qquad \Lambda_i = \frac{i\pi}{3}; \qquad for\ i = 1,3,5 \tag{7.6}$$

$$\lambda_i = \lambda_{i-1} + \frac{2\pi}{3}, \qquad \Lambda_i = \Lambda_{i-1}; \qquad for\ i = 2,4,6 \tag{7.7}$$

Solving Equation 7.3 using Equations 7.1, 2, 4, 5, 6 and 7 gives the nominal lengths for all six legs of the robot platform for any given input of $x, y, z, \varphi, \theta,$ and Ψ.

7.4.2 Simulation

In order to validate the inverse kinematics derived in the previous section, a simulation of the *HexaSlide* Manipulator type designed by *Merlet* and *Gosselin* [164] was created in MATLAB that simulated the movement of a 6 DoFs model receiving inputs from the Novint Falcon. The desired position (x, y, z) and orientation (φ, θ, Ψ) of the end-effector was specified and Equations 7.1-7 were used to calculate the nominal leg lengths of each of the six platform legs. The leg lengths were plotted in real-time on a 3-D model figure as can be seen in Figure 136. The simulation structure consists of three main subsections: the model construct, the graphical user interface (GUI) to initialise, and the draw function.
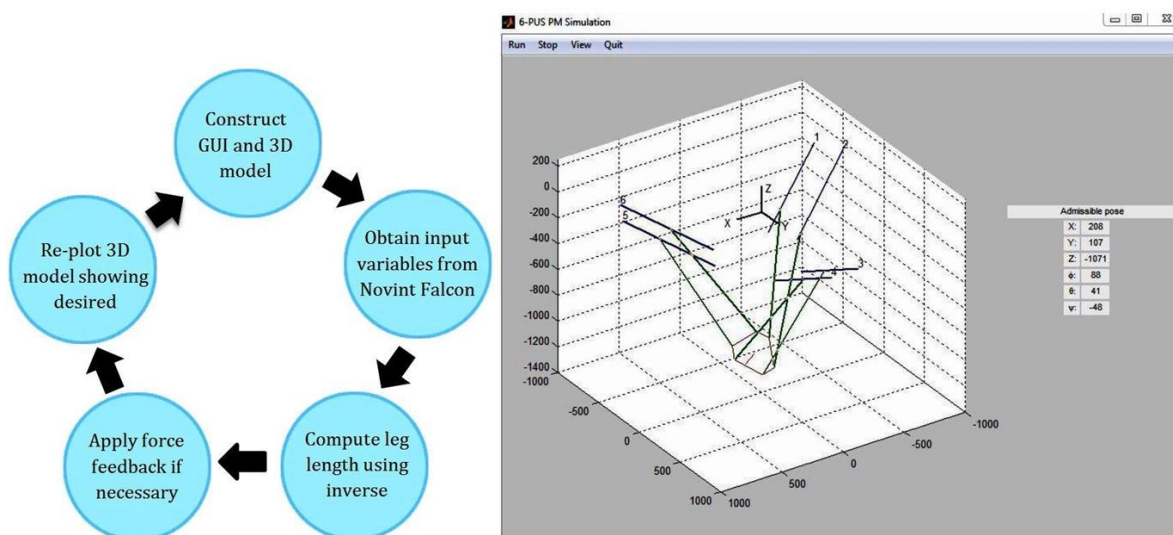
Figure 136: Logic flow chart of the simulation (left) and the resultant simulation of Stewart Platform displayed in MATLAB GUI (right)

The model construct script serves to initialise and create the figure. This involves defining the manipulator geometry including the tool, base and legs in a fixed coordinate system. The second script is the GUI initialise. Here, the on-screen user interface is created including a menu bar, labels and position values display the orientation and location of the end effector. The final script involved in this simulation is the draw function, which is the part of the code where MATLAB reads the input from the Novint Falcon and performs the inverse kinematics to obtain the six leg lengths. It then progresses to plot the updated legs on the figure to be displayed on the screen. The draw function runs in an infinite loop so as to continuously update the figure of the robot platform in real time until the simulation is closed. Regional

constraints were implemented by inducing force feedback when an inadmissible position is reached. As is common with all robot manipulators, there is a set workspace beyond which the robot will not be able to reach due to the physical limitations of the actuation and/or geometry of the robot. Thus, kinaesthetic haptics, or active constraints, are used to keep the user within a certain predefined spatial area, which is the robot platform's workspace.

7.4.3 Electronics

After constructing the robot platform in Chapter 6 and having done sufficient work in validating key ideas, this section will detail all electronics used along with the associated program code that implements full positional control of the platform.
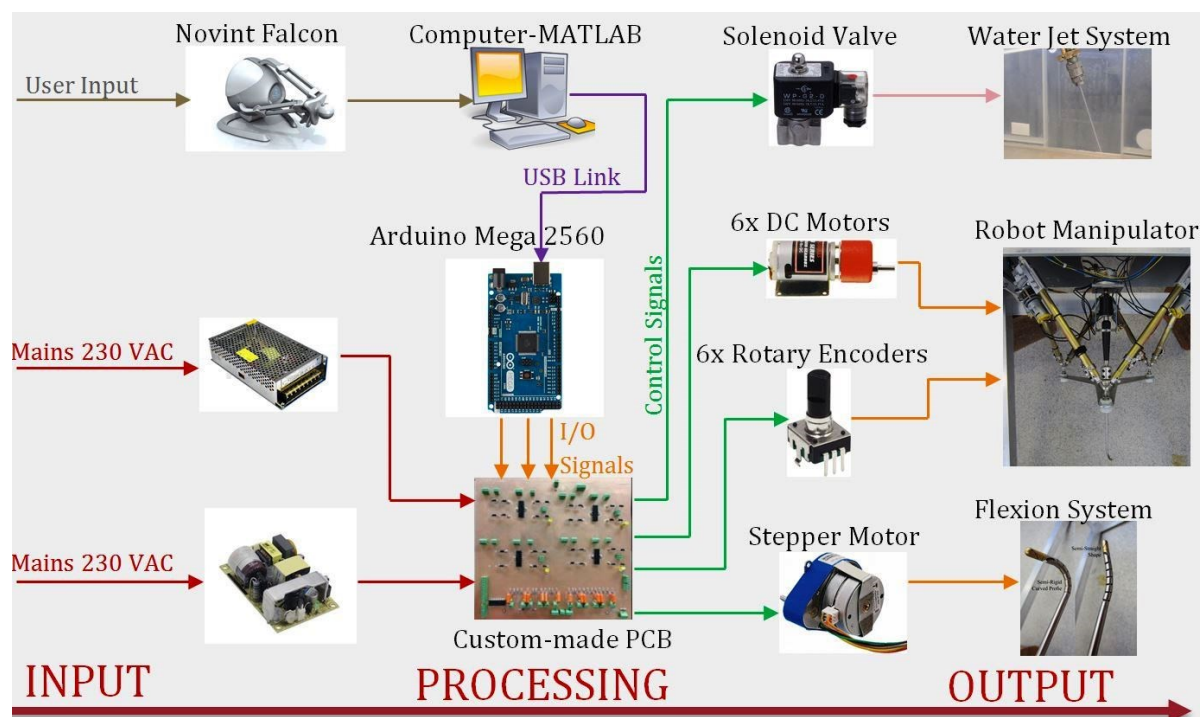
Figure 137: Component layout of the system. The system is separated into three main stages. Input stage is the supply of the user information and power to the system. All the calculations and control commands are determined at processing stage. The last stage is the system's output functions, these include: positioning of the probe, actuating the probe and operating the water jet unit.

I.   Electronic Components

The layout of the electronic components can be seen in Figure 137. The figure illustrates how each electronic component is connected, powered and controlled electronically from the input through to the output.

II.   Custom Built Printed Circuit Board (PCB)

The electronics are all connected to a central core, the PCB. Two PCBs were designed using DesignSpark PCB 5.0 and fabricated using Advanced Circuit Board Plotters (*LPKF*

ProtoMat S63). The first was made in the early stages of the project and served as a prototype board for testing, and the second board (Figure 138) was an improvement of the first incorporating additional circuits that helped consolidate the overall electronics onto a single board. The PCB is made up of four main circuits: the DC motor driver circuit, rotary encoder filter circuit, stepper motor control circuit, and water jet control unit.
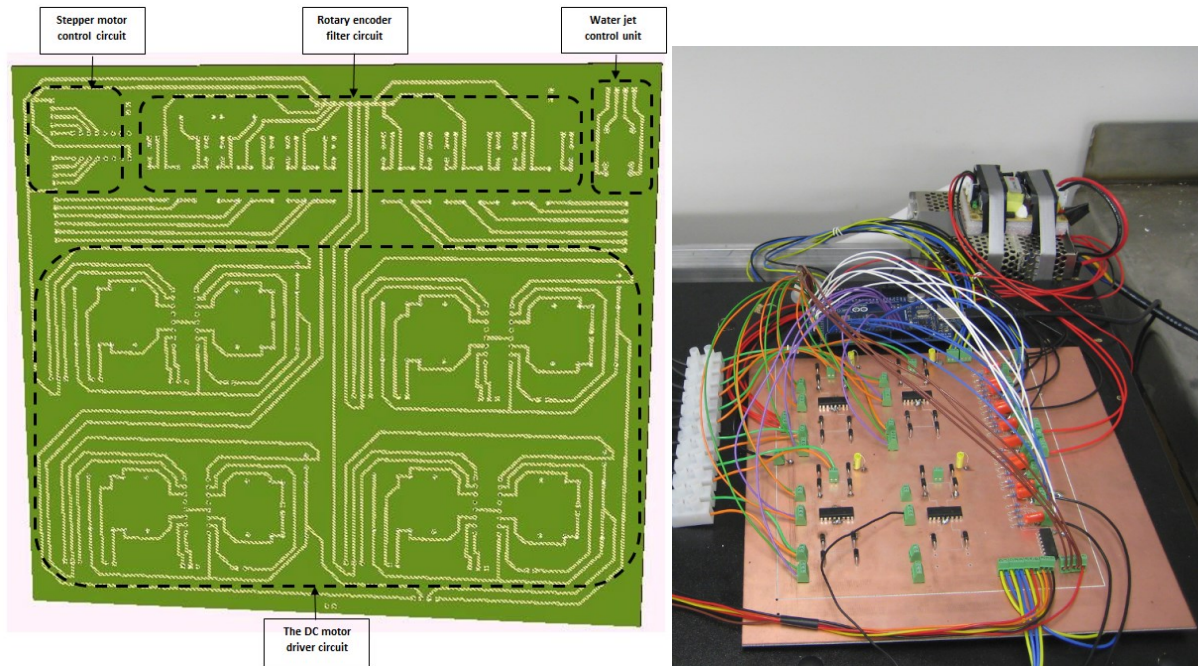
Figure 138: The second iteration of the PCB. The bottom view of the design of the PCB showing the four main circuits: the DC motor driver circuit, rotary encoder filter circuit, stepper motor control circuit, and water jet control unit (left). The actual PCB with addition of the all electronics componenets (right).

III.   The DC Motor Driver Circuit

There are four identical sets of this circuit located on the *PCB*. Three are used and the last serves as a backup in case a fault occurs in any of the other three circuits. The schematic diagram of this circuit is shown below in Figure 139. The diagram highlights the logic connections to the Arduino unit (red), the power connections to the power supply unit (PSU), (blue), and the output motor connections (green).

Diodes D1 to D8 and capacitor C1 are included in the circuit to suppress inductive transient loads, which cause the motor to stall when reversing directions in quick succession. The second iteration PCB was designed to include an inbuilt heat sink at ground connections at pins 4, 5, 12 and 13, as highlighted in Figure 146 by the two purple dots. As the DC Motor, the *MFA 950D* [165], connected to the *L293* chipset draws current at the max current rating

of the *IC* (1A) [166], a heat sink is required to dissipate heat and to ensure that the circuit does not overheat, as was the case with the preliminary prototype PCB which ran very hot.
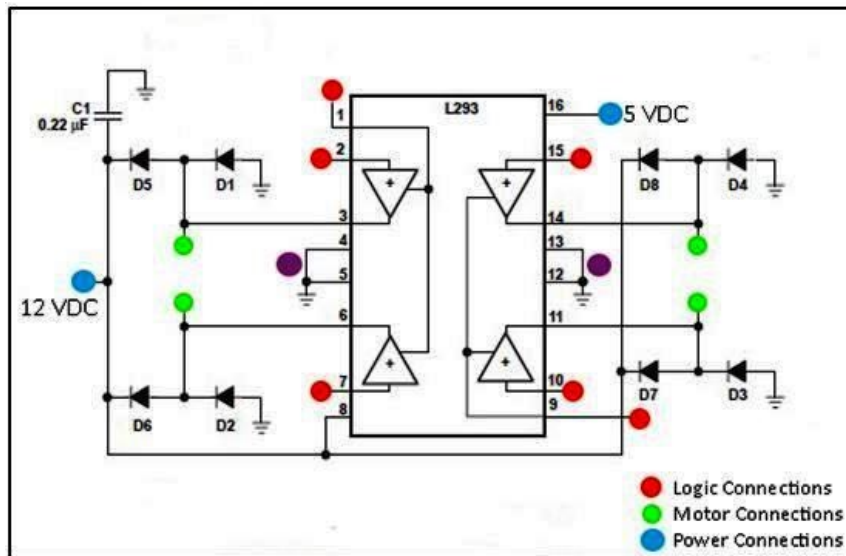
Figure 139: DC motor driver circuit schematic diagram highlighting the logic, motor, and power connections.

This heat sink is in the form of a copper board cutout from the PCB as shown in Figure 140. The key dimension here is the length of the sides of the square-form heat sink (*l*); this parameter was set as 30 mm, balancing available space and performance. The graph of thermal resistance and power dissipation of *L293* IC is shown in Figure 144[167]. It can be seen from the graph that 30 mm is an optimum point for both curves.
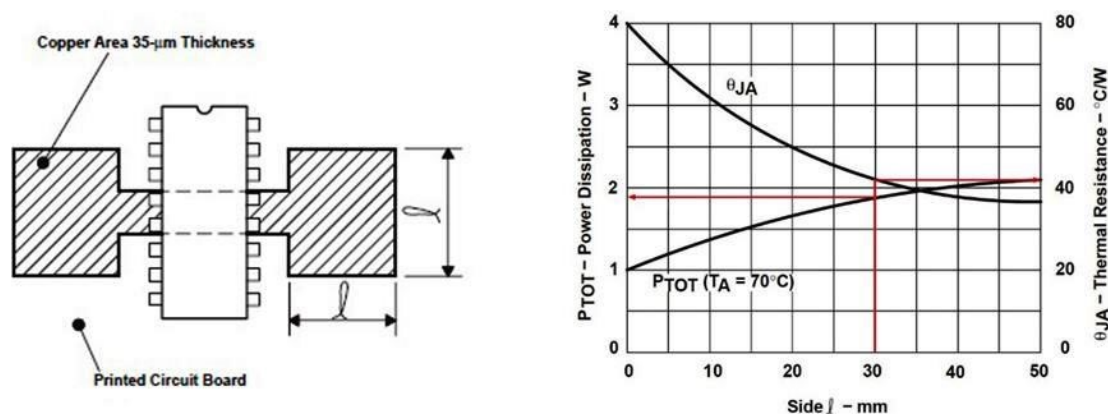
Figure 140: PCB heatsink design (left) and performance curves (right) showing thermal resistance and power dissipation of L293 IC. (Image source: Texas Instruments Incorporated (167))

IV.   Rotary Encoder Filter Circuit

Rotary encoders are notoriously susceptible to signal noise. When the quadrature encoder is rotated, it acts like two switches producing cyclical outputs, A and B, operating at 90° out of

phase with one another. This phase shift allows the software to determine if the shaft is rotating clockwise or anticlockwise.
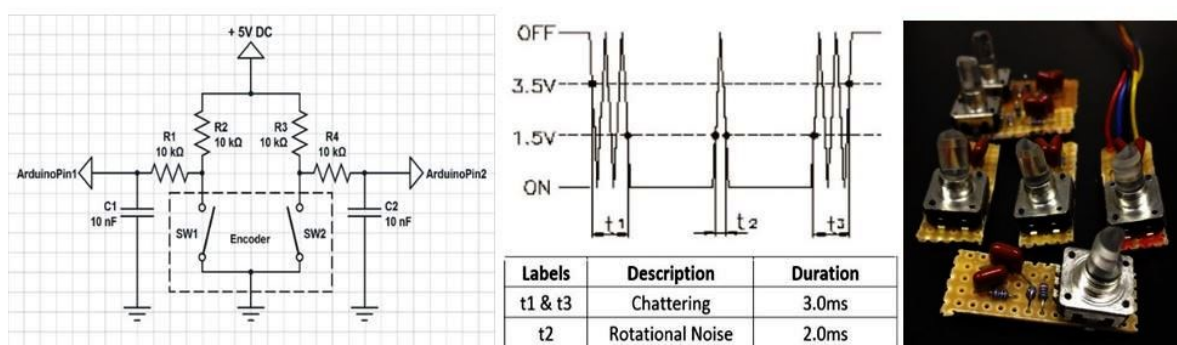
Figure 141: Schematic diagram of the filter circuit (left), profile of the noise signal with associated values (centre)(image source: Tyco Electronics (168)) and the first iteration of filter circuits mounted on Veroboards with the encoders (right)

These switches produce noise when they latch on and latch off. The extent of the noise is a property of the particular encoder in use.

In our case, Tyco Electronics *DPL12* Rotary Encoder produces [168] chattering noise and rotational noise, also known as "bounce", shown in and detailed in Figure 141. These signal artifacts, if not dealt with, falsely trigger the software interrupts, which lead to highly inaccurate encoder readings. There are two ways of eliminating the signal noise: a hardware filter, also known as "*debouncer* circuits", and a software filter. Both methods are employed in the control structure to ultimately produce a robust and accurate encoder. The software debouncer was implemented by introducing a simple timer script that waits 3.0ms every time the interrupt is called before checking the signal again to ascertain if the signal was noise; disregarding it if it is. A passive filter circuit with schematics shown in Figure 145 was also used. In the first iteration of the PCB, the combination of software and hardware filters were successfully implemented and yielded excellent results in eliminating switch noise. However, the location of the hardware filter circuit was less than ideal in the first design, together with the encoders as shown in Figure 141. This led to mechanical meshing and a large amount of vibration. Thus, the second iteration of the PCB opted to put the debounce circuit on the PCB instead of the encoder and do the filtering on the PCB instead of at the encoder.

V.   Stepper Motor Control Circuit

A stepper motor connected to the tensioning screw located at the proximal end of the flexible probe was used to precisely actuate the probe tip angle of flex. The circuit shown in Figure 142 is used to send the required stepping pattern control signals to the stepper motor.
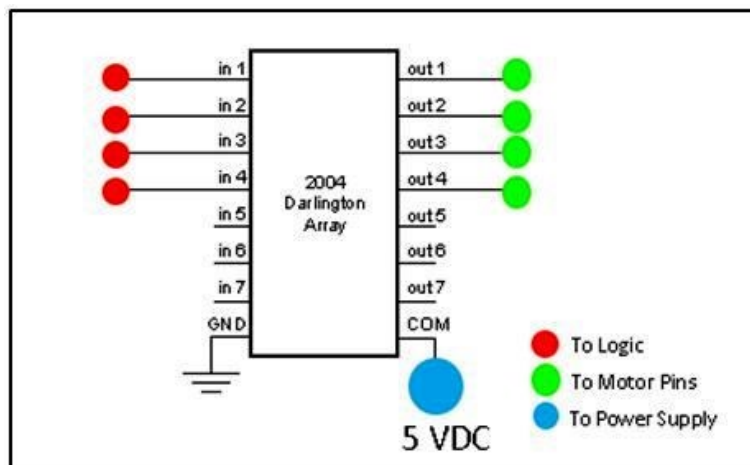
Figure 142: The ULN2003a and relevant connections of the logic, motor and power supply.

VI.　　Water Jet Control Unit

This is the circuit responsible for controlling the state of the water jet cutting head. This assembly consists of a solid-state relay (SSR) to act as a bridge to allow the low voltage, low current logic control signal to operate the high voltage high current solenoid valve.

7.5　Haptic Technology

In this section, two forms of haptic technology will be explored; haptic rendering of rigid surfaces and trajectory supervision. It is important to limit the position of the robot to a certain application-defined workspace as unconstrained robot movements can risk causing severe and potentially life-threatening injuries to the patient.

7.5.1 Haptic Rendering

Haptic rendering is implemented to restore the surgeon's perception of forces in response to interaction with objects in the surgical environment. The ideal exact emulation of the robot's interaction with its physical environment in free space is a very challenging problem to solve completely. Hence, we will simplify the problem and the solution can then be scaled to represent the whole space. Considering the rendering of rigid walls, haptic rendering, when viewed from a control theory perspective, is a constrained control problem. The set of constraints and boundaries that are impermissible or inadmissible to the robot are defined in a constraint set.

The basic structure of the control loop used for haptic rendering can be seen in Figure 143.
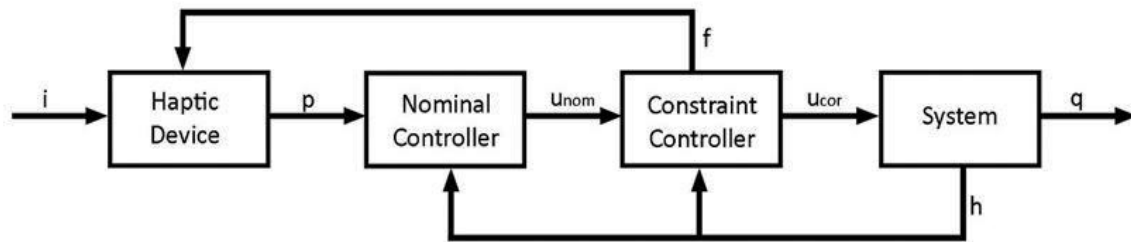
Figure 143: Control loop structure for haptic rendering. User input information (P) is sent to the nominal controller to provide signals (U_{nom}) to control the system's output within permissible regions. Otherwise, the constraint controller is involved to generate forces (f) that keep the system's output within permissible region.

A nominal controller receives an input set (p) which in our case is the 6-by-1 matrix specifying the desired position and orientation of the end-effector. The nominal controller carries out the inverse kinematics and all the necessary computations to determine the nominal control signals (u_{nom}) for the system to achieve the desired position not taking into account any constraints while doing this. The constraint controller monitors the state of the system and only becomes active at the boundaries of the constraint set when the system is on the verge of entering a forbidden region. Here, the constraint controller modifies the nominal control signals (u_{nom}) and outputs a corrected control signal (u_{cor}) which prevents the system from entering the forbidden region. It also computes a feedback force whose magnitude is proportional to the severity of the constraint exceeded. The constraint controller also determines the suitable direction that this force should be induced, which is in the opposite direction to the direction of error, normal to the boundary at which the constraint it applied. This force vector f is then sent to the haptic device to provide corrective kinaesthetic haptic feedback to the user. Both the nominal and constraint controller forming a closed-loop feedback control structure monitors the real-time state of the system h, in this case, the orientation of the robot platform.

To identify how the constraint controller determines the appropriate force output f and corrected control signal (u_{cor}) to output, the constraint controller block in Figure 143 is expanded to show the code logic applied within this program. The control logic is shown in Figure 144.
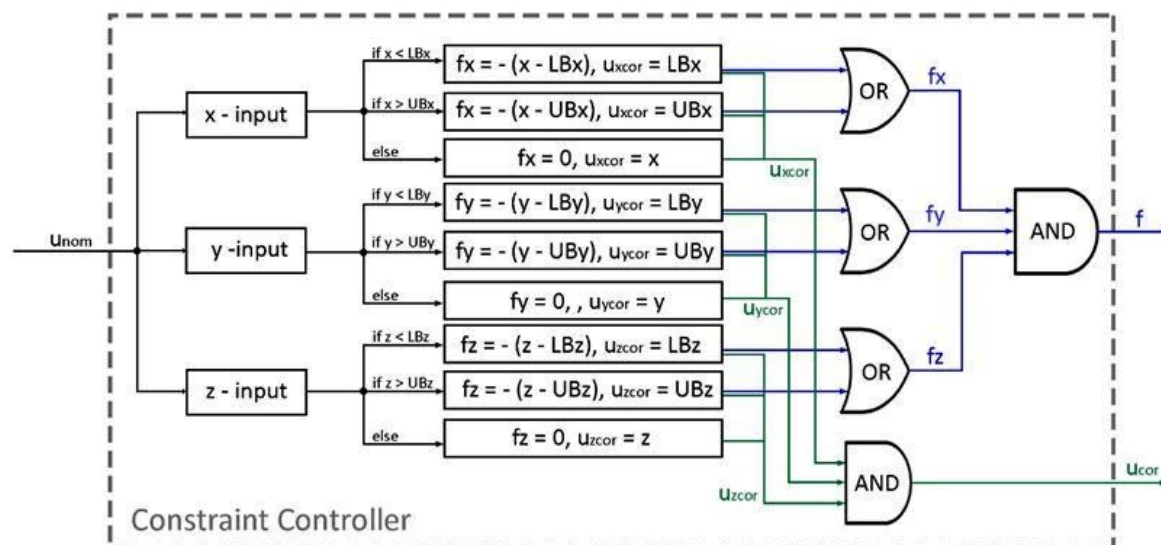
Figure 144: Constraint controller control logic. The nominal controller signals are used to control the systems output within the pre-defined boundaries. The constraint controller becomes active at the boundaries of constraint region, generating forces that keep the system within pre-defined boundaries.

In order to test the control loop detailed above, a virtual environment is created, with a few basic types of constraints. By modifying the constraint set by which the constraint controller samples, the output of the haptic device and the robot platform are controlled. Based on the work done by *A. Kapoor, et al.* [154] in highlighting the 5 basic geometric constraints relevant for constrained control in surgical assistant robots, this section devised five main types of constraints from which any system of boundaries can be defined by method of superposition and linear combination. These five constraint sets are shown in Table 7.

Table 7: The five basic types of constraints

Constraint Type	Description	Example of Physical Uses
Point limit	Limits the robot end effector to a particular point	A set of point limits can be superimposed to create a 3D path
Cuboid Constraint	Restricts the robot to motion within a cuboid-shaped region	Used to define the robot's workspace
Plane Constraint	Prevent the robot from penetrating a plane	A combination of planes can be generated to recreate a particular environment
Cylindrical Constraint	Confines the robot to a cylindrical region	Linear combination with point limit to give hard and soft constraint for motion along a path
Spherical Constraint	Defines a critical spherical region	Limiting the robot's functional space to a 3D curved surface

As haptic device produces force feedback in the three translational coordinates (x, y and z), there exists a set of 3-D boundary conditions for each of the five types of constraints listed above. For the first and simplest case, the point limit, the boundary conditions can be seen in Table 8.

Table 8: Constraint set for point limit constraint type

Point limit at point (x_0, y_0, z_0)		
Axis	**Region**	**Value**
x	Upper boundary, UBx	x_0
	Lower boundary, LBx	x_0
y	Upper boundary, UBy	y_0
	Lower boundary, LBy	y_0
z	Upper boundary, UBz	z_0
	Lower boundary, LBz	z_0

For the second and third constraint types, a similar method is employed to compute the corrected control signals and force vectors. Table 9 below shows an example set of constraints for a cuboid region with vertices as shown in Figure 145 and also a plane constraint for a horizontal plane $y = y_3$.
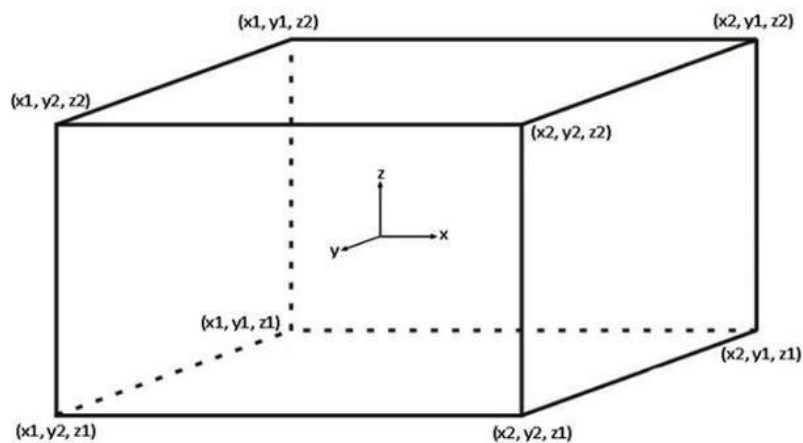
Figure 145: Cuboid Constraint showing the generalised upper and lower boundaries for x, y, and z.

Table 9 shows the constraint set for two examples of the two constraint types. These boundary conditions are non-exhaustive and many other constraint sets can be formulated based on the constraint needed. For example, the plane constraint above is for a horizontal plane $y = y_3$, but it is a trivial matter to formulate the other constraint sets for boundary planes such as for a constant vertical plane, $x = x_3$ or a horizontal plane, $z = z_3$ or even a slanted plane with equation, $ax + by + cz + d = 0$.

Table 9: Constraint sets for the cuboid constraint and plane constraint

Constraint Type	Axis	Region	Value
Cuboid Constraint	x	Upper boundary, UBx	x_2
		Lower boundary, LBx	x_1
	y	Upper boundary, UBy	y_2
		Lower boundary, LBy	y_1
	z	Upper boundary, UBz	z_2
		Lower boundary, LBz	z_1
Plane Constraint	x	Upper boundary, UBx	None
		Lower boundary, LBx	None
	y	Upper boundary, UBy	None
		Lower boundary, LBy	y_3
	z	Upper boundary, UBz	None
		Lower boundary, LBz	None

Table 9 shows the constraint set for two examples of the two constraint types. These boundary conditions are non-exhaustive and many other constraint sets can be formulated based on the constraint needed. For example, the plane constraint above is for a horizontal plane $y = y_3$, but it is a trivial matter to formulate the other constraint sets for boundary planes such as for a constant vertical plane, $x = x_3$ or a horizontal plane, $z = z_3$ or even a slanted plane with equation, $ax + by + cz + d = 0$.

The final two constraint types, the cylindrical constraint and spherical constraint, require an extra step to determine the correct direction of the force vector. This stems from the fact that polar coordinates are used to define the system, which is natively defined in Cartesian coordinates. In the case of a cylinder with axis coinciding with the z-axis, there exist four quadrants as shown in Figure 146-left. On the other hand, when dealing with a sphere with the origin coinciding with the origin of the Cartesian axes there exists an octant (8 regions) as illustrated in the Figure 146-centre [169]. The derivation of the constraint set for the more complex constraint type, the spherical constraint, is detailed here and the cylindrical constraint boundaries can later be determined by simplifying the solution of the spherical constraint.
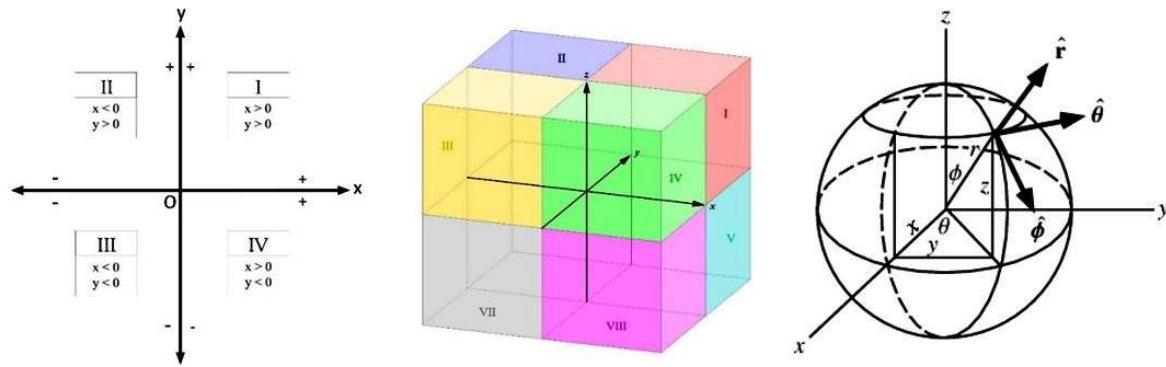
Figure 146: 4 quadrants for 2-D polar coordinates (left), 8 octants for 3D polar coordinates (centre), and a sphere with radius r cantered about the origin O (right)

Considering a sphere with radius *r* and centred about the origin *O*, as shown in Figure 146-right. The polar equations for the sphere are:

$$r = \sqrt{x^2 + y^2 + z^2} \qquad \theta = tan^{-1}\left(\frac{y}{x}\right) \qquad \varphi = cos^{-1}\left(\frac{z}{r}\right) \qquad (7.8)$$

Thus, the constraint set of the sphere, including LB and UB of the Cartesian coordinates (*x, y* and *z*) can be found as follows (Table 10):

Table 10: the constraint set of the sphere

Spherical Constraint for sphere with radius r and center O		
Axis	**Region**	**Value**
x	Upper boundary, UBx	$r.\cos\theta.\sin\varphi$
	Lower boundary, LBx	$-r.\cos\theta.\sin\varphi$
y	Upper boundary, UBy	$r.\sin\theta.\sin\varphi$
	Lower boundary, LBy	$-r.\sin\theta.\sin\varphi$
z	Upper boundary, UBz	$r.\cos\varphi$
	Lower boundary, LBz	$-r.\cos\varphi$

Following from this, the appropriate direction of the force vector is determined depending on which of the 8 octants the robot is in, so as to act to force the user inwards towards the centre of the sphere. The correct direction of each of the force vectors ($f_x, f_y,$ and f_z) for the 8 octants is shown in Table 11.

Table 11: Direction variables for a spherical constraint

Octant	Description	Direction of fx	Direction of fy	Direction of fz
1	$(x > 0),\ (y > 0),\ (z > 0)$	1	1	1
2	$(x < 0),\ (y > 0),\ (z > 0)$	-1	1	1
3	$(x < 0),\ (y < 0),\ (z > 0)$	-1	-1	1
4	$(x > 0),\ (y < 0),\ (z > 0)$	1	-1	1
5	$(x > 0),\ (y > 0),\ (z < 0)$	1	1	-1
6	$(x < 0),\ (y > 0),\ (z < 0)$	-1	1	-1
7	$(x < 0),\ (y < 0),\ (z < 0)$	-1	-1	-1
8	$(x > 0),\ (y < 0),\ (z < 0)$	1	-1	-1

Having defined the octants and set the directions of the force vectors the same constraint controller logic in Figure 147 can be used with the addition of three variables: $xdir, ydir,$ and $zdir$, which are the force direction variables. Where previously the force vector fx was given by the expressions:

$$fx = -(x - LBx) \tag{7.9}$$

$$fx = -(x - UBx) \tag{7.10}$$

The new expressions for the spherical constraint incorporating the direction variables are:

$$fx = -xdir(x - LBx) \tag{7.11}$$

$$fx = -xdir(x - UBx) \tag{7.12}$$

Similar expressions for both fy and fz can be formformed, including r and $zdir$ variables respectively. Thus, the constraint controller script is modified to include the three direction variables, which are then set to equal 1 when using the first three types of constraints. This consequently returns equation 7.11 and 7.12 to become equation 7.9 and 7.10 respectively.

To solve the cylindrical constraint type a similar approach can be used with only 4 quadrants instead of 8 octants. The 2-D polar equations are used to define the system.

$$r = \sqrt{x^2 + y^2} \qquad \theta = tan^{-1}\left(\frac{y}{x}\right) \tag{7.13}$$

The direction variables are determined in a similar fashion and the same equations are used to compute the required force vectors. For completeness, the constraint set and direction variables for a cylinder whose axis coincides with the z-axis, with length $(z_5 - z_4)$ and radius r is shown in Table 12 and Table 13.

Table 12: Constraint set for a cylindrical constraint

Constraint Type	Axis	Region	Value
Cylindrical Constraint	x	Upper boundary	$r.\cos\theta$
		Lower boundary	$-r.\cos\theta$
	y	Upper boundary	$r.\sin\theta$
		Lower boundary	$-r.\sin\theta$
	z	Upper boundary	z_5
		Lower boundary	z_4

Table 13: Direction variables for a cylindrical constraint

Quadrant	Description	$xdir$	$ydir$	$zdir$
1	$(x > 0), \ (y > 0)$	1	1	1
2	$(x < 0), \ (y > 0)$	-1	1	1
3	$(x < 0), \ (y < 0)$	-1	-1	1
4	$(x > 0), \ (y < 0)$	1	-1	1

By inverting the constraint set, instead of staying within the boundaries, the constraint controller will act to keep the robot outside the boundaries. Take for example the cylindrical constraint set with direction variables shown in Table 12. By simply inverting all the $xdir$, $ydir$ and $zdir$ values, as shown in Table 14, the boundary surface normal vector is flipped to face outwards instead of inwards, as it was previously. This acts to keep the robot outside of the boundary. This can be done with all the five types of constraints by inverting the direction variables.

Table 14: Inverted direction variables for a cylindrical constraint

Quadrant	Description	$xdir$	$ydir$	$zdir$
1	$(x > 0), \ (y > 0)$	-1	-1	-1
2	$(x < 0), \ (y > 0)$	1	-1	-1
3	$(x < 0), \ (y < 0)$	1	1	-1
4	$(x > 0), \ (y < 0)$	-1	1	-1

The MATLAB demonstration of the geometrical constraint of point, circle, box, and sphere is represented in Figure 147.
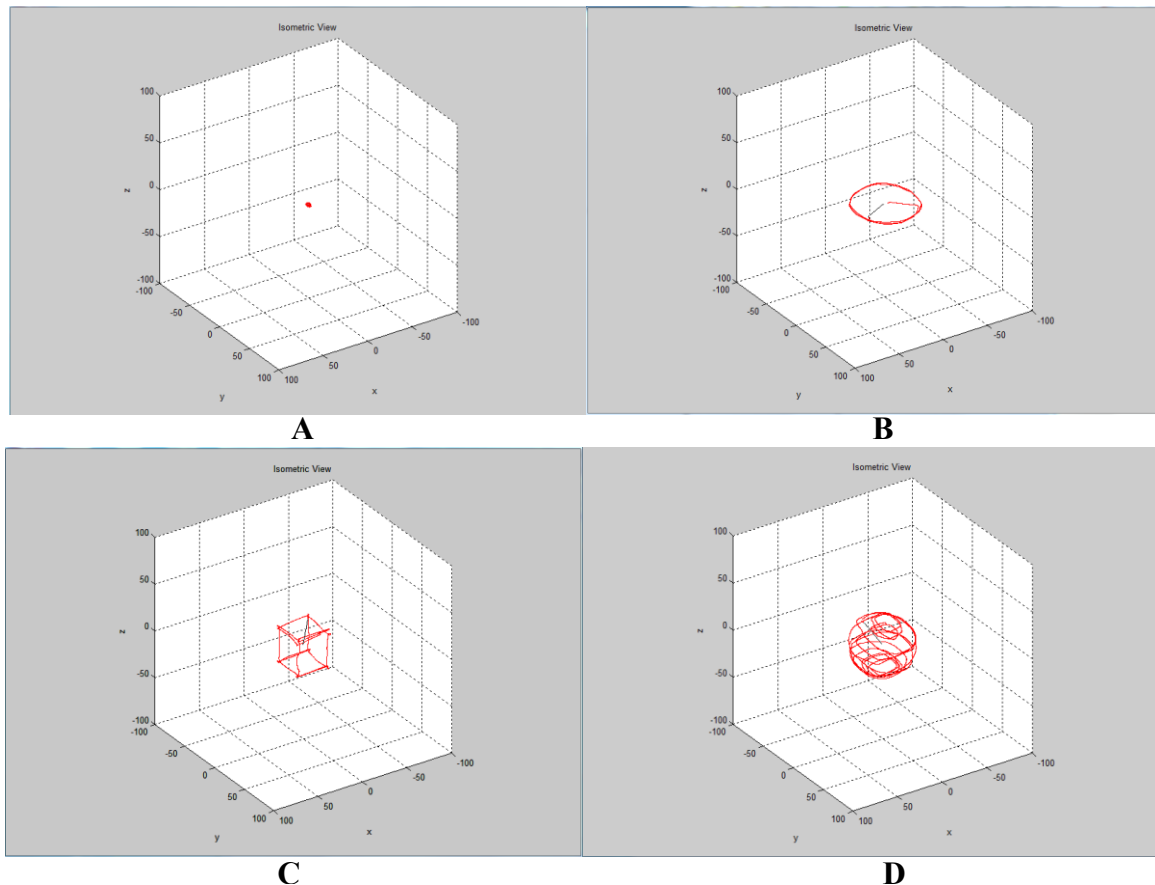
Figure 147: MATLAB demonstration of various geometrical constraints. (A) point, (B) circle, (C) box, and (D) sphere.

7.5.2   Trajectory Supervision

While many complex methods of trajectory control have been developed, such as the invariant controller [155], to resolve and control the robot's trajectory to stay within a constrained region, in the context of our project a simpler approach can be adopted. Since the path of the robot is not designed to run autonomously from, one point to another, there isn't a need to model the trajectories of the robot. Due to the real-time nature of the application of the robot, it is sufficient for us to ensure that the position of the end-effector is within a permissible threshold value of the input position. As the input control the constraint controller, the trajectory, monitors signals or path, of the robot's end-effector will never enter an inadmissible region so long as the real-time position of the end effector is always equal to the input. In other words, if the real-time position of the robot's end-effector is always equal to the corrected control position signal, the end-effector will never enter a restricted region, since the corrected control position signal will never output a signal that is inadmissible. Thus, the trajectory supervision of the robot is achieved by incorporating a control loop feedback mechanism. In this case, a proportional-integral-derivative (PID) controller was

implemented to ensure that the leg lengths of the robot platform extend to the desired length in the ideal time. This is illustrated by the signal h in Figure 147. The constraint controller incorporates two additional constraint sets: the first, a velocity limit set and the second, an allowable threshold set.

The system has mass and, hence, inertia. Thus, the system requires time to accelerate and decelerate to reach a target orientation. When the rate of change of the input targets is critically high, the system will not have enough time to respond to the target orientations in an acceptable manner. To illustrate this, Figure 148 shows the identical path inputs of u_{cor} in black arrows. Note that the arrows never enter the inadmissible region, which is expected since the constraint controller will constrain this input. However, two separate instances of the system response trajectory are shown in Figure 148. The dotted red trajectory is for an input velocity, which is below the critical velocity. As can be seen, the system has sufficient time to respond and the PID controller is effective in keeping the trajectory of the robot to within an acceptable threshold of the input signal in real-time. Notice what happens when the input velocity is increased to a velocity that is above the critical velocity. The resultant trajectory, shown in dotted blue, shows the path of the robot's end-effector crossing the inadmissible region.
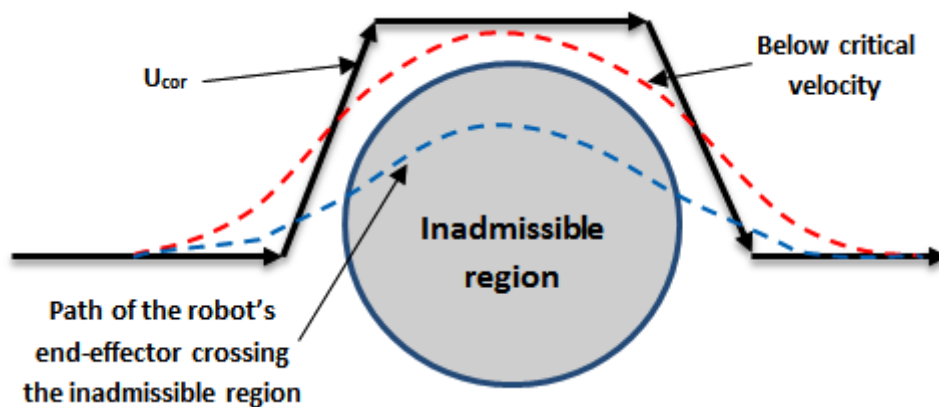
Figure 148: Illustrative diagram showing the effects of input signal velocity. The figure highlights the identical path input (black arrow), the trajectory of an input velocity which is below the critical velocity (dotted red), and the path of the robot's end-effector crossing the inadmissible region (dotted blue).

To avoid this, the input velocity must be limited to be below the critical value at all times. This is done by incorporating a velocity limit constraint that generates a haptic force that slows the user down if the critical velocity is exceeded.

It can be seen from Figure 148 that the real-time path of the robot does not exactly coincide with the control signal trajectory, u_{cor} . As the input velocity is reduced, Δt will increase, and the robot trajectory will closely follow the input signal. However, as the input signals are continuously changing, it is impossible for the path of the robot to be the same as these inputs. Hence, it is to be expected that an error will always exist so long as the inputs change, as the system requires time to respond to the inputs. Since it is impossible to eliminate this error, a suitable acceptable error threshold must be established, beyond which the constraint controller must act to correct the motion. Through empirical tests, 10 mm was found to be an acceptable value of this threshold. This provided an optimum balance between permissible velocity and end-effector precision.

7.6   Results and Testing

The system was designed and built to the specifications detailed in previous sections. Controlled tests were devised to ascertain the accuracy and reliability of the system. Two main tests were conducted: the first, a unit motor cell was tested for reliability and the second, the performance of the complete robot was evaluated in a mock surgery.

7.6.1   Motor-Encoder Functional Test Cell

Before assembling the robot, individual functional cells were tested separately for accuracy and robustness. There are, in total, 6 motor-encoder functional cells incorporated in the robot. The test cell setup is shown in Figure149 and consists of the DC Motor, the rotary encoder and an adapter.
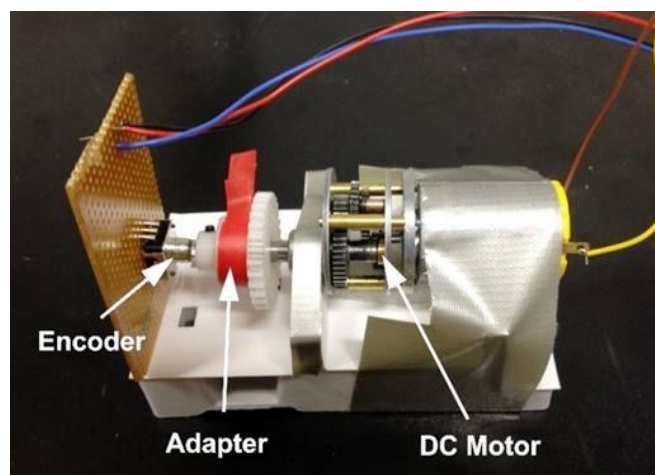
Figure 149: Motor-encoder test cell. The encoder was attached to the DC motor via adapter.

From the encoder datasheet [168] we know that one revolution of the encoder produces 96 pulses. Due to the susceptibility of the quadrature encoders to switch noise, a filter circuit was installed as discussed in Section 7.4.3.
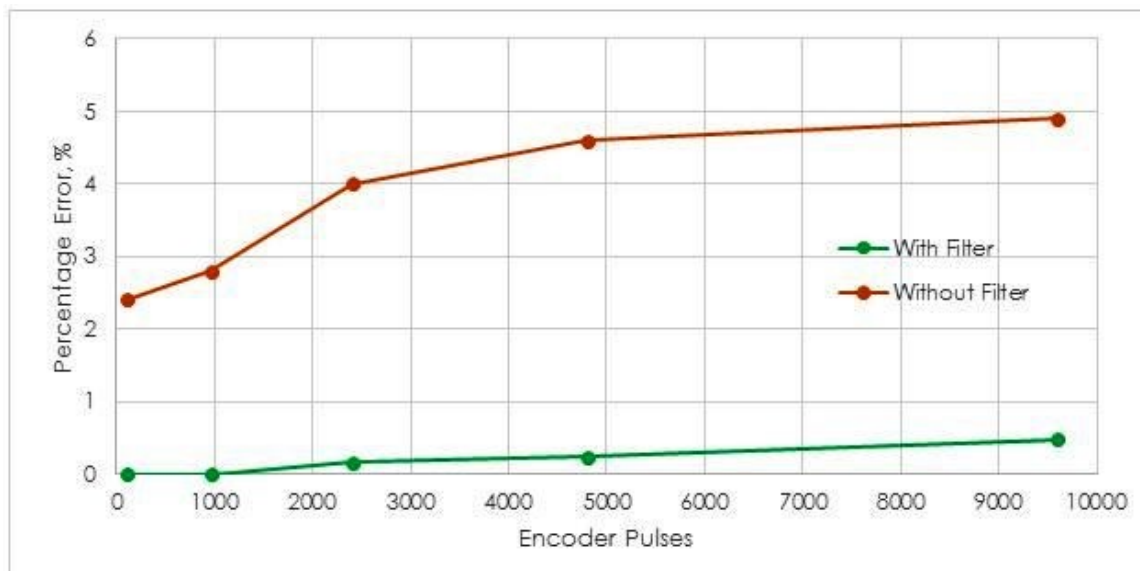
Figure 150: Graph of percentage errors against number of encoder pulses for motor test cell with filter and without filter.

To test the accuracy of the functional cell, an array of target encoder pulses were sent to the DC motor. The responding variable in this experiment is the DC motor's number of revolutions. The motor speed was kept at a constant 60 rpm which is the nominal speed of the quadrature encoder [168]. Figure 150 compares the magnitude of the error for different number of pulses between the encoder with the filter circuit and the encoder without the filter circuit. Data for motor test cell accuracy with filter circuit vs without filter circuit can be found in Table 19 (Appendix 6.1).

The graph shows the effectiveness of the filter circuit; the resultant errors with the filters are decreased by over 90%. From the dimensions of the gears in the robot's leg, it was calculated that a single revolution of the motor gearbox output shaft corresponds to a 3.1 mm change in leg length. Based on the range (or 'sroke') of the leg ($L_{max} - L_{min} = 491 - 306 = 185\ mm$), it would take a total of 59.68 rotations (5730 encoder pulses) to span the whole leg range. At this value, a percentage error of about 0.2% can be expected using the filter circuit. This corresponds to 11.46 pulses, 0.11937 rotations or 0.37 mm. This is a very small error and for the purposes of this project, well within the acceptable level of accuracy. It should be noted that all the observed values of rotations were always less than or equal to the expected value. This is indicative of noise being the main source of error.

A second test was carried out to determine the effects of motor rotational speed in revolutions per minute (rpm) on the encoder errors. Pulse width modulation was used to control the speed of the motor. The results for three different motor rotational speeds are tabulated in Table 20, Appendix 6.2, and Figure 151 shows the graph that was plotted to compare the effects of increasing the motor speed.
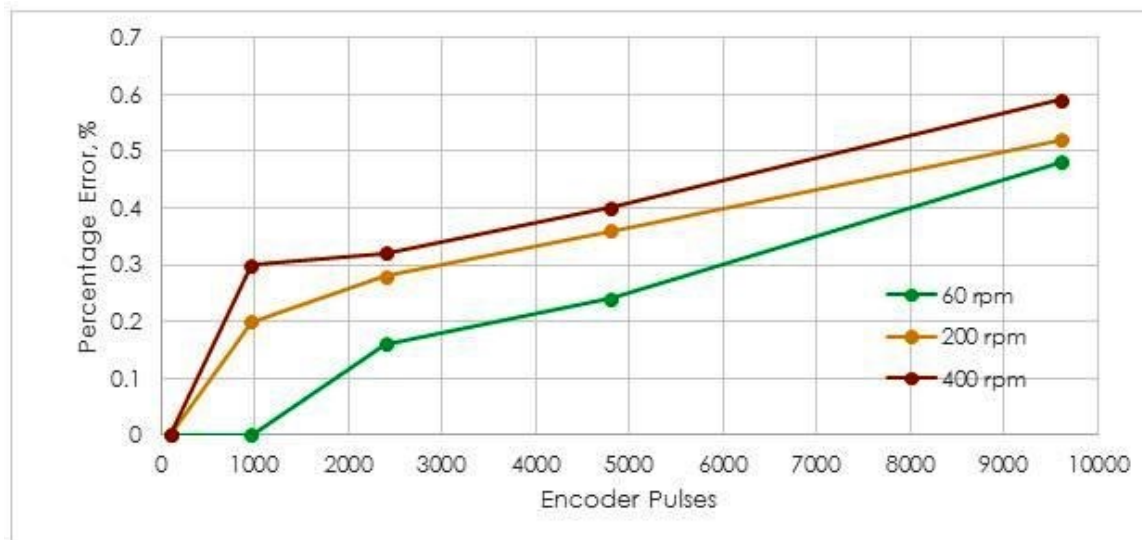
Figure 151: Graph of percentage error of rotation against encoder pulses for different motor speeds

It can be seen from the graph that there is an increase in error of about 0.1% when increasing from the nominal 60 rpm to more than three times the nominal speed, 200 rpm. The large increase in error is likely due to the rotary encoder running at more than three times its rated speed. A further increase to 400 rpm shows a lesser increase of about 0.03%. We can infer from this result that the errors brought about by the encoder running at above nominal speed are relatively constant at higher speeds.

It is beneficial for the motor to run at as high a speed as permitted since this would quicken the system response time since the higher the motor speed, the shorter the time taken for the leg to achieve a target extension or retraction. At the DC motor's maximum speed, 400 rpm, the error brought about per leg range span (185 mm) is equal to 0.45% or 0.832 mm. This is a 125% increase in linear position error compared to the encoder functioning at a nominal 60 rpm. While the percentage is large, the absolute value of the error is very small, of the order 10^{-4} m. Hence, it is an acceptable tradeoff to run the motors at maximum speed.

7.6.2 Mock Surgery

A surgical environment was replicated to represent a typical surgical procedure on the lower lumbar section of the body. The water jet system was connected to the functional head and the aim of the test was to assess the effectiveness and performance of the robot in the following procedure:

1. Enter the body cavity from the posterior position

2. Navigate the probe tip to the target surgical site (the tissue located on the anterior surface of the spine)

3. Use the robot to conduct a dissection of the tissue (beef topside meat) controlling the orientation and curvature of the probe tip

4. Exit the body cavity avoiding contact with any internal organs

The entire platform (Figure 152) was inverted over the test rig and encased in a plastic sheet to protect all the electronic components. The water jet system incorporated a 100 bar pressure washer, which produced a large amount of vibration. This component was isolated from the system to prevent interference with the electrical connection.

Three different positioning and actuation configurations of the flexible surgical probe were applied. Semi-straight, 45°, and J-shaped configuration were compared to each other in term of amount of tissue that has been dissected. The importance of utilising flexible surgical probe in removing tissue surrounding the spinal column is demonstrated in Figure 153. Applying different configuration while performing spinal surgery will improve this type of complex surgical applications. Overall, the meat was successfully dissected and the robot functioned well in carrying out the procedure. Depending on the type of configuration, the overall operating time taken was between 5-6 min from start to finish and this time is likely to improve with practice and improvements to the platform hardware. These improvements are discussed in Chapter 8. The actual duration of applying the water jet is 5-10 sec. Applying different configuration while performing spinal surgery will improve this type of complex surgical applications.
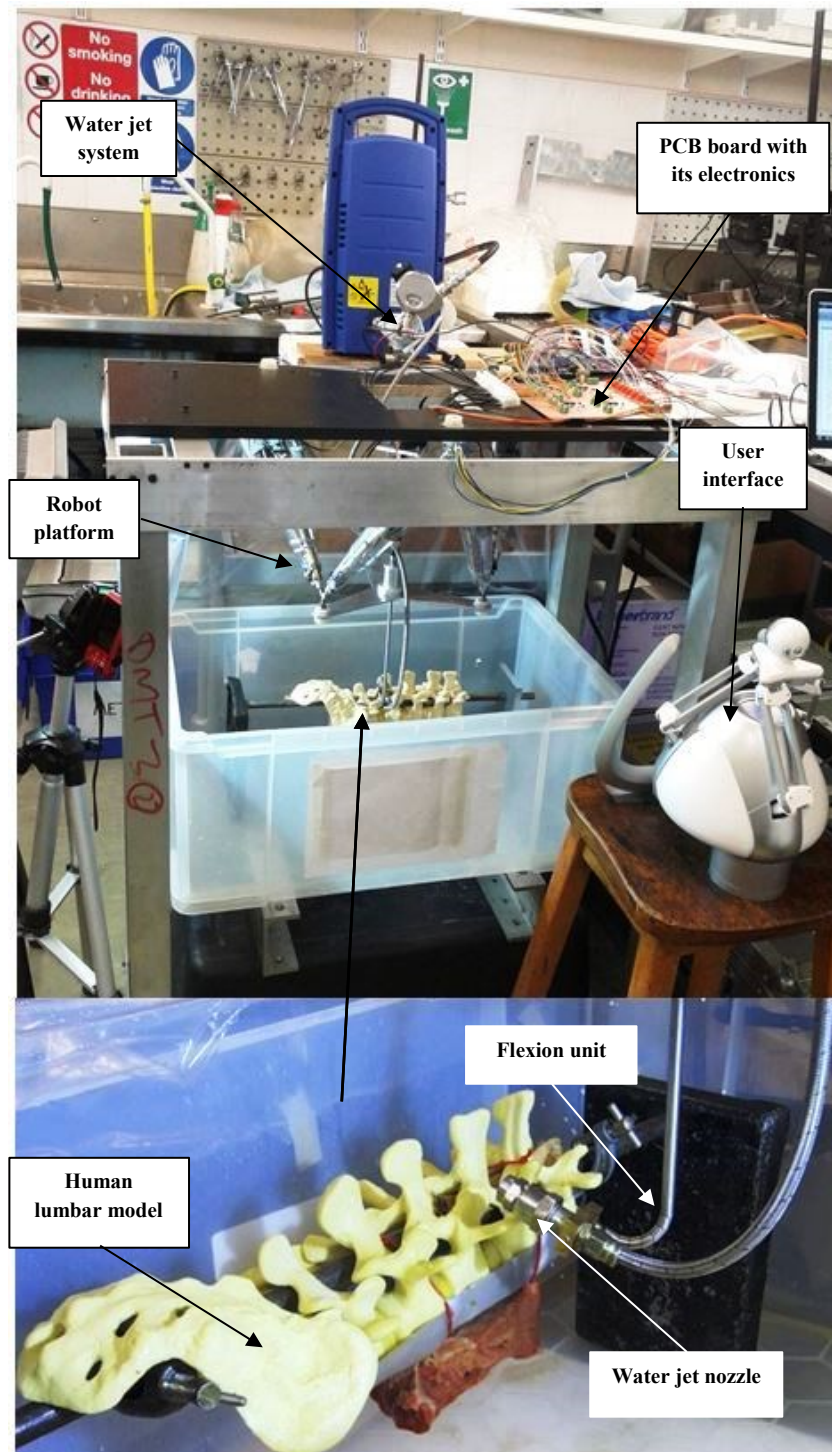
Figure 152: Experimental mock surgery setup with the flexion probe equipped with water jet nozzle. The user interface was used for controlling the movement of the robot, operating the water jet cutting system, and actuating the flexible probe. A piece of animal tissue attached at the interior side of human lumber model (bottom) was used as a target object for performing tissue dissection around corners.

The length of the cut of each probe configuration was measured using image trace analysis. The size of the images was re-dimensioned to the actual size, and then the length of cut was measured. By knowing the water jet flow, pressure and measuring the nozzle stand-off

distance, the extra tissue that the water jet tool is able to cut can be predicted according to the experimental outcomes of controlling the depth of water jet cut (section 5.5).
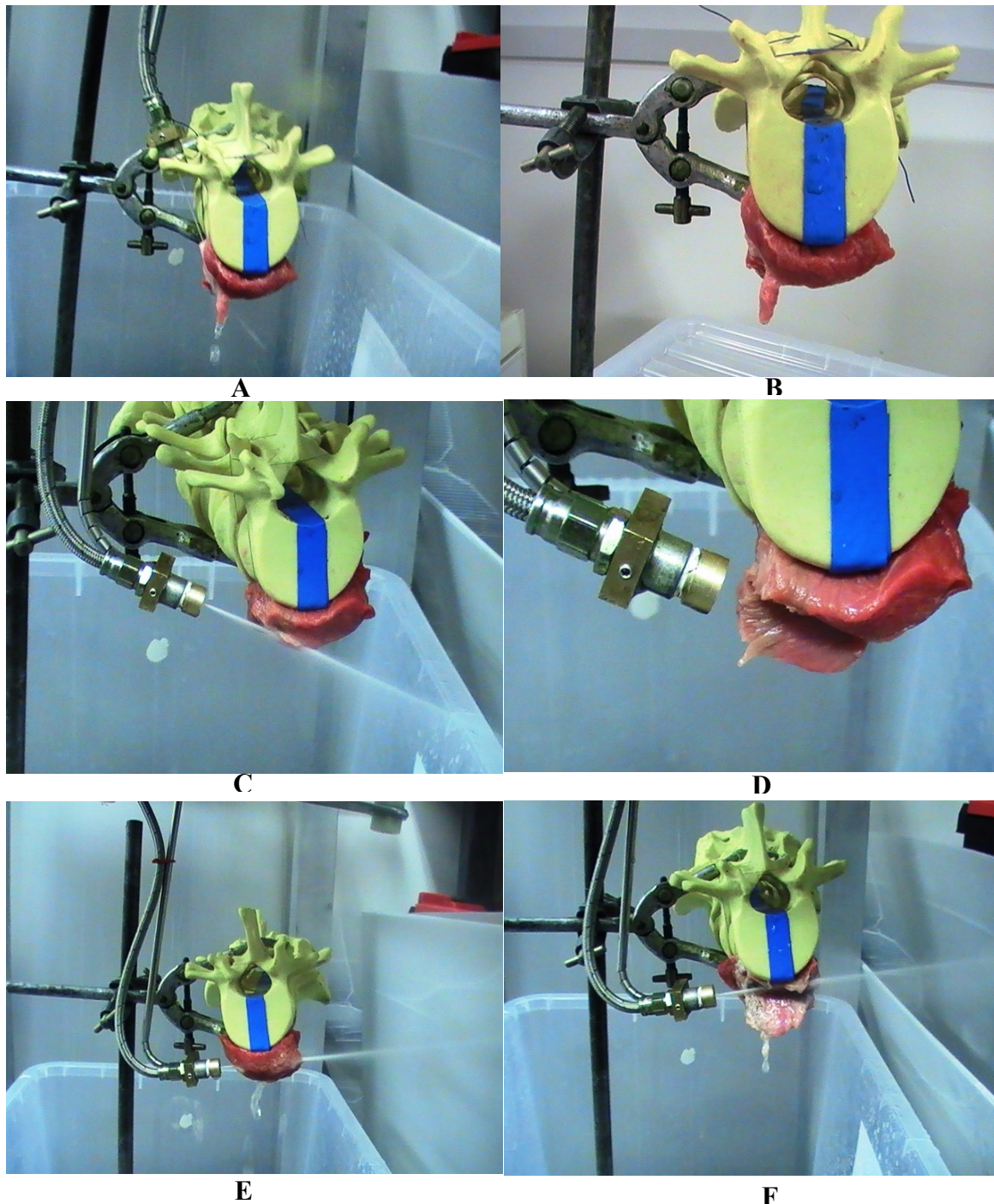
Figure 153: In vitro surgical procedure on the dissection of tissue at the anterior side of human lumbar model. Applying the surgical water jet cutter and the dissected section of semi- straight configuration (A,B), 45° configuration (C,D), and J-shaped configuration ((E,F)

In addition, the approximate shapes and volumes (V) of removed tissue during the mock surgery were calculated using image trace analysis. Figure 154 shows the shapes of removed cut for each configuration with highlighted values of volumes.
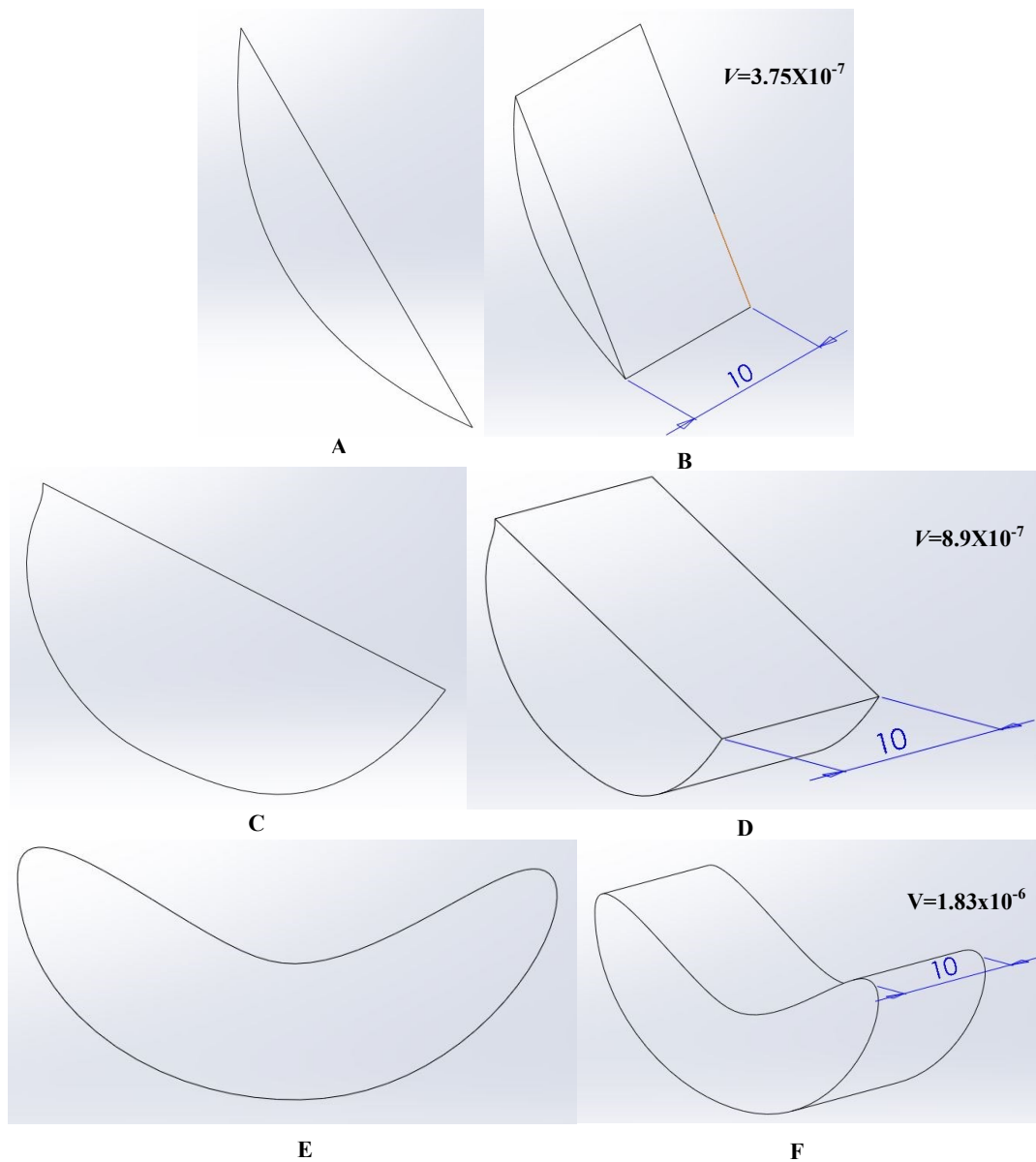
Figure 154: Front and isometric view of approximate shapes of removed tissue during mock surgery applying different configuration of the flexible probe, with values of the volumes inset. (A, B) for semi-straight configuration, (B, C) for 45° bending configuration, (E, F) for J-shaped configuration

Table 15 shows the actual and predicted length of cut for each probe configuration under pre-defined water jet parameters, and the amount of tissue removed off the original tissue.

Table 15: The actual and predicted length of cut and the volume of removed tissue for the three configurations of the flexible probe during the mock surgery

Probe configuration	Pre-defined pressure (bars)	Measured stand-off nozzle (mm)	Actual length of cut (mm)	Predicted length of cut (mm)	%Volume of removed tissue from the original tissue
Straight	25	21.04	17.37	20	16%
45° bending	25	2.8	15.94	24	40%
J-shaped configuration	25	4.44	20.96	23	82%

The table shows the significance of using a flexible surgical probe combined with 6 DoFs parallel robots in dissecting tissues around complex corners of the spinal column. This was confirmed by the amount of tissue that can be removed (82%) compared to the use of rigid surgical tools (16%) used currently in the operating theatre.

7.7   Haptic Control of the Depth of Water Jet Cut

Up to this point, it has been shown how the tip of the probe (end effector) can be controlled with the integration of the haptic method. As explained above, the active regional constraint would restrict the movement of the tip from entering a predefined geometric region. This method can be used in the controlling the depth of water jet cut by applying the outcomes obtained from the experimental testing of the water jet cutting animal tissue as presented in section 5.5.5.

With reference to Figure 156, assuming that a known size of cancerous tissue (red sphere) is centred inside a predefined cube dimension. The cube represents a regional constraint that prevents the tool, in this case the water jet nozzle, from entering the forbidden region. If we position the water jet nozzle on the boundary of the forbidden region, then we know exactly the nozzle stand-off distance, which is the distance between the nozzle and target tissue/ cancerous tumour.

Based on the experimental data analysis and using the relationship between the depth of cut as a function of flow pressure and the stand-off distance of the nozzle, we can specify the depth of water jet cut as a function of flow pressure and duration of the cut. This can be done

by using the stand-off distance as a reference and then adjusting the amount of pressure and the duration of applied water jet.

 In a surgical procedure, the haptic method of controlling the position of the probe (described in section 7.5) would allow it to be safely put into position. Then if the nozzle's stand-off distance is known (say, 5mm), and the diameter of the tumour is 20mm, then according to Figure 78 and Figure 79 the flow pressure can be set to 20 bar for a nozzle diameter of 0.84mm, and then the water jet can be applied for a duration of 10s. The surgeon could then safely control the depth of cut by varying the duration of application of the water jet. The integration of this technique with the haptic control of the probe would be the next stage of development.

The combination of experimental water jet information and haptic technology would offer a degree of control over the depth of water jet cut, and restrict the jet from cutting beyond the target tissue. This would prevent damage to the tissue that is not involved in the surgery and consequently make the procedure safer.
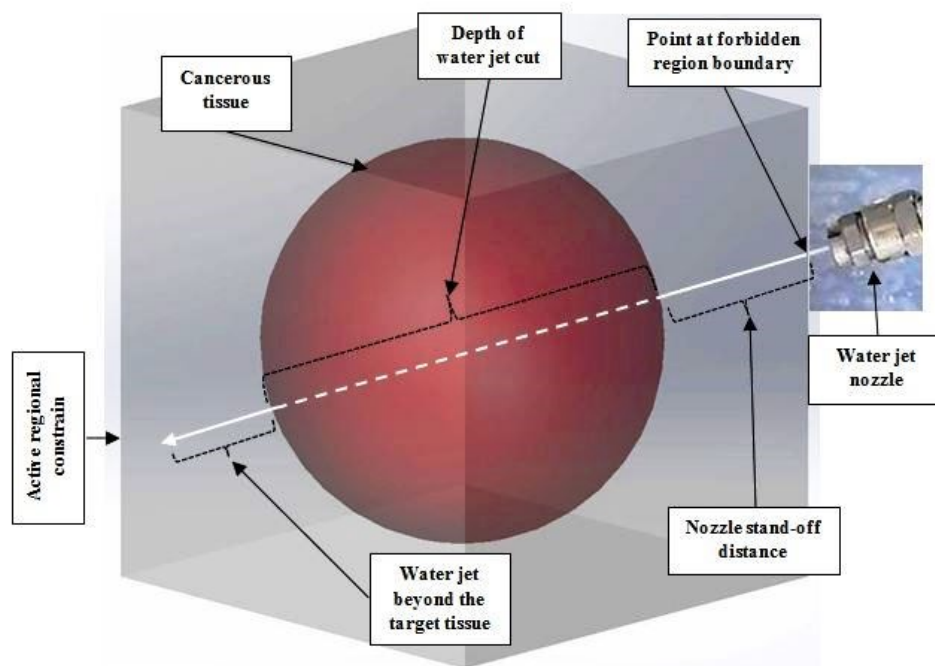
Figure 156: A plot showing the combination of experimental water jet data and active regional constraint (haptic feedback). The water jet cutting nozzle is constraint from entering the active regional constraint. The white arrow represents the path of the water jet cutting through a cancerous tissue (red sphere).

7.8 Discussion and Conclusion

The aim of the chapter was to develop and test a working positional control structure that incorporates haptic technology in a flexible surgical probe. A computer simulation model was successfully developed in MATLAB and validated the inverse kinematic equations described in Section 7.4.1. The hardware, software and electronics needed were installed respectively and a position control code was successfully implemented, incorporating haptic rendering and trajectory supervision. The accuracy and robustness of the system was tested as detailed in section 7.5. Finally, the robot successfully undertook a mock surgery replicating, as closely as possible, the surgical procedure and environment. Results and discussions have been detailed in Chapter 7.6.1 and Chapter 7.6.2.

It was found in the literature review that work done by *B. Bethea, et al.* [170] shows that the digital interface, which a robot inherently provides, offers a platform for motion scaling. This allows the surgeon to control the robot end-effector on a microscopic scale through means of scaling down the macroscopic movements of the system input device. It was found during the robot mock surgery test that it was particularly difficult to obtain a precisely controlled cut with the water jet as the probe end-effector was very sensitive to the movements of the input device, the Novint Falcon. This problem could be resolved by introducing a scaling system into the control scheme. An example of what the scaling code logic would look like is shown in Figure 157.

The scaling controller will sit in between the input devices and the nominal controller. Signal p is altered to produce signal $\hat{p}$, which is the scaled control output signals. $\hat{p} = p$ when operating in the macro scale. As an example of operating in the micro scale, when the input needed to be scaled down by a factor of $\hat{p} = p/100$. This scaling factor can be adjusted to give any level of precision in control that may be necessary. The overall effect of the scaling controller is to enhance the dexterity of the surgeon to levels of precision that were previously unobtainable.
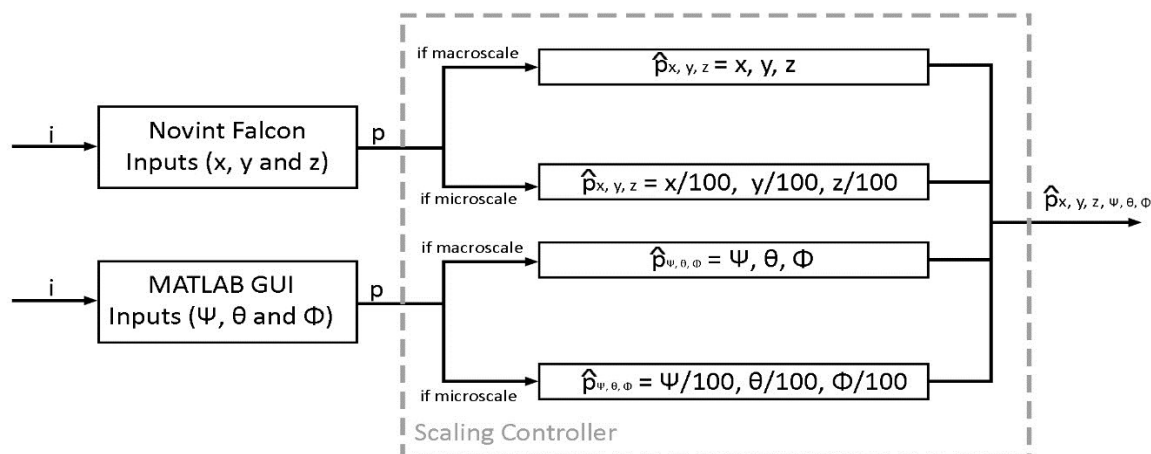
Figure 157: Scaling controller logic flow chart. Position and orientation information from the user interface (P) will be scaled down by the scaling controller before entering the nominal controller.

The Novint Falcon is only capable of inputting 3 DoFs. This is insufficient to fully define the orientation of the robot's end-effector. The problem has been partially resolved in this project by creating a MATLAB GUI to specify the remaining three DoFs. In future versions of this device, it is highly recommended that a proper 6 DoFs haptic input device be used to replace the Novint and the GUI. This will make the overall control of the robot more intuitive and induce a lower cognitive burden on the surgeon during an operation. An example of a 6 DoFs haptic device is the *Phantom Omni*.

The robot platform built used high-speed geared DC motors to couple to lead screw to extend and retract the platform's legs. While cost effective, the DC motors are inadequate in actuating the lengths of the legs in a timely manner. This gave rise to many problems, especially with the supervision of the trajectory path. As discussed in Section 7.5.2, trajectory control is obtained by limiting the input velocity to within a certain threshold in order to allow sufficient time for the system to catch up with the input signals. The slow leg extensions caused by the use of DC motors made the threshold value very small which meant that the velocity of the input signals was limited to a very low value as well. Instead of DC motors, pneumatics or linear actuators can be used. These actuators have desirable response times and deliver sufficient accuracy and holding torque for the surgical application at hand. These systems cost considerably more than the current DC motor setup, but the extra cost may be justified as they bring about many desirable qualities. Besides the DC motor system, the unipolar stepper motor used to control the angle of flex of the tip of the flexible probe should be replaced. Currently a 125:1 geared unipolar stepper motor is used [171]. The motor

supplies 1Nm of force which is desirable, but because it is geared 125:1, the motor sacrifices speed for this large torque. Hence, it is recommended that future iterations of this robot incorporate a faster stepper motor with similar torque output. Furthermore, the robot should be encased in a fitted polymer jacket to protect the electrical components during operation. The jacket can be disposed after every operation and the probe can be autoclaved post-op to ensure that no cross contamination occurs.

A surgical environment was replicated in vitro to represent a typical procedure on the anterior side of the lumber vertebrates. This test was conducted to examine the capabilities of the robot platform in guiding and positioning the surgical tool, and perform tissue dissection on the anterior side of the spinal column. In this test, the surgical tool performed cutting from various positions. Three different arrangements of cutting positions were studied, semi-straight, 45° bend, and J-shaped. The test has revealed the significant advantage of a flexible surgical probe, using J-shaped configuration, over a semi-straight rigid surgical tool. The volume of tissue was calculated and tabulated in section 7.6.2, which are shows that 82% of tissue removed by applying a flexible probe compared to 16% of tissue removed by applying rigid tool.

The combination of experimental water jet data and haptic regional constraint would accurately control the depth of water jet cut and restrict the jet from cutting outside the target tissue. This would prevent damage to the tissue that is not involved in the surgery and consequently making the procedure safer. One of the main limitations of this method is the variability in the structural properties of cancerous tissue (i.e. How durable, it is when being cut). This factor could affect the accuracy of measured depth of cut. Therefore, an analysis of the physical properties of the type of cancerous tissue intended to be dissected should be performed in advance.

8 Conclusions and Future Work

8.1 Summary of thesis achievements

The progression of surgery over last two decades has been motivated by the desire to reduce the invasiveness of the surgical procedures. The introduction of minimal invasive surgery (MIS) has attributed to a reduction in patient trauma, resulting in faster recovery and lower hospitalisation cost. However, performing MIS, which involves the use of long, rigid tools inserted into the patient via small incisions, can introduce a range of ergonomic and safety challenges. The loss of wrist articulation together with the fulcrum effect and poor hand-eye coordination has, up to now, imposed limits on the manual dexterity of the surgeon.

One of the main benefits of emerging robotic technology in surgery is improved control and dexterity. Robotically enhanced surgical tools, together with the introduction of master-slave control have compensated for the loss of wrist articulation and contributed to the safety and consistency of surgical procedures. However, tools that are rigid require careful port placement to ensure the required access and workspace for a given procedure. Therefore, it is important to develop specialised instrumentation to provide enhanced flexibility and stability to reach to the operative target.

The work presented in this thesis addresses the technical issues related to the development of such a flexible surgical system, particularly in the application of spinal surgery, with a specific focus on its design optimisation and position control. The key purpose of this system is to provide the flexibility required to navigate around the spinal column and dissect cancerous tumours at the anterior side of the vertebral body. Developing such, a system is challenging on many fronts and the work presented in this thesis makes the following key technical and clinical contributions:

- Development of a prototype that provides a surgeon with the ability to navigate through complex anatomical structures and has the capability of integrating with other surgical tools.
- Establishment of the principles of and presenting design for a flexible surgical drill able to navigate around small bones.
- Development of a novel flexible surgical water jet cutting system that is able to go around corners and dissect tissues in the application of spinal surgery.

- Demonstration of the ability of surgical water jet to cut a variety of tissues.

- Development and evaluation of a method of controlling the depth of water jet cut.

- Development of a new design of a 6 DoFs parallel robot with a novel (patented) connector joints. The robot can be integrated with various external surgical tools.

- The design of a system that controls 6 DoFs motion of the robot manipulator with the aid of the force feedback method based on active positional constraints.

- Demonstration of the use of a single user interface able to control all the functions of the surgical robot system, including controlling the movement of the robot end effector, controlling the articulation of the flexible probe, and controlling the operation of the water jet system.

- Derivation of a control algorithm that can be directly applied to a variety of robot architectures.

- Principles of haptic control of the depth of water jet cut were established. This was done by combining the experimental results of measuring the depth of the water jet cut with the haptic feedback method of controlling the movement of the tool, by applying active regional constraints.

Each of the chapters in this thesis contributed to the present-derived solutions to the technical and clinical challenges outlined in Chapter 1 (Table 16). Chapter 3 presented a preliminary solution to both Challenge 1 and Challenge 2 through the development of a flexible probe prototype. The device offers the ability to perform tissue dissection around corners. In this chapter, the tool size and degree of angulation required for spinal surgery application were established. This was obtained by performing computer modelling of both the prototype and the spinal vertebrae.

As outlined in Challenge 1 and Challenge 2, Chapter 4 presents the design and as manufactured configuration of a flexible surgical tool. The configuration of the new tool is based on the design principles gained from the preliminary design of the flexible surgical probe in Chapter 3. The tool is an integration of a flexion unit with a mechanical drilling unit that was created to overcome the limitations in the preliminary prototype.

Table 16: How the individual chapters relate to the challenges outlined in Chapter 1

Chapter No.	Challenge/s addressed	Key contribution
Chapter 3	1,2	Development of a surgical flexible tool
Chapter 4	1,2	Development of a surgical flexible tool
Chapter 5	2	Design a surgical cutting device able to dissect soft tissues
Chapter 6	3	Design and build a robot platform
Chapter 7	4,5	Design and built a master - slave system incorporate haptic technology

Chapter 5 addresses Challenge 2 by presenting a new flexible surgical device for applying a water jet cutting method. The performance of the device was demonstrated by cutting various animal tissues. The main challenge of using the water jet-cutting device in surgery is the control of the depth of water jet that may hit/damage organs beyond the targeted tissue. This was experimentally studied, and data of the critical elements/parameters that influence the characteristics of water jet were obtained and analysed. This showed promising solutions by controlling the time and/or the pressure of the applied water jet.

Chapters 3-5 of the thesis concentrated on the first major part of the surgical robot, the surgical device. From Chapter 6 onwards the thesis deals with the other major aspect of surgical robots, which is the 'robot' itself.

In Chapter 6, a robot manipulator with 6 DoFs was designed and fabricated to address challenge 3. The construction of the robot manipulator that was chosen for the particular clinical application is based on the parallel configuration type, which has a number of advantages over other configurations in terms of stability and accuracy. This robot manipulator has served as a mount for the surgical tools as well as providing a wide range of movements.

Chapter 7 comprises the largest section of the thesis, tackling Challenge 4 and Challenge 5, as it analyses the control of the robot platform, with its entire hardware and software, along with the haptic feedback method. The movement of the robot manipulator is achieved via position control of the end effector based mainly on the inverse kinematics scheme. The

control programs were successfully managed to control the entire surgical robot's function using a single user interface. This significantly simplified the system architecture and would increase the control and the focus of the user on the surgical task. The method of active regional constraints was applied to generate force feedback to the user. Applying this method prevents the user from entering forbidden regions by generating feedback forces on the user interface.

8.2   Future Research Directions

A key achievement of the work presented in this thesis is the development of a surgical robot, for the application of spinal surgery, and a robotic control algorithm to improve the usability and effectiveness of flexible robotic devices in surgery.

Prior to discussing the possible future directions of the thesis, it is important to mention all the potential inputs that could improve the surgical robot constructed in this project. The elements of improvements are listed below:

- Upgrade the high speed geared DC motors used in the construction of the robot platform to power the extension and retraction of the platform's legs, to pneumatics or linear actuators to improve response times and deliver sufficient accuracy and holding torque for the surgical application.
- Upgrade the stepper motor used to control the angle of flex of the tip of the flexible probe, to a faster stepper motor with similar torque output.
- Upgrade the user interface, the Novint Falcon, which is only capable of inputting 3 dogs, to a proper 6 DoFs haptic input device such as Phantom Omni.
- Apply a motion scaling system, which allows the surgeon to control the robot end-effector on a microscopic scale through means of scaling down the macroscopic movements of the system input device.

This thesis presents an interdisciplinary project, which could develop in many research directions with extensive future work. Looking initially at the future direct expansion of the work presented in this thesis, the possibility of combining the flexible surgical device with a real time scanning method to give the surgeon a good vision of the operation field is obvious. This could be an optical endoscopic camera integrated with the flexible surgical device via a connector with multiple hole/sections. This will lead us to another apparent direction, which is installing a suction system to remove debris simultaneously with dissection of the tissue.

This would result in reducing the amount of equipment and number of hands involved in the procedure, as well as reducing the time needed to interchange between the instruments. In addition, a good suction system would significantly clear the vision of the real time imaging device, especially with the use of water jet cutting systems.

The work done on haptic rendering for boundaries and free objects in space done in Section 7.5 demonstrates how a simple boundary region can be specified and imposed onto the system.

Figure 158: 3-D model of human lumber vertebrae. The model created in solid works based on image tracing of actual human vertebrae form.

It is also possible to import 3-D model surfaces from 3-D CAD packages such as SolidWorks into MATLAB, Simulink and have MATLAB convert the surfaces into boundaries. Doing this, MATLAB can automatically calculate the surface normal vectors at which the feedback force vectors are applied and specify the boundaries of the constraint set. A 3-D solid model of the lower lumbar vertebrae is shown in Figure 158.

Extrapolating the capability of such a situation, it would also be worth investigating the feasibility of scanning a patient's body using Magnetic Resonance Imaging (MRI) or other imaging techniques to obtain the exact physical locations of the boundaries relevant to the surgery. This image could then be uploaded into MATLAB or similar computing software to calculate the necessary constraint sets. This would enhance the overall capability of the system and make the use of the robot in surgery more viable, practical and customizable. In

the future, the possible use of real-time scans, mentioned above, of the surgical environment will continuously update the constraint set of the system so that the robot can respond to changes in real-time.

Controlling the depth of water jet cut has been investigated with use of animal tissue. The two possible methods are controlling the time and the pressure of the applied water jet. These methods, however, are prone to inaccuracy if applied to different types of tissues. Therefore, a broad experimental study of controlling the depth of water jet cutting system can be demonstrated on cancerous tissue. By doing this the specific time/or pressure required to cut to a certain depth will be coupled with the specific properties of the tissue. In any case, a theoretical study of combining the experimental outcome of controlling the depth of water jet to the haptic regional constraint will be needed, and further practical work is desirable to significantly improve the depth control.

One of the most important future research aspects in using surgical robots in the operating theatre is the use of navigation and tracking technology. Surgical robot systems are currently guided by two main sources of data: global spatial data and local data. The two sets of information are sampled during a planning phase and processing phase respectively. Nevertheless, they lack resolution, segmentability, or non-continuous sampling. However, there are applications for which an additional information type is necessary to cope with uncertainty, measurement errors, and incompleteness of data [172].

The use of data from motion sensors to estimate change in position over time of mobile robots is typically imprecise, thus exact global localisation is only possible with the aid of a global positioning system or the vicinity of markers. When neither is available, the robot has to rely on estimations for both updating and reading from the spatial map of the environment, which introduces uncertainty. In addition, the value of continuous sensor data sampling of the environment model is decreases due to position inaccuracy. Hence, the robot is continually re-registering itself with the inaccurate map, based on uncertain measurements.

On the other hand, surgical navigation systems, such as infrared (IR) optical trackers, magnetic or ultrasound trackers, are useful for tracking the absolute position of both instruments and the patient within the operating theatre. This ability has been developed for conventional, computer-assisted interventions, where the surgeon performs the action with enhanced sense of the position and orientation of his instruments relative to structures. This allows complex interventions to be performed precisely. The main advantages of applying

navigation systems in medicine are intra-operative localisation of anatomical structures, intra-operative illustration of pre-operative and intra-operative structures, reduction of invasive interventions, reduction of operating time and cost. Figure 159 [173] illustrates the setup of IR optical tracking system that could be applied for robot-patient registration.
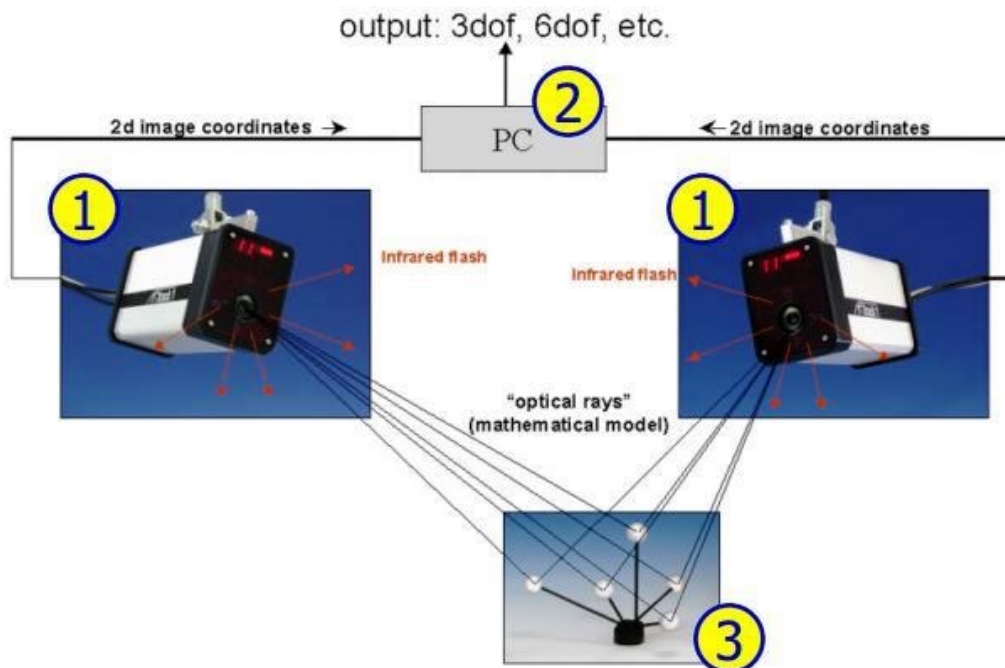
Figure 159: Illustration of the IF tracking setup. (1) Tracking cameras, (2) software with PC, and (3) single markers. (Image source: AR-tracking (173))

References

1.   L. Frasson, S.Y.Ko, A. Turner, T Parittotokkaporn, J F Vincent, and F Rodriguez y Baena, *STING: a soft-tissue intervention and neurosurgical guide to access deep brain lesions through curved trajectories.* J. Engineering in Medicine, 2010. 224 Part H: p. 775-788.

2.   K-W. Kwok, K.H.Tsoi, V. Vitiello, J. Clark, G. Chow, W. Luk, and G-Z. Yang, *Dimensionality Reduction in Controlling Articulated Snake Robot for Endoscopy Under Dynamic Active Constraints.* IEEE TRANSACTIONS ON ROBOTICS, 2013. **29**(1): p. 15-31.

3.   Institute of Spine Physicians, *Spinal Tumors.* 2014; Available from: http://spinephysiciansinstitute.com/conditions-view/spinal-tumors/.

4.   Y. S. Kwoh, J.Hou, E. A. Jonckheere, and S. Hayati, *A Robot with Improved Absolute Positioning Accuracy for CT Guided Stereotactic Brain Surgery.* Transactions on Biomedical Engineering, 1988. **35**: p. 153-160.

5.   B. L. Davies, R.D.Hibberd, M. J. Coptcoat and J. E. A. Wickham *A surgeon robot prostatectomy - a laboratory evaluation.* Journal of Medical Engineering & Technology, 1989. **13**(6): p. 273-277.

6.   S.J. Harris, Q.Mei, R.D. Hibberd, B.L. Davies. . *Experiences Using a Special Purpose Robot for Prostate Resection*. in *International Conference on Advanced Robotics*. 1997. Monterey, CA: IEEE.

7.   D. Glauser, P. Flury, C.W. Burckhardt, Mechanical concept of the neurosurgical robot 'Minerva'. Robotica 1993. 11: p. 567-575.

8.   T. A. Mattei, A.H.Rodriguez, D. Sambhara, E. Mende, Current state-of-the-art and future perspectives of robotictechnology in neurosurgery. Neurosurg Review, 2014. 3: p. 357-366.

9.   W. L. Bargar, A.Bauer, and M. Borner, *Primary and Revision Total Hip Replacement Using the Robodoc@ System.* Clinical Orthopaedics and Related Research, 1998(354): p. 82-91.

10.   J. R. Otero, P.Paparel, D. Atreya, K. Touijer and B. Guillonneau, *History, Evolution And Application Of Robotic Surgery In Urology. Urology Robotic Surgery.* Urology Robotic Surgery, 2007. **60**(4): p. 335-341.

11.   R. H. Taylor, J.Funda, B. Eldridge, S. Gomory, K. Gruben, D. LaRose, M. Talamini, L. Kavoussi, and J. Anderson, *A telerobotic assistant for laparoscopic surgery.* IEEE Engineering in Medicin and Biology Magazine, 1995. **44**(3): p. 279-288.

12.   G. S. Guthart and J. K. Salisbury, *The intuitive telesurgery system: Overview and application*, in *International Conference on Robotics and Automation* 2000, IEEE: San Francisco, CA.

13.   J. M. Sackier and Y. Wang, *Robotically assisted laparoscopic surgery. From concept to development.* Surgical Endoscopy, 1994. **8**: p. 63-66.

14.   C. Detter, H.Reichenspurner, D.H. Boehm and B. Reichart, *Robotic manipulators in cardiac surgery: the computer-assisted surgical system ZEUS.* Minimally Invasive Therapy & Allied Technologies, 2001. **10**(6).

15.   P. Gomes, *Surgical robotics:Reviewing the past,analysing the present, imagining the future.* Robotics andComputer-IntegratedManufacturing, 2011. **27**: p. 261-266.

16.   B. Davies, *A review of robotics in surgery.* Proceedings of the Institution of Mechanical Engineers, Part H: Journal of Engineering in Medicine, 2000. **214**: p. 129-140.

17.   C. Bergeles, and G.Yang, *From Passive Tool Holders to Microsurgeons: Safer, Smaller, Smarter Surgical Robots.* IEEE Transactions On Biomedical Engineering, 2014. **61**(5): p. 1565-1576.

18.   D.B. Camarillo, J.K. Salisbury, *Robotic technology in surgery: past, present, and future.* The American Journal of Surgery, 2004. **188**: p. 2s-15s.

19.   R.A. Beasley, *Medical Robots: Current Systems and Research Directions.* Journal of Robotics, 2012. **2012**(ID 401613): p. 14.

20.   R. H. Taylor, and D.Stoianovici, *Medical Robotics in Computer-Integrated Surgery.* IEEE Transactions On Robotics And Automation, 2003. **19**(5): p. 765-781.

21.   J. E. Speich, and J. Rosen, *Medical Robotics*, in *Encyclopedia of Biomaterials and Biomedical Engineering*2004, Marcel Dekker, Inc.: New York. p. 983-993.

22.   R. Zigeuner, *Laparoscopy in Urology: An Overview*, in *Laparoscopy - An Interdisciplinary Approach*, I. Meinhold-Heerlein, Editor 2011, InTech. p. 3-20.

23.   R. H. Taylor, A.Menciassi, G. Fichtinger, P. Dario, *Medical Robotics and Computer Integrated Surgery*, in *Springer Handbook of Robotics*, a.O.K. B. Siciliano, Editor 2008, Springer: Berlin. p. 1199-1222.

24.   S.C. Low and L. Phee, *A Review of Master-Slave Robotic Systems for Surgery*. in *Proceedings of the IEEE Conference on Robotics, Automation and Mechatronics*. 2004. Singapore: IEEE.

25.   E.B. Wilson, H.Bagshahi,V. Woodruff, Overview of general advantages, limitations, and strategies, in Robotics in General Surgery, K.C. Kim, Editor. 2014, Springer: New York. p. 17-24.

26.   K. Hongo, T.Goto, T. Miyahara, Y. Kakizawa, J. Koyama, Y. Tanaka, *Telecontrolled micromanipulator system (NeuRobot) for minimally invasive neurosurgery*. Medical Technologies in Neurosurgery, 2006. **98**: p. 63-66.

27.   S. Najarian, and E. Afshari, *Evolutions and Future Directions of Surgical Robotics: A Review.* International Journal of Clinical Medicine, 2012. **3**: p. 75-82.

28.   J.M. Albani, *The Role of Robotics in Surgery: A Review.* Missouri Medicine, 2007. **104**(2): p. 166-172.

29.   B. Jaffray, *Minimally invasive surgery.* Archives Diseases in Childhood, 2005. **90**: p. 537-542.

30.   R.H. Taylor, *A Perspective on Medical Robotics*. in *Proceedings of the IEEE*. 2006. IEEE.

31.   A. R. Lanfranco, A.E.Castellanos, J.P. Desai, and W. C. Meyers, *Robotic Surgery A Current Perspective.* Annals of Surgery, 2004. **239**(1): p. 14-21.

32.   L. S. Leddy, T.S.Lendvay, and R. M. Satava, *Robotic surgery: applications and cost effectiveness.* Open Access Surgery, 2010. **3**: p. 99-107.

33.   L.B. Rosenberg, *Virtual fixtures: Perceptual tools for telerobotic manipulation*, in *Virtual Reality Annual International Symposium*1993, IEEE: Seattle. p. 76 - 82.

34.   J. Ren, R.V.Patel, K.A. McIsaac, G. Guiraudon, T.M. Peters, *Dynamic 3-D virtual fixtures for minimally invasive beating heart procedures.* IEEE Transactions on Medical Imaging, 2008. **27**(8): p. 1061 - 1070.

35.   B.L. Davies, K.L.Fan, R.D. Hibberd, M. Jakopec, S.J. Harris *ACROBOT - Using Robots and Surgeons Synergistically in Knee Surgery. .* in *Proceedings., 8th International Conference on Advanced Robotics*. 1997. Monterey, CA: IEEE.

36.   G. H. Ballantyne, and F. Moll, *The da Vinci telerobotic surgical system: the virtual operative field and telepresence surgery.* Surgical Clinics of North America, 2003. **83**: p. 1293–1304.

37.   A. Degania, H.Choset, A.Wolf, and M. A. Zenati *Highly Articulated Robotic Probe for Minimally Invasive Surgery.* in *IEEE International Conference on Robotics and Automation.* 2006. Orlando, Florida: IEEE.

38.   P. S. Green, J.W.Hill, J. F. Jensen, and A. Shah, *Telepresence surgery.* IEEE, Engineering in Medicine and Biology Magazine, 1995. **14**(3): p. 324-329.

39.   H. Meenink, *Vitreo-retinal eye surgery robot: sustainable precision*, 2011, Eindhoven University of Technology: Eindhoven. p. 145.

40.   R. Hendrix, N.Rosielle, H. Nijmeijer, *Design of a haptic master interface for robotically assisted vitreo-retinal eye surgery*, in *ICAR 2009. International Conference on Advanced Robotics*2009, IEEE: Munich. p. 1-6.

41.   K. Salisbury, F. Conti, F. Barbagli, Haptic rendering: introductory concepts. Computer Graphics and Applications, 2004. 24(2): p. 24-32.

42.   K. Ikuta, M.Tsukumoto, and S. Hirose. *Shape Memory Alloy Servo Actuator System with Electric Resistance Feedback and Application for Active Endoscope.* in *IEEE International Conference on Robotics and Automation.* 1988. Philadelphia, PA: IEEE.

43.   A. Eickhoff, J.V.Dam, R. Jakobs, V. Kudis, D. Hartmann, U. Damian, U. Weickert, D. Schilling, and J. F. Riemann, *Computer-Assisted Colonoscopy (The NeoGuide Endoscopy System): Results of the First Human Clinical Trial ("Pace Study").* American Journal of Gastroenterology, 2007. **102**: p. 261-266.

44.   K. Ikuta, S. Daifu, T. Hasegawa, and H. Higashikawa, *Hyper-finger for Remote Minimally invasive Surgery in Deep Area*, in *Medical Image Computing and Computer-Assisted Intervention -MICCAI 2002-Lecture Notes in Computer Science*, T. Dohi and R. Kikinis, Editor 2002, Springer: Berlin. p. 173-181.

45.   A. Degani, H. Chose, A. Wolf, and M. A. Zenati. *Highly articulated robotic probe for minimally invasive surgery.* in *ICRA 2006. Proceedings 2006 IEEE International Conference on Robotics and Automation,.* 2006. Orlando, FL: IEEE.

46.   T. Ota, A.DDegani, D. Schwartzman, B. Zubiate, J. McGarvey, H. Choset, and M. A. Zenati, *A Novel Highly Articulated Robotic Surgical System For Epicardial Ablation*, in *Engineering in Medicine and Biology Society, 2008.*

*EMBS 2008. 30th Annual International Conference of the IEEE*2008, IEEE: Vancouver, BC. p. 250 - 253.

47.   P. E. Dupont, J.Lock, B. Itkowitz, and E. Butler, *Design and Control of Concentric-Tube Robots.* IEEE Transaction on Robotics, 2010. **26**(2): p. 209-225.

48.   S. Okazawa, R.Ebrahimi, J. Chuang, S. E. Salcudean, and R. Rohling,, *Hand-Held Steerable Needle Device.* IEEE/ASME Transactions on Mechatronics, 2005. **10**(3): p. 285-296.

49.   M. Mahvash and M. Zenati, *Toward a hybrid snake robot for single-port surgery*, in *2011 Annual International Conference of the IEEE, Engineering in Medicine and Biology Society, EMBC,* 2011, IEEE: Boston, MA. p. 5372-5375.

50.   D. Salle, P.Bidaud, and G. Morel. *Optimal design of high dexterity modular MIS instrument for coronary artery bypass grafting.* in *Proceedings. ICRA '04. 2004 IEEE International Conference on Robotics and Automation.* 2004. New Orleans USA: IEEE.

51.   J. Peirs, D.Reynaerts, H. Van Brussel, *A miniature manipulator for integration in a self-propelling endoscope.* Sensors and Actuators, 2001. **92**(3): p. 343{349.

52.   N. Simaan, R.Taylor, and P. Flint. *A Dexterous System for Laryngeal Surgery.* in *Proceedings. ICRA '04. 2004 IEEE International Conference on Robotics and Automation.* 2004. New Orleans, USA: IEEE.

53.   K. Xu, and N. Simaan, *Actuation Compensation for Flexible Surgical Snake-like Robots with Redundant.* in *Proceedings of the 2006 IEEE International Conference on Robotics and Automation.* 2006. Orlando, Florida: IEEE.

54.   J. Peirs, H.Van Brussel, D. Reynaerts, and G. De Gersem, *A Flexible Distal Tip with Two Degrees of Freedom for Enhanced Dexterity in Endoscopic Robot Surgery* The 13th Micromechanics Europe Workshop, 2002: p. 271-274.

55.   Y. Sekiguchi , Y. Kobayashi , Y. Tomono , H. Watanabe , K. Toyoda , K. Konishi , M. Tomikawa , S. Ieiri , K. Tanoue , M. Hashizume , M.G. Fujie, *Development of a Tool Manipulator Driven by a Flexible Shaft for Single Port Endoscopic Surgery*, in *International Conference on Biomedical Robotics and Biomechatronic*2010, IEEE: Tokyo. p. 120-125.

56.   D.A. Summers, *Waterjetting Technology*1995, London: E&FN Spon.

57.   C. A. Fourness and C. M. Pearson*Paper metering, cutting, and reeling*, 1935, Paper Patents Co: US.

58.   C. Johnson, *Method for cutting up plastic and semi-plastic masses*, 1959, Durox Internat S A.

59.   B.G. Schwacha, *Liquid cutting of hard materials*, 1961, North American Aviation Inc.

60.   P. Rice, *Process for cutting and working solid materials*, in *US Patents*1965, Union Carbide Corp.

61.   N.C. Franz, *High velocity liquid jet*, 1970, Franz Norman C.

62.   N. Franz, *Very high velocity fluid jet nozzles and methods of making same*, 1973, Franz N.

63.   R. Chadwick, *Nozzle for producing fluid cutting jet*, 1973, Bendix Corp.

64.   M. A. Hashish, M.J.Kirby, Y-H. Pao, *Method and apparatus for forming a high velocity liquid abrasive jet*, in *US Patent*1987, Flow Industries, Inc.: USA.

65.   KMT. *Waterjet Cutting Systems*. 2014; Available from: http://www.kmt-waterjet.com/waterjet-cutting-solutions.aspx.

66.   R. Eggers, *Industrial High Pressure Applications: Processes, Equipment, and Safety*2012, Germany: Wily-VCH. 422.

67.   J. Wang, and D.K. Shanmugam, *Cutting meat with bone using an ultrahigh pressure abrasive waterjet.* Meat Sci, 2009. **81**(4): p. 671-7.

68.   K. Schwieger, V.Carrero, R. Rentzsch, A. Becker, N. Bishop, E. Hille, H. Louis, M. Morlock, M. Honl, *Abrasive water jet cutting as a new procedure for cutting cancellous bone--in vitro testing in comparison with the oscillating saw.* J Biomed Mater Res B Appl Biomater, 2004. **71**(2): p. 223-8.

69.   D.N. Papachristou and R. Barters, *Resection of the liver with a waterjet.* British journal of Surgery, 1982. 69: p. 93-94.

70.   B.G. Persson, B. Jeppson, K. Tranberg, K. Roslund, S. Bengmark *Transection of the liver with a water jet.* Surg Gynecol Obstet, 1989. 168: p. 267-268.

71.   Y. Une, J.Uchino, T. Horie, Y. Sato, K. Ogasawara, A. Kakita, F. Sano *Liver resection using a water jet.* Cancer Chemother Pharmacol 1989. 23(S74-S77).

72.   H.U. Baer, G.J. Maddern and L.H. Blumgart, *Hepatic Surgery Facilitated By a New Jet Dissector.* HPB Surgery, 1991. **4**: p. 137-146.

73.   H.U. Baer, G.J. Maddern, and L.H. Blumgart, *New water-jet dissector: initial experience in hepatic surgery.* Br. J. Surg, 1991. **78**: p. 502-503.

74. R. Izumi, K.Yabushita, K.Shimizu, M. Yagi, A. Yamaguchi, K. Konishi, T. Nagakawa, and I. Miyazaki, *Hepatic Resection Using a Water Jet Dissector.* Jpn. J. Surg, 1992. **23**: p. 31-35.

75. C.M. Vollmer, E.Dixon, A. Sahajpal, M.S. Cattral, D.R. Grant, S. Gallinger, B.R. Taylor, P.D. Greig, *Water-jet dissection for parenchymal division during hepatectomy.* HPB (Oxford), 2006. **8**(5): p. 377-85.

76. J. Piek, J.Oertel, and M. R. Gaab, *Waterjet dissection in neurosurgical procedures: clinical results in 35 patients.* J Neurosurg, 2002. **96**: p. 690-696.

77. J. Oertel, M.R.Gaab, A. Knapp, H. Essig, R. Warzok,and J. Piek, *Water Jet Dissection In Neurosurgery: Experimental Results In The Porcine Cadaveric Brain.* Neurosurgery, 2002. **52**: p. 153-159.

78. J. Oertel, M.R.Gaab, T. Schiller, H. W. Schroeder, R. Warzok, J. Piek, *Towards waterjet dissection in neurosurgery: experimental in-vivo results with two different nozzle types.* Acta Neurochir (Wien), 2004. **146**(7): p. 713-20.

79. J. Oertel, M.Gen, J. K. Krauss, M. Zumkeller, M. R. Gaab, , *The use of waterjet dissection in endoscopic neurosurgery.* J Neurosurg, 2006. **105**: p. 928-931.

80. J. Hubert, E.Mourey, J. M. Suty, A. Coissard, J. Floquet, and P. Mangin, *Water-jet dissection in renal surgery: experimental study of a new device in the pig.* Urol Res, 1996. **24**: p. 355-359.

81. R. D. Penchev, J.E.Losanoff, and K. T. Kjossev, *Reconstructive Renal Surgery Using a Water Jet.* the journal of Urology, 1999. **162**: p. 772-774.

82. R.F. Basting, N.Djakovic, and P. Widmann, *Use of Water Jet Resection in Organ-Sparing Kidney Surgery.* Journal Of Endourology, 2000. **14**(6): p. 501-505.

83. R. Gurunluoglu, *Experiences with waterjet hydrosurgery system in wound debridement.* World J Emerg Surg, 2007. **2**: p. 10.

84. H.O. Rennekampff, H.E.Schaller, D. Wisser, M. Tenenhaus, *Debridement of burn wounds with a water jet surgical tool.* Burns, 2006. **32**(1): p. 64-9.

85. S. Hloch, J.Valíček, D. Kozak, *Preliminary Results Of Experimental Cutting Of Porcine Bones By Abrasive Waterjet.* Technical Gazette, 2011. **18**(3): p. 467-470.

86. Water Jets. *waterjet equipment*. 2014; Available from: http://waterjets.org/index.php?option=com_frontpage&Itemid=1.

87. Flow Waterjet. *Waterjet Cutting Technology*. 2014; Available from: http://www.flowwaterjet.com/en/waterjet-technology.aspx.

88. C. L. Dym, W.H.Wood, M. J. Scott, *Rank ordering engineering designs: pairwise comparison charts and Borda counts*. Research in Engineering Design, 2002. **13**: p. 236-242.

89. J.E. Shigley, and C.R. Mischke, *Mechanical Engineering Desgin*. 6th ed2001, New York: McGraw-Hill.

90. S.H. Zhou , I.D.M cCarthy, A.H. McGregor , R.R. Coombs , S.P.Hughes *Geometrical dimensions of the lower lumbar vertebrae--analysis of data from digitised CT images*. Eur Spine J, 2000. **9**(3): p. 242-248.

91. S.J. Leach, and G.L. Walker, *Some Aspects of Rock Cutting by High Speed Water Jets*. Philosophical Transactions, 1966. **260**(1110): p. 295-310.

92. P K. Kundu, I.M.Cohen, D R. Dowling, *Fluid Mechanics*. 5th ed2012, UK: Elsevier Inc.

93. G. Devol, *Programmed Article Transfer*, in *USA Patent Office*, U. Patent, Editor 1961. p. 20.

94. H.D. Taghirad, *Parallel Robots: Mechanics and Control*2013, Boca Raton: CRC Press. 519.

95. J.E. Gwinnett, *Amusement device*, in *US Patent*1931. p. 5.

96. L. Bonev, *The True Origins of Parallel Robots*. 2003; Available from: http://www.parallemic.org/Reviews/Review007p.html.

97. W.L. Pollard, *Position controlling apparatus*, US Patent No. 1,789,680, 1942.

98. V. E. Gough, and S. G. Whitehall, *Universal tyre test machine*. in *Proceedings of the FISITA Ninth International Technical Congress*. 1962.

99. J.P. Merlet, *Parallel Robots* Second ed2006, The Netherlands: Springer.

100. M. Suliteanu and W. R. La Valley, *Antenna support*, US Patent No. 3,229,941, 1966.

101. E.R. Peterson, *Movable and rotatable top*, US Patent No. 3,288,42, 1966.

102. K.L. Cappel, *Motion Simulator,* US Patent No. 3,295,224, 1967.

103. D. Stewart, *A Platform with six degree of freedom.* Proc Instn Mech Engrs 1965. **180**: p. 371-386.

104. R. Clavel, *Device for the movement and positioning of an element in space*, 1990. US Patent 4976582.

105.   X-J. Liu and J. Wang, *Parallel Kinematics: Type, Kinematics, and Optimal Design*2014, New York: Springer. 309.

106.   N.E. Technology, *Motion-Basics-and-Standards*. 2015; Available from: https://www.newport.com/Motion-Basics-and-Standards/140230/1033/content.aspx.

107.   Maplesoft. *Robot Manipulators Forward Kinematics of Serial Manipulators*. Engineering Fundamentals; Available from: http://www.maplesoft.com/content/EngineeringFundamentals/14/MapleDocument_14/Forward%20Kinematics.pdf.

108.   Maplesoft. *Robot Manipulators Forward Kinematics of Serial Manipulators*. Engineering Fundamentals; Available from: http://www.maplesoft.com/content/EngineeringFundamentals/14/MapleDocument_14/Forward%20Kinematics.pdf.

109.   A. Akbas, *Application of Neural Networks to Modeling and Control of Parallel Manipulators*, in *Parallel Manipulators, New Developments*, J.-H. Ryu, Editor 2008, I-Tech Education and Publishing: Vienna, Austria. p. 21-40.

110.   S. V. Sreenivasan, K.J.Waldron, and P. Nanua *Closed-Form Direct Displacement Analysis Of A 6-6 Stewart Platform.* Mech. Mach. Theory, 1994. **29**(6): p. 855--86.

111.   C.C. Nguyen, S.S.Antrazi, J-Y Park and Z-L Zhou, *Trajectory Planning and Control of a Stewart Platform-Based End-Effector with Passive Compliance for Part Assembly.* Journal of lntelligent and Robotic Systems, 1992. **6**: p. 263-281.

112.   T-Y. Lee, and J.-K.Shim., *Forward Kinematics of the General 6-6 Stewart Platform Using Algebraic Elimination.* Mechanism and Machine Theory, 2001. **36**: p. 1073-1085.

113.   C. Innocenti, *Direct Kinematics in Analytical Form of the 6-4 Fully-Parallel Mechanism* Journal of Mechanical Design 1995. **117**: p. 89-95.

114.   K.H.Hunt, *Structural Kinematics of In- Parallel-Actuated Robot-Arms.* Journal of Mechanisms, Transmissions, and Automation in Design, 1983. **105**: p. 705-712.

115.   K. H. Hunt, and E.I.F. Primrose, *Assembly Configurations Of Some In-Parallel-Actuated Manipulators* Mech. Mach. Theor, 1993. **28**(1): p. 3142.

116.   W. Lin, M.Griffis, and J. Duffy, *Forward Displacement Analyses of the 4-4 Stewart Platforms* Transactions of the ASME 1992. **114**: p. 444-450.

117.   Z. Shao, X.Tang, and L. Wang, *Optimum Design of 3-3 Stewart Platform Considering Inertia Property*. Advances in Mechanical Engineering, 2013. Volume 2013(Article ID 249121): p. 10 pages.

118.   S. Staicu, *Dynamic Analysis Of The 3-3 Stewart Platform*. U.P.B. Sci. Bull., Series D, 2009. **71**(2): p. 3-18.

119.   Y. D. Patel, P.M.George, *Parallel Manipulators Applications—A Survey*. Modern Mechanical Engineering, 2012. **2**: p. 57-64.

120.   J. Angeles, *Fundamentals of Robotic Mechanical Systems: Theory, Methods, and Algorithms*. Second ed, ed. F.F. Ling2003, New York: Spriger.

121.   G. Brandt, A.Zimolong, L. Garrat, P. Merloz, H-W. Staudte, K. Radermacher, S. Lavallée, H. -W. Staudte, G. Rau, *CRIGOS: A Compact Robot for Image-Guided Orthopedic Surgery*. IEEE Transactions on Information Technology in Biomedicine, 1999. **3**(4): p. 252-260.

122.   M. Girone, G.Burdea, M. Bouzit and V. Popescu, *A Stewart Platform-Based System for Ankle Telerehabilitation*. Autonomous Robots, 2001. **10**: p. 203-212.

123.   J.E. Deutsch, J.Latonio, G. Burdea, and R. Boian *Rehabilitation of Musculoskeletal Injuries using the Rutgers Ankle Haptic Interface: 3 case reports*, in *EuroHaptics Conference*2001, EuroHaptics: Birmingham, UK. p. 11-16.

124.   R. Boian, M.Bouzit, G. Burdea, and J. Deutsch. *Dual Stewart Platform Mobility Simulator* in *Proceedings of the 26th Annual International Conference of the IEEE EMBS* 2004. San Francisco: IEEE.

125.   R. Boian, M.Bouzit, G. Burdea, J. Lewis and J. Deutsch. *Dual Stewart Platform Mobility Simulator*. in *ICORR 2005. 9th International Conference on Rehabilitation Robotics,*. 2005. Chicago: IEEE.

126.   T. Onodera, M.Ding, H. Takemura, and H. Mizoguchi, *Design and Development of Stewart Platform-Type Assist Device For Ankle–Foot Rehabilitation*, in *First International Conference on Innovative Engineering Systems (ICIES),*2012, IEEE: Alexandria. p. 1-6.

127.   H. Lin , J.Q.Wang, W. Han, *Parallel Manipulator Robot Assisted Femoral Fracture Reduction on Traction Table*, in *35th Annual International Conference of the IEEE EMBS*2013, IEEE: Osaka, Japan. p. 4847 - 4850.

128.   D. Barkana, *Design and implementation of a control architecture for robot-assisted orthopaedic surgery.* The International Journal Of Medical Robotics And Computer Assisted Surgery, 2010. **6**(1): p. 42-56.

129.   H. Tian, D.Wu, Z. Du, J. Ma, L.Sun. *Development of a Robot System Assisting Artificial Cervical Disc Replacement Surgery*. in *Proceedings of the 2010 IEEE International Conference on Robotics and Biomimetics*. 2010. Tianjin, China: IEEE.

130.   M. Shoham, M.Burman, E. Zehavi, L.Joskowicz, E.Batkilin, and Y. Kunicher, *Bone-Mounted Miniature Robot for Surgical Procedures: Concept and Clinical Applications.* IEEE Transactions on Robotics and Automation, 2003. **19**(5): p. 893 - 901.

131.   A. Wolf, B.Jaramaz, B. Lisien, and A. M. DiGioia, *MBARS: Mini Bone Attached Robotic System for Joint Arthroplasty.* International Journal of Medical Robotics and Computer Assissted Surgery, 2005. **1**(2): p. 101-121.

132.   A. Wolf, and B. Jaramaz, *MBARS: Mini Bone Attached Robotic System for Joint Arthroplasty*, in *BioRob 2006. The First IEEE/RAS-EMBS International Conference on Biomedical Robotics and Biomechatronics.*2006, IEEE: Pisa. p. 1053 - 1058.

133.   C. Plaskos, P.Cinquin, S Lavalle´ e, A J Hodgson, *Praxiteles: a miniature bone-mounted robot for minimal access total knee arthroplasty.* International Journal Medical Robotics and Computer Assisted Surgery, 2005. **1**(4): p. 67–79.

134.   L. B. Kratchman, G.S.Blachon, T. J. Withrow, R. Balachandran, R. F. Labadie, and R.J. Webster Design of a Bone-Attached Parallel Robot for Percutaneous Cochlear Implantation. IEEE Transactions on Biomedical Engineering, 2011. 58(10): p. 2904 - 2910.

135.   D. Raabe, K.Alemzadeh, A.J.L. Harrison, A.J. Ireland *The chewing robot: a new biologically-inspired way to evaluate dental restorative materials* in *Annual International Conference of the IEEE Engineering in Medicine and Biology Society EMBC*2009, IEEE: Minneapolis, MN. p. 6050 - 6053.

136.   D. Raabe, A.Harrison, A. Ireland, K. Alemzadeh, J. Sandy, S. Dogramadzi, C. Melhuish and S Burgess, *Improved single- and multi-contact life-time testing of dental restorative materials using key characteristics of the human masticatory system and a force/position-controlled robotic dental wear simulator.* Bioinspiration & Biomimetics, 2012. **7**(1): p. 1-17.

137.   T. Tsai, and Y. Hsu, *Development of a Parallel Surgical Robot with Automatic Bone Drilling Carriage for Stereotactic Neurosurgery*, in *2004 IEEE International Conference on Systems, Man and Cybernetics*2004, IEEE: Hague, Netherlands. p. 2156-2161.

138.   M. Zimmermann, R.Krishnan, A. Raabe, and V. Seifert, *Robot-assisted navigated endoscopic ventriculostomy: implementation of a new technology and first clinical results.* Acta Neurochir (Wien), 2004. **146**(7): p. 697-704.

139.   H.Yu, J.Shen, K. M. Joos, and N. Simaan, *Design, Calibration and Preliminary Testing of A Robotic Telemanipulator for OCT guided Retinal Surgery*, in *2013 IEEE International Conference on Robotics and Automation (ICRA)*2013, IEEE: Karlsruhe, Germany. p. 225-231.

140.   The Royal College of Ophthalmologists, *Vitreoretinal Surgery - General Description*. 2014; Available from: http://www.rcophth.ac.uk/Revalidation/page.asp?section=731&sectionTitle=Vitreoretinal+Surgery+-+General+Description.

141.   T. Nakano, N.Sugita, T. Ueta, Y. Tamaki, and M. Mitsuishi, *A parallel robot to assist vitreoretinal surgery.* International Journal of Computer Assisted Radiology and Surgery, 2009. **4**(6): p. 517-526.

142.   Institute of Mechanical Engineers, *Kinetic Frame Needs New Backers*. 2015; Available from: http://www.imeche.org/news/engineering/kinetic-frame-needs-new-backers.

143.   P. Harkin, *Adjustable Structures*, W. PCT, Editor 2014: UK. p. 34.

144.   P. Harkin, *form changing structures*; Available from: http://www.formchangingstructures.com/.

145.   N. Rojas, and F. Thomas, *The octahedralmanipulator revised,*. IEEE International Conference on Robotics and Automation,, 2012: p. 2293-2298,St. Paul, Minn, USA.

146.   J. Wendlandt, *Stewart Platform Mechanical System*. 2009; Model and simulate the physical components and synthesize controllers of the Stewart Platform]. Available from: http://uk.mathworks.com/matlabcentral/fileexchange/2334-stewart-platform-mechanical-system.

147.   A.M. Okamura, *Haptic Feedback in Robot-Assisted Minimally Invasive Surgery.* Curr Opin Urol, 2009. **19**(1): p. 102–107.

148.   H. Xina, J.S.Z eleka, H. Carnahanb, *Laparoscopic surgery, perceptual limitations and force: A review*, in *First Canadian Student Conference on Biomedical Computing*2006: Kingston, Ontario, Canada.

149.   E.H. Aly, *Laparoscopic Surgery for Rectal Cancer: Approaches, Challenges and Outcome*, in *Contemporary Issues in Colorectal Surgical Practice*, Y.-H. Ho, Editor 2012, Intech.

150.   B. Hannaford, A.M.Okamura, *Haptics*, in *Springer Handbook of Robotics*, a.O.K. B. Siciliano, Editor 2008, Springer: Berlin. p. 719-739.

151.   A. El Saddik, M.Orozco, M. Eid *Haptics Technologies: Bringing Touch to Multimedia*2011, Berlin: Springer.

152.   M.A. Srinivasan, and C. Basdogan, *Haptics in Virtual Environments: Taxonomy, Research Status, and Challenges.* Computers and Graphics, 1997. **21**(4): p. 393-404.

153.   P-L. Yen, and B. L. Davies, *Active constraint control for image-guided robotic surgery.* J. Engineering in Medicine, 2010. **224** part H(Special Issue Paper): p. 623-631.

154.   A. Kapoor, M. Li and R. H. Taylor, *Constrained Control for Surgical Assistant Robots*. In *Proceedings of the 2006 IEEE International Conference on Robotics and Automation*. 2006. Orlando, Florida: IEEE.

155.   M. Scent, J. Wolff, and M. Buss, *Invariance Control in Robotic Applications: Trajectory Supervision and Haptic Rendering*, in *American Control Conference*2008: Seattle, WA. p. 1436 - 1442.

156.   H. Seraji, and B. Bon, *Real-Time Collision Avoidance for Position-Controlled Manipulators.* IEEE Transac- tions on Robotics and Automation,, 1999. **15**(4): p. 670-677.

157.   O. Khatib. *Real-time obstacle avoidance for manipulators and mobile robots*. in *1985 IEEE International Conference on Robotics and Automation. Proceedings*. 1985. IEEE.

158.   A. A. Maciejewski, and C. A. Klein, *Obstacle Avoidance for Kinematically Redundant Manipulators in Dynamically Varying Environment.* The International Journal of Robotics Research, 1985. **4**(3): p. 109-116.

159.   Z. Bingul and O. Karahan, *Dynamic Modeling and Simulation of Stewart Platform*, in *Serial and Parallel Robot Manipulators - Kinematics, Dynamics, Control and Optimization*, D.S. Kucuk, Editor 2012, InTech.

160.   S. Song and D. Kwon, *New Direct Kinematic Formulation of the 6 D.O.F Stewart-Gough Platforms Using the Tetrahedron Approach.* Transactions on Control Automation and Systems Engineering, 2002. **4**(3): p. 217-223.

161.   L. Rolland, *Certified solving of the forward kinematics problem with an exact algebraic method for the general parallel manipulator*, in *Parallel Manipulators, towards New Applications*, H. Wu, Editor 2008, INTECH.

162.   S-H. Lee, J.-B.Song, W-C. Choi, D. Hong, *Position control of a Stewart platform using inverse dynamics control with approximate dynamics.* Mechatronics, 2003. **13**: p. 605–619.

163.   NOVINT Falcon, *Six Degrees of Freedom Haptic Controller*; Available from: http://www.novint.com/index.php/novintfalcon.

164.   L. Bonev, *A geometrical method for computing the constant-orientation workspace of 6-PRRS parallel manipulators.* Mechanism and Machine Theory, 2001. **36**: p. 1-13.

165.   MFA/Comodrills. *950D Series Single Ratio Metal Gearbox*; Available from: http://www.mfacomodrills.com/gearboxes/950d_series.html.

166.   Datasheet Catalog. *L293, L293D Quadruple Half-H Drivers*; Available from: http://pdf.datasheetcatalog.com/datasheet/texasinstruments/l293d.pdf.

167.   Texas Instruments Incorporated, *L293, L293D Quadruple Half-H Drivers*, 2004: Dallas, Texas. p. 1-17.

168.   Tyco Electronics DPL12 Rotary Encoder Datasheet; Available from: http://www.te.com/commerce/DocumentDelivery/DDEController?Action=srchrt rv&DocNm=1-1773449 0_DPL12_SERIES&DocType=DS&DocLang=English&s_cid=1046.

169.   Wolfram Math World, *Spherical Coordinates*; Available from: http://mathworld.wolfram.com/SphericalCoordinates.html.

170.   B. T. Bethea, A.M.O., M. Kitagawa, T. P. Fitton, S. M. Cattaneo, V. L. Gott, W. A.Baumgartner,   and D. D. Yuh, *Application of Haptic Feedback to Robotic Surgery.* J Laparoendosc Adv Surg Tech A, 2004. **14**(3): p. 191–195.

171.   McLennan Servo Supplies, *Geared Stepper Motor P542-M48 Series Data Sheet*.

172.   D. Henrich, and P. Stolka, *Principles Of Navigation In Surgical Robotics*, in *MRVN 2004 – Medical Robotics, Navigation and Visualisation*2004: Remagen, Germany. p. 1-10.

173.   M. Schneberger, *Infrared Optical TrackingSystems Mathematicaland Operation*

Appendices

1.1 Surgical Robots

1.1 Surgical CAD/CAM Systems

Table 17: Sampler of surgical CAD/CAM systems

System	Institution	Coun-try	Year	Guid-ance/Cont rol	Clinical Area	Applied to	Commercial / Regulatory Status	Mount	Positioning Arm	DOF	RCM Type	Back-driv-ability
Acrobot	Imperial College	UK	2001	Synergetic	Orthope-dic	Human	-	Floor trolley Table clamps	6 dof active + brakes	3	-	Low
Arthrobot	KAIST	Korea	2002	Gauge-Based	Orthope-dic	Phantom	-	Bone	-	4	Program-mable	Low
Brigham MRI	AIST / Brigham & Women Hospital	Japan / USA	1999	MRI Guided	Prostate Brachy-therapy	Phantom	Non-commercial	MRI Scanner	-	5	-	Low
Breast MRI System	Karlsruhe University	Ger-many	2000	MRI Guided	Bresst Biopsy	Animal	-	Scanner Table	-	6	-	Low
CyberKnife	Accuray	USA	1999	X-Ray Guided	Radiosur-gery	Human	Commercial	Floor	-	6	-	Very Low
GRIGOS	Helmholz Inst; TIMC-IMAG	Ger-many; France	1997	Surgical CAD /CAM	Ortho-paedics	Phantom	-	Table	-	6	-	Low
KEN-MRI	University of Tokio	Japan	1995	MRI Guided	Neuro-surgery	Phantom	-	Table	-	6	Goniometer Arc	Low
Minerva	University of Lausanne	Switzer-land	1993	X-Ray Guided	Neuro-surgery	Human	-	Floor	3 transl dof	3	-	Low
IGOR	Grenoble University	France	1992	Preoperat. Imaging and Tracking	Neuro-surgery	Human	Non-commercial	Floor	-	6	-	Very Low
Neuro Mate	Integrated Surgical Systems	France / USA	1996	Preoperat. Imaging and Tracking	Neuro-surgery	Human	Commercial / FDA Cleared	Floor Trolley	-	6	-	Very Low
PAKY-RCM	Johns Hopkins	USA	1998-2003	X-Ray Guided	Percuta-neous Access	Human	Transfer/FDA - IDE	Table Mount	7 dof	3	Belt Parallelo-gram	Very Low
PADyC	TIMC/IMAG	France	1995 - 2001	Synergetic	Cardiac	Animal	-	Floor	-	6	-	Very High with Brakes
PinPoint	Philips / Marconi Medical Systems	USA	2000	CT Tracker Arm	CT Interven-tions	Human	Commercial	Ceiling	6	-	-	Very High
PROBOT	Imperial College	UK	1995	US Guided	Urology	Human	Non-commercial	Floor	Slider	3	Goniometer Arc	Low
ROBODOC	Integrated Surgical Systems	USA	1992	CT-based preop. plan	Orthope-dic	Human	Commercial/ Cleared in Europe	Floor with fixator to bone	Modified SCARA	6	-	Low
Robards-breast	Robards Research Inst.	Canada	2001	Ultrasound	Breast biopsy	animal	-	Table	Cartesian	3	-	Low
RX-90	Karlsruhe University / ortoMarquet	Ger-many	1999	Synergetic	Maxillo-facial	Animal	Commercial	Floor	-	6	-	Low
Siemens CT	Siemens, AG	Ger-many	2000	Manual + Active	In-CT percuta-neous	Animal	-	Table	Passive arm + 2dof active	2	5 bar parallel lnkage	Low?
SS-Orthop	Scuola Superiore Saint'Anna	Italy	1998	CT-based preop plan	TKA	Cadaver	-	Floor?	-	5	-	Low
AcuBot	Johns Hopkins / Georgetown University	USA	2001	X-ray & CT Guided	Percuta-neous Access	Cadaver	Transfer / FDA - IDE	Bridge Scanner Table Mount	7 dof	6	Belt Parallelo-gram	Very Low
WAM	Z-KAT Inc. / Barrett Tech-nology	USA	2002	Synergetic	Spine	Phantom	-	Floor	-	4+1	-	Low

217

1.2   Surgical Assistant Systems

Table 18: Samplers of surgical assistant systems

System	Institution	Country	Year	Guidance/Control	Clinical Area	Applied to	Commercial / Regulatory Status	Mount	Positioning Arm	DOF	RCM Type	Back-driv-ability
AESOP	Computer Motion	USA	1992	Pad, Foot, Voice, Remote	Laparo-scopy	Human	Commercial / FDA Cleared 1994	Cart and Table Mount	-	3	Passive	Low
BlueDRAGON	University of Washington, Seattle	USA	2002	Haptic Device	Laparo-scopy	Phantom	-	Table	-	4	Bar Parallelo-gram	Very High
CLEM	TIMC/IMAG	France	2002	-	Laparo-scopy	Phantom	-	Table	-	3	Compliant	High
daVinci	Intuitive Surgical	USA	1999	Master-Slave	Laparo-scopy	Human	Commercial / FDA Cleared 2000	Floor Trolley	Passive, breaks	2*6 +4	Bar Parallelo-gram	High
LARS	IBM	USA	1995	Synergetic / Image Guided	Laparo-scopy / Percuta-neous Access	Animal	-	Floor Trolley	-	6	Bar Parallelo-gram	Low
SCALPP	LIRMM	France	2001	Surgical Assistant	Skin harvesting	?	-	Floor	Augmented SCARA	6	-	?
SS-Colon	Scuola Superiore Saint'Anna	Italy	1997-2002	Surgical Assistant; Master-slave	Colono-scopy	Cadaver	-	Free mount	-	1?	-	Low
Steady Hand	Johns Hopkins	USA	1999	Synergetic	microsur-gery	cadaver	Non-commercial	Table	-	7	Belt Parallelo-gram	Mixed
SurgiScope	Humboldt University / Jojumarie Intelligente Instrumente /Elekta	Germany	1997	Navigation + Surgeon inputs	Micro-scope holder; brachy-therapy	Human (micro-scopes); animals (brachy-therapy)	Commercial	Ceiling	Parallel	6	-	Low
TER	TIMC/IMAG	France	2001	Master-slave	Tele-Echogra-phy	phantom	-	Table/patient	Parallel	2	Constraint at entry port	High
UBC-US	University of British Columbia	Canada	1999	3D Ultra-sound	Arterial exams	Human	-	Floor Trolley	-	6	5 Bar Par-allelogram	High
UBC-MW	University of British Columbia	Canada	1997	Master-slave	Micro-surgery	phantom	-	Table	6DOF active robot	6	-	High
UCB/UCSF	UC Berkeley UC San Fran.	USA	1999, 2003	Master-slave	Laparo-scopy	Animal	-	Floor trolley	6 DOF	6	Passive	High
UT-LAP	University of Tokyo	Japan	1999	Gyro Sensor / Foot	Laparo-scopy	Phantom	-	Table	-	4	Passive (Bar Par-allelogram Included)	High
Zeus	Computer Motion	USA	1998	Master-Slave	Laparo-scopy	Human	Commercial	Table Mount	-	3	Free wrist with con-strained isocenter	Low

1.2 Design Process and Analysis

1.3 Quality Function Deployment (QFD 1)

Customer Requirement (Whats)	Weights		interface with monitoring device	weight	time to cut	bending capacity	durable	twisting	max. external tempreature	diameter	smooth edges	sharp end	easy to set up	fine end	control the movement	control console	suction machine	sensors	waterpump			
Flexibility	0.1847	0.207				9									9		1					
Cutting the tissue	0.1847	0.207			3		3	3	1			9										
Small as possible	0.0923	0.104		1						9				1			3	3				
Easy to use	0.0617	0.069		3	1	1		3					3		3	3	1					
Monitoring the procedure	0.0617	0.069	9			9				9	3				9							
Providing water	0.0617	0.069				3				3	1								9			
Sucking the waste	0.0617	0.069				3				9	1						9					
Tele-operating	0.0464	0.052														9		9				
Force feedback	0.0464	0.052														3		9				
Safe to surrounding tissues	0.0909	0.102						1	9	3	9	9		3	3		1	3				
Last long time							9											3	3			
Precise cut														1		1	3	1				
Check Sum		1.00																				
Goal Value																						
Threshold Value																						
Weighted Performance			0.6	0.3	0.7	3.0	0.6	0.9	1.1	2.7	1.3	2.8	0.2	0.4	3.0	0.8	1.3	1.6	0.6	0.0	0.0	0.0
Percent Performance			0.028	0.014	0.031	0.135	0.028	0.042	0.051	0.123	0.058	0.127	0.009	0.019	0.137	0.038	0.060	0.071	0.028	0.000	0.000	0.000

Figure 160: Spread sheet shows the process of QFD1 showing the translation of Customer Requirements into measurable Technical Requirements.

1.4 Quality Function Deployment (*QFD2*)

Design Characteristics (Whats)	Weights		flexible tool	cooling machine	cutting tools	material	torque	waterproof	angle of view	lightweight	time to instal bit	direction control tools	tele-operation	light source	water source	monitoring device	vacume pump
			Units	Units	Units	Units	Units	Units	Units	Units	Units	Units	Units	Units	Units	Units	Units
interface with monitoring device	0.028	0.028	3		3					3				9		9	
weight	0.014	0.014								3							
time to cut	0.031	0.031			3							3					
bending capacity	0.135	0.135	9		9	3			9								
durable	0.028	0.028			3												
twisting	0.042	0.042						9									
max. external tempreature	0.051	0.051		9													
diameter	0.123	0.123			3												
smooth edges	0.058	0.058				3						3					
sharp end	0.127	0.127			9												
easy to set up	0.009	0.009			3				1		9	3					
fine end	0.019	0.019			3												
control the movement	0.137	0.137	9	9						3		9					
control console	0.038	0.038											3				
suction machine	0.060	0.060											9			9	
sensors	0.071	0.071						9					9				
waterpump	0.028	0.028											3		9		
Check Sum		1.00															
Goal Value																	
Threshold Value																	
Weighted Performance			2.5	1.7	3.1	0.6	0.4	0.6	1.2	0.5	0.1	1.5	1.4	0.3	0.3	0.3	0.5
Percent Performance			0.169	0.113	0.206	0.039	0.026	0.043	0.082	0.036	0.006	0.102	0.092	0.017	0.017	0.017	0.036

Figure 161: Spread sheet shows the process of QFD2 showing the translation of Technical Requirements into compliant Design Solution Requirements (functions)

1.3 Manual Bending Test of the Flexible Tip

Table 19: Table shows the raw and calculated data of the manual bending test of the flexible tip

mass(g)	mass(Kg)	weight(N)	deflection δy(mm)	deflection δx(mm)	NORMdeflection δy(m)	elasticity E (N/m^2)	elasticity E (MPa)
0	0	0	25	0	0	#DIV/0!	#DIV/0!
5	0.005	0.04905	30	0	0.005	2779911839	2779.911839
6	0.006	0.05886	33	0	0.008	2084933879	2084.933879
10	0.01	0.0981	38	4	0.013	2138393722	2138.393722
15	0.015	0.14715	45	5	0.02	2084933879	2084.933879
18	0.018	0.17658	48	5	0.023	2175583178	2175.583178
20	0.02	0.1962	51	6	0.026	2138393722	2138.393722
25	0.025	0.24525	60	10	0.035	1985651313	1985.651313
30	0.03	0.2943	65	12	0.04	2084933879	2084.933879
35	0.035	0.34335	70	15	0.045	2162153652	2162.153652
39	0.039	0.38259	71	16	0.046	2356881776	2356.881776
44	0.044	0.43164	75	18	0.05	2446322418	2446.322418
49	0.049	0.48069	80	20	0.055	2476648729	2476.648729
55	0.055	0.53955	85	30	0.06	2548252519	2548.252519
60	0.06	0.5886	86	30	0.061	2734339514	2734.339514
70	0.07	0.6867	88	31	0.063	3088790932	3088.790932
75	0.075	0.73575	90	32	0.065	3207590583	3207.590583
		0.115	75		0.05	651763224.2	651.7632242
3.97*10E-12		0.73575	115		0.09	2316593199	2316.593199
3.375*10E-3							

1.4 Calculation for Testing the Shape of the Output Jet:

$$m_0 = bucket\ weight = 269.5g$$

$$m_1 = m_0 + water\ weight = 1677g$$

$$m_w = water\ weight = m_1 - m_0 = 1407.5g$$

$$T = Time = 20s$$

$$\dot{m} = mass\ flow\ rate = m_w/T = 1407.5/20 = 70.4\ g/s$$

To calculate the output jet velocity:

$$\dot{m} = \rho V A$$

$$\therefore V = 127m/s$$

Where

ρ: Density of the water in kg/m^3

V: Flow speed, in m/s

A: Flow area, in m^2

$\dot{m}$: Mass flow rate, in kg/s

1.5 Calculating the Momentum Flow Rate Using Equations 5.3,5,6

Revolution (*turn*)	Flow Velocity *v* (*m/s*)	Momentum flow rate *F* (*kg m/s²*)
0.25	90.00	2.1
0.5	83.5	1.7
0.75	76.4	1.4
1	69.7	1.2
1.25	62.4	0.9
1.5	58.3	0.8
1.75	55.5	0.7
2	49.3	0.6
2.25	47.6	0.57
2.5	44.1	0.51
2.75	42.2	0.46
3	39.2	0.42

1.6   Motor-Encoder Functional Test Cell

1.5   Raw data of the accuracy test of the motor-encoder test cell

Table 20: Data for motor test cell accuracy with filter circuit vs. without filter circuit

| | Encoder Pulses | Observed Number of Revolutions | | | | | Observed Average | Expected | Error (%) |
| | | Trial number | | | | | | | |
		1	2	3	4	5			
With Filter	96	1	1	1	1	1	1	1	0
	960	10	10	10	10	10	10	10	0
	2400	24.9	25	25	24.9	25	24.96	25	0.16
	4800	50	49.8	49.9	49.8	49.9	49.88	50	0.24
	9600	99.4	99.6	99.5	99.6	99.5	99.52	100	0.48
Without Filter	96	0.98	0.95	0.98	0.99	0.98	0.976	1	2.4
	960	9.7	9.8	9.8	9.7	9.6	9.72	10	2.8
	2400	23.5	24.5	23.5	24	24.5	24	25	4
	4800	48	47.5	47.5	48.5	47	47.7	50	4.6
	9600	95	94	96	95	95.5	95.1	100	4.9

1.6   Raw data of the motor speed test

Table 21: Percentage error of rotation for different motor speeds

| | Rotational Speed, rpm | Encoder Pulses | Observed Number of Revolutions | | | | | Observed Average | Expected | Error (%) |
| | | | Trial number | | | | | | | |
			1	2	3	4	5			
With Filter	60	96	1	1	1	1	1	1	1	0
		960	10	10	10	10	10	10	10	0
		2400	24.9	25	25	24.9	25	24.96	25	0.16
		4800	50	49.8	49.9	49.8	49.9	49.88	50	0.24
		9600	99.4	99.6	99.5	99.6	99.5	99.52	100	0.48
	200	96	1	1	1	1	1	1	1	0
		960	9.95	10	9.95	10	10	9.98	10	0.2
		2400	24.9	24.95	24.9	25	24.9	24.93	25	0.28
		4800	49.9	49.8	49.7	49.8	49.9	49.82	50	0.36
		9600	99.4	99.6	99.5	99.4	99.5	99.48	100	0.52
	400	96	1	1	1	1	1	1	1	0
		960	9.9	10	10	10	9.95	9.97	10	0.3
		2400	24.9	24.95	24.9	24.9	24.95	24.92	25	0.32
		4800	49.5	49.9	49.8	49.9	49.9	49.8	50	0.4
		9600	99.3	99.4	99.45	99.5	99.4	99.41	100	0.59

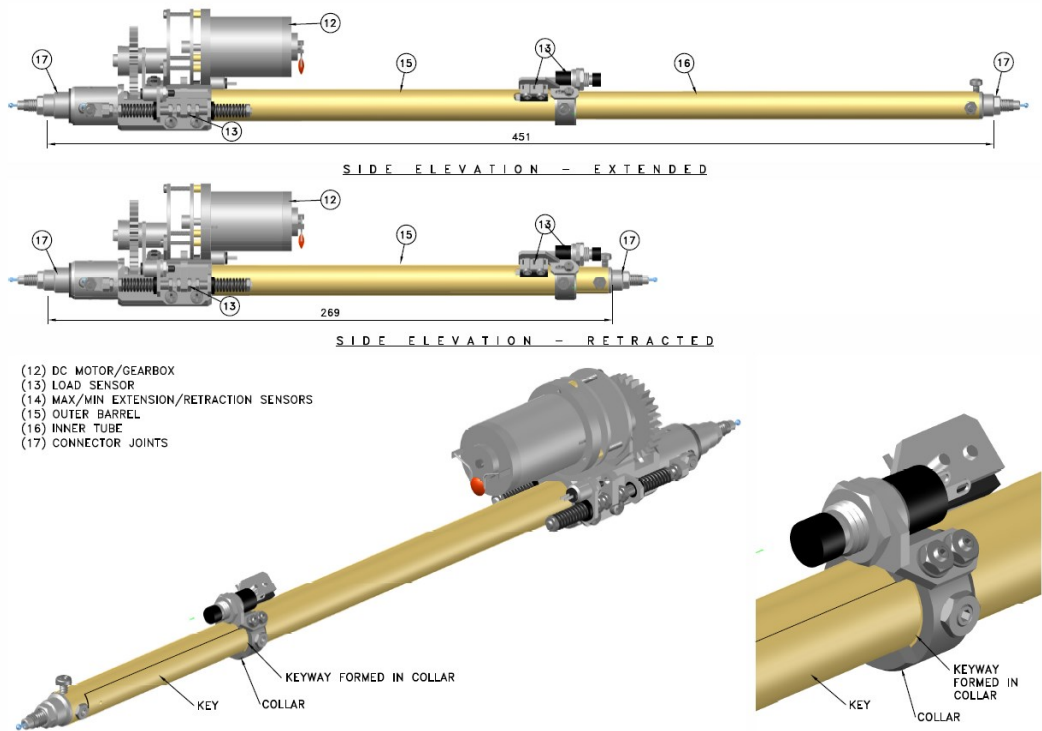## 1.7 Engineering Drawings of the Linear Actuator

Figure 162: Real view drawing of the completed linear actuator at minimum contraction and maximum extention (top), mechanism using key and keyway to prevent the actuator tubes from rotation (bottom).
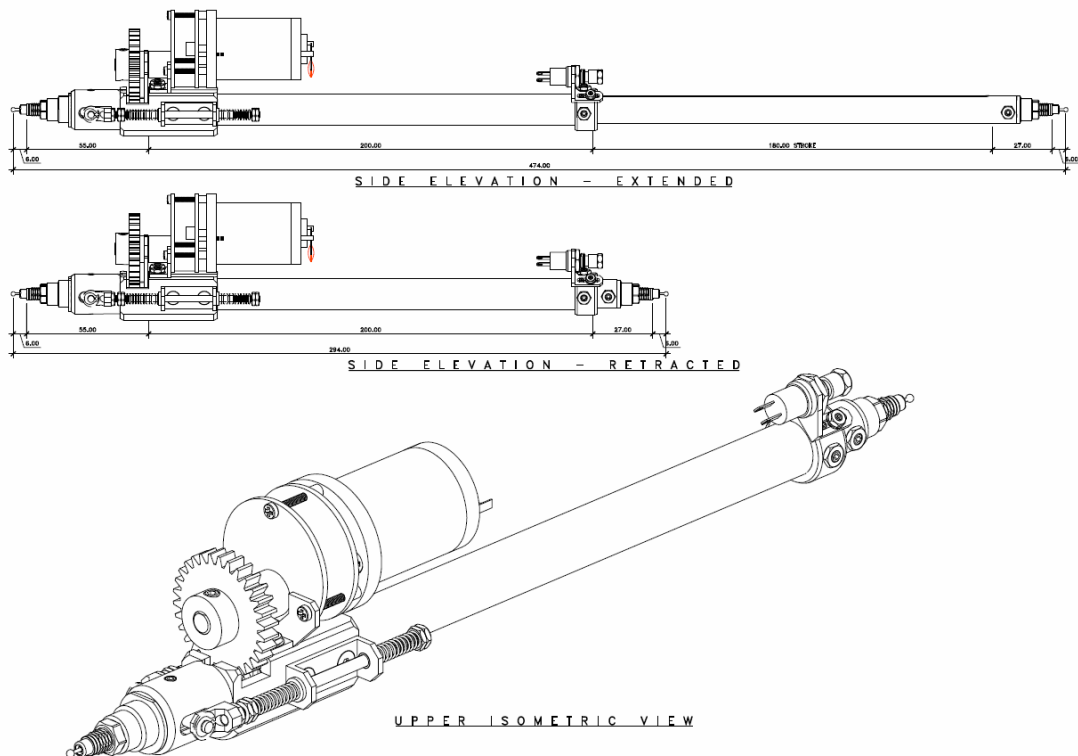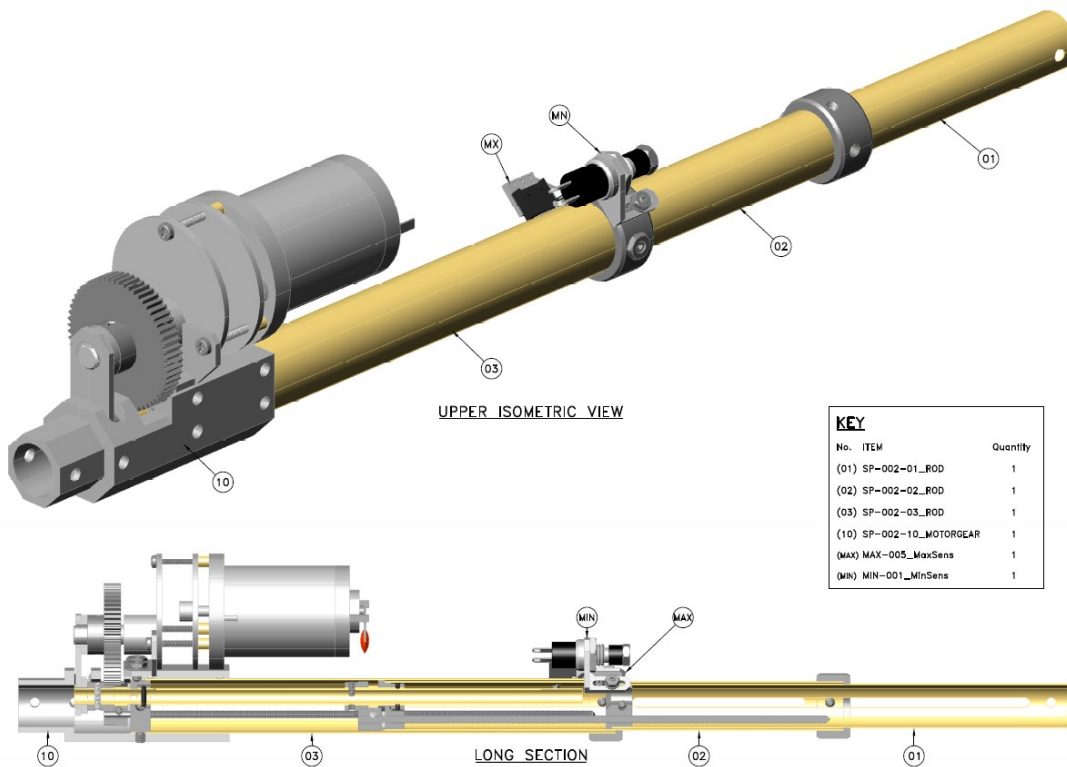

Figure 163: Drawing of the completed linear actuator at minimum contraction and maximum extention (top), isometric view of full actuator (bottom).

223

KEY

No.	ITEM	Quantity
(01)	SP–002–01_ROD	1
(02)	SP–002–02_ROD	1
(03)	SP–002–03_ROD	1
(10)	SP–002–10_MOTORGEAR	1
(MAX)	MAX–005_MaxSens	1
(MIN)	MIN–001_MinSens	1

Figure 164: the attachment of the motor and the switches with the tubes of the link (top). The internal assemblies of the actuator showing the attachment of the rod/lead screw with the barrel and the piston (bottom).
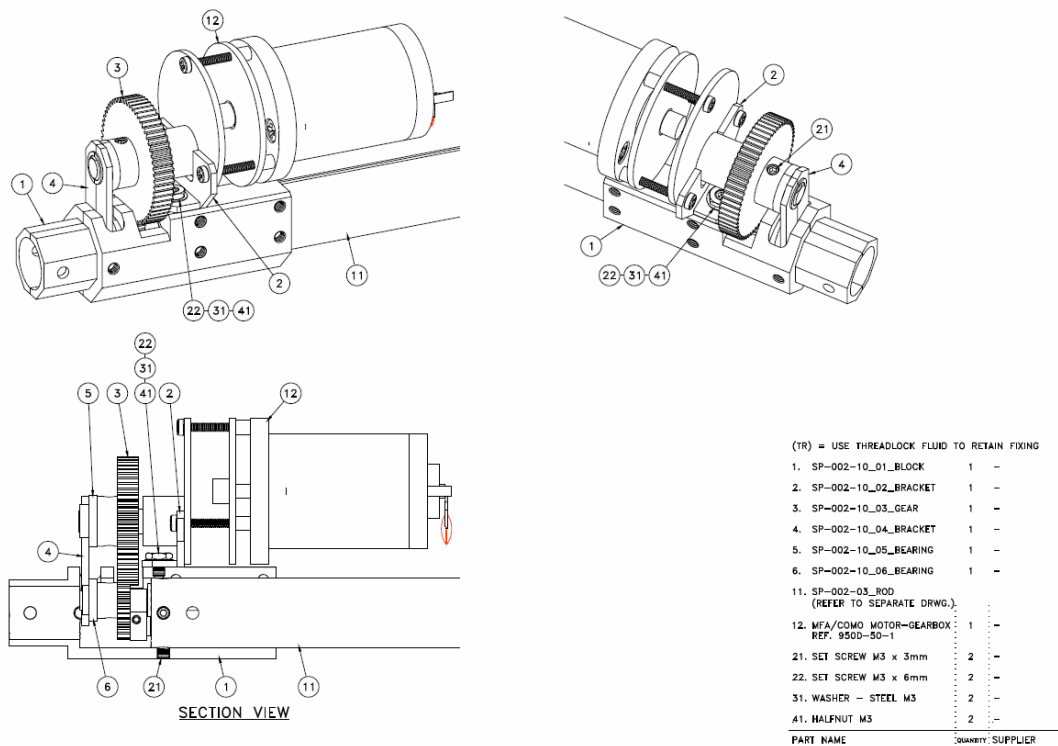
(TR) = USE THREADLOCK FLUID TO RETAIN FIXING

	PART NAME	QUANTITY	SUPPLIER
1.	SP–002–10_01_BLOCK	1	–
2.	SP–002–10_02_BRACKET	1	–
3.	SP–002–10_03_GEAR	1	–
4.	SP–002–10_04_BRACKET	1	–
5.	SP–002–10_05_BEARING	1	–
6.	SP–002–10_06_BEARING	1	–
11.	SP–002–03_ROD (REFER TO SEPARATE DRWG.)		
12.	MFA/COMO MOTOR-GEARBOX REF. 950D–50–1	1	–
21.	SET SCREW M3 x 3mm	2	–
22.	SET SCREW M3 x 6mm	2	–
31.	WASHER – STEEL M3	2	–
41.	HALFNUT M3	2	–

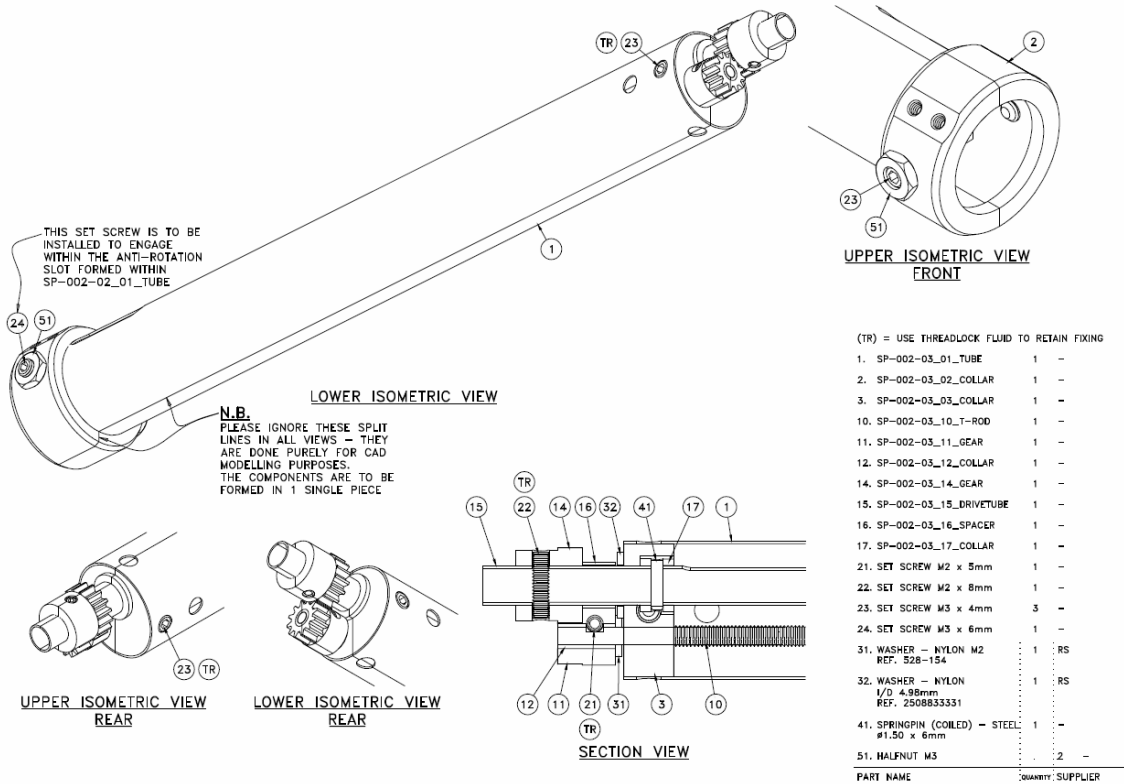**Figure 165:** Detailed drawing of the motor gears and motor bracket.

224

Figure 166: Detail drawings of the barrel part of the actuator with all parts that attached to it, which is connecting the barrel to the motor and the piston.

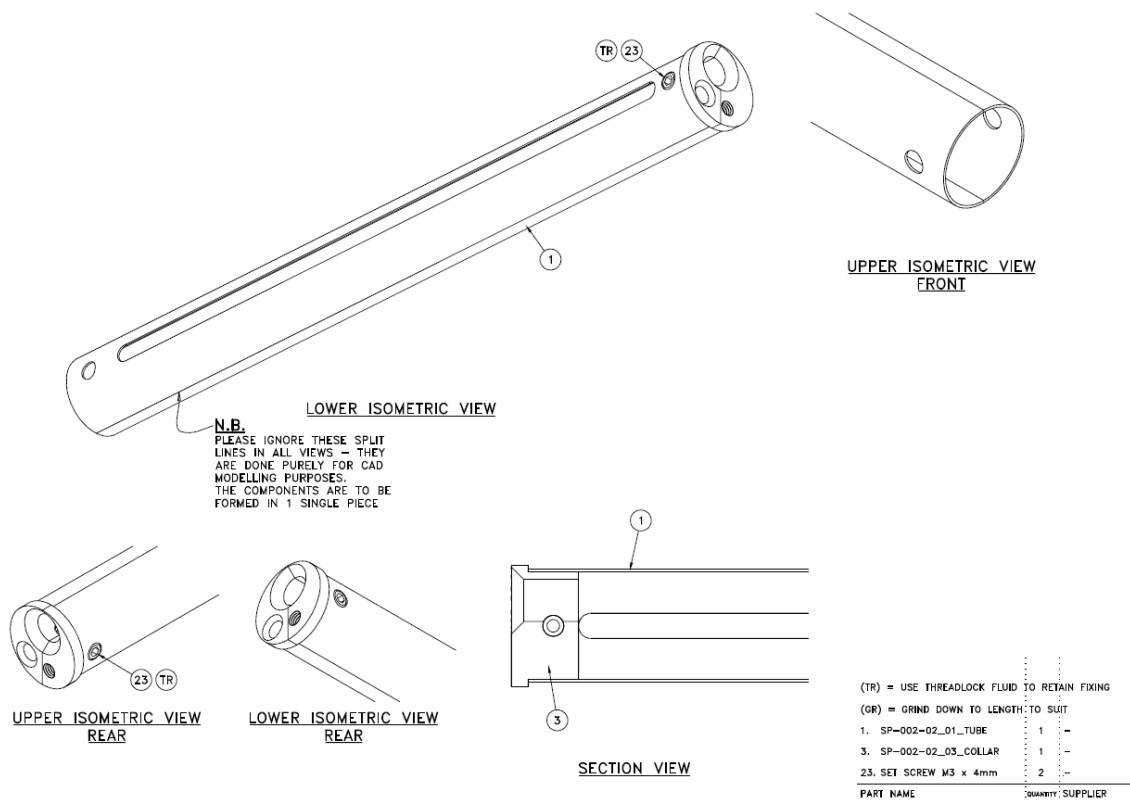**Figure 167:** Detail drawings of the piston part of the actuator with all parts that attached to it, which is connecting the piston to the barrel.